

**Synthesis of Nanomaterials for Energy Conversion and  
Environmental Applications**

By

**Pallavi Singhal**

**CHEM01201504011**

**Bhabha Atomic Research Centre, Mumbai-85**

*A Thesis submitted to the  
Board of Studies in Chemical Sciences  
In partial fulfillment of requirements  
For the Degree of*

**DOCTOR OF PHILOSOPHY**

*of*

**HOMI BHABHA NATIONAL INSTITUTE**



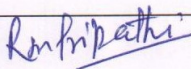
**December, 2018**



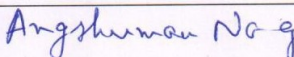
## Homi Bhabha National Institute<sup>1</sup>

### Recommendations of the Viva Voce Committee

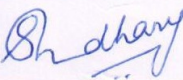
As members of the Viva Voce Committee, we certify that we have read the dissertation prepared by Ms. Pallavi Singhal entitled “**Synthesis of Nanomaterials for Energy Conversion and Environmental Applications**” and recommend that it may be accepted as fulfilling the thesis requirement for the award of Degree of Doctor of Philosophy.

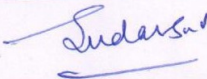
Chairman - Dr. R. M. Tripathi  Date: 21/12/2018

Guide/Convener - Dr. S. K. Jha  Date: 21-12-2018

Examiner - Prof. Anshuman Nag  Date: 21-12-2018

Member 1 - Prof. H. N. Ghosh  Date: 21/12/2018

Member 2 - Dr. Sangita D Kumar  Date: 21.12.18

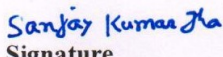
Member 3 - Dr. V. Sudarsan  Date: 21/12/2018

Final approval and acceptance of this thesis is contingent upon the candidate's submission of the final copies of the thesis to HBNI.

I/We hereby certify that I/we have read this thesis prepared under my/our direction and recommend that it may be accepted as fulfilling the thesis requirement.

Date: 21-12-2018

Place: Mumbai

  
Signature  
Guide

<sup>1</sup> This page is to be included only for final submission after successful completion of viva voce.



## **STATEMENT BY AUTHOR**

This dissertation has been submitted in partial fulfillment of requirements for an advanced degree at Homi Bhabha National Institute (HBNI) and is deposited in the Library to be made available to borrowers under rules of the HBNI.

Brief quotations from this dissertation are allowable without special permission, provided that accurate acknowledgement of source is made. Requests for permission for extended quotation from or reproduction of this manuscript in whole or in part may be granted by the Competent Authority of HBNI when in his or her judgment the proposed use of the material is in the interests of scholarship. In all other instances, however, permission must be obtained from the author.

**(Pallavi Singhal)**



## **DECLARATION**

I, hereby declare that the investigation presented in the thesis has been carried out by me. The work is original and has not been submitted earlier as a whole or in part for a degree / diploma at this or any other Institution / University.

**(Pallavi Singhal)**



## List of Publications

### Journal:

1. Ultrafast Hole/Electron Transfer Dynamics in a CdSe Quantum Dot Sensitized by Pyrogallol Red: A Super-Sensitization System. **Pallavi Singhal** and Hirendra N. Ghosh. **The Journal of Physical Chemistry C**, 2014, 118 (30), 16358-16365.
2. Hot-Hole Extraction from Quantum Dot to Molecular Adsorbate. **Pallavi Singhal** and Hirendra N. Ghosh. **Chemistry–A European Journal**, 2015, 21 (11), 4405-4412.
3. Exciton delocalization and hot hole extraction in CdSe QDs and CdSe/ZnS type 1 core shell QDs sensitized with newly synthesized thiols. **Pallavi Singhal**, Prashant V Ghorpade, Ganapati S Shankarling, Nancy Singhal, Sanjay K Jha, Raj M Tripathi, Hirendra N. Ghosh. **Nanoscale**, 2016, 8 (4), 1823-1833.
4. Metal-Ligand Complex Induced Ultrafast Charge Carrier Relaxation and Charge Transfer Dynamics in CdX (X= S, Se, Te) Quantum Dots Sensitized Nitro Catechol. **Pallavi Singhal**, P. Maity, S. K. Jha, and Hirendra. N. Ghosh. **Chemistry–A European Journal**, 2017, 23 (44), 10590-10596.
5. Electron-Transfer-Mediated Uranium Detection Using Quasi-Type II Core–Shell Quantum Dots: Insight into Mechanistic Pathways. **Pallavi Singhal\***, S. K. Jha, B. G. Vats, and Hirendra. N. Ghosh, 2017, **Langmuir**, 2017, 33 (33), 8114-8122.
6. Green, Water-Dispersible Photoluminescent On–Off–On Probe for Selective Detection of Fluoride Ions. **Pallavi Singhal\***, B. G. Vats, S. K. Jha, S. Neogy. **ACS Applied Material & Interfaces**, 2017, 9 (24), 20536–20544.

7. Rapid extraction of uranium from sea water using  $\text{Fe}_3\text{O}_4$  and humic acid coated  $\text{Fe}_3\text{O}_4$  nanoparticles. **Pallavi Singhal\***, Sanjay K. Jha, Shailaja P. Pandey, and Suman Neogy. **Journal of Hazardous Materials**, 2017, 335, 152–161.

8. Hot Charge Carrier Extraction from Semiconductor Quantum Dots. **Pallavi Singhal** and Hirendra. N. Ghosh, **The Journal of Physical Chemistry C** (Feature Article), 2018, 122 (31), 17586-17600.

## **Conferences:**

1. Ultrafast Hole/Electron Transfer Dynamics in CdSe Quantum Dot sensitized by Pyrogallol red (PGR): A Super-Sensitization System. **Pallavi Singhal**, and Hirendra N. Ghosh, Trombay Symposium on Radiation & Photochemistry (TSRP), BARC, Mumbai, India, 2014, Best Poster.

2. Ultrafast Hole Transfer Dynamics in CdSe Quantum Dots and CdSe/ZnS Core Shell Quantum Dots By Thiols. **Pallavi Singhal**, Ganapati S. Shankarling, and Hirendra N. Ghosh. Proceedings of Interdisciplinary Symposium on Materials Chemistry (ISMC), BARC, Mumbai, India, 2014, 346.

3. Hot Hole Extraction from CdSe/ZnS Type 1 Core Shell QD System using Newly Synthesized Thiols. **Pallavi Singhal**, Sanjay K. Jha, Raj M. Tripathi, and Hirendra N. Ghosh. Proceedings of Frontiers in advanced materials (FAM), IISc Bangalore, India, 2015, 72.

4. Charge Transfer Dynamics in CdX (X = S, Se, Te) Quantum Dots Sensitized with Nitro-Catechol. **Pallavi Singhal**, Partha Maity, Sanjay K. Jha, Raj M. Tripathi, and Hirendra N. Ghosh. Proceedings of Frontiers in advanced materials (FAM), IISc Bangalore, India, 2015, 73.

5. Effect of electron withdrawing group on Charge Transfer Dynamics in CdX (X = S, Se, Te) Quantum Dots Sensitized with Nitro-Catechol. **Pallavi Singhal**, Partha Maity, Sanjay K. Jha and Hirendra N. Ghosh. DAE Theme meeting on Ultrafast Science (UFS), BARC Mumbai, India, 2016, 53.
6. Quantum Dots as a Probe to Detect Uranium. **Pallavi Singhal**, Sanjay. K. Jha and Raj M. Tripathi. Proceedings of DAE-BRNS 6<sup>th</sup> interdisciplinary symposium on material chemistry (ISMC), BARC Mumbai, India, 2016, 234.
7. Sorption Studies of Cs<sup>+</sup>, Sr<sup>2+</sup> on the Fe<sub>3</sub>O<sub>4</sub> Nanoparticles (NPs) and Their Effect on Settlement Rate of NPs. **Pallavi Singhal**, Sanjay. K. Jha and Raj M. Tripathi. IARP 2016.
8. Extraction of Uranium from Sea Water Using Fe<sub>3</sub>O<sub>4</sub> and Humic Acid Coated Fe<sub>3</sub>O<sub>4</sub> Nanoparticles. **Pallavi Singhal**, Sanjay. K. Jha and Raj M. Tripathi. NUCAR, 2017, 272.
9. Uranium Detection Using Gold Nanoparticles. **Pallavi Singhal**, Vandana Pulhani and S. K. Jha. IARP, 2018.
10. An Ultra Trace Level Uranium Detection Using CdSe/CdS Quasi Type II Core Shell Quantum Dots. **Pallavi Singhal**, Sanjay K. Jha and Hirendra N. Ghosh. Symposium on Selenium Chemistry & Biology (SSCB-2017).
11. Carbon Quantum Dots as Green Water dispersible Photoluminescent *on-off-on* Probe for Selective Detection of Fluoride Ions. **Pallavi Singhal**, BalGovind Vats and Sanjay K. Jha. EAS-8, 2017, CSIR-NIIST, Thiruvananthapuram.

**(Pallavi Singhal)**



# DEDICATIONS

*To My Family and  
Well Wishers...*



## **ACKNOWLEDGEMENTs**

The work presented in this thesis would not have been possible without my close association with many people. I take this opportunity to extend my sincere gratitude and appreciation to all those who made their contribution in this Ph.D. thesis.

First and foremost, my heartfelt regard goes to my family members for their love, faith and support. Until their endless support my Ph.D. work would not be completed.

When it comes to scientific field, first and foremost I would like to extend my sincere gratitude to my mentor Prof. Hirendra N. Ghosh for introducing me to such an exciting field of research. His advice, patience and positive energy was always a source of inspiration to me and helped me to come out from odd circumstances. At this point I would like to take this opportunity to thank him for his valuable time and suggestions which helped me a lot to improve my work.

I would like to extend my sincere gratitude to my supervisor Dr. S. K. Jha for his continuous support during my work and helping me out under all circumstances.

I am obliged to Dr. R. S. Ningthoujam (BARC), Dr. Amitava Das (CSMCRI, Bhavnagar, India), Dr. K. K. Swain (BARC) for their excellent support. Their valuable suggestions helped me to improve the quality of my work.

I am also thankful to Homi Bhabha National Institute (HBNI), Government of India for providing me such a beautiful research facilities.

I wish to express my words of thanks to Dr. K. S. Pradeepkumar, Associate Director, HS&EG group, Dr. R. M. Tripathi, Head, Health Physics Division (BARC, India) for providing me their help during my research work.

I express my sincere thank to all of my Doctoral Committee members for their important suggestions during the annual review periods which help me to reach of the end of my dissertation.

My sincere thank to Dr. Anindya Datta (IITB, India), Dr. H. Pal (BARC), Dr. P. A. Hassan (BARC), Dr. A. K. Sanjukta (BARC) for letting me use the facilities at their laboratories.

I express my heartfelt gratitude's to all my lab mates and co-workers. I am indebted to all of them for their support but Govind, Tushar, Partha, Jayanta, Shitaljit, Sourav, Joshiji, Sugandhi mam, Rupali didi, Vandana Mam, Mausami, Kusum, Shuchita, Pragati, Akansha call for a special mention. The valuable discussions that we had and the co-operation they extended contributed significantly to my research work. Thank you all for being such a gem of a team which made daily work enjoyable and fun.

Finally, I am thankful to all the members of the Department of Atomic Energy (DAE) including the administrative and security stuffs for cooperation.

**(Pallavi Singhal)**

BARC, Mumbai

August, 2018.

# **List of Contents**

	<b>Page No.</b>
<b>Synopsis</b>	(i-xii)
<b>List of Figures</b>	(xiii-xxiii)
<b>List of Schemes</b>	(xxiv-xxv)
<b>List of Tables</b>	(xxvi-xxvii)
<b>Chapter 1: Introduction</b>	<b>1-30</b>
1.1. General Background	1
1.2. Nanomaterials	7
1.2.1. Surface Effect	8
1.2.2. Quantum Size Effect	9
1.3. Quantum Dot (QDs)	10
1.3.1. Electronic Structure of the QDs: Theoretical Framework	12
1.3.1.1. Particle-in-a-Sphere Model	12
1.3.1.2. Effective Mass Approximation	13
1.3.1.3. Band Structure	14
1.3.1.4. Energy Structure of QDs	15
1.3.2. Dark Exciton and Stoke Shift	16
1.3.3. Charge Carrier Relaxation in QDs	18
1.3.3.1. Phonon Bottleneck	18
1.3.3.2. Electron-Hole Energy Transfer	19
1.3.3.3. Multi-Exciton Generation and Augur Recombination	19
1.3.3.4. Involvement of Defect States	20
1.3.4. Charge Separation in QDs	20
1.3.4.1. Charge Separation in Core-Shell Heterostructure	20

1.3.4.2. Metal-Semiconductor Heterostructure	22
1.3.4.3. Dye-Semiconductor Heterostructure	22
1.3.5. Synthesis of QDs	23
1.4. Quantum Dot Solar Cell (QDSC)	24
1.5. Theory of Electron Transfer	25
1.6. Magnetic Nanoparticles	27
1.7. Overview and Scope of the Thesis	28
<b>Chapter 2: Experimental Techniques</b>	<b>31-67</b>
2.1. X-Ray Diffraction (XRD)	31
2.2. Transmission Electron Microscopy (TEM)	34
2.3. Fourier Transform Infrared Spectroscopy (FTIR)	36
2.4. Thermogravimetric analysis (TGA)	37
2.5. Zeta Potential	38
2.6. Vibrating Sample Magnetometer (VSM)	39
2.7. Inductively Coupled Plasma Mass Spectrometer (ICP-MS)	39
2.8. UV-Visible Absorption Spectroscopy	41
2.9. Photoluminescence (PL) Spectroscopy	43
2.10. Fluorescence Lifetime Measurements	46
2.10.1. Time Correlated Single Photon Counting (TCSPC)	48
2.10.1.1. Pulsed Excitation Source	49
2.10.1.2. Constant Fraction Discriminator (CFD)	50
2.10.1.3. Time to Amplitude Converter (TAC)	50
2.10.1.4. Multichannel Analyzer (MCA)	51
2.10.1.5. Start and the Stop PMTs	51

2.10.1.6. Time Calibration of the MCA Channels in a TCSPC Spectrometer	51
2.10.1.7. Analysis of the Fluorescence Decay Curves Measured in a TCSPC Instrument	51
2.10.1.7.1. Reduced Chi-square ( $\chi_r^2$ ) Values	52
2.10.1.7.2. Distribution of Weighted Residuals	53
2.10.2. Fluorescence Up-Conversion Measurements	54
2.11. Femtosecond Transient Absorption (TA) Spectroscopy: Pump-Probe Technique	56
2.11.1. Ultrashort Pulse Generation: Ti-Sapphire Oscillator	59
2.11.2. Chirped Pulse Amplification (CPA)	60
2.11.2.1. Pulse Stretcher	61
2.11.2.2. Pulse Picker	62
2.11.2.3. Confocal Multipass Ti:Sapphire Amplifier (MPA)	62
2.11.2.4. Pulse Compressor	63
2.11.3. Second Harmonic Generation (SHG)	63
2.11.4. White Light Generation (WLG)	64
2.11.5. Pump-probe Transient Absorption Spectrometer	65
2.12. Pulse Radiolysis	66

### **Chapter-3: Ultrafast Charge Carrier Dynamics in QDs/Molecular Adsorbate System:**

<b>An Implication to High Efficiency Quantum Dot Solar Cell</b>	<b>68-131</b>
3.1. Introduction	68
3.2. Experimental	73
3.2.1. Chemicals	73
3.2.2. Synthesis of CdX QDs	73
3.2.3. Synthesis of CdSe/ZnS Type-I core shell QDs	74

3.3. Results & Discussions	75
3.3.1. Ultrafast Hole/Electron Transfer Dynamics in CdSe QDs Sensitized by PGR: A Super-Sensitization System	75
3.3.2. Hot Hole Extraction in QDs/Catechol and QDs/Thiol composite System	84
3.3.2.1. Hot hole extraction dynamics in CdSe QDs/Catechol composite system	84
3.3.2.2. Hot hole extraction dynamics in CdSe QDs/thiols composite system	97
3.3.3. Metal-Ligand Complex Induced Ultrafast Charge Separation and Electron Relaxation Dynamics in CdX (X = S, Se, Te) Quantum Dots Sensitized Nitro Catechol	115
3.4. Conclusions	129
<b>Chapter-4: Quantum Dots as a Probe to Detect Uranium and Fluoride Ions</b>	<b>132-165</b>
4.1. Introduction	132
4.2. Experimental	137
4.2.1. Materials	137
4.2.2. Synthesis of CdSe/CdS Quasi Type-II core shell QDs	138
4.2.3. Synthesis of water dispersible MPA capped QDs and core shell QDs via ligand exchange	138
4.2.4. Synthesis of Carboxylic acid functionalized CQDs	139
4.3. Results and Discussions	139
4.3.1. CdSe/CdS core shell QDs for uranium detection	139
4.3.2. CQDs as a probe for fluoride ion detection	152
4.4. Conclusions	164

<b>Chapter-5: Metal Ion Extraction Using Magnetic and Functionalized Magnetic Nanoparticles</b>	<b>166-182</b>
5.1. Introduction	166
5.2. Experimental	168
5.2.1. Materials	168
5.2.2. Synthesis of Fe <sub>3</sub> O <sub>4</sub> NPs	168
5.2.3. Synthesis of HA coated Fe <sub>3</sub> O <sub>4</sub> NPs.	169
5.3. Results and Discussions	169
5.3.1. Structural and morphology studies	169
5.3.2. Sorption Studies of uranium on Fe <sub>3</sub> O <sub>4</sub> and HA coated Fe <sub>3</sub> O <sub>4</sub> NPs	172
5.4. Conclusions	181
<b>Chapter-6: Summary and Outlook</b>	<b>183-188</b>
6.1. Summary	183
6.2. Outlook	187
<b>References</b>	<b>189-214</b>



## **SYNOPSIS**

Over the last 30 years, nanomaterials have revolutionized the field of chemistry in number of fields such as bioimaging, environmental decontamination, solar energy conversion, and catalysis. The extremely small size of nanomaterials results in a high percentage of atoms at the surface making these nanomaterials more reactive as compared to their larger size material. Examples of such engineered nanomaterials include quantum dots (QDs) and magnetic nanoparticles (NPs), the two nanomaterials used in the present thesis work. QDs are semiconductor nanocrystals having size less than their bohr excitonic radius and have different optical and electrical properties depending on their size<sup>1</sup>. This property allows their use in number of applications including drug delivery, energy conversion, environmental remediation etc. Magnetic NPs, the other class of nanomaterials show superparamagnetic behaviour and high saturation magnetization<sup>2</sup>. This property makes their separation from matrix very easy leading to their use in number of applications. In the present thesis work we have studied the use of these two nanomaterials for solar energy conversion and environmental remediation. The work carried out in the present thesis is divided into six chapters. A brief summary about the content of each chapter is given below:

### **CHAPTER 1: General Introduction**

This chapter describes the application of nanomaterials for toxic ions detection, their separation from environmental matrices and for solar energy conversion. Nowadays different contaminants are present in environment with concentrations more than the permissible limits<sup>3,4</sup>. Therefore, to ensure the protection of environment it is utmost important to detect the presence of these contaminants at trace concentrations and to separate them from different environmental matrices. Two different nanomaterials, QDs and magnetic NPs have been used for this purpose and a brief description about their application as a chemo-sensor and as a

scavenger has been discussed. This chapter also covers in detail the application of QDs for solar energy conversion and working principle of quantum dot solar cell (QDSC). The basic properties and electronic structure of QDs have been discussed utilizing quantum mechanical model. Different properties of magnetic NPs such as saturation magnetization, hysteresis loop have been described.

## **CHAPTER 2: Experimental Techniques**

The present thesis work involves synthesis of QDs and magnetic NPs for energy conversion and environmental remediation. Different characterization techniques such as X-ray diffraction (XRD), high resolution transmission electron microscopy (HRTEM), Fourier transform infrared spectroscopy (FTIR), thermogravimetric analysis (TGA), zeta Potential, vibrating sample magnetometer (VSM), inductively coupled plasma mass spectrometry (ICP-MS), steady state optical absorption and emission techniques, time resolved emission techniques, femtosecond transient absorption (TA) spectroscopy were used to characterize these materials and study their properties. Crystal structure and crystallite size was determined using XRD. Particle size was determined using HRTEM measurements. Functional group analysis was carried out by FTIR. Amount of organic coating was determined by TG measurements. Trace metal concentrations was determined by ICP-MS. Optical properties of QDs were determined using steady state optical absorption and emission studies. Rate of electron transfer and hole transfer processes were determined by time resolved techniques. Charge carrier dynamics in ultrafast time scale was monitored by TA spectroscopy. This chapter describes the basic principle and optical layout of above techniques.

## **CHAPTER 3: Ultrafast Charge Carrier Dynamics in QDs/Molecular Adsorbate System: An Implication to High Efficiency Quantum Dot Solar Cell**

Solar energy is one of the most important and clean sources of energy and a variety of materials have been explored to convert and harvest it into electricity. Among them quantum dots (QDs) are one of the most probable candidates because of their exciting properties such as higher solar radiation absorption coefficient, optical tunability, slow charge carrier relaxation, multiple exciton generation and hot charge carrier extraction<sup>1-5</sup>. Till date the highest conversion efficiency achieved in quantum dot solar cell (QDSC) is ~12%<sup>6</sup>. However the theoretical conversion efficiency in any QDSC is ~31%<sup>7</sup>. This calls for an improvement in QDSC efficiency and to understand the reasons for its lower efficiency. Photo-excitation of QDs material generates electron and hole pair. To get higher efficient QDSC, it is utmost important to extract these charge carriers prior to their recombination. It has been observed that electron transfer rate from QDs was much faster and takes place in ultrafast time scale. However hole transfer rate was reported to be slow<sup>8,9</sup>. This slow hole transfer process increases the recombination probability between photo-generated electron and hole and considered to be the main reasons for lower efficiency of QDSC. This chapter describes the ultrafast charge carrier dynamics of QDs/molecular adsorbate systems where different molecular adsorbates were chosen that act as hole transporting molecules for QDs. We have demonstrated that hole can be extracted at a comparable rate to that of electron. This chapter is divided into three parts.

In the first part of this chapter we have introduced the concept of super sensitization. In super sensitization, QDs and molecular adsorbate both absorb solar radiation creating photo-excited electron and hole. The energetic of the process is such that after photo-excitation one of the charge carriers, (either electron or hole) will be localized in QDs while other will be localized in molecular adsorbate resulting in grand charge separation. This we have demonstrated in a coupled system of CdSe QDs and pyrogallol red (PGR) where both CdSe QDs and PGR absorb solar radiation generating electron and hole. Redox energy level

suggest that hole transfer from QDs to PGR and electron transfer from PGR to QDs is thermodynamically favourable processes. Femtosecond transient absorption spectroscopy has been carried out which suggest the formation of PGR cation radical and electrons in QDs resulting in grand charge separation. Hole transfer and electron transfer time were observed to be ~500 fs and ~150 fs respectively.

In the second part of this chapter we have described the hot hole extraction processes from QDs and core shell quantum dots (CSQDs) to catechols and thiols. It has been demonstrated that efficiency of QDSC can reach upto 66%<sup>10</sup> if the hot charge carriers can be extracted prior to their cooling. Researchers have reported hot electron extraction process from QDs<sup>11,12</sup> however no study were available on hot hole extraction which is also an equally important process to get higher efficient QDSC. In this part, experimental results pertaining to hot hole extraction from QDs in a composite system of QDs and catechols/thiols were discussed. Experiments were also carried out in presence of type 1 shell over CdSe core to find whether hot hole extraction process is still possible or not. Ultrafast transient absorption spectroscopy and femtosecond fluorescence upconversion techniques were used to monitor different processes in ultrafast time scale. The effect of electron withdrawing and electron donating groups on charge carrier dynamics was also studied.

In the third part of this chapter we have described the effect of interfacial complex on charge carrier dynamics of CdX (X=S, Se, Te) QDs sensitized with nitro catechol (NCAT). We have chosen a composite system of CdX QDs and NCAT where NCAT serve as a hole transporting molecule for CdX QDs. Interestingly a complex formation was observed between CdX QDs and NCAT that results because of interaction between Cd<sup>2+</sup> ions on QDs surface and NCAT. A detailed study were performed to study the effect of this complexation on charge carrier dynamics of CdX/NCAT composite system and observed that complex formation favours better charge separation.

## CHAPTER 4: Quantum Dots as a Probe to Detect Uranium and Fluoride Ions

Uranium, a well known nephrotoxic element has maximum permissible concentration of ~35 ppb and 60 ppb in drinking water, as suggested by WHO<sup>13</sup> and AERB respectively. A large part of the country, for ex. Punjab has high concentration of uranium in potable water. Therefore, it is utmost important to detect uranium if the concentration is more than this limit. Along with uranium, the design of fluoride ion sensors is also an active area of investigation because of its high toxicity and widespread availability in drinking water, toothpaste, and osteoporosis drugs. It is considered as one of the major water pollutants with maximum concentration in drinking water ~1.5 mg/L<sup>14</sup>. Therefore, there is a great need to design systems which can quickly detect the presence of these contaminants at trace concentrations. Several methods, including atomic absorption spectroscopy, inductively coupled plasma atomic emission spectrometry, electrochemical sensing, titration, chromatographic methods have been used to measure the toxic ion concentration. However these methods require complex instrumentation and trained personals. At the same time these techniques are expensive and therefore cannot be carried out in minimal resourced laboratories. To overcome these limitations optical sensing approaches<sup>3,4</sup> have attracted great attention. Different organic molecules with high fluorescence yield and specific binding groups have been used for detection of contaminants<sup>3</sup>. But the synthesis of these organic molecules is a challenging task. Also most of the detection require aqueous medium and therefore further treatment is required to make these organic molecules water dispersible. For this purpose, QDs are attracting a substantial attention because of their high fluorescence quantum yield<sup>4</sup> and high aqueous dispersibility. Recently trace element detection by luminescence quenching of different QDs have been reported by many research groups<sup>4</sup>. However not many reports are available on detection of uranium and fluoride ions using QDs. This chapter covers the

work carried out to demonstrate QDs as a probe to detect uranium and fluoride ions. This chapter is divided into two sections.

In the first part of this chapter we have discussed the application of QDs as a tool to detect uranium and described the complete mechanistic pathways of detection. Uranium detection using amine modified CdS QDs has been demonstrated earlier by Dutta and Kumar<sup>15</sup> where they have observed a detection limit of ~5ppb. However a clear mechanism of detection was not given which is extremely important for making efficient detection technology. For this purpose we have synthesized high luminescent water dispersible CdSe QDs and CdSe/CdS CSQDs with three different thickness of CdS shell. Steady state luminescence studies suggest a quenching in QDs luminescence intensity on addition of uranium. Redox levels of QDs and uranium suggests that electron transfer process from photo-excited QDs to uranium is thermodynamically viable process, which has subsequently been confirmed by time resolved studies. Stern-Volmer plot of CSQDs with uranium suggests that the detection limit of this method is 74.5 ppb. The method has an advantage over other reported methods for being simple, low cost and least sample processing and a clear mechanism of detection has been demonstrated which in turn will help in future to design more efficient detection systems.

In the second part of this chapter, we have demonstrated a coupled system of carbon quantum dots (CQDs) and  $\text{Eu}^{3+}$  where photoluminescence property of CQDs was used for fluoride ion sensing. A number of composite of QDs have been used earlier for this purpose<sup>14</sup>. However their applicability in real samples has not been demonstrated. At the same time to design and develop better detection probes it is very important to understand the working mechanism of the probe which is still lacking in literature. For this purpose we have used a composite system of CQDs and  $\text{Eu}^{3+}$  and described a complete mechanism of detection. On addition of  $\text{Eu}^{3+}$  ions luminescence quenching in CQDs emission was observed

(switch-off) and is due to both electron transfer from CQDs to  $\text{Eu}^{3+}$  and aggregation of CQDs. Interestingly luminescence regains after the addition of fluoride ions into the CQDs/ $\text{Eu}^{3+}$  system (switch-on). This has been assigned to the  $\text{Eu}^{3+}$  removal from CQDs surface due to the formation of  $\text{EuF}_3$  and is confirmed by XRD and HRTEM measurements. Experiments with other competing ions suggest that the probe is highly selective in nature and can be used for real sample analysis. The suggested probe is green, economical, rapid, efficient, and most importantly selective and can be used for detection of fluoride ions in real samples.

## **CHAPTER 5: Metal Ion Extraction Using Magnetic and Functionalized Magnetic Nanoparticles**

Exposure to radioactive environment can lead to serious consequences on both human health and environment. Therefore the separation of these ions from the environment, mainly from water bodies is necessary to keep the environment protected. The most widely used methods for this includes liquid-liquid extraction, solid-phase extraction (SPE), co-precipitation, floatation and electrochemical deposition<sup>16</sup>. Among these, SPE has become increasingly popular as compared with classical liquid-liquid extraction method because of its advantages of high enrichment factor, high recovery, rapid phase separation, low cost and low consumption of organic solvents. A variety of materials<sup>16</sup> have been explored as solid phase extractant however each has its own limitations such as non selectivity and difficult separation from the matrix. To overcome these limitations magnetic NPs attain a lot of attention in recent years<sup>2</sup> and a number of reports are available where their application in environmental remediation<sup>2</sup> has been demonstrated. In this chapter we have demonstrated the use of  $\text{Fe}_3\text{O}_4$  NPs for removal of different metal ions. We have also synthesized humic acid coated  $\text{Fe}_3\text{O}_4$  NPs and explored its use for uranium extraction from sea water matrix. We have observed ~90% uranium sorption at ppb concentrations from water samples. A theoretical model for ion sorption on NPs surface has been proposed.

## CHAPTER 6: Summary and Outlook

In summary, we have synthesized and characterized different nanomaterials and use them for solar energy conversion and environmental detoxification. One of the major limitations in any QDSC is slow hole transfer rate from QDs materials as compared to electron. We have investigated a series of molecular adsorbates which can extract hole from QDs materials at a comparable rate to that of electron which in turn will help to increase the efficiency of QDSC. We have also described the use of QDs as a probe to detect uranium and fluoride ions where CdSe/CdS CSQDs and carbon QDs were used for this purpose. The study brings out a clear understanding on the detection mechanism involved which in turn will help in future to design and develop better detection technology. Work with magnetic NPs as a sorbent suggests that these NPs can trap contaminants from large volume sample.

### REFERENCES:

- (1) Alivisatos, A. P.: Semiconductor Clusters, Nanocrystals, and Quantum Dots. *Science* **1996**, *271*, 933-937.
- (2) Lu, A.-H.; Salabas, E. L.; Schüth, F.: Magnetic Nanoparticles: Synthesis, Protection, Functionalization, and Application. *Angewandte Chemie International Edition* **2007**, *46*, 1222-1244.
- (3) Quang, D. T.; Kim, J. S.: Fluoro- and Chromogenic Chemodosimeters for Heavy Metal Ion Detection in Solution and Biospecimens. *Chemical Reviews* **2010**, *110*, 6280-6301.
- (4) Lou, Y.; Zhao, Y.; Zhu, J.-J.: Ultrasensitive optical detection of anions by quantum dots. *Nanoscale Horizons* **2016**, *1*, 125-134.
- (5) Klimov, V. I.: Optical Nonlinearities and Ultrafast Carrier Dynamics in Semiconductor Nanocrystals. *The Journal of Physical Chemistry B* **2000**, *104*, 6112-6123.

- (6) Du, J.; Du, Z.; Hu, J.-S.; Pan, Z.; Shen, Q.; Sun, J.; Long, D.; Dong, H.; Sun, L.; Zhong, X.; Wan, L.-J.: Zn–Cu–In–Se Quantum Dot Solar Cells with a Certified Power Conversion Efficiency of 11.6%. *Journal of the American Chemical Society* **2016**, *138*, 4201-4209.
- (7) Shockley, W.; Queisser, H. J.: Detailed Balance Limit of Efficiency of p-n Junction Solar Cells. *Journal of Applied Physics* **1961**, *32*, 510-519.
- (8) Kamat, P. V.: Quantum Dot Solar Cells. Semiconductor Nanocrystals as Light Harvesters *The Journal of Physical Chemistry C* **2008**, *112*, 18737-18753.
- (9) Kamat, P. V.: Quantum Dot Solar Cells. The Next Big Thing in Photovoltaics. *The Journal of Physical Chemistry Letters* **2013**, *4*, 908-918.
- (10) Ross, R. T.; Nozik, A. J.: Efficiency of hot-carrier solar energy converters. *Journal of Applied Physics* **1982**, *53*, 3813-3818.
- (11) Pandey, A.; Guyot-Sionnest, P.: Hot Electron Extraction From Colloidal Quantum Dots. *The Journal of Physical Chemistry Letters* **2010**, *1*, 45-47.
- (12) Tisdale, W. A.; Williams, K. J.; Timp, B. A.; Norris, D. J.; Aydil, E. S.; Zhu, X.-Y.: Hot-Electron Transfer from Semiconductor Nanocrystals. *Science* **2010**, *328*, 1543-1547.
- (13) Manos, M. J.; Kanatzidis, M. G.: Layered Metal Sulfides Capture Uranium from Seawater. *Journal of the American Chemical Society* **2012**, *134*, 16441-16446.
- (14) Mohapatra, S.; Sahu, S.; Nayak, S.; Ghosh, S. K.: Design of Fe<sub>3</sub>O<sub>4</sub>@SiO<sub>2</sub>@Carbon Quantum Dot Based Nanostructure for Fluorescence Sensing, Magnetic Separation, and Live Cell Imaging of Fluoride Ion. *Langmuir* **2015**, *31*, 8111-8120.
- (15) Dutta, R. K.; Kumar, A.: Highly Sensitive and Selective Method for Detecting Ultratrace Levels of Aqueous Uranyl Ions by Strongly Photoluminescent-Responsive Amine-Modified Cadmium Sulfide Quantum Dots. *Analytical Chemistry* **2016**, *88*, 9071-9078.
- (16) Duff, M. C.; Hunter, D. B.; Hobbs, D. T.; Fink, S. D.; Dai, Z.; Bradley, J. P.: Mechanisms of Strontium and Uranium Removal from High-Level Radioactive Waste

Simulant Solutions by the Sorbent Monosodium Titanate. *Environmental Science & Technology* **2004**, 38, 5201-5207.

### **Publications in Refereed Journal:**

#### **a. Published**

1. Ultrafast Hole/Electron Transfer Dynamics in CdSe Quantum Dot Sensitized by Pyrogallol red (PGR): A Super-Sensitization System. **Pallavi Singhal**, and Hirendra N. Ghosh. **J. Phys. Chem. C**, 2014, 118, 16358-16365.
2. Hot Hole Extraction from Quantum Dot to Molecular Adsorbate, **Pallavi Singhal**, and Hirendra N. Ghosh. **Chem. Eur. J.**, 2015, 21, 4405-4412.
3. Exciton delocalization and hot hole extraction in CdSe QDs and CdSe/ZnS type 1 core shell QDs sensitized with newly synthesized thiols. **Pallavi Singhal**, Prashant V. Ghorpade, Ganapati S. Shankarling, Nancy Singhal, Sanjay K. Jha, Raj M. Tripathi, and Hirendra N. Ghosh. **Nanoscale**, 2016, 8 (4), 1823-1833.
4. Metal-Ligand Complex Induced Ultrafast Charge Carrier Relaxation and Charge Transfer Dynamics in CdX (X= S, Se, Te) Quantum Dots Sensitized Nitro Catechol. **Pallavi Singhal**, P. Maity, S. K. Jha, and Hirendra. N. Ghosh. **Chem. Eur. J.**, 2017, 23 (44), 10590-10596.
5. Electron-Transfer-Mediated Uranium Detection Using Quasi-Type II Core–Shell Quantum Dots: Insight into Mechanistic Pathways. **Pallavi Singhal\***, S. K. Jha, B. G. Vats, and Hirendra. N. Ghosh, 2017, **Langmuir**, 2017, 33 (33), 8114-8122.
6. Green, Water-Dispersible Photoluminescent On–Off–On Probe for Selective Detection of Fluoride Ions. **Pallavi Singhal\***, B. G. Vats, S. K. Jha, S. Neogy. **ACS Appl. Mater. Interfaces**, 2017, 9 (24), 20536–20544.

7. Rapid extraction of uranium from sea water using  $\text{Fe}_3\text{O}_4$  and humic acid coated  $\text{Fe}_3\text{O}_4$  nanoparticles. **Pallavi Singhal\***, Sanjay K. Jha, Shailaja P. Pandey, and Suman Neogy. **Journal of Hazardous Materials**, 2017, 335, 152–161.

**b. Communicated**

1. Spectroscopic Investigation on Hot Charge Carrier Extraction from Semiconductor Quantum Dots: A Step toward High Efficiency Quantum Dot Solar Cell. **Pallavi Singhal** and Hirendra. N. Ghosh , **JPCC** (under revision)

**Conference Publications:**

1. Ultrafast Hole/Electron Transfer Dynamics in CdSe Quantum Dot sensitized by Pyrogallol red (PGR): A Super-Sensitization System. **Pallavi Singhal**, and Hirendra N. Ghosh, Trombay Symposium on Radiation & Photochemistry (TSRP), BARC, Mumbai, India, 2014, **Best Poster**.

2. Ultrafast Hole Transfer Dynamics in CdSe Quantum Dots and CdSe/ZnS Core Shell Quantum Dots By Thiols. **Pallavi Singhal**, Ganapati S. Shankarling, and Hirendra N. Ghosh. Proceedings of Interdisciplinary Symposium on Materials Chemistry (ISMC), BARC, Mumbai, India, 2014, 346.

3. Hot Hole Extraction from CdSe/ZnS Type 1 Core Shell QD System using Newly Synthesized Thiols. **Pallavi Singhal**, Sanjay K. Jha, Raj M. Tripathi, and Hirendra N. Ghosh. Proceedings of Frontiers in advanced materials (FAM), IISc Bangalore, India, 2015, 72.

4. Charge Transfer Dynamics in CdX (X = S, Se, Te) Quantum Dots Sensitized with Nitro-Catechol. **Pallavi Singhal**, Partha Maity, Sanjay K. Jha, Raj M. Tripathi, and Hirendra N. Ghosh. Proceedings of Frontiers in advanced materials (FAM), IISc Bangalore, India, 2015, 73.

5. Effect of electron withdrawing group on Charge Transfer Dynamics in CdX (X = S, Se, Te) Quantum Dots Sensitized with Nitro-Catechol. **Pallavi Singhal**, Partha Maity, Sanjay K. Jha and Hirendra N. Ghosh. DAE Theme meeting on Ultrafast Science (UFS), BARC Mumbai, India, 2016, 53.
6. Quantum Dots as a Probe to Detect Uranium. **Pallavi Singhal**, Sanjay. K. Jha and Raj M. Tripathi. Proceedings of DAE-BRNS 6<sup>th</sup> interdisciplinary symposium on material chemistry (ISMC), BARC Mumbai, India, 2016, 234.
7. Sorption Studies of Cs<sup>+</sup>, Sr<sup>2+</sup> on the Fe<sub>3</sub>O<sub>4</sub> Nanoparticles (NPs) and Their Effect on Settlement Rate of NPs. **Pallavi Singhal**, Sanjay. K. Jha and Raj M. Tripathi. IARP 2016.
8. Extraction of Uranium from Sea Water Using Fe<sub>3</sub>O<sub>4</sub> and Humic Acid Coated Fe<sub>3</sub>O<sub>4</sub> Nanoparticles. **Pallavi Singhal**, Sanjay. K. Jha and Raj M. Tripathi. NUCAR, 2017, 272.
9. Uranium Detection Using Gold Nanoparticles. **Pallavi Singhal**, Vandana Pulhani and S. K. Jha. IARP, 2018.
10. An Ultra Trace Level Uranium Detection Using CdSe/CdS Quasi Type II Core Shell Quantum Dots. **Pallavi Singhal**, Sanjay K. Jha and Hirendra N. Ghosh. Symposium on Selenium Chemistry & Biology (SSCB-2017).
11. Carbon Quantum Dots as Green Water dispersible Photoluminescent *on-off-on* Probe for Selective Detection of Fluoride Ions. **Pallavi Singhal**, BalGovind Vats and Sanjay K. Jha. EAS-8, 2017, CSIR-NIIST, Thiruvananthapuram.

## List of Figures

**Figure 1.1(A)** Energy level diagram of a bulk semiconductor and quantum dot. **(B)** A schematic representation of the continuous absorption spectrum of a bulk semiconductor (curved line), compared to the discrete absorption spectrum of a QD (vertical bars).

**Figure 1.2:** Band energy diagram of **(A)** direct and **(B)** indirect bulk semiconductor.

**Figure 1.3:** Valence band (VB) splitting of the bulk CdSe in **(A)** diamond and **(B)** wurtzite like structure at  $k=0$  point.

**Figure 1.4.** Optical absorption spectrum of CdSe QDs and assignment of different excitonic states. In schematic diagram the lowest energy allowed interband (VB to CB) transitions are shown for CdSe QDs.

**Figure 1.5(A)** Fine structure splitting of band edge transition of CdSe QDs **(B)** Schematic of dark and bright state. Blue arrow shows absorption and red arrows shows emission from bright (bold) and dark (dotted) state.

**Figure 1.6:** Schematic of **(A)** Multi-Exciton Generation and **(B)** Augur process.

**Figure 1.7:** Schematic of **(A)** electron and **(B)** hole trapping in surface defects.

**Figure 1.8:** Illustration of charge carrier distribution in different types of core-shell heterostructure.

**Figure 1.9:** Band alignment of **(A)** metal-QDs and **(B)** Dye-QDs heterostructure.

**Figure 1.10:** Nucleation and growth stage for colloidal particle in La Mer growth model.

**Figure 1.11:** Schematic diagram illustrating the structure and operation of QDSC.

**Figure 1.12:**  $\ln(k_{eT})$  vs.  $G^0$  plot shows three different region of electron transfer reaction.

**Figure 2.1:** Illustration of Bragg law in a crystal.

**Figure 2.2.** Schematic presentation of a XRD instrument.

**Figure 2.3:** Schematic illustration of a typical TEM instrument.

**Figure 2.4:** Layout of FTIR Spectrometer

**Figure: 2.5.** Schematic of an ICP-MS system.

**Figure: 2.6.** Diagram of quadruple mass filter.

**Figure 2.7:** Optical layout of double beam UV-Vis spectrophotometer.

**Figure 2.8:** Block diagram of spectrofluorimeter

**Figure 2.9:** Layout of a TCSPC instrument.

**Figure 2.10:** Layout of femtosecond fluorescence upconversion set up.

**Figure 2.11:** Scheme of the states involved in a pump-probe experiment (a) excitation of ground state molecules using pump, (b) excitation of ground state molecules using probe, (c) stimulated emission from excited state molecules, (d) excited state photoinduced absorption.

**Figure 2.12:** Schematic layout of femtosecond transient absorption spectrometer.

**Figure 2.13.** Optical scheme of TISSA 50 femtosecond Ti:Sapphire oscillator (CDP, Russia).

**Figure 2.14:** Illustration of the principle of femtosecond pulse stretcher.

**Figure 2.15:** Optical schematic of two-mirror confocal multipass Ti: Sapphire amplifier. The radiation pattern on the confocal mirror has shown in the right side.

**Figure 2.16:** Illustration of the principle of two grating pulse compressor.

**Figure 2.17.** Optical layout of pump-probe set up.

**Figure 3-1:** Optical absorption spectra of CdSe QDs (1  $\mu\text{M}$ ) with different concentration of PGR. PGR concentrations are (a) 0.0, (b) 1  $\mu\text{M}$ , (c) 10  $\mu\text{M}$ , (d) 50  $\mu\text{M}$ , (e) 100  $\mu\text{M}$ ; (f) 100  $\mu\text{M}$  PGR without CdSe QDs. **Inset:** Absorption spectra of pure CdSe QDs.

**Figure 3-2:** Emission (right side) and excitation (left side) spectra of CdSe QDs with different concentration of PGR. PGR concentrations are (a) 0.0, (b) 1  $\mu\text{M}$ , (c) 10  $\mu\text{M}$ , (d) 50  $\mu\text{M}$ , (e) 100  $\mu\text{M}$  and (f) emission spectra of pure PGR at 100  $\mu\text{M}$  concentrations. Both emission and excitation spectra of CdSe QDs are shown in the composite system after doing OD correction at exciting wavelength ( $\lambda_{\text{ex}} = 400\text{nm}$ ) for CdSe QDs absorption.

**Figure 3-3:** Time-resolved emission decay traces of CdSe QDs at 625 nm on addition of a) 0.0  $\mu\text{M}$ , b) 50  $\mu\text{M}$  and c) 100  $\mu\text{M}$  PGR molecules after exciting the QDs at 406 nm.

**Figure 3-4:** Transient absorption spectra of (A) CdSe (top panel), (B) PGR (middle panel) and (C) CdSe/PGR composite materials (bottom panel) in water at different time delay after excitation at 400 nm laser light.

**Figure 3-5:** Transient absorption spectrum of the cation radical of PGR obtained from one-electron oxidation in pulse radiolysis.

**Figure 3-6:** Kinetic decay traces at **A:** (a) 690 nm and b) 900 nm for CdSe, at **B:** (c) 690 nm and (d) 900 nm for PGR and at **C:** (e) 690 nm and f) 900 nm for CdSe/PGR system in water after exciting the samples at 400 nm laser light.

**Figure 3-7A:** Steady state absorption spectrum of CdSe QDs. **B:** Steady state absorption spectrum of CdSe QDs with different catechol derivatives. QDs/Catechol concentration is 1:1000.

**Figure 3-8A:** Steady state emission spectrum of CdSe QDs in absence (a) and in presence of CAT (b), QDs/CAT concentration is 1:1000. **B:** CV curve of CAT (a) with ferrocene and (b) without ferrocene in chloroform.

**Figure 3-9A:** Change in quantum yield of CdSe QDs in presence of different catechols derivatives at different concentration of catechols (a) 3-CH<sub>3</sub> (b) 4-CH<sub>3</sub> (c) CAT (d) 3-OCH<sub>3</sub> (e) 4-NO<sub>2</sub> (f) 4-CHO. **Inset:** Energy levels of valence band and conduction band of CdSe QD

and HOMO levels of different catechol derivatives. **B:** Time resolved emission studies of CdSe QDs with different catechol derivatives (a) CdSe (b) CdSe/4-CH<sub>3</sub> (c) CdSe/3-CH<sub>3</sub> (d) CdSe/Cat (e) CdSe/4-CHO (f) CdSe/4-NO<sub>2</sub> (g) CdSe /3-OCH<sub>3</sub> (C<sub>CdSe</sub>=0.16 μM, C<sub>Catechols</sub>=1.6 μM). **Inset** (a) CdSe (h) CdSe/3-OCH<sub>3</sub> (C<sub>CdSe</sub>=0.16 μM, C<sub>Catechols</sub>=0.16 mM).

**Figure 3-10:** Fluorescence upconversion decay traces of CdSe QDs ( $\lambda_{ex}$  - 400 nm and  $\lambda_{em}$  - 620 nm) with and without catechol derivatives. (a) pure QDs (b) CdSe/3-CH<sub>3</sub> (c) CdSe/4-CH<sub>3</sub> (d) CdSe/Cat (e) CdSe/4-CHO (f) CdSe/4-NO<sub>2</sub> (g) CdSe/3-OCH<sub>3</sub>. **Inset:** Plot of change of HT rate with Gibbs free energy of CT reaction.

**Figure 3-11A:** Fluorescence upconversion decay traces of CdSe QDs in absence and in presence of catechol derivatives. **B:** Fluorescence upconversion decay traces of CdSe QDs in absence and in presence 3-OCH<sub>3</sub>.  $\lambda_{ex}$ - 400 nm,  $\lambda_{em}$ - 560 nm. **C:** Mechanistic scheme of HT reaction from hot excitonic state of CdSe QDs to 3-OCH<sub>3</sub>.

**Figure 3-12:** Transient absorption spectra of (A) CdSe QDs and (B) CdSe QDs in presence of 3-OCH<sub>3</sub> at different time delay after exciting the samples at 400 nm laser light. (C) Transient spectra at 3 ps time delay for CdSe QDs (a) in absence and (b) in presence of 3-OCH<sub>3</sub> after normalizing the bleach at 590 nm (1S exciton). (D) Steady state optical absorption spectra of pure CdSe QDs showing different excitonic position.

**Figure 3-13A:** Bleach recovery kinetics of (a) CdSe (b) CdSe/3-OCH<sub>3</sub> (c) CdSe/Cat at 490 nm; **B:** Bleach recovery kinetics of (d) CdSe (e) CdSe/3-OCH<sub>3</sub> (f) CdSe/Cat at 530 nm after exciting the sample at 400 nm. **C:** Bleach recovery kinetics of CdSe QD at 530 nm monitored in absence and in presence of different catechol derivatives.

**Figure 3-14:** Bleach recovery kinetics of CdSe QDs at 590 nm (a) in absence and in presence of (b) CAT (c) 3-OCH<sub>3</sub> (d) 3-CH<sub>3</sub> (e) 4-CH<sub>3</sub> (f) 4-NO<sub>2</sub> (g) 4-CHO. **Inset:** Variation of CR reaction rate with Gibbs free energy ( $-\Delta G_{CR}$ ) of reaction.

**Figure 3-15A:** Steady state optical absorption spectra of CdSe QDs with different concentration of (A) AAT (C) ADPT (D) APT, (a) Pure QD, (b) QD:Thiol= 1:10, (c) QD:Thiol = 1:100 (d) QD: Thiol = 1:1000, (e) QD: Thiol = 1:5000. **Inset:** change in  $\Delta R$  value with increase in concentration of Thiol. **B:** Schematic diagram of ligand exchange of oleic acid with thiols on QD surface in presence of large concentration of thiols.

**Figure 3-16:** Steady state optical absorption spectra of CdSe/ZnS CSQD at different time in presence of (A) ADPT (B) APT and (C) AAT. (Thiol:CdSe/ZnS=1000:1) (a) Pure CSQD, (b) CSQD/Thiol at 4 h, (c) CSQD/Thiol at 16 h, (d) CSQD/Thiol at 24 h. **Inset:** Steady state optical absorption spectra of CSQD after 24 h in presence of thiols (Thiol:QD=10:1).

**Figure 3-17A:** Steady state absorption spectra of CSQDs in presence and absence of  $Zn^{2+}$  ions and thiols. **B:** Schematic diagram of interaction of thiols with CSQDs.

**Figure 3-18A:** Steady state emission spectra of CdSe QDs (a) in absence and in presence of the thiols (b) AAT, (c) APT and (d) ADPT. **Inset:** Time-resolved emission spectra of CdSe QDs (a') in absence and in presence of the thiols (b') AAT, (c') APT and (d') ADPT. **B:** Steady state emission spectra of CdSe/ZnS CSQDs (e) in absence and in presence of thiols (f) AAT, (g) APT and (h) ADPT. **Inset:** Time-resolved emission spectra of CdSe/ZnS CSQDs (e') in absence and in presence of the thiols (f') AAT, (g') APT and (h') ADPT. Concentration ratio for thiol:QDs and thiol:CSQDs were 1000:1.

**Figure 3-19:** Differential pulse voltammetry curve of ADPT.

**Figure 3-20:** Transient absorption spectra of (A) CdSe QDs (B) CdSe/ZnS CSQDs at different time delay after exciting at 400 nm.

**Figure 3-21:** Transient absorption spectra CdSe QDs and CdSe/ZnS CSQDs with Thiols at different time delay after exciting at 400 nm.

**Figure 3-22A:** Transient spectra at 2 ps time delay for CdSe QDs (a) in absence and (b) in presence of AAT after normalizing the bleach at 558 nm (1S exciton). **B:** Steady state optical absorption spectra of CdSe QDs (a') in absence and (b') in presence of AAT showing different excitonic position. **C:** Transient spectra at 2 ps time delay for CdSe/ZnS CSQDs (c) in absence and in presence of (d) AAT and (e) APT after normalizing the bleach at 575 nm (1S exciton). **D:** Steady state optical absorption spectra of CdSe/ZnS CSQDs (c') in absence and in presence of (d') AAT and (e') APT showing different excitonic position.

**Figure 3-23:** Bleach recovery kinetics of (A) CdSe QDs and (B) CdSe/ZnS CSQDs in absence and in presence of the thiols at 525 nm and 535 nm respectively (2S excitonic position).

**Figure 3-24:** Fluorescence upconversion decay traces of (a) CdSe QDs (b) CdSe/AAT (c) CdSe/ADPT (d) CdSe/APT at 580 nm. **Inset:** Fluorescence upconversion decay traces of (e) CdSe/ZnS (f) CdSe/ZnS/AAT (g) CdSe/ZnS/ADPT (h) CdSe/ZnS/APT at 590. Excitation wavelength was kept at 400 nm in all the systems. Concentration ratio for both thiols:QDs and thiols:CSQDs were kept 1000:1.

**Figure 3-25:** Fluorescence upconversion decay traces of (A) CdSe QDs (B) CdSe/ZnS CSQDs with different thiols at 2S luminescence position ( $\lambda_{\text{ex}}$ - 400 nm,  $\lambda_{\text{em}}$ - 540 nm for CdSe QDs and 550 nm for CdSe/ZnS CSQDs).

**Figure 3-26:** Bleach recovery kinetics of A) CdSe QDs and B) CdSe/ZnS CSQDs in absence and in presence of the thiols. Bleach kinetics was monitored at 560 nm and at 570 nm for CdSe QDs and for CdSe/ZnS CSQDs respectively.

**Figure 3-27:** Steady state absorption spectra of QDs with NCAT. **A:** CdS QDs, **B:** CdSe QDs, **C:** CdTe QDs (a) pure QDs (b) QDs/NCAT (c) NCAT (d) QDs+NCAT (e) b-d.

**Figure 3-28:** Complex spectrum of CdS QDs, CdSe QDs, CdTe QDs and Cd<sup>2+</sup> ion with NCAT.

**Figure 3-29A:** Steady state absorption spectra of (a) CAD (b) CAD/NCAT (c) NCAT (d) CAD+NCAT (e) b-d. **Inset:** (a') C (b') NCAT (c') CAD/NCAT in CHCl<sub>3</sub>. **B:** Schematic diagram for the QDs/NCAT complex formation.

**Figure 3-30:** Steady state absorption spectra of (A) CdSe QDs, (B) CdTe QDs and (C) CAD in absence and presence of CAT.

**Figure 3-31:** Schematic diagram for the interaction of NCAT with QDs surface. **Inset:** Steady state absorption spectra of CdS QDs in absence and presence of CAT.

**Figure 3-32:** Change in luminescence intensity of (A) CdS QDs (B) CdSe QDs (C) CdTe QDs in absence and presence of CAT and NCAT at CAT/NCAT to QDs ratio 100:1. (a) CdS QDs, (b) CdS/CAT,  $\lambda_{ex}$ - 430 nm, (c) CdS/CAT,  $\lambda_{ex}$ - 400 nm, (d) CdS/NCAT,  $\lambda_{ex}$ - 430 nm, (e) CdS/NCAT,  $\lambda_{ex}$ - 400 nm, (a') CdSe QDs, (b') CdSe/CAT,  $\lambda_{ex}$ - 500 nm, (c') CdSe/CAT,  $\lambda_{ex}$ - 400 nm, (d') CdSe/NCAT,  $\lambda_{ex}$ - 500 nm, (e') CdSe/NCAT,  $\lambda_{ex}$ - 400 nm, (a'') CdTe QDs, (b'') CdTe/CAT,  $\lambda_{ex}$ - 600 nm, (c'') CdTe/CAT,  $\lambda_{ex}$ - 400 nm, (d'') CdTe/NCAT,  $\lambda_{ex}$ - 600 nm, (e'') CdTe/NCAT,  $\lambda_{ex}$ - 400 nm.

**Figure 3-33:** Change in luminescence intensity of (A) CdS QD (B) CdSe QDs (C) CdTe QDs in presence of CAT and NCAT at two different excitation wavelengths at different concentration of CAT/NCAT to QDs ratio.

**Figure 3-34:** Time resolved decay traces of (A) CdS QDs,  $\lambda_{ex}$ - 406 nm,  $\lambda_{em}$ - 475 nm (B) CdSe QDs,  $\lambda_{ex}$ - 406 nm,  $\lambda_{em}$ - 575 nm (C) CdTe QD,  $\lambda_{ex}$ - 406 nm,  $\lambda_{em}$ - 735nm in absence and presence of CAT and NCAT. **Inset:** Time resolved decay traces of (A) CdS QDs,  $\lambda_{ex}$ - 445 nm,  $\lambda_{em}$ - 475 nm (B) CdSe QDs,  $\lambda_{ex}$ - 445 nm,  $\lambda_{em}$ - 575 nm (C) CdTe QD,  $\lambda_{ex}$ - 636 nm,  $\lambda_{em}$ -

735nm in absence and presence of CAT and NCAT. **D:** Redox potential of QDs and CAT and NCAT with respect to normal hydrogen electrode (NHE).

**Figure 3-35:** Transient absorption spectrum of **(A)** CdS QDs **(C)** CdSe QDs **(E)** CdTe QDs. Bleach recovery dynamics of **(B)** CdS QDs,  $\lambda_{\text{mon}}=460$  nm **(D)** CdSe QDs,  $\lambda_{\text{mon}}=550$  nm **(F)** CdTe QDs,  $\lambda_{\text{mon}}=670$  nm in presence and absence of CAT and NCAT (a) pure QDs, (b) QDs/CAT, (c) QDs/NCAT.

**Figure 4-1A:** XRD spectra of OA capped (a) CdSe QDs (b) CdSe@CdS 2.5 (c) CdSe@CdS 3.5 (d) CdSe@CdS 4.5 CSQDs. **B:** FTIR spectra of OA capped (a) CdSe QDs (b) CdSe@CdS 2.5 (c) CdSe@CdS 3.5 (d) CdSe@CdS 4.5 CSQDs (e) pure OA. **C:** XRD spectra of MPA capped (a) CdSe QDs (b) CdSe@CdS 2.5 (c) CdSe@CdS 3.5 (d) CdSe@CdS 4.5 CSQDs. **D:** FTIR spectra of MPA capped (a) CdSe QDs (b) CdSe@CdS 2.5 (c) CdSe@CdS 3.5 (d) CdSe@CdS 4.5 CSQDs (e) pure MPA.

**Figure 4-2:** Steady state absorption and emission (inset) spectra of OA capped CdSe QDs and CdSe/CdS CSQDs. Both the spectra are normalized.

**Figure 4-3A:** Steady state emission spectra of CdSe QDs with and without uranium (a') Pure QDs (b') QDs/1 nM uranium (c') QDs/10 nM uranium (d') QDs/100 nM uranium (e') QDs/1  $\mu\text{M}$  uranium (f') QDs/10  $\mu\text{M}$  uranium (g') QDs/50  $\mu\text{M}$  uranium. **Inset:** Steady state absorption spectra of CdSe QDs with and without uranium (a) Pure QDs (g) QDs/50  $\mu\text{M}$  uranium (h) 50  $\mu\text{M}$  uranium. **B)** Schematic diagram of energy level of CdSe QDs and uranyl depicting electron transfer process from QDs to uranium. **C)** Time resolved emission spectra of (a'') CdSe QDs (d'') QDs/100 nM uranium (g'') QDs/50  $\mu\text{M}$  uranium. (L) Lamp profile.  $\lambda_{\text{ex}} = 445$  nm,  $\lambda_{\text{em}} = 570$  nm.

**Figure 4-4:** Steady state emission spectra of **A:** CdSe@CdS 2.5, **B:** CdSe@CdS 3.5 and, **C:** CdSe@CdS 4.5 CSQDs in absence and presence of uranium (a) Pure CSQDs (b) CSQDs/100 nM uranium (c) QDs/10  $\mu$ M uranium (d) QDs/100  $\mu$ M uranium.

**Figure 4-5:** Different processes involved on interaction of uranium in **(A)** CdSe QDs and in **(B)** CdSe@CdS 3.5 CSQDs. Process a refers to the photo-excitation of QDs and CSQDs to generate e-h pair followed by hole delocalization into MPA shell. Process b refers to the hole delocalization process on addition of uranium at 100 nm concentrations. Process c refers to the ET process from photo-excited QDs and CSQDs to uranium leading to luminescence quenching.

**Figure 4-6:** Redox potential of EDTA with respect to NHE in water.

**Figure 4-7:** Steady state luminescence spectra of CdSe QDs and CdSe/CdS CSQDs with (b) and without EDTA (a). **(A)** CdSe QDs **(B)** CdSe@CdS 2.5 **(C)** CdSe@CdS 3.5 **(D)** CdSe@CdS 4.5 CSQDs.

**Figure 4-8:** Time resolved emission spectra of **A:** CdSe@CdS 2.5 ( $\lambda_{em} = 600$  nm), **B:** CdSe@CdS 3.5 ( $\lambda_{em} = 610$  nm) and, **C:** CdSe@CdS 4.5 (a) Pure CSQDs (b) QDs/100 nM uranium (c) QDs/10  $\mu$ M uranium (d) QDs/100  $\mu$ M uranium (L) Lamp profile.  $\lambda_{ex} = 445$  nm. **D:** Plot of ET rate as a function of CdS shell thickness.

**Figure 4-9:** Emission spectra of CSQDs with different concentrations of  $UO_2^{2+}$  in DI water (A) CdSe@CdS 3.5 (B) CdSe@CdS 4.5 CSQDs. Uranium concentration increases from 1  $\mu$ M to 100  $\mu$ M. **Inset:** Stern-Volmer plot of (A) CdSe@CdS 3.5 and (B) CdSe@CdS 4.5 CSQDs with uranium.

**Figure 4-10A:** HRTEM image of CQDs, **B:** XRD pattern of CQDs, **C:** FTIR spectrum of CQDs, **D:** Deconvoluted spectrum of C 1s XPS.

**Figure 4-11A:** Steady state excitation spectra of CQDs at two different emission wavelengths,  $\lambda_{em}$ - 450 nm and 380 nm. **Inset:** Steady state absorption spectrum of CQDs. **B:** Steady state emission spectra of CQDs at different excitation wavelengths. CQDs concentration was 50 ppm.

**Figure 4-12:** Steady state absorption spectra of CQDs and CQDs/Eu<sup>3+</sup> complex.

**Figure 4-13A and B:** Steady state emission spectrum of CQDs in absence and presence of different concentration of Eu<sup>3+</sup> (A)  $\lambda_{ex}$ - 280 nm, (B)  $\lambda_{ex}$ - 340 nm, (a) [Eu<sup>3+</sup>] = 0 ppm (b) [Eu<sup>3+</sup>] = 10 ppm, (c) [Eu<sup>3+</sup>] = 20 ppm, (d) [Eu<sup>3+</sup>] = 50 ppm, (e) [Eu<sup>3+</sup>] = 100 ppm, (f) [Eu<sup>3+</sup>] = 250 ppm. **C:** Comparison of emission intensity of CQDs on addition of Eu<sup>3+</sup> at two different excitation wavelengths,  $\lambda_{ex}$ - 280 nm and  $\lambda_{ex}$ - 340 nm. CQDs concentration for all above experiments was 50 ppm.

**Figure 4-14A and B:** Time resolved emission decay trace of CQDs in presence of Eu<sup>3+</sup>, (A)  $\lambda_{ex}$ - 292 nm,  $\lambda_{em}$ - 340 nm, (B)  $\lambda_{ex}$ - 374 nm,  $\lambda_{em}$ - 450 nm, (a) pure CQDs, (b) CQDs + 50 ppm Eu<sup>3+</sup>, (c) CQDs + 250 ppm Eu<sup>3+</sup>. CQDs concentration for all above experiments was 50 ppm. **C:** HRTEM image of CQDs on addition of 2500 ppm of Eu<sup>3+</sup>. CQDs concentration for HRTEM measurements was 500 ppm.

**Figure 4-15A:** Photoluminescence spectra of CQDs-Eu<sup>3+</sup> with increase in concentration of fluoride ion in water. **B:** Respective graphical relationship of the Photoluminescence intensity against concentration of fluoride ion. CQDs and Eu<sup>3+</sup> concentration are 50 ppm each. Bottom panel shows the mechanism of interaction involved.

**Figure 4-16:** Photoluminescence spectra of CQDs with increase in concentration of fluoride ion in water. CQDs concentration is 50 ppm.

**Figure 4-17A:** XRD pattern of EuF<sub>3</sub>, **B:** HRTEM image of EuF<sub>3</sub>. **B inset:** TEM image of EuF<sub>3</sub>.

**Figure 4-18:** Bar diagram for the selectivity test results obtained with the addition of different anions into the CQDs/Eu<sup>3+</sup> system. CQDs and Eu<sup>3+</sup> concentration are 50 ppm each. Concentrations of anions are 100 ppm each.

**Figure 5-1 (A)** XRD pattern of (a) Fe<sub>3</sub>O<sub>4</sub> (b) Fe<sub>3</sub>O<sub>4</sub>/HA 1 (c) Fe<sub>3</sub>O<sub>4</sub>/HA 2 (d) Fe<sub>3</sub>O<sub>4</sub>/HA 3 NPs after correcting with silicon as a standard. **(B)** FTIR spectra of (a) Fe<sub>3</sub>O<sub>4</sub> (b) Fe<sub>3</sub>O<sub>4</sub>/HA 3 NPs (c) HA. **Inset** shows the FTIR spectra of all three compounds in expanded view. **(C)** TG analysis of (a) Fe<sub>3</sub>O<sub>4</sub> (b) Fe<sub>3</sub>O<sub>4</sub>/HA 1 (c) Fe<sub>3</sub>O<sub>4</sub>/HA 2 (d) Fe<sub>3</sub>O<sub>4</sub>/HA 3 NPs. **(D)** Magnetic measurements of (a) Fe<sub>3</sub>O<sub>4</sub> (b) Fe<sub>3</sub>O<sub>4</sub>/HA 1 (c) Fe<sub>3</sub>O<sub>4</sub>/HA 2 (d) Fe<sub>3</sub>O<sub>4</sub>/HA 3 NPs.

**Figure 5-2 (A)** TEM image of Fe<sub>3</sub>O<sub>4</sub> NPs. **(B)** HRTEM image of a single Fe<sub>3</sub>O<sub>4</sub> NPs. **(C)** TEM image of Fe<sub>3</sub>O<sub>4</sub>/HA 3 NPs **(B)** HRTEM images of Fe<sub>3</sub>O<sub>4</sub>/HA 3 NPs

**Figure 5-3:** % Uranium sorbed on NPs surface at different concentration of uranium. (a) Fe<sub>3</sub>O<sub>4</sub> (b) Fe<sub>3</sub>O<sub>4</sub>/HA 1 (c) Fe<sub>3</sub>O<sub>4</sub>/HA 2 (d) Fe<sub>3</sub>O<sub>4</sub>/HA 3. V/m ratio was kept at 200 mL/g.

**Figure 5-4:** Equilibrium data for uranium sorption (V/m=1000 mL/g, contact time ~1h, initial uranium concentration 5-100 ppm) **(A)** Fe<sub>3</sub>O<sub>4</sub>, **(B)** Fe<sub>3</sub>O<sub>4</sub>/HA 1, **(C)** Fe<sub>3</sub>O<sub>4</sub>/HA 2, **(D)** Fe<sub>3</sub>O<sub>4</sub>/HA 3. Red line represents the fitting of data with Langmuir model.

**Figure 5-5:** Settlement of NPs in presence and absence of 20 ppb-20 ppm uranium concentrations (a) Fe<sub>3</sub>O<sub>4</sub> (b) Fe<sub>3</sub>O<sub>4</sub>/HA 1 (c) Fe<sub>3</sub>O<sub>4</sub>/HA 2 (d) Fe<sub>3</sub>O<sub>4</sub>/HA 3 NPs. **Inset:** Picture of real samples in presence of magnet.

**Figure 5-6:** Calibration curve and concentration of uranium after sorption with all four NPs in different sea water samples. The initial concentration of added uranium was 10 ppb. **Inset** shows that extraction of uranium from sea water matrix without any addition of uranium externally. Black dot (•) shows the intensity corresponding to the natural concentration of uranium in each sea water prior to sorption with NPs.

## List of Schemes

**Scheme 3-1:** Basic processes involved in hot carrier quantum dot solar cell: 1) photo-excitation of QD, 2) hot electron transfer, 3) hot hole transfer, 4) hole cooling, 5) electron cooling, 6) thermalized electron transfer and 7) thermalized hole transfer.

**Scheme 3-2:** Different processes involved after photo-excitation of QD materials with photon energy  $> 2E_g$ . **Process 1:** Generation of hot charge carriers, **Process 2:** Carrier multiplication (CM) followed by multiple exciton generation (MEG), **Process 3:** Non radiative Auger recombination, **Process 4:** Charge carrier dissociation in presence of hole accepting adsorbate.

**Scheme 3-3.** Charge transfer processes in CdSe/PGR composite materials are depicted in the Scheme. Photoexcitation of CdSe QDs below 550 nm radiation generates electron ( $e^-$ ) and hole ( $h^+$ ) pairs where hole ( $h^+$ ) is captured by PGR molecule, on the other hand photoexcited PGR by below 650 nm radiation injects electron in the CB of CdSe. Molecular structure of PGR is shown in the scheme.

**Scheme 3-4:** Energy level diagram of CdSe QDs showing different discrete states of both CB and VB. HOMO level of 3-OCH<sub>3</sub> is also shown. The scheme demonstrates both thermalized and hot hole extraction by 3-OCH<sub>3</sub> from CdSe QDs.

**Scheme 3-5:** Energy level diagram of CdSe/ZnS CSQDs showing different discrete states of both CB and VB. HOMO level of ADPT is also shown. The scheme demonstrates both thermalized and hot hole extraction by ADPT from CdSe QDs.

**Scheme 3-6:** Different processes involved on photo-excitation of QDs with NCAT.

**Scheme 4-1:** Different processes involved during interaction of metal ions with QDs surface. **(A)** Ligand desorption from QDs surface. **(B)** Energy transfer or CT from QDs to metal ion.

(C) Cation exchange on QDs surface leading to both luminescence enhancement and quenching.

**Scheme 4-2:** CQDs and its interaction with  $\text{Eu}^{3+}$ . (A) Photoexcitation of core state of CQDs and subsequent electron transfer to  $\text{Eu}^{3+}$  (B) Photoexcitation of surface state of CQDs and subsequent electron transfer to  $\text{Eu}^{3+}$  (a) and aggregation of CQDs on  $\text{Eu}^{3+}$  addition (b).

**Scheme 5-1:** Interaction of  $\text{Fe}_3\text{O}_4$  (upper panel) and  $\text{Fe}_3\text{O}_4/\text{HA}$  3 NPs (lower panel) with different species of uranium at different uranium concentrations (a, a') 200 ppm (b, b') 2 ppm (c, c') 20 ppb uranium.

## List of Tables

**Table 3-1:** Redox levels of different catechol derivatives with respect to NHE. Values are corrected by taking ferrocene as an internal standard.

**Table 3-2:** Parameters for multi-exponential fit of emission decay traces for CdSe QDs in absence and in presence of different catechol derivatives monitoring at 620 nm after exciting at 400 nm.

**Table 3-3:** Parameters for multi-exponential fit of emission decay traces for CdSe QDs in absence and in presence of different catechol derivatives monitoring at 560 nm after exciting at 400 nm.

**Table 3-4:** Multi-exponential fitting parameters for bleach recovery kinetics at different excitonic wavelengths (490 nm and 530 nm) of CdSe QDs in absence and in presence of catechol (CAT) and 3-OCH<sub>3</sub> after exciting the samples at 400 nm.

**Table 3-5:** Multi-exponential fitting parameters for the bleach recovery kinetics of CdSe QDs/catechol derivatives. Change in CR rate with free energy of CR reaction in different CdSe QDs/catechol derivatives composites.

**Table 3-6:** Time resolved emission decay parameters in nanosecond time scale resolution ( $\lambda_{\text{ex}}=400\text{nm}$ ,  $\lambda_{\text{em}}^{\text{CdSe}}=580\text{ nm}$ ,  $\lambda_{\text{em}}^{\text{CdSe/ZnS}}=590\text{ nm}$ )

**Table 3-7:** Transient absorption fitting parameters ( $\lambda_{\text{ex}}=400\text{nm}$ ,  $\lambda_{\text{monitoring}}^{\text{CdSe}}=525\text{ nm}$ ,  $\lambda_{\text{monitoring}}^{\text{CdSe/ZnS}}=530\text{ nm}$ ).

**Table 3-8:** Femtosecond fluorescence upconversion fitting parameters ( $\lambda_{\text{ex}}=400\text{nm}$ ,  $\lambda_{\text{em}}^{\text{CdSe}}=580\text{ nm}$ ,  $\lambda_{\text{em}}^{\text{CdSe/ZnS}}=590\text{ nm}$ ).

**Table 3-9:** Femtosecond fluorescence upconversion fitting parameters ( $\lambda_{\text{ex}}=400\text{nm}$ ,  $\lambda_{\text{em}}^{\text{CdSe}}=540\text{ nm}$ ,  $\lambda_{\text{em}}^{\text{CdSe/ZnS}}=550\text{ nm}$ ).

**Table 3-10:** Transient absorption fitting parameters ( $\lambda_{\text{ex}}=400\text{nm}$ ,  $\lambda_{\text{monitoring}}^{\text{CdSe}}=560\text{ nm}$ ,  $\lambda_{\text{monitoring}}^{\text{CdSe/ZnS}}=570\text{ nm}$ ).

**Table 3-11:**  $G_{\text{HT}}^{\dagger}$  value for QDs/CAT/NCAT pairs.

**Table 3-12:** Multi-exponential fitting parameters for the bleach recovery kinetics of CdX QDs in absence and in presence of CAT and NCAT.

**Table 4-1:** QY of OA and MPA capped CdSe QDs and CdSe/CdS CSQDs by taking rhodamine 6G as standard.

**Table 4-2.** Zeta potential of QDs and CSQDs before and after uranium interaction.

**Table 4-3:** Time resolved fitting parameters of MPA capped CdSe and CdSe/CdS CSQDs with and without uranium ( $\lambda_{\text{ex}} = 445\text{ nm}$ ).

**Table 4-4:** Photoluminescence intensities of 5 batches (A1 to A5) of CSQDs.

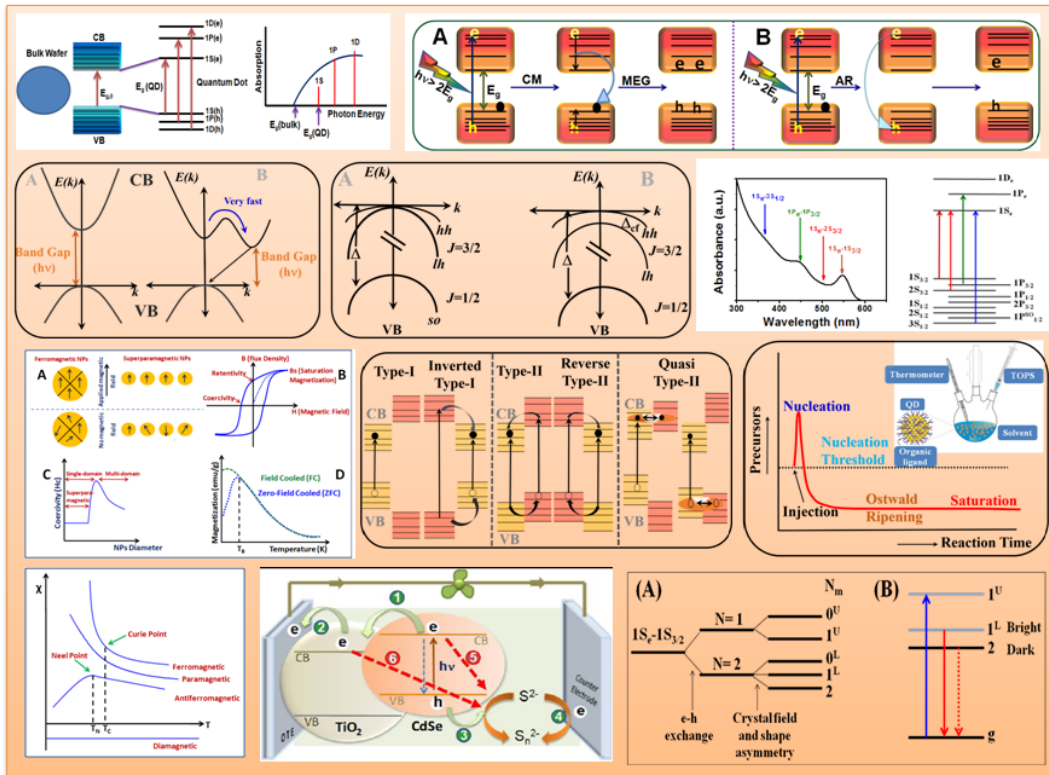
**Table 4-5:** Zeta potential values of CQDs in presence and absence of  $\text{Eu}^{3+}$  and fluoride ions.

**Table 5-1.** pH, Zeta potential of NPs in presence and absence of different concentrations of uranium. The variation in results is within  $\pm 5\%$ .



# CHAPTER-1

## Introduction





### *1.1. General Background*

The present work demonstrates the application of nanomaterials for solar energy conversion and environmental remediation. In this chapter, a brief discussion about nanoparticles (NPs), quantum dots (QDs), quantum dot solar cell (QDSC), magnetic NPs, theoretical aspect of their structural properties and their application in solar energy conversion and environmental remediation has been demonstrated.

India is one the largest energy consumer in the world and its need for energy supply continues to climb as a result of the country's dynamic economic growth and modernization over the past several years. Today, fossil fuel accounts for 90% of the energy consumption, however, the long-term availability of fossil fuel is limited<sup>1</sup>. Also, the widespread use of fossil fuels is plagued with problems such as emission of greenhouse gases and the related climate changes we are witnessing. Therefore, to meet the future energy demand and transform the world's energy systems to combat climate change it is utmost important to explore the other alternative sources of energy which are clean and do not have any detrimental effect on the environment<sup>2</sup>. These energy sources include solar energy, nuclear energy, tidal energy, wind energy etc. In a country like India where the other sources of energy are limited, solar energy is one of the most promising candidates because of its widespread availability and clean technology<sup>3</sup>. There are vast tracts of land suitable for solar power in all parts of India exceeding 8% of its total area which is unproductive barren and devoid of vegetation. Taking this fact into account, a number of industries have come up to produce highly efficient solar cells. However, the conversion of solar energy into electrical energy is a challenging task and a lot of modifications are still needed to achieve maximum efficiency. In light of this, nanotechnology has played an extremely important role in synthesis, and characterization of various novel materials which can be used to harvest solar

energy into electricity. In the present thesis, application of semiconductor nanocrystals, mainly quantum dots (QDs) as a solar energy harvesting material has been discussed.

Solar cell technologies have been divided into three generations<sup>4</sup>. The first generation solar cells are based on silicon technology<sup>5, 6</sup> and show a record efficiency of ~24.4% under ambient condition. This high efficiency is due to the favourable band gap of silicon ~1.1 eV which matches well with the solar flux incident on the earth. These types of solar cells dominate the market and are mainly seen on rooftops. The benefits of this solar cell technology lie in their good performance, as well as high stability. However, silicon is an indirect band gap material, therefore, a thick layer of silicon (~100 $\mu$ m) is required otherwise light would simply pass through without generating any charge carriers. At the same time purity of the crystal has to be very high (>99.9999%) so that the photo-generated charge carriers can reach the p-n junction. Both of these processes lead to an overall increase in cost and are one of the main drawbacks of this solar cell. To avoid these problems polycrystalline thin film solar cells, also known as second generation solar cell were evolved<sup>7</sup>. These solar cells were based on amorphous silicon, CIGS ( $\text{CuIn}_x\text{Ga}_{1-x}\text{Se}_2$ ) and CdTe and a record efficiency of ~19.6% have been achieved in these solar cells. Since the second generation solar cells avoid the use of silicon wafers and have a lower material consumption, the overall production cost of these solar cells is less as compared to the first generation. However, the production of second generation solar cells includes vacuum processes and high-temperature treatments that require large energy consumption. Furthermore, second generation solar cells are based on scarce elements such as Cd, Te which increases the overall production cost. At the same time, these solar cells require more area to generate the same power as compared to the first generation solar cells because of the lower efficiency in former as compared to later. To overcome these limitations, third generation solar cells have come up as a promising candidate. This solar cell includes organic and polymer solar cell, dye-sensitized solar cell

(DSSC), quantum dot solar cell (QDSC) and the very recent one, perovskite solar cell (PSC). The main advantages of using these materials as compared to silicon are their absorption band tunability, easy charge transport, and solubility. Although, the performance and stability of third generation solar cells are still limited as compared to the first and second generation solar cells, they have great potential and a lot of work is going on to further improve their performance. Among the third generation solar cell materials a lot of work has been carried out in DSSC and till date, the maximum efficiency reported to be ~13% in specially designed porphyrin molecule endowed with D- $\pi$ -A push-pull groups<sup>8</sup>. However, DSSC has issues such as poor stability towards solar radiation and solar radiation absorption tunability. Also, the excess energy absorbed by the dye molecule (i.e. excess energy than its HOMO-LUMO gap) always lost as heat. To overcome the above limitations, QDSC has come up<sup>9</sup>. Here the advantage of absorption band tunability and large solar energy absorption coefficient are present in a single system<sup>10, 11</sup>. The size of QDs can be tuned easily using different synthetic conditions and solar radiation absorption in different solar regime can be realized<sup>12</sup>. QDSC efficiency as a function of band gap was predicted by Schokley Queisser where they demonstrated the theoretical conversion efficiency of QDSC is a function of band gap and can reach to a highest value of 31% based on thermal charge carrier extraction<sup>13</sup> and if hot charge carriers can be extracted then this efficiency can increase up to ~66%<sup>14</sup>. Recently a modification to this has also come up where both band gap and film thickness is taken into account to determine the efficiency and is known as spectroscopic limited maximum efficiency<sup>15,16</sup>. In the present thesis, composite systems of QDs with different molecules were chosen and their charge carrier dynamics were studied with an aim to achieve high-efficiency QDSC.

Along with energy crises, the other major issue is environmental contamination<sup>17-20</sup>. The rapid growth of industrialization results in high demand for metals in various products,

such as storage batteries, automobile fuels, photographic films, explosives, coating materials, aeronautics, and steel industries. Because of these activities, a number of toxic metals are present in the environment with concentrations more than the permissible limits<sup>17-20</sup> and becomes a potential hazard to human safety and environmental stability<sup>21, 22</sup>. Transition metals such as Fe, Cu, Mn, and Zn, which are essential for a healthy life at low concentrations becomes toxic at higher concentrations. These metal ions bind with the ligands of biological matter resulting in a change in the structure of proteins, thereby leading to the inhibition in enzyme activity<sup>23-27</sup>. Also, some of the metal ions such as  $\text{Hg}^{2+}$ ,  $\text{Cd}^{2+}$ ,  $\text{Pb}^{2+}$ ,  $\text{UO}_2^{2+}$ , and  $\text{As}^{3+}$  are not essential to the human body and even at trace concentrations, they are toxic. Accumulation of these metal ions in the human body leads to serious debilitating illnesses and known to affect central nervous system, kidney, and liver<sup>28, 29</sup>. These metals are also not biodegradable and therefore, remain in ecological systems and in the food chain indefinitely. For these reasons, safe limits or maximum contaminant levels have been defined for these metal ions. For example, uranium, a well known nephrotoxic element has a maximum permissible limit of ~35 ppb in drinking water, as given by WHO<sup>30</sup>. Therefore, there is a great need to develop systems which can detect the presence of these metal ions at such low concentrations. Along with metals ions, selective detection of various anions in aqueous solution is also very important because of their high toxicity and widespread availability in different environmental matrices<sup>22, 31, 32</sup>. Fluoride, a commonly added anion in toothpaste and drugs cause dental or even skeletal fluorosis<sup>33</sup> at high concentrations. Because of these harmful effects, it is necessary to develop techniques which are highly selective and can detect the presence of these ions at trace concentrations. Several methods including atomic absorption spectroscopy, inductively coupled plasma mass spectrometry, electrochemical sensing, titration, chromatographic techniques, flow injection methods make it possible to detect a trace level of ions<sup>34-37</sup>. However, these methods require

expensive equipment and involve time-consuming and laborious procedures that can be carried out only by trained professionals. To overcome these limitations, optical sensing approach has attracted great attention because of its low cost, reliability, ease of preparation, reproducibility and, accuracy<sup>21</sup>. Considerable efforts have been made to develop this method by exploiting different strategies such as supramolecular recognition<sup>38-40</sup>, hydrogen bonding<sup>38, 41</sup>, Lewis acid–base interactions<sup>38, 42, 43</sup>. However, in most of the above-stated strategies, organic molecules are being utilized<sup>40-43</sup> and the synthesis of these molecules is a challenging task<sup>37</sup>. More importantly, most of these molecules are water insoluble<sup>39, 42, 43</sup>. Hence, the detection of ions using these molecules cannot be done directly in water and further treatment is required to make them water dispersible. At the same time, interference from other competing ions is an issue that has to be resolved. Therefore, there is a need to develop new methods for detection that are much simpler and can overcome most of the above-stated limitations.

In light of this, QDs have attracted substantial interest because of their advantageous characteristics such as size/shape controlled absorption/luminescence properties, high fluorescence quantum yield, and high stability. These properties altogether make them an interesting candidate to study their application for optical sensing<sup>22</sup>. Recently trace element detection by luminescence quenching of different QDs have been reported by many research groups<sup>44-55</sup>. However, not many reports are available in the literature on detection of uranium metal ion using QDs except the report by Dutta and Kumar<sup>51</sup> in amine modified CdS QDs. Although they have shown trace level detection of uranium using these QDs, a clear mechanism of QDs luminescence quenching by uranium has not been discussed which is extremely important for making efficient detection methodology. Along with uranium, the design of fluoride ion sensors is also an active area of investigation<sup>38-41, 56-63</sup> because of its high toxicity<sup>64</sup> and widespread availability in drinking water, toothpaste, and osteoporosis

drugs<sup>43, 56</sup>. A number of commercially developed methods are available for fluoride ion detection however, most of the methods have limitations such as the requirement of complex instrumentation, well-equipped laboratories, and trained personnel. To overcome these limitations, QDs based detection methods are emerging as an alternate<sup>64-67</sup>. A number of reports are published<sup>64-67</sup> where researchers have demonstrated the application of QDs for fluoride ion detection. However, still more improvement is needed. At the same time, to design and develop better detection probes it is very important to understand the working mechanism of the probe and its applicability in real environmental samples which is still lacking in the literature. In the present thesis, the application of QDs as a probe to detect uranium and fluoride ions has been discussed and a complete mechanistic pathway involved in detection has been described.

Along with detection, there is also a critical need to find suitable host matrix that can be used to trap and separate toxic ions from environmental matrices to ensure the protection of the environment. The most widely used techniques for this includes liquid-liquid extraction, solid-phase extraction (SPE), co-precipitation, floatation and electrochemical deposition, etc<sup>68-79</sup>. Among these, SPE has become increasingly popular as compared with classical liquid-liquid extraction method because of its advantages such as high enrichment factor, high recovery, rapid phase separation, low cost, low consumption of organic solvents and the ability to combine with different detection techniques in on-line or off-line mode. A variety of solid extractants<sup>68-79</sup> has been explored nowadays for environmental detoxification however, each has its own limitations such as non-selectivity, difficult separation from the matrix, low sorption capacity etc. Precipitation is an alternative process that is widely used for separating target ions from liquids. It has an advantage of being simple, fast, and low operation cost, however, it requires a high concentration of at least one component of the precipitates and therefore, cannot be used at trace level concentrations<sup>76</sup>. Solvent-extraction is

another process for radioactive decontamination, however, the process involves the use of organic solvents which occupy significant fire hazard and the formation of the third phase is a problem<sup>80</sup>.

In recent years, new solid nanosized materials have become more important due to their special physical and chemical properties. Since the diameter of nanoparticles (NPs) is less than 100 nm and most of their atoms are present on the surface. These surface atoms are unsaturated and can bind with other atoms that possess high chemical activity. A number of NPs have been explored for this purpose that includes TiO<sub>2</sub>, ZnO, ZrO<sub>2</sub>, CeO<sub>2</sub> etc. The result indicates that these materials have a very high adsorptive capacity and give promising results when used for trace metal analyses of different types of sample solutions<sup>68, 69, 81</sup>. However, their separation from the matrix is difficult that makes the process tedious. To overcome this issue, magnetic NPs attain a lot of attention in recent years. Magnetic NPs show super-paramagnetic behaviour<sup>82, 83</sup> and this property make their separation from the matrix very easy. Researchers have demonstrated the application of magnetic NPs in a number of fields including biotechnology/biomedicine<sup>84, 85</sup>, catalysis<sup>83, 86</sup>, magnetic resonance imaging<sup>87</sup>, data storage<sup>88</sup> and environmental remediation<sup>89-93</sup>, where they have utilized super-paramagnetic behaviour of magnetic NPs. In the present thesis work, use of magnetic NPs as a sorbent for uranium has also been explored.

### ***1.2. Nanomaterials***

The word “nano” is derived from the Greek word “nanos” which means dwarf. Nanomaterials are sized between 1 - 100 nm. At this size scale, a drastic change in physical, chemical, optical, electrical, catalytic, magnetic properties of the material is observed. The size at which material displays properties different from that of the bulk is material dependent as well as property dependent i.e., different nanomaterial show transition from the bulk at different size scales. Over the last 30 years, nanomaterials have revolutionized the field of

chemistry in a number of fields such as bioimaging, environmental remediation, solar energy conversion, and catalysis. Extremely small sizes of nanomaterials result in a high percentage of atoms at the surface leading to the high reactivity of these materials as compared to a larger size material with the same chemical composition. Also, nanomaterials show size, shape and composition-dependent properties, therefore, a single material can show a wide range of properties and applications depending on the size<sup>11</sup>. Depending on the number of dimensions which are reduced to the nanometer size range, nanomaterials can be classified as zero-dimensional (QDs), one-dimensional (nanowires, nanorods, and nanotubules) and two-dimensional (quantum well, nanosheet, graphene)<sup>11</sup>. In zero-dimensional nanomaterials, all the three dimensions are reduced to nanometer range. In one-dimensional nanomaterials, two dimensions are in the nanometer range and one can remain large. In two-dimensional nanomaterials, one dimension is reduced to nanometer range and the other two dimensions remain large. The origin of unique physical, chemical, optical, electrical, catalytic, magnetic properties of NPs, that are neither similar to bulk nor to individual atoms or molecules, can be explained either in terms of surface effect or quantum-size effect owing to quantum-mechanical rule.

### 1.2.1. Surface Effect

For bulk materials, usually greater than one micron, the percentage of atoms at the surface is infinitesimally small compared to the total number of atoms of the material. As the size of the material is reduced, the ratio of surface atoms to inner atoms starts increasing. This results in low coordination number of the surface atoms as compared to inner atoms and because of this, surface atoms are highly chemically reactive, catalytically active and polarisable in comparison with the inner atoms. This high proportion of the surface atoms in nanomaterials result in some of the interesting and unexpected properties that are different from the bulk properties. For example, bulk gold is an inert noble metal, but gold

nanoparticles are an excellent catalyst with size-dependent catalytic ability. Absorption of solar radiation in photovoltaic cells is much higher in materials composed of nanomaterials as compared to that in thin films of continuous sheets of material, i.e. the smaller the particles, greater is the solar radiation absorption.

### 1.2.2. Quantum Size Effect:

An important parameter of a semiconductor material is the width of the energy gap that separates the conduction band (CB) from the valence band (VB) (Figure 1.1A). In semiconductor of macroscopic sizes, the width of this gap is a fixed parameter which is determined by material's identity. However, the situation changes in the case of semiconductor nanomaterials having size  $<10$  nm (Figure 1.1A). This size range corresponds to the regime of quantum confinement for which the electronic excitations “feel” the presence of particle boundaries and respond to changes in particle size by adjusting their energy

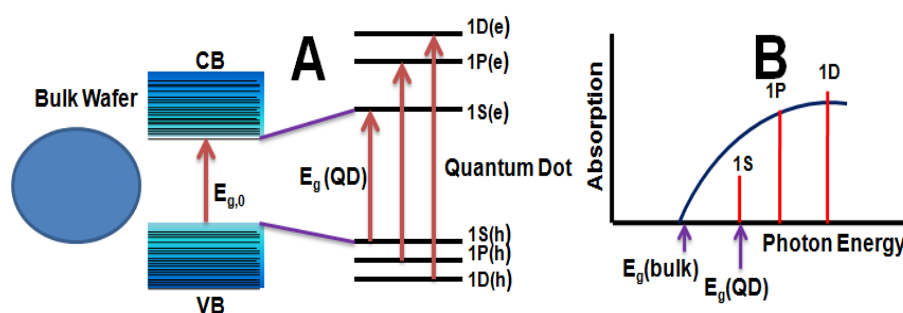


**Figure 1.1** (A) Energy level diagram of a bulk semiconductor and quantum dot. (B) A schematic representation of the continuous absorption spectrum of a bulk semiconductor (curved line), compared to the discrete absorption spectrum of a QD (vertical bars). Adapted after modification from ref<sup>94</sup>

spectra. This phenomenon is known as “quantum size effect”. Because of this effect, the same material will show different optical and electronic properties as the size changes. In nanomaterials, since the size of the particle is in nanometer range, therefore, the optical properties changes with the change in size.

In the present work, quantum dots (QDs), a class of nanomaterials have been used for solar energy conversion and environmental applications. The next section will discuss various aspects of QDs, their structural and charge carrier transfer properties.

### 1.3. Quantum Dot (QDs)

QDs<sup>94-96</sup> are semiconductor nanocrystals which show “quantum confinement effect”. Quantum confinement effect occurs when the size of the particle becomes comparable or smaller to the natural length scale of electron and hole. This natural length scale is known as Bohr radius<sup>97</sup> and is given by equation 1.1.

$$a_B = \epsilon \frac{m}{m^*} a_0 \quad (1.1)$$

where,  $a_B$  is Bohr radius of the particle,  $\epsilon$  is the dielectric constant of the material,  $m^*$  is the mass of the particle,  $m$  is the rest mass of the electron and  $a_0$  is the Bohr radius of the H-atom ( $\sim 0.52\text{\AA}$ ). In QDs the fundamental charge carriers are electron and hole. The bound electron and hole in a small size regime are called an exciton. Depending upon the size of the particle, three confinement region forms<sup>98</sup>. If the radius ( $a$ ) of the nanocrystal is smaller than the Bohr radii of the electron ( $a_e$ ), hole ( $a_h$ ) and exciton ( $a_{exc}$ ) i.e.  $a < a_e, a_h, a_{exc}$ , in this situation electron and hole are considered to be confined by the potential energy boundary of the nanocrystal. This condition is known as a strong confinement regime. On the other hand, when the radius,  $a$ , is smaller than both electron and hole Bohr radii but larger than the exciton Bohr radius (i.e.  $a_e, a_h < a < a_{exc}$ ) the situation is referred to as weak confinement regime. The intermediate situation arrives when the radius of the nanocrystals is in between  $a_e$  and  $a_h$ . In the intermediate confinement regime either electron or hole is strongly confined while other is not. Therefore, confinement of a particle depends on the size of the nanomaterials. For example, Bohr radius of III-V semiconductor InAs<sup>99</sup> is 36 nm which is much larger than the typical size of nanocrystals ( $< 10$  nm). This situation is referred as strong

confinement regime. Conversely, Bohr radius of CuCl (0.7 nm) is very small and, therefore these nanocrystal are in weak confinement regime. The exciton Bohr radius of II-VI semiconductors such as CdS, CdSe and CdTe are in the range of 4-7 nm therefore, these materials are either in strong or intermediated confinement regime depending on the size of the nanocrystal. Although, QDs is relatively a new term, however, the confinement effect has been established since 1960's when the researchers have observed a spectral shift in the absorption of colloidal semiconductor with the change in size<sup>100, 101</sup>. Later on, this energy size relationship was explained using “quantum box model”. According to this model, as the size of QDs decreases, energy gap increases leading to solar radiation absorption in the blue region of the solar spectrum. For a spherical QD with radius R, the model predicts the size-dependent contribution to energy gap is simply proportional to  $1/R^2$  and is given by equation 1.2.

$$E_g(QD) = E_{g,0} + \frac{h^2}{8m_{eh}R^2} \quad (1.2)$$

where  $E_{g,0}$  is the band gap of the bulk semiconductor,  $E_g(QD)$  is the band gap of QDs having radius R.  $m_{eh}$  is called as reduced mass and is defined as

$$m_{eh} = \frac{m_e m_h}{m_e + m_h} \quad (1.3)$$

where  $m_e$  and  $m_h$  are the effective masses of electron and hole respectively.

Equation 1.2 represents the separation between the lowest electron ( $1S_e$ ) and hole state ( $1S_h$ ) of QDs. In addition to an increase in energy gap, quantum confinement leads to a collapse of the continuous energy band of bulk material into discrete, “atomic” energy levels. These well separated QD states are labeled as (1S, 1P, 1D etc.) as illustrated in Figure 1.1A. The discrete energy states of QDs leads to the discrete absorption spectrum as shown in

Figure 1.1B, which is in contrast to the absorption band of a bulk semiconductor (Figure 1.1B).

QDs bridge the gap between clusters molecules and bulk materials. Now the question arises what is the boundary between QDs, clusters and bulk materials. In general ~100 - 10,000 atoms in a particle are a crude estimate at which nanocrystal regime occurs. The lower limit is decided by the stability of the bulk crystalline structure with respect to isomerization into molecular structure. The upper limit corresponds to the size range for which the energy level spacing is approaching the thermal energy  $kT$ , means that particle becomes mobile inside the QDs<sup>102,103</sup>.

### 1.3.1. Electronic Structure of the QDs: Theoretical Framework

#### 1.3.1.1. Particle-in-a-Sphere Model

In QDs, the size quantization effect occurs because of the quantum confinement effect. However, the quantitative description of the size-dependent electronic properties is difficult to imagine without considering any model. As the charge carriers are confined in all three dimension, QDs can be considered as a particle- in-a- sphere model<sup>102, 103</sup>. According to this model, the energy of a particle having mass " $m$ " confined in a spherical potential of radius " $a$ " can be given as:

$$E_{n,l} = \frac{\hbar^2 k_{n,l}^2}{2m} = \frac{\hbar^2 \alpha_{n,l}^2}{2ma^2} \quad (1.4)$$

As the particle-in-a-sphere model consider zero potential energy, the energy term in equation 1.4 is the kinetic energy of a free electron and is strongly dependent on the size of the particle. The model suggests that the particle inside the sphere is free from any kind of perturbation i.e. the sphere is empty. However, in a semiconductor crystal, several atoms are present. This limitation can be overcome by considering effective mass approximation<sup>104, 105</sup>.

### 1.3.1.2. Effective Mass Approximation

The electronic wavefunctions in a bulk semiconductor crystal can be written according to Bloch's theorem as follows

$$\Psi_{nk}(r) = \mu_{nk}(r) \exp(ik \cdot r) \quad (1.5)$$

here 'n' and 'k' are the band index and wave vectors of the wavefunction and  $\mu_{nk}$  is a function that varies with the periodicity of the crystal lattice. The energy of these wavefunctions is typically given by  $E$  vs.  $k$  band diagram as shown in Figure 1.2. For simplicity in effective mass approximation, the bands are assumed to be parabolic. Generally, two types of the semiconductor can be classified under this approximation, direct band gap, and indirect band gap semiconductor. In direct band gap semiconductor, the minimum of both VB and CB lies at  $k=0$  position (Figure 1.2A) whereas in indirect band gap semiconductor CB remains away

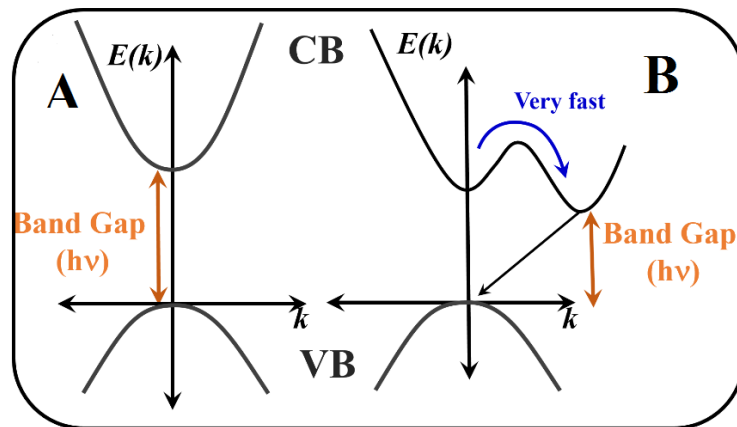


**Figure 1.2.** Band energy diagram of (A) direct and (B) indirect bulk semiconductor.

from  $k=0$  (Figure 1.2B) as a result, electronic transitions from VB to CB involves absorption of photons in order to obey Frank-Condon principle. In effective mass approximation approach, the energy of the CB and VB can be given as:

$$E_k^C = \frac{\hbar^2 k^2}{8\pi^2 m_{eff}^C} + E_g \quad (1.6)$$

$$E_k^V = -\frac{\hbar^2 k^2}{8\pi^2 m_{eff}^V} \quad (1.7)$$

where,  $E_g$  stands for energy difference between the maximum point of the VB and the minimum point of the CB. In this approximation, the charge carriers behave as free particles with an *effective mass*,  $m_{eff}^c$  and  $m_{eff}^v$  for electron in CB and hole in VB respectively. With this effective mass approximation technique, the periodicity of the crystal lattice is completely ignored and the charge carriers (electron and hole) are considered as a free particle having different masses.

### 1.3.1.3. Band Structure

Theoretical calculations suggest that the bulk CB and VB are parabolic in nature. However, the real band structure of II-VI semiconductor is more complicated. In case of CdSe the CB obeys the effective mass approximation however, VB does not. The CB of the CdSe arises from the cadmium's 5s orbital which is only 2-fold degenerate at  $k=0$ . On the other hand, more complicated VB is made from the 4p orbital of the selenium which is 6-fold degenerate at  $k=0$ <sup>106</sup>. The VB degeneracy of the two different structural forms (diamond and wurtzite) of CdSe is presented in Figure 1.3. In diamond like structure due to strong spin-orbit coupling ( $\Delta=0.42$  eV)<sup>107</sup> the degenerate VB split into two,  $p_{3/2}$  and  $p_{1/2}$ , states at  $k=0$

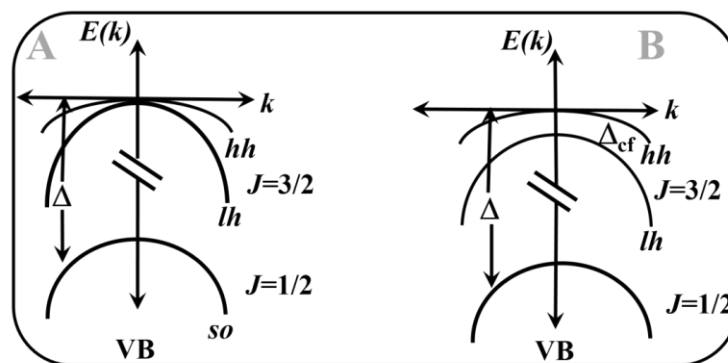


**Figure 1.3.** Valance band splitting of bulk CdSe in (A) diamond and (B) wurtzite like structure at  $k=0$  point. Adapted after modification from ref<sup>94</sup>

point. The subscript (3/2 and 1/2) arises due to spin-orbit coupling and refers as *angular momentum* ( $J=l+s$ ). For selenium atom, the 4p orbital contains four electrons, the angular contribution  $l=1$  while the spin contribution  $s=1/2$ . Away from  $k=0$  point the band  $p_{3/2}$  further split into two subbands,  $J_z=\pm 3/2$  and  $J_z=\pm 1/2$ , where  $J_z$  is the projection of  $J$ . These three bands are usually referred as heavy-hole ( $hh$ ,  $J=3/2$  and  $J_z=\pm 3/2$ ), light-hole ( $lh$ ,  $J=3/2$  and  $J_z=\pm 1/2$ ) and split-off-hole ( $so$ ,  $J=1/2$ ). However, in the wurtzite (hexagonal) structure the heavy-hole and the light-hole levels are no longer degenerate at  $k=0$  point due to crystal field splitting ( $\Delta_{cf}$ )<sup>106, 108</sup>.

#### 1.3.1.4. Energy Structure of QDs:

In absence of any band mixing effect, each bulk band gives rise to several independent quantized states<sup>109-115</sup>. Each quantized state can be defined by two quantum numbers,  $L$ , an angular momentum wave function which describes the carrier motions in the nanocrystals and  $n$ , which describes the number of states in a series of given symmetry. Generally, the notation of electron and hole states are used as  $nL_e$  and  $nL_h$ . For  $L = 0, 1, 2$ , the typical notation for  $L$  are S, P, D. Thus the electron states are defined as  $1S_e, 1P_e, 1D_e$  and the hole states are as  $1S_h, 1P_h, 1D_h$  corresponds to  $n=1$ . The valance band Hamiltonian contains both crystal lattice and nanocrystals confinement potential, as a result, the total angular momentum can be expressed as  $F=L+J$  where  $J$  is the sum of Bloch function angular momentum. In general, the VB states are denoted by  $nL_F$ . For CdSe nanocrystals, size dependent hole energy calculation by taking into account mixing between heavy hole, light hole and split-off hole shows the lowest energy hole states are  $1S_{3/2}, 1P_{3/2}, 2S_{3/2}$ . The lowest energy excitons are thus expressed as  $1S_e-1S_{3/2}$  (1S),  $1S_e-2S_{3/2}$  (2S) and  $1P_e-1P_{3/2}$  (1P). In optical absorption spectra of a good quality of colloidal CdSe QDs all these states are well resolved as shown in Figure 1.4.

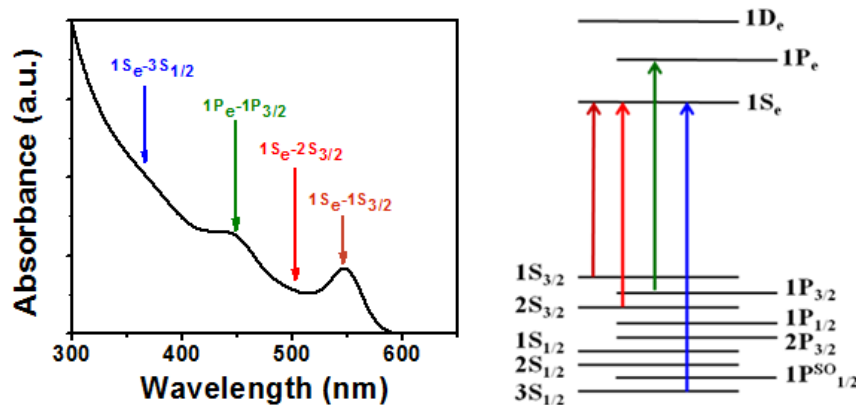


**Figure 1.4.** Optical absorption spectrum of CdSe QDs and assignment of different excitonic states. In the schematic diagram the lowest energy allowed interband (VB to CB) transitions are shown for CdSe QDs.

### 1.3.2. Dark Exciton and Stoke Shift

The excited state charge carrier recombination time of the bulk II-IV semiconductor is reported  $\sim 1$  ns<sup>116</sup> while for QDs it extends up to several  $\mu$ s. Many researchers have reported that this long lifetime is due to the surface state in which electron and hole are trapped. However, for high quality QDs this longer excited state lifetime can't be explained using surface state phenomenon and was described in terms of dark exciton model. This model accounts for the fine structure splitting of band edge exciton produced by e-h exchange interaction as well as anisotropy associated with crystal field and shape of a nanocrystal. The e-h exchange interaction energy largely depends on the electron-hole wavefunction overlap. As a result, this effect is more pronounced in nanocrystal as compared to their bulk counterpart. In such strong e-h interaction, lower energy electron and hole states (e.g.  $1S_e$  and  $1S_{3/2}$ ) cannot be considered independently and are treated as a combined state of a single particle (exciton) having total angular momentum  $N$ . With e-h exchange interaction within the exciton, the total angular momentum  $N$  can split into two states,  $N=1$ , a high energy optically active bright exciton and  $N=2$ , low energy optically passive dark exciton. Again

these two states are further split into five substates due to wurtzite nature of the CdSe lattice and its non-spherical shape (CdSe has the prolate shape). Two manifold of the upper (U) and lower (L) substates are formed which are labelled according to the magnitude of projection of total angular momentum of the exciton,  $N_m$  along the unique crystal axis. However, the effect of additional level splitting does not change the optically passive nature of the lowest energy exciton (dark exciton) which is characterized by  $N_m=2$ . The bright exciton which is optically active can be characterized by  $N_m=1^L$  (Figure 1.5). The thermal redistribution of excitons between these two levels ( $N_m=2$  and  $1^L$ ) leads to strong dependence of single exciton radiative lifetime of CdSe NC with sample temperature. At low temperature (liquid He temperature) the radiative recombination primarily occurs from low oscillator strength dark exciton which gives lifetime in the range of microsecond. At room temperature, the excitons can populate a bright state by thermal excitation which leads to radiative recombination from bright state and lifetime in nanosecond timescale was observed. Again, this band edge fine structure also responsible for Stokes shift observed in such nanocrystal. In most of the CdSe QDs the absorption is dominated by superposition of two upper manifold exciton states (i.e.  $1^U$  and  $0^U$ ). However, the luminescence state always dominated by either bright or dark

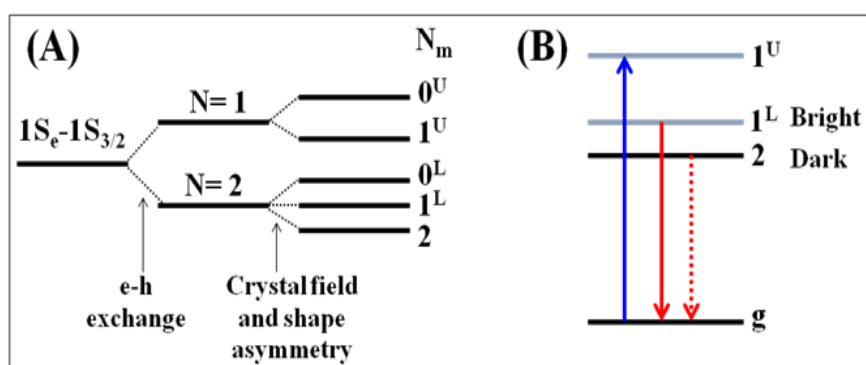


**Figure 1.5** (A). Fine structure splitting of band edge transition of CdSe QDs (B) Schematic of dark and bright state. Blue arrow show absorption and red arrows shows emission from bright (bold) and dark (dotted) state. Adapted after modification from ref<sup>94</sup>.

exciton states ( $1^L$  and 2) both of which are separated from their upper counterpart by energy equivalent to  $\sim 20$  to  $80\text{meV}$  (depending on the size of nanocrystal) which is the typical stokes shift value observed in most of the nanocrystals.

### 1.3.3. Charge Carrier Relaxation in QDs

Photo-excitation of QDs with energy equal to or more than the band gap energy generates hot charge carriers (electron and hole). Afterwards, both hot electron (in the CB) and hot hole (in the VB) relaxes to the lowest CB and VB state respectively through different pathways. In bulk semiconductor the energy spacing between intraband states are smaller than thermal energy as a result, the electron and hole relaxation can occur via phonon emission. However, in QDs this separation energy is much higher than thermal energy. Therefore, electron and hole relaxation to the lowest energy states occurs via several processes as summarized below.

#### 1.3.3.1. Phonon Bottleneck

In QDs, hot excitons can relax to the lowest electronic state by a process known as phonon bottleneck<sup>117, 118</sup>. Typically for QDs the confined states for electrons can have energy hundreds of meV however, the phonon has energy in the order of  $20\text{meV}$ . Therefore, carrier relaxation involves emission of multiple phonons. Such multi-phonon relaxation time can be estimated by,

$$\tau_c \sim \omega^{-1} \exp(\Delta E/KT) \quad (1.8)$$

where,  $\tau_c$  is the hot carrier cooling time,  $\omega$  is the phonon frequency, T is the temperature, K is the Boltzmann constant and  $\Delta E$  is the energy separation between quantized levels. However, such multi-phonon emission process is hindered due to the restriction imposed by selection rules. As a result, electron cooling becomes extremely slow which is known as phonon

bottleneck. Although, due to a high surface to volume ratio, scattering from surface plays an important role to overcome the selection rules to some extent.

### 1.3.3.2. Electron-Hole Energy Transfer

In the previous section, it has been discussed that VB of II-VI nanocrystals are degenerate which leads to a higher density of states in VB as compared to CB. Therefore, intraband transitions in VB for holes are much faster as compared to electrons in the CB. In such a strongly confined nanocrystal coulombic interaction between electron and hole plays an important role. Such coulomb interaction can transfer energy from electron to hole leading to faster electron cooling<sup>119</sup>.

### 1.3.3.3. Multi-Exciton Generation (MEG) and Auger Recombination

When the excitation energy of a photon is at least two times or more than two times the band gap of semiconductor ( $h\nu > 2E_g$ ), the process of MEG can be realized. During relaxation of the hot exciton, generated after the photo-excitation of QDs, excess energy can generate another exciton within the semiconductor leading to bi-exciton generation (Figure 1.6 A). Depending on the photon energy and band gap of the materials, it is also possible to generate more than two excitons. The MEG process<sup>110, 120, 121</sup> is more efficient in low band

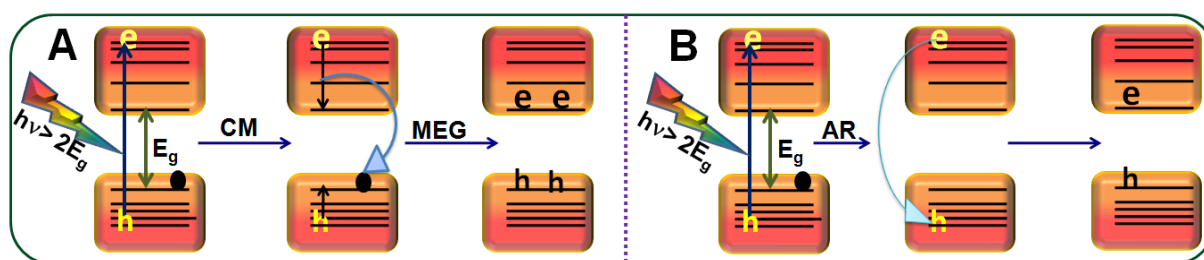


**Figure 1.6.** Schematic of (A) Multi-Exciton Generation and (B) Auger process.

gap materials such as PbS, PbSe, CdTe etc. Sometimes, this process is also referred to as impact ionization. Auger process (AR) is reverse to the MEG process. In this mechanism, the semiconductor having more than one exciton can transfer energy to another exciton as a

result hot exciton is created (Figure 1.6 B). The hot exciton can undergo relaxation in many different pathways.

#### 1.3.3.4. Involvement of Defect States

In QDs, the surface to volume ratio is very high which leads to surface defects in their structure. Such defects could arise due to dangling bond, capping agent, crystal mismatch etc. When this defect has energy within the mid-band gap region of semiconductor (Figure 1.7), then charge carrier (either electron or hole) can be trapped which alters their carrier relaxation process. Sometimes the defect sites can lie above the VB or CB edge that leads to surface resonance which also can influence carrier cooling mechanism.

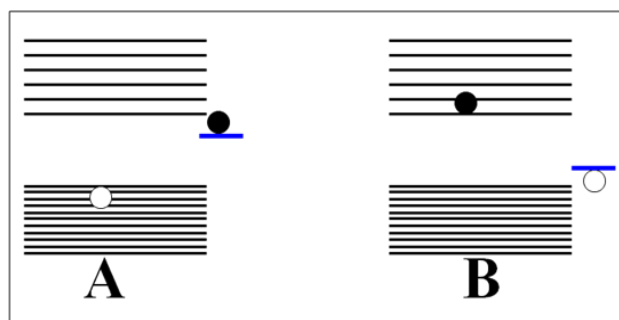


**Figure 1.7.** Schematic of (A) electron and (B) hole trapping in surface defects.

#### 1.3.4. Charge Separation in QDs

To obtain high efficiency in QDSC, it is very important to separate charge carriers from QDs materials before their own recombination. A number of composites are utilized for this purpose and described below

##### 1.3.4.1. Charge Separation in Core-Shell Heterostructure

When a core-shell heterostructure using two QDs are formed, the newly formed structure has different properties such as interfacial charge transfer, charge carrier relaxation, surface defects, etc. Depending on the energy level of each semiconductor the core-shell structures are generally classified as Type-I and Type-II heterostructure. In a Type-I

heterostructure, the smaller band gap materials are confined in the core and the wider band gap material is present as a shell<sup>122</sup>. The reverse band alignment of this heterostructure is referred to as inverted Type-I core-shell<sup>123</sup>. In both of these Type-I heterostructures, charge carriers are localized in one of the semiconductors, either core or shell. The situation is reversed in a Type-II core/shell structure, where band alignments are such that one of the charge carriers, either electron or hole is localized in the core while other will be localized into the shell resulting in charge separation within the material<sup>124-126</sup>. Apart from this Type-I

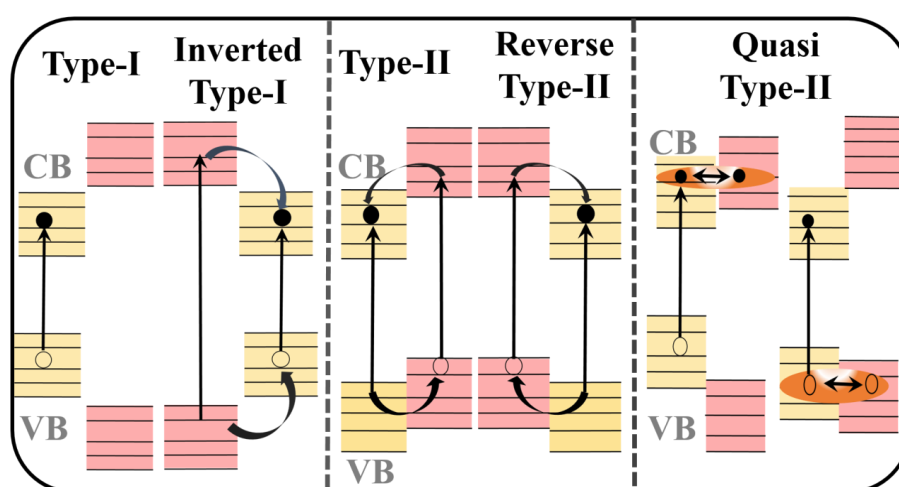


**Figure 1.8.** Illustration of charge carrier distribution in different types of the core-shell heterostructure.

and Type-II heterostructures, another important class of heterostructure is quasi Type-II or Type-I<sup>1/2</sup>core/shell<sup>127-130</sup>. In quasi Type-II core/shell, the band alignment of the heterostructure is like Type-I however, due to less difference in CB or the VB offset energy, either of the charge carriers is delocalized in two nanocrystals. This type of heterostructure is more useful in terms of quality as well as application. The wider band materials passivate the core of the nanocrystals while the charge delocalization increases charge separation. The energy level band structures of these core-shell heterostructures are shown in Figure 1.8.

### 1.3.4.2. Metal-Semiconductor Heterostructure

Generally, metal NPs have Fermi level below the CB of most of the semiconductors which allow metal NPs to act as an electron sink. Thus metal-semiconductor offers charge separation by decoupling electron and hole leading to a quenching in QDs luminescence. A number of reports are available in literature where researchers used this property to detect metal ions<sup>50-52</sup>. A shift in Fermi level of metal is also reported after transferring an electron from QDs to metal which increases the charge separation yield. Commonly used metals are Au, Ag, Pt metal NP along with TiO<sub>2</sub>, ZnO, CdSe, CdS etc. semiconductor to form metal-semiconductor heterostructure. Figure 1.9A demonstrates the energy level alignment of QDs and metals.

### 1.3.4.3. Dye-Semiconductor Heterostructure

Another approach for charge separation from QDs is to use a dye molecule which has high affinity to extract one of the carriers from the photo-excited QDs. For this, the HOMO-LUMO level of the dye molecule should matches with the energy levels of QDs in such a way so that one of the carriers can be transferred to the dye molecule. Figure 1.9B demonstrates the energy level alignment of QDs and dye molecules for charge separation.

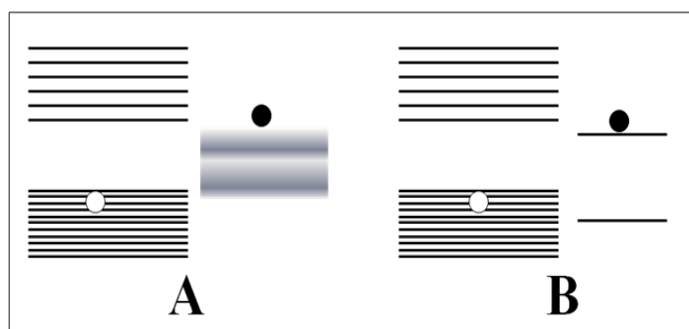


**Figure 1.9.** Band alignment of (A) metal-QDs and (B) Dye-QDs heterostructure.

In the present thesis, a composite system of CdSe/ZnS core-shell QDs (CSQDs) with thiols was studied to monitor the charge carrier dynamics. Coupled systems of CdSe/CdS

CSQDs with uranium and carbon QDs with  $\text{Eu}^{3+}$  were studied to demonstrate the charge separation from QDs to metal. A composite system of CdSe QDs with pyrogallol red dye was studied to demonstrate hole transfer process from QDs to dye molecule.

### 1.3.5. Synthesis of QDs

To achieve high luminescence quantum yield and high stability of QDs, different synthetic strategies are being employed. Two main methodologies for QDs synthesis are top-down and bottom-up approaches. In top-down approach, the synthesis is started with bulk material and subsequently the size is reduced to nanoscale by different techniques such as lithography, laser ablation, ion beam etching etc<sup>131, 132</sup>. These methods are costly and require high energy input. In bottom-up approach, the miniaturization of materials components (up to atomic level) with further self-assembly process leads to the formation of NPs from the colloidal dispersion. All chemical synthetic methods e.g. colloidal route, sol-gel, metal organic chemical vapour deposition (MOCVD), molecular beam epitaxy (MBE)<sup>133</sup> fall under this category. In the present thesis, high quality QDs were synthesized using colloidal route<sup>134</sup>. This procedure is the most successful in terms of quality and size distribution where pyrolysis of the metal-organic precursor in hot non-coordinating solvent occurs. At  $T > T_N$  (nucleation temperature) and  $C_P$  (precursor concentration)  $> C_N$  (threshold concentration for nucleation), nucleation event occurs. As  $C_P < C_N$  rapid growth of nanocrystals occurs. Once the monomer concentrations are sufficiently reduced, the growth of nuclei proceeds through Ostwald ripening process (La Mer model, Figure 1.10). In this stage, smaller particles get dissolved which leads to the formation of larger particles. To get narrow size distribution, it is necessary to avoid Ostwald ripening process and therefore rapid cooling of the reaction mixture after the fast rapid growth is required. A very good size distribution (standard deviation,  $\sigma < 10\%$ ) can be achieved by controlling precursor concentration, reaction time and temperature of the reaction mixture<sup>135</sup>. Size distribution can be improved further by carrying

out size selective precipitation using a polar non-polar solvent mixture. In case of oleic acid capped QDs polar solvent like ethanol, methanol or acetone etc. are used to clean the QDs<sup>136</sup>.<sup>137</sup>. The precipitate is re-dissolved in chloroform/hexane/toluene and precipitated again in a polar solvent for 2-3 times. With this process, a size distribution of ~5% can be achieved.

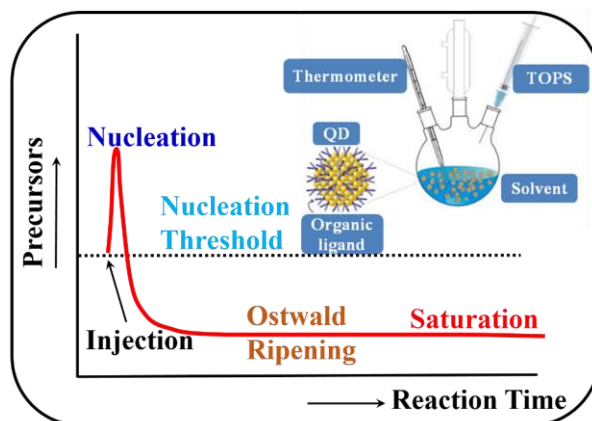


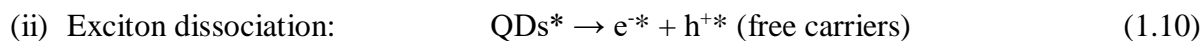
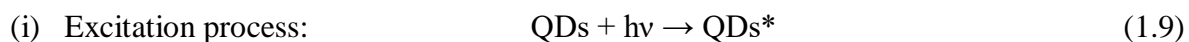
**Figure 1.10.** Nucleation and growth stage for the colloidal particle in La Mer growth model.

Adapted after modification from ref<sup>94</sup>

The present work involves the synthesis of II-VI (CdX, X=S, Se, Te) semiconductor QDs where CdO was used as cadmium precursor and oleic acid was used as capping agents. S, Se, and Te were injected into the reaction mixture at ~300°C temperature. The detailed experimental procedure of the QDs synthesis is described in chapter 3 and 4. Synthesized materials were characterized using different characterization techniques. These techniques are described in chapter 2.

#### 1.4. Quantum Dot Solar Cell (QDSC)

In present work, composite of QDs with different molecular adsorbates were described with an aim to achieve higher efficiency in QDSC. Therefore, it is important to understand the structure and operating principle of QDSC. The structure of QDSC is shown in Figure 1.11. Operation of the cell can be described by the following steps and the corresponding equations



where C.E. stands for counter electrode. The counter electrode is identical to the photoelectrode where the nanostructured  $\text{TiO}_2$  is deposited. QDs are neutralized by a redox mediator as shown in process 3 and 4 in Figure 1.11. Most common electrolytes used in QDSCs are aqueous polysulfide. Overall, the generation of electric power in this type of cells causes no permanent chemical transformation. To get higher efficiency in QDSC, it is very important to extract the photo-generated charge carriers, electron and hole. It has been reported that the electron extraction rate from QDs is much faster ( $\sim\text{ps}$ ) however, the hole transfer rate is observed to be slow and is one of the main reasons for the low efficiency of QDSC. In the present work, we have focused on this issue and suggested different molecular adsorbate which can extract hole at a comparable rate to that of an electron. These features are discussed in detail in chapter 3.

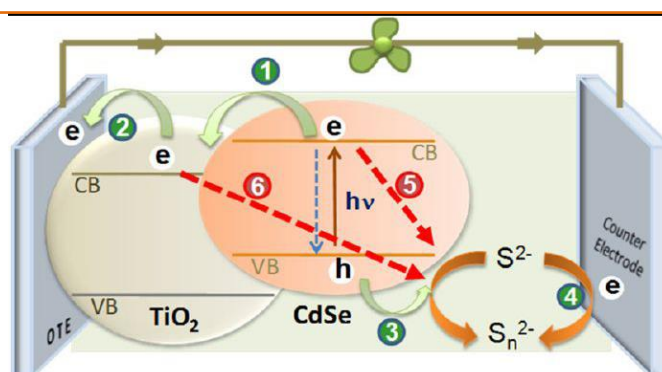


**Figure 1.11:** Schematic diagram illustrating the structure and operation of QDSC. Adapted with permission from ref<sup>256</sup>. Copyright 2012 American Chemical Society.

## 1.5. Theory of Electron Transfer

Electron transfer theory between donor (D) and acceptor (A) pair is based on the Marcus electron transfer model<sup>138, 139</sup>. To describe the model, the harmonic oscillator approximation is used where the reactant (D-A) transform to the products (D<sup>+</sup>-A<sup>-</sup>) via transition states (D<sup>---</sup>A). The rate of electron transfer is expressed by the Arrhenius equation

$$k_{eT} = k_t v_n \exp\left(\frac{-\Delta G^\ddagger}{k_B T}\right) \quad (1.13)$$

where,

$$\Delta G^\ddagger = \left(\frac{-(\Delta G^0 + \lambda)^2}{4\lambda}\right) \quad (1.14)$$

here  $\lambda$  is reorganization energy and can be expressed as the sum of energy involved in solvation and vibration, ( $\lambda = \lambda_s + \lambda_v$ ) and  $\Delta G^0$  is change in free energy. Equation 1.13 suggests that the electron transfer rate depends on  $\lambda$  as well as  $\Delta G^0$ . Depending on the value of  $\lambda$  and  $\Delta G^0$  electron transfer process can be recognized in three different regions and are illustrated in Figure 1.12.

- (i) Normal region,  $-\Delta G^0 < \lambda$  : here rate of electron transfer increases with increase in  $-\Delta G^0$ .
- (ii) Barrierless region,  $-\Delta G^0 = \lambda$  : here rate is maximum.
- (iii) Inverted region,  $-\Delta G^0 > \lambda$  : here rate decreases with increase in  $-\Delta G^0$ . Inverted region is the most counterintuitive prediction of Marcus theory<sup>140, 141</sup>.

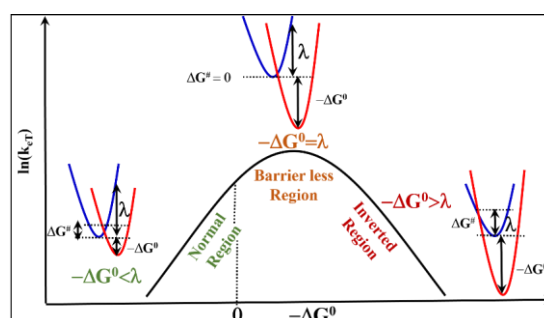


**Figure 1.12.**  $\ln(k_{eT})$  vs.  $G^0$  plot shows three different regions of electron transfer reaction.

However, Marcus theory is limited to the classical electron transfer theory where all reactants are considered to form product (transmission co-efficient =1). Under quantum mechanical treatment, transmission coefficient explicitly depends on electron tunnelling probability which governs by donor-acceptor overlap function ( $H_{AB}$ ). For classical electron transfer theory,  $H_{AB}$  considered being small and the reaction is nonadiabatic. However, for adiabatic reaction,  $H_{AB}$  has an important role in determining electron transfer reaction. Under such circumstances, electron transfer rate can be expressed by Marcus-Hush equation<sup>140</sup>,

$$k_{eT} = \frac{2\pi}{\hbar} [H_{DA}^2] \frac{1}{\sqrt{4\pi\lambda k_B T}} \exp\left(\frac{-(\Delta G^0 + \lambda)^2}{4\lambda}\right) \quad (1.15)$$

In the present thesis, composites of QDs with molecular adsorbates having different electron withdrawing and electron releasing groups were chosen and their charge transfer rate was monitored with the change in  $\Delta G^0$ . Marcus curve has been plotted for these systems and described in detail in chapter 3.

Along with QDs, magnetic NPs are also used in the present work. The next section will discuss the various aspects of magnetic NPs and their properties.

## 1.6. Magnetic Nanoparticles

Magnetic nanoparticles (MNPs) are NPs that show some response to an applied magnetic field. The magnetic moment of a material is mainly due to electron motion. An atom contains many electrons, each spinning about its own axis and moving in its own orbit. The magnetic moment associated with each kind of motion is a vector quantity, parallel to the axis of spin and normal to the plane of the orbit, respectively. The magnetic moment of the atom is the vector sum of all its electronic moments. Based on the magnetic moment, materials can be classified as paramagnetic, diamagnetic, ferromagnetic, ferrimagnetic and antiferromagnetic.

## 1.7. Overview and Scope of the Thesis

The present thesis demonstrates the application of QDs and magnetic NPs for solar energy conversion and environmental applications. As mentioned above that one of the major limitations in QDSC is slow hole transfer rate. The work carried out in thesis demonstrates the composite system of QDs with different molecular adsorbates where a hole can be extracted from QDs in sub-picosecond timescale. For this purpose, II-VI semiconductor QDs (CdX, X=S, Se, Te) are synthesized using hot injection route and their optical properties are monitored by employing steady state absorption and emission measurements. Different molecular adsorbates such as pyrogallol red (PGR) dye, catechols and thiols are chosen as hole transporting molecules. The systems are designed with an aim to achieve higher solar radiation absorption and faster hole transfer rate from QDs materials so that high efficiency QDSC can be realized. Time-resolved emission and ultrafast transient absorption study were employed to monitor charge transfer processes in ultrafast time scale and hole transfer process is demonstrated. While studying these composite systems, different processes such as super-sensitization, grand charge separation, hot hole extraction and interfacial metal-ligand complexation are observed. Super-sensitization and grand charge separation processes are observed in a composite system of CdSe QDs with PGR. These processes have advantages of higher solar radiation absorption and charge separation in a single system which ultimately can enhance the efficiency of QDSC. Earlier researchers have demonstrated the hot electron extraction from QDs however, to achieve high efficiency QDSC, it is also important to extract hot hole from the system on which no reports were available till then. In the present thesis, hot hole extraction from CdSe QDs to different catechols and thiol derivatives are demonstrated. Also, a series of catechols are chosen having different electron withdrawing and electron donating group and their effect on hole extraction and hot hole extraction is discussed. As mentioned above that core-shell heterostructure enhances the stability and

improves the optical properties of QDs. Hole extraction and hot hole extraction are also demonstrated in presence of type 1 shell, ZnS over CdSe core. Earlier, few reports were available where hole transporting molecule can also form a charge transfer (CT) complex with QDs and CT complex formation was observed from VB of QDs to the LUMO of adsorbate resulting in solar radiation absorption in the red region of the solar spectrum. However, any QDs surface has excess ions (either  $\text{Cd}^{2+}$  or  $\text{X}^{2-}$ ) depending on the synthesis conditions employed and these excess ions can bind with the molecular adsorbate. This binding can change the solar radiation absorption and charge carrier extraction properties. This is demonstrated in a coupled system of CdX QDs with nitro catechol (NCAT). NCAT forms a complex with excess  $\text{Cd}^{2+}$  ions on QDs surface and because of this complexation both solar radiation absorption and charge separation becomes significantly better. Such complex induced charge separation has not been discussed in the literature and gives a better understanding of interface property and its effect on charge carrier dynamics of QDs.

The second area where the work carried out in present thesis focuses is the detection of toxic ions. Application of QDs for detection of uranium and fluoride ions in water samples has been demonstrated. For this purpose more sophisticated techniques such as ICP-MS, chromatography etc. are used which are costly and require complex instrumentation. In the present work, luminescence property of QDs is used to detect trace level of toxic ions. Oleic acid capped CdSe/CdS CSQDs are synthesized and characterized. Ligand exchange experiment is performed to make these CSQDs water dispersible. Interaction of these CSQDs with uranium is monitored. It is observed that these CSQDs can detect trace levels of uranium and a detection limit of  $\sim 75$  ppb has been achieved. Along with detection, mechanism of detection is also demonstrated which help in optimizing the shell thickness and to achieve better detection limit. An understanding mechanism at a fundamental level will help in future to design and develop better detection probe. For fluoride ion detection, a photoluminescent

*on-off-on* probe based on carbon QDs (CQDs) and  $\text{Eu}^{3+}$  are designed. COOH functionalized, high luminescent CQDs are synthesized and characterized. Steady state optical absorption and emission studies are carried out to monitor its interaction with  $\text{Eu}^{3+}$ . CQDs/ $\text{Eu}^{3+}$  system is used to detect fluoride in water and working mechanism is described using different techniques such as X-ray diffraction, high resolution transmission electron microscopy and time resolved emission studies. The probe is found to be selective for fluoride ion and used for detection of fluoride ions in toothpaste samples.

The present thesis also describes the application of magnetic NPs as a sorbent for uranium. A number of sorbents are reported earlier, however, their separation from the matrix is a challenging task. In present work, the advantage of the magnetic property is used to separate sorbent from solution. Humic acid coated  $\text{Fe}_3\text{O}_4$  NPs are also synthesized and their applicability for uranium extraction from sea water matrix has been demonstrated.

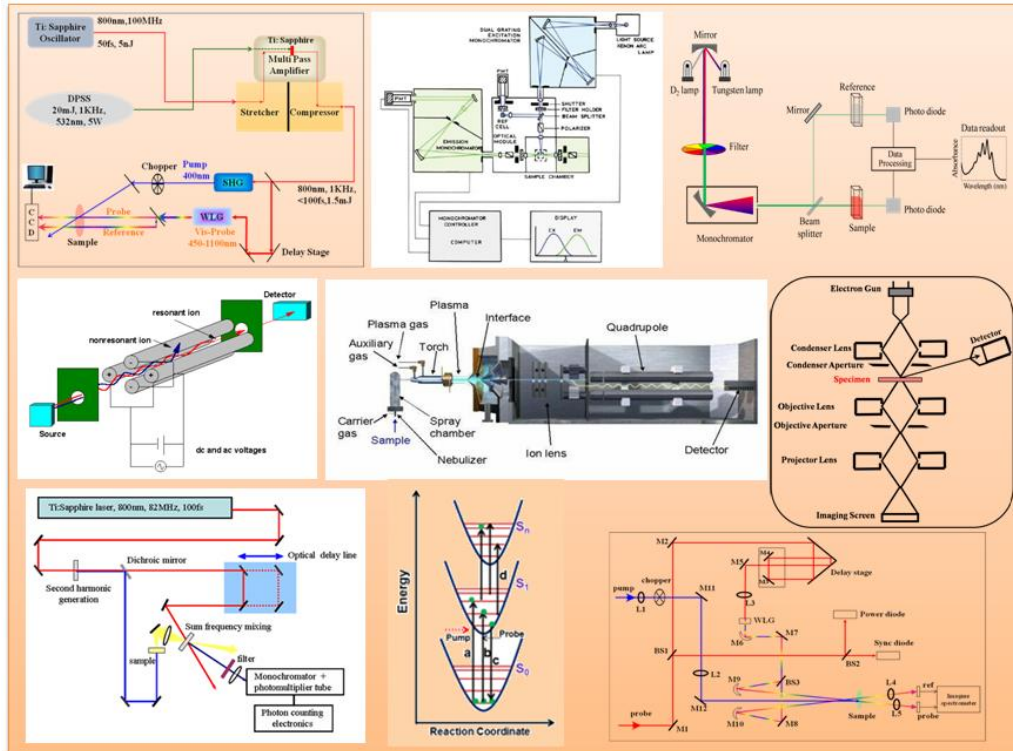
Overall the work carried out in the present thesis improves the knowledge over hole transfer from QDs materials which is a major limitation of QDSC. This work also enlightens the application of QDs for uranium and fluoride ion detection and demonstrates the mechanistic pathways involved in the detection which in turn will help in future to design better detection probe. The work also supports magnetic NPs as promising sorbent material where their magnetic property is utilized to separate them from samples and tedious processes such as centrifugation can be avoided.





# CHAPTER-2

## Experimental Techniques





The main objective of the present thesis is the synthesis of nanomaterials for solar energy conversion and environmental applications. For this purpose different nanomaterials were synthesized and characterized using different techniques such as X-ray diffraction (XRD), transmission electron microscopy (TEM), Fourier transform infrared spectroscopy (FTIR), thermogravimetric analysis (TGA), zeta potential, vibrating sample magnetometer (VSM), inductively coupled plasma mass spectrometer (ICP-MS), UV-Vis absorption and photoluminescence (PL) spectroscopy, time-correlated single photon counting (TCSPC), femtosecond fluorescence up-conversion and femtosecond transient absorption spectroscopy. A brief discussion about these techniques is described in this chapter.

### **2.1. X-Ray Diffraction (XRD)**

X-ray crystallography is the most extensively used technique to identify crystal structure and to determine crystallite size of a compound<sup>141, 142</sup>. Since the wavelength of X-ray is comparable to atoms, they are used to find the structural arrangement of atoms inside a material. In XRD, a beam of X-ray interacts with the electrons of the atoms in the crystal which causes the electrons to oscillate with the same frequency as the incident X-ray frequency. During this oscillation, they become a new source of electromagnetic radiation emission. In certain cases the emission will be in phase and reinforce one another resulting in constructive interference while in other cases, emission will be out of phase resulting in destructive interference. Diffraction occurs only when Bragg's Law is satisfied. According to Bragg's law (Figure 2.1) when the scattered waves interfere constructively, the difference between the path lengths of the two waves is equal to an integer multiple of the wavelength. The path difference between the two waves undergoing interference is given by  $2d\sin\theta$ , where  $\theta$  is the scattering angle. According to Bragg's condition for diffraction

$$n\lambda = 2d_{hkl} \sin \theta \quad (2.1)$$

Where  $n$  is an integer and referred as the order of diffraction. For first-order diffraction  $n=1$ , second order diffraction  $n=2$  and so on.  $\lambda$  is the wavelength of X-ray, and  $d_{hkl}$  is the interplanar spacing in a crystal corresponding to Miller indices  $hkl$ .  $d_{hkl}$  is related to the dimensions of unit cell by equation 2.2

$$\frac{1}{d_{hkl}^2} = \frac{h^2}{a^2} + \frac{k^2}{b^2} + \frac{l^2}{c^2} \quad (2.2)$$

Where  $a$ ,  $b$ ,  $c$  are the dimensions of unit cell in X, Y, and Z directions respectively.

For the cubic crystal,  $a = b = c$ , therefore, equation 2.2 can be simplified to

$$\frac{1}{d_{hkl}^2} = \frac{h^2 + k^2 + l^2}{a^2} \quad (2.3)$$

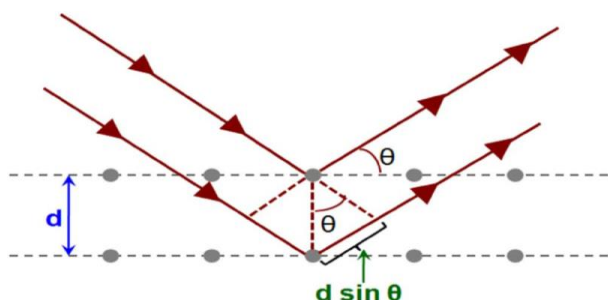


**Figure 2.1.** Illustration of Bragg law in a crystal.

X-ray instrument (Figure 2.2) consists of an X-ray source, a sample chamber and a detector to detect the diffracted X-rays. X-ray source is a sealed X-ray tube consisting of a metal ion (Cu, Mo usually) as a target. A beam of high energy electrons from a hot filament (often tungsten) is bombarded on this metal target. The incident beam will ionize electrons from the K-shell (1s) of the target atom and this electron vacancy in K-shell is filled by the electrons from subsequent outer shells, L and M. During this transition X-rays are emitted. Sharp intense monochromatic X-rays are necessary for performing diffraction experiment which is done with the help of suitable filters. For powder X-ray diffraction, the samples are taken in powder form on an amorphous substrate (glass window) in presence of a binder. The

scattered x rays are detected by a scintillation detector which is scanned over different angles. The intensities are plotted with respect to the angle of diffraction of x-ray beam and the peak is observed when Bragg's condition gets satisfied.

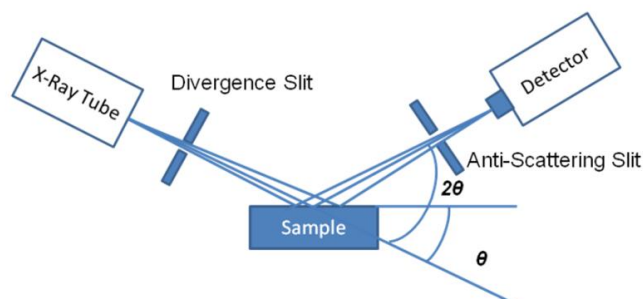


**Figure 2.2.** Schematic presentation of an XRD instrument.

A typical XRD pattern is a plot of  $2\theta$  versus intensity. The intensity of the scattered X-ray beam depends on the angle of scattering and atomic scattering factors which in turn depends upon the density of the electrons in the scattering center. Therefore, the higher the number of electrons, greater is scattering from that particular atom. Also, the width of the lines gives useful information about the nature of the sample, crystalline or nano-crystalline, and the crystallite size. For spherical particles, the crystallite size can be calculated from XRD pattern using Scherrer's equation

$$d = \frac{.9\lambda}{w \cos \theta} \quad (2.4)$$

Where  $d$  is the crystallite size and  $w$  is the full width at half maxima (FWHM) of the diffraction peak. As can be seen from equation 2.4 that for crystalline samples  $d$  will be large therefore  $w$  will be small and peaks will be the sharp while for nano-crystalline samples,  $d$  will be small and correspondingly  $w$  will be large and peaks will be broader. XRD also gives useful information about the crystalline phase. In the present study, synthesis of QDs and NPs was done where more than one phase may form depending on synthetic conditions and precursors used. A number of properties such as quantum yield (QY), charge carrier

relaxation, shell formation depends on the crystal phase. The phase characterization of the synthesized materials can be done using XRD by comparing the diffraction pattern obtained for samples with that of previously reported patterns given by database from Joint Committee on Powder Diffraction Standards (JCPDS, 1969), replaced by International Centre for Diffraction Data (ICDD, 1978)<sup>143</sup>.

For the present work, Philips X-ray machine, model-PW 1710 with Ni filtered Cu K $\alpha$  radiation ( $\lambda=1.54178$  Å), using silicon as an external standard was used. Experiments were performed in an angle range 10°-70° in a continuous scan mode, with a step width of 0.02°, and the scan of 1° per minute. The results were analyzed using the Joint Committee on Powder Diffraction Standards (JCPDS, 1969).

## **2.2. Transmission Electron Microscopy (TEM)**

As interaction of foreign ions, as well as sorption, depends on particle size and shape, in the synthesis of nanomaterials, it is very important to get the information about these properties. One of the versatile techniques for this is transmission electron microscopy (TEM). Particles size distribution, the presence of different planes, the nature of crystallinity can be analyzed using TEM<sup>144, 145</sup>. In TEM, electrons are used as probes since their wavelength can be tuned according to energy. In modern TEMs accelerating voltage of ~100-1500 keV are used. The wavelength of electrons for these voltages is in Pico meters; therefore TEM can in principle image lattice planes. Additionally, one can perform electron diffraction and obtain crystallinity and crystal structure<sup>146</sup>.

The basic layout of TEM instrument is shown in Figure 2.3. TEM usually consists of an electron source, an illumination system, sample specimen, objective lens, projector lens, magnification system and detector. An electron gun is used as a source of electron based on thermionic emission metal. These electrons are accelerated by the positive potential down the

column. After this, a condenser lens is used which focus the stream of the electron beam to a single spot size as the emitted electron beams from the metal surface are diverging in nature. A condenser aperture is a thin disk or strip of metal with a small circular through-hole. It is

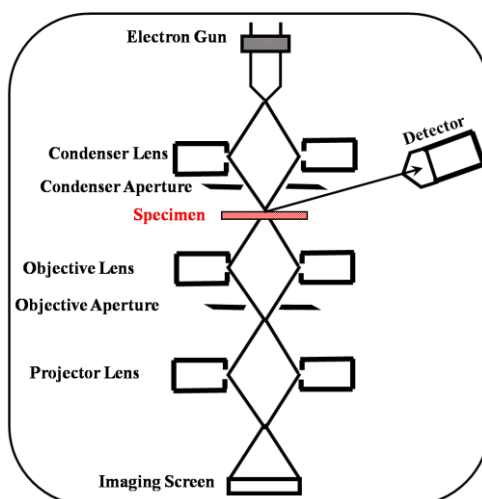


**Figure 2.3.** Schematic illustration of a typical TEM instrument.

used to restrict the electron beams and filter out unwanted scattered electrons before image formation<sup>145, 147-149</sup>. After this electron beam interacts with the sample. The sample should be thin enough to interact with the electron. The beam from the condenser aperture strikes the sample and the electron-sample interaction takes place. The main imaging part of the TEM is an objective lens having a very small focal length which results in the high converging ability to produce an enlarged image. Such lens also reduces the aberrations of ejecting electrons which are scattered at large angles. Objective apertures are used to examine the periodic diffraction of an electron by ordered arrangements of atoms in the sample. Projector lens is used to expand the beam onto the imaging screen. Imaging systems in a TEM consist of a phosphor screen, film, CCD camera, image plate etc. The image strikes the phosphor screen and light is generated, allowing the users to see the image. The darker areas of the image represent those areas of the sample where fewer electrons are transmitted. The lighter areas of the image represent those areas of the sample where more electrons are transmitted.

Besides imaging operation, TEM instrument is also used to record selected area electron diffraction (SAED) pattern. In a crystalline sample presence of long-range order gives rise to rings or spots arising from constructive interference of scattering from different planes. The angular position of spots or rings is related to crystalline structure or symmetry. Since the magnification parameters of TEM are known, lattice spacing can be obtained.

For the present work, TEM 2000 FX, JEOL, Japan instrument was used. ~5 mg of sample was dispersed in the suitable solvent under ultrasonic vibration for 1 h. A drop of the dispersed particles was put over the carbon-coated copper grid and evaporated to dryness at room temperature and particle size and SAED pattern were determined.

### **2.3. Fourier Transform Infrared Spectroscopy (FTIR)**

Fourier transform infrared spectroscopy (FTIR) is used to obtain an infrared spectrum of a solid, liquid or gas. FTIR is a fingerprint technique which gives information about the functional groups present in a material. In the present study, different QDs and nanomaterials were synthesized and functional groups analysis was carried out using FTIR.

FTIR is typically based on the Michelson Interferometer experimental setup as shown in Figure 2.4. The interferometer consists of a beam splitter, a fixed mirror, and a mirror that translates back and forth, very precisely. The beam splitter is made of a special material that transmits half of the radiation striking on it and reflects the other half. Radiation from the source strikes the beam splitter and separates into two beams. One beam is transmitted through the beam splitter to the fixed mirror and the second is reflected off the beam splitter to the moving mirror. The fixed and moving mirrors reflect the radiation back to the beamsplitter. Again, half of this reflected radiation is transmitted and half is reflected at the beam splitter, resulting in one beam passing to the detector and the second back to the source. Ideally, 50% of the light is refracted towards the fixed mirror and 50% is transmitted towards

the moving mirror. Light is reflected from the two mirrors back to the beam splitter and some fraction of the original light passes into the sample compartment. There the light is focused on the sample. On leaving the sample compartment the light is refocused on to the detector. The difference in optical path length between the two arms to the interferometer is known as the retardation or optical path difference (OPD). An interferogram is obtained by varying the retardation and recording the signal from the detector for various values of the retardation. An interferogram is converted to a spectrum by Fourier transformation. The result of Fourier transformation is a spectrum of the signal at a series of discrete wavelengths.

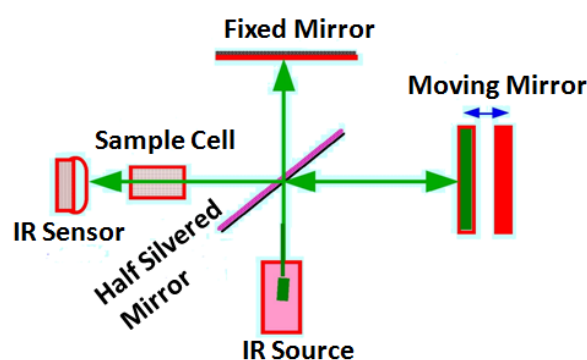


**Figure 2.4.** The Layout of FTIR Spectrometer

In the present work, FTIR spectra were recorded using platinum attenuated total reflection (ATR) technique. All spectra were obtained using a resolution of  $4\text{ cm}^{-1}$  (wave number) and equal measurement conditions ( $3900\text{--}450\text{ cm}^{-1}$ , 40 scans, scans means 16 repetitions of a single FTIR measurement).

#### 2.4. Thermogravimetric analysis (TGA)

Thermogravimetric analysis (TGA) is a method in which changes in physical and chemical properties of materials are measured as a function of increasing temperature (with constant heating rate) or as a function of time (with constant temperature and/or constant mass loss). TGA is commonly used to determine selected characteristics of materials that exhibit either mass loss or gain due to decomposition, oxidation, or loss of volatiles.

In the present work, TGA analysis was carried out to determine the amount of organic coating on the NPs surface. Measurements were carried out using Mettler Thermoanalyzer (model: TGA/SDTA851<sup>e</sup>/MT5/LF/1600) in the air. Around 100 mg of sample was heated in an alumina crucible with the gas flow rate of 100 mL min<sup>-1</sup> from room temperature to 900 K at the heating rate of 10 K min<sup>-1</sup>. All the weight changes were corrected for buoyancy correction, obtained under identical experimental conditions.

## 2.5. Zeta Potential

Zeta potential is the potential difference between the dispersion medium and the stationary layer of fluid attached to the dispersed particle. It is caused by the net electrical charge contained within the region bounded by the slipping plane, and also depends on the location of that plane. The magnitude of the zeta potential indicates the degree of electrostatic repulsion between adjacent, similarly charged particles in the dispersion. For molecules and particles that are small enough, a high zeta potential will confer stability, i.e., the solution or dispersion will resist aggregation. When the potential is small, attractive forces may exceed this repulsion and the dispersion may break and flocculate. So, colloids with high zeta potential (negative or positive) are electrically stabilized while colloids with low zeta potentials tend to coagulate or flocculate. Zeta potential can be calculated using electrophoretic mobility by Henry equation.

$$U_E = \frac{2\varepsilon Z}{3\eta} \quad (2.5)$$

Where,  $U_E$  - Electrophoretic mobility,  $z$  - Zeta potential,  $\varepsilon$  - Dielectric constant,  $\eta$  - Viscosity.

To measure electrophoretic mobility a cell is used with electrodes at either end to which a potential is applied. Particles move towards the electrode of opposite charge and their velocity is measured using laser Doppler velocimetry.

In the present work, zeta potential measurements were carried out using a PSS/NICOMP 380 ZLS system with a red He–Ne laser diode at 632.8 Å in a fixed angle 90° plastic cell. Measurements were performed at 25° C after a temperature homogenization time of 5 min. For reproducibility, at least three measurements were conducted. The instrument calibration was checked before each experiment using a latex suspension of known zeta potential (i.e., 55±5 mV).

### **2.6. Vibrating Sample Magnetometer (VSM)**

VSM is a research tool for determining magnetic properties of a variety of paramagnetic, ferromagnetic, antiferromagnetic, diamagnetic and ferrimagnetic materials<sup>150</sup>. VSM is based on Faraday's law which states that an electromagnetic force is generated in a coil when there is a change in flux linking the coil. VSM uses an induction technique to measure the magnetic moment ( $\mu$ ) of the sample. If any material is placed in a uniform magnetic field, the induced dipole moment in the sample is proportional to the product of the sample susceptibility and the applied magnetic field. If the sample is made to undergo sinusoidal motion, the resulting magnetic flux near the sample changes which induces an electrical signal in a set of suitably placed stationary coils. The signal generated is proportional to the moment, amplitude, and frequency of vibration<sup>151</sup>.

In the present work, the magnetic hysteresis measurements were carried out using a vibrating sample magnetometer (VSM) (Cryogenic Ltd., UK) at room temperature (300 K) over applied magnetic fields of +9 to -9 Tesla.

### **2.7. Inductively Coupled Plasma Mass Spectrometer (ICP-MS)**

ICP-MS is a widely accepted powerful technique for elemental analysis<sup>152</sup> and provides rapid, multi-element analysis with detection limits at ppb or below, for about 60 elements in solution with a dynamic range of  $10^4$  to  $10^8$ . A typical ICP-MS combines a high-temperature

---

inductively coupled plasma (ICP) source with a mass spectrometer. A block diagram of the same is shown in Figure 2.5. The liquid sample is introduced in ICP plasma in the form of an aerosol using a nebulizer. Once the sample aerosol is introduced in the ICP torch, it is completely desolvated and the elements in the aerosol are converted first into gaseous atoms and then ionized. The ions are then brought into the mass spectrometer via the interface

---

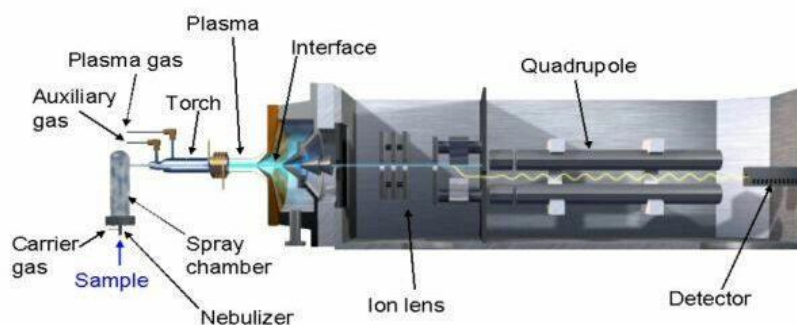


**Figure 2.5.** Schematic of an ICP-MS system

---

cones. The interface region in the ICP-MS transmit the ions from a region of atmospheric pressure (1- 2 torr) to a low-pressure region of the mass spectrometer ( $<1 \times 10^{-5}$  torr). This is done using two interface cones, the sampler, and the skimmer. In the mass spectrometer, ions are separated by their mass to charge ratio with the help of a quadrupole mass filter. The quadrupole mass filter is made up of four stainless steel rods which are mounted with stringent tolerances as shown in Figure 2.6. Opposing pairs of rods are connected to radio frequency (RF) power supply with a direct current (DC) offset. The voltage applied to one pair is opposite to the polarity of the other pair. These voltages are then rapidly switched along with an RF-field. The result is that at any instant of time only ions of a particular mass-to-charge ratio ( $m/e$ ) are allowed to pass through the rods to the detector. The detector used in ICP-MS is a channeltron detector. It is a continuous dynode based electron multiplier in which a high voltage is applied between the input and output ends of the detector. When an ion strikes the detector, secondary electrons are produced and accelerated which in turn strike the wall of the dynode, generating more electrons. At the output end, these electrons are

collected. Components such as the nebulizer, spray chamber, plasma torch, interface, and detector are common to any ICPMS system but can differ significantly in the design of the mass spectrometer.

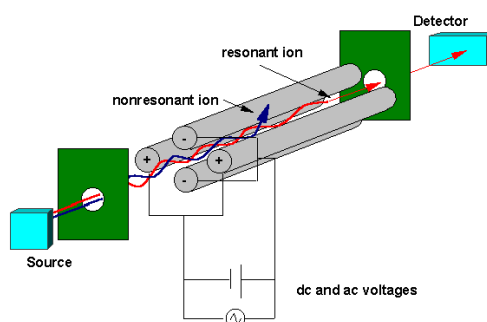


**Figure 2.6.** Diagram of quadrupole mass filter

In the present work, quadrupole based ICPMS instrument developed by TPD-BARC was used. Aqueous solutions were introduced into ICP at an uptake rate of 0.3mL/min by a concentric nebulizer and Peltier-cooled spray chamber. The nebulized sample was ionized in the high-temperature argon plasma, which was generated in a Fassel type quartz torch by coupling a Radio frequency power to argon gas using 2 ½ turn load coil and 1700 W at 27.12 MHz from an RF generator.

## 2.8. UV-Visible Absorption Spectroscopy

To understand the effect of light on materials, it is very important to know the detailed absorption characteristics of the systems under investigation. Different chemical species have different electronic energy levels and transition from ground to excited state results in absorption of solar radiation in different regions. UV-Vis absorption spectroscopy, being dependent on the electronic structure and the environment of the absorbing material allows the characterization of different materials and their environment. It relates the absorbance of a compound to the wavelength. An absorbance of a sample can be related to the concentration and thickness as per Lambert-Beer's law which states that the absorption of a material is

directly proportional to the concentration and thickness of the absorbing molecules and can be written as:

$$A = \log_{10} \frac{I_0}{I} = \epsilon Cl \quad (2.6)$$

Where A - Absorbance of the sample

$I_0$  - Intensity of the incident radiation,

$I$  - Intensity of the transmitted radiation,

$\epsilon$  = constant for each absorbing material and known as the molar extinction coefficient having unit " $\text{mol}^{-1} \text{dm}^3 \text{cm}^{-1}$ ",

$l$  = the path length of the absorbing solution in "cm"

$c$  = the concentration of the absorbing species in " $\text{mol dm}^{-3}$ "

The value of " $\log_{10} (I_0/I)$ " is known as absorbance of the solution, A (also referred as optical density) and can be read directly from the spectrum, often as 'absorbance units'. The Lambert-Beer law is true only for dilute solutions and if the concentration is higher, the sample needs to be diluted. It is interesting to observe from equation 2.6 that absorbance depends on both concentration and thickness while  $\epsilon$  is independent of both and give information about the quality of the material for light absorption. However,  $\epsilon$  is wavelength dependent property and is different at different wavelengths. Another useful parameter is  $\lambda_{max}$ , the wavelength at which maximum absorption occurs. This is an important parameter for QDs where  $\lambda_{max}$  relate to the size of QDs<sup>153</sup>. Also, the concentration can be determined by finding both absorbance<sup>154-157</sup> and  $\epsilon$  at  $\lambda_{max}$ . Therefore, by recoding the UV-vis spectra of QDs two most important information, size and concentration can be determined. The scan over the entire UV-Vis region gives rise to absorption spectra which forms the basis of this technique. Block diagram of a UV-Vis spectrophotometer is depicted in Figure 2.7. Two

different excitation sources were used to cover the entire wavelength range required. Deuterium lamp covers the ultraviolet range (190-420 nm), and tungsten filament (350-2500 nm) covers the visible range. A diffraction grating is used to separate each wavelength followed by a narrow slit. The slit ensures that the radiation is of a very narrow waveband. The light photons interact with the sample and depending upon the concentration and “ $\epsilon$ ” some amount of light will be absorbed while other will be transmitted. Also, a part of the light is passed through the reference cell containing only solvent to get the  $I_0$  value. These radiations are detected by a photodiode that converts photons into tiny electrical currents. Depending upon the number of photons reaching photodiode, the amount of current will be different. Spectrum is produced by comparing the currents generated by the sample and the reference beams.

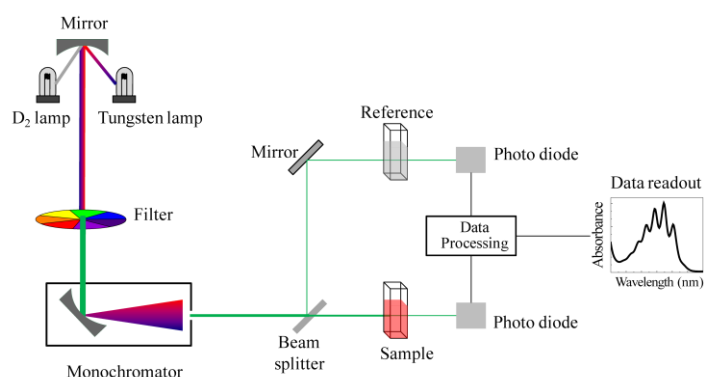


**Figure. 2.7.** Optical layout of double beam UV-Vis spectrophotometer.

In the present study, UV-Vis absorption spectra were collected using JASCO-640 model UV-visible spectrophotometer with a range of 200-900 nm and a resolution of 1 nm.

## 2.9. Photoluminescence (PL) Spectroscopy

Photoluminescence spectroscopy, commonly known as fluorescence spectroscopy is an extremely powerful technique to investigate various photochemical processes that occur in the excited state<sup>157, 158</sup>. The intensity of fluorescence emission and emission maximum give

useful information about the sample. Luminescence from a material arises from the excited state after the absorption of light photons in the ground state. In the excited state, molecules undergo a number of processes and finally returns to the ground electronic state either by emitting light photon or through non-radiative decay. Depending on these two, fluorescence properties of the materials are different. In luminescence measurement, samples are excited at a particular wavelength and emission is recorded. Emission spectra are a plot of emission intensity versus wavelength<sup>159-161</sup>. Apart from the PL, it is also possible to record the excitation spectra of the samples. Excitation spectra are the mirror image of the absorption spectra if the compound is fluorescence and is important to find the states responsible for emission. In excitation spectra, the emission wavelength is fixed and the excitation wavelength is varied.

Quantum yield<sup>157, 162</sup> (QY) is frequently used to characterize the property of any luminescent material. QY of fluorescence ( $\phi_{\text{fluorescence}}$ ) is defined as the ratio of the number of fluorescence photons emitted from the sample to the number of light quanta absorbed by the sample.  $\phi_{\text{fluorescence}}$  is expressed by the following equation.

$$\phi_{\text{Fluorescence}} = \frac{\text{Number of photons emitted}}{\text{Number of photons absorbed}}$$

Determination of the absolute number of photons absorbed and emitted by the sample is very difficult and sophisticated techniques such as intergraded sphere is required for its measurement. QY of an unknown sample is normally determined by a comparative method where the integrated emission intensity of the sample is compared with that of an optically matched (very close absorbance at the excitation wavelength) reference sample whose QY is already known. Thus, keeping the excitation wavelength same for both the sample and the reference, QY of the sample ( $\phi_{\text{sample}}$ ) can be expressed with respect to the QY of the reference ( $\phi_{\text{reference}}$ ) by using equation 2.7

$$\phi_s = \phi_r \frac{I_s OD_r n_s^2}{I_r OD_s n_r^2} \quad (2.7)$$

Where, “OD” is the optical density at the excitation wavelength, and “ $\eta$ ” is the refractive index of the solvent. The subscript “s” and “r” refer to the measured and reference sample, respectively. The equation becomes simplify when the experimental and the reference samples are taken in the same solvent

$$\phi_s = \phi_r \frac{I_s OD_r}{I_r OD_s} \quad (2.8)$$

To avoid the inner filter effect, the optical density of the measured and reference samples are kept below 0.1.

In the present work, PL and QY of QDs, CSQDs, and the dye molecules were measured using Hitachi model 4010 spectrofluorometer. The instrument employed a 75W high-pressure xenon lamp as the excitation source, different monochromators for excitation and emission wavelengths and photomultiplier tube (PMT) as the detector. The wavelength range covered in the present instrument is 250-1150 nm. The schematic of a typical steady-state spectrofluorimeter is shown in Figure 2.8.

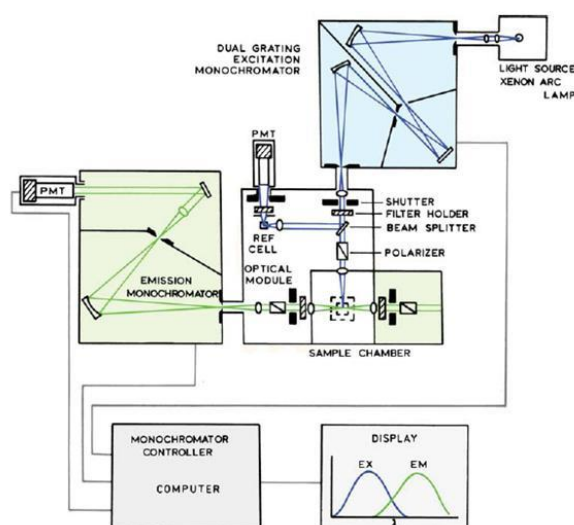


**Figure 2.8.** Block diagram of the Spectrofluorimeter

## 2.10. Fluorescence Lifetime Measurements

One of the major factors that decide the efficiency of any QDSC is the extraction of photo-generated charge carriers. Therefore, to enhance the solar cell efficiency it is very important to extract these charge carriers before their recombination. A number of processes occur when a molecule is excited from ground state to excited state. Time-resolved fluorescence measurements are an important tool to derive information on kinetics and dynamics of various photochemical processes involved in the deactivation of the excited molecules. Excitation of a sample with a very short pulse of light results in an initial population ( $n_0$ ) of molecules in the excited state. Since emission from the individual excited molecules is a random process, for a given time window following photo-excitation with an ultrashort light pulse each of the excited fluorophores should have the same probability to emit a fluorescence photon. This condition effectively results in the excited state population to decay following a first-order rate equation as<sup>157</sup>

$$\frac{dn(t)}{dt} = -(k_{nr} + k_r)n(t) \quad (2.9)$$

where  $n(t)$  is the number of excited molecules at time  $t$  following the very short pulse excitation of the sample,  $k_r$  is the radiative decay rate constant and  $k_{nr}$  is the nonradiative decay rate constant of the excited fluorophores. In an actual experiment, it is often difficult to know the exact number of the excited molecules present in the sample. However, knowing the fact that the fluorescence intensity is directly proportional to the number of excited molecules present in the solution, equation 2.9 can be expressed in terms of time-dependent intensity  $I(t)$  and the integration of the resulting equation gives us the expression for the fluorescence decay  $I(t)$  as

$$I(t) = I_0 \exp\left(-\frac{t}{\tau_f}\right) \quad (2.10)$$

where  $I_0$  is the intensity at time zero and  $\tau_f$  is the fluorescence lifetime of the sample.  $\tau_f$  is related to the radiative and nonradiative decay rate constants as

$$\tau_f = \frac{1}{k_{nr} + k_r} \quad (2.11)$$

If the width of the excitation pulse is unusually short ( $\delta$ -pulse) and the response time of the detection system is very fast compared to the fluorescence lifetime of the sample, the fluorescence lifetime can be obtained from the observed fluorescence decay by using the following two procedures. In the first method,  $\tau_f$  can be obtained simply by noting the time at which the fluorescence intensity decreases to  $1/e$  of its initial value. In the other method, the lifetime can be determined from the slope of the plot of  $\log I(t)$  versus  $t$ <sup>157</sup>. In cases where the fluorescence lifetime of the sample is quite short such that the excitation pulse width and/or the response time of the detection system distorts the observed decay, it is not possible to apply the above two simple analysis procedures to obtain the fluorescence lifetime of the sample. In such cases, the observed fluorescence decays are analyzed following a deconvolution procedure. This will be described in the later part of this section. Regarding the fluorescence decay, however, it is important to mention here that since the excited fluorophores emit randomly, different molecules spend the different length of times in the excited states. Thus, for an ensemble of excited molecules in the system, some may emit at very short times following the excitation but others may emit at times much longer than the measured fluorescence lifetime of the sample. It is thus evident that the estimated lifetime from the observed fluorescence decay is actually the statistical average of the times that the excited molecules spend in the excited state. Different techniques are available to determine the lifetime with each having its own limitations. In this section, a brief discussion about the fluorescence time-resolved techniques used in the present work is given.

### 2.10.1 Time-Correlated Single Photon Counting (TCSPC)

TCSPC is one of the sophisticated technique which provides the excited state lifetime of a fluorophores<sup>163, 164</sup> in the nanosecond to picosecond time scales. The principle of TCSPC measurement relies on the fact that the time-dependent probability distribution of single photon emission from an excited state molecule following its excitation is equivalent to the time-dependent changes in the fluorescence intensity of the sample following its  $\delta$ -pulse excitation. The schematic diagram of a typical TCSPC set up is shown in Figure 2.9. An excitation pulse from the pulsed excitation source is split into two parts, one part is used to

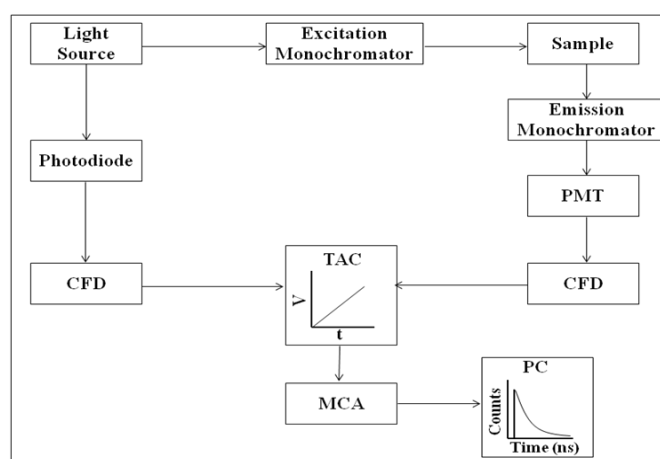


**Figure 2.9.** A layout of a TCSPC instrument.

excite the sample and the other part of the pulse is directed to a start PMT. The optical signal at the start PMT generates an electrical START pulse, which is routed through a constant fraction discriminator (CFD) to the START input of the time to amplitude converter (TAC) unit to initiate its charging operation. On receiving the start pulse, the TAC continues to undergo charging linearly with time. The part of the optical pulse, which excites the sample, effectively gives rise to the emission photons. These photons are then detected one by one by the stop PMT (at the right angle to the direction of excitation) to generate electrical STOP pulses for each of the individual photons received. The STOP pulses thus generated in the stop PMT routed through a CFD and serve as a STOP input of the same TAC unit. On

receiving the first STOP pulse, the TAC unit stops its charging operation and subsequently generates an electrical output pulse (TAC-output), having an amplitude proportional to the time difference ( $\Delta t$ ) between the START and the STOP pulses reaching the TAC unit. The TAC output pulse is then fed to the input of a Multichannel Analyzer (MCA) through an Analog-to-Digital Converter (ADC). The ADC generates a numerical value proportional to the height of the TAC output pulse and thus selects the corresponding memory address (channel) in the MCA, where a single count is added up. The above cycle (from the triggering of the pulsed excitation light source to the data storage in the MCA) is repeated for a large number of times and thus a histogram of counts is collected in the MCA channels. The distribution of the counts against the channel number in the MCA then represents the fluorescence decay curve of the sample. One of the main conditions of TCSPC is that the collection rate of the emission photons by the stop PMT is kept very low, only about 2% or less, compared to the repetition rate of the excitation pulses<sup>163-166</sup>. This experimental condition effectively means that following an excitation pulse, in no circumstances more than one emission photon can be detected by the stop PMT. Such a low count rate is essential to maintain the time-dependent probability distribution of the photon emission from a single excited molecule following its excitation process. Since the success rate in TCSPC is very low, it follows poisson distribution. From the measured fluorescence decay curves, the fluorescence lifetimes of the samples are estimated following a suitable analysis procedure<sup>163-166</sup>. The important components of the present TCSPC instrument are given below.

#### **2.10.1.1. Pulsed Excitation Source**

The different light emitting diodes (LED's) and diode lasers, having different emission wavelengths between 373 nm to 636 nm are used as the excitation sources. The repetition rate for excitation pulses is usually kept at 1 MHz.

### 2.10.1.2. Constant Fraction Discriminator (CFD)

In a typical TCSPC instrument, the signals from the two PMTs (START and STOP PMTs) are routed through two independent CFDs to achieve the following two goals: (1) To improve the signal to noise ratio (S/N) by discarding the signals below a threshold height such that the counts recorded by the instrument are genuinely due to the photons detected by the PMTs and not due to spurious electrical noises. (2) To provide the correct timing information for the START and STOP inputs to the TAC unit such that the timing jitter in the detection is minimized. As the simple leading edge discriminators are always associated with significant timing errors, the CFDs are recognized to be the best-suited discriminators for the TCSPC measurements to obtain accurate timing information for the START and STOP events.

### 2.10.1.3. Time to Amplitude Converter (TAC)

In the TCSPC instrument the time-correlation between the START and STOP event is carried out by using the TAC unit. TAC is the heart of any TCSPC instrument. On receiving the START pulse, a timing capacitor in the TAC start charging linearly with time from a constant current source. The capacitor continues to charge until it gets a STOP pulse. Once the charging process is stopped, the TAC unit generates an output pulse and the amplitude of this pulse is proportional to the charge accumulated on the TAC capacitor which in turn is a measure of the time difference ( $\Delta t$ ) between the arrivals of the START and STOP pulses to the TAC. Following a START pulse, if no STOP pulse is received (i.e. no emission photon detected) by the TAC within a predefined time period, called the "TAC range", the capacitor charging is automatically discontinued without recording the event and the TAC gets reset within a short time span. Start indicates the initiation of the charging process. Stop signal can arrive at the TAC unit at any time within the TAC range depending upon the lifetime of the

sample. A suitable TAC range is judiciously selected for a particular TCSPC measurement depending on the expected fluorescence lifetime of the sample.

#### **2.10.1.4. Multichannel Analyzer (MCA)**

MCA used in TCSPC instrument can be operated either in the pulse height analysis (PHA) mode (for measuring fluorescence decays) or in the multichannel scaling (MCS) mode (for measuring time-resolved emission spectra). The data stored in the MCA channels are transferred to a computer for further analysis and processing.

#### **2.10.1.5. Start and the Stop PMTs:**

In a typical TCSPC instrument, a nanosecond flash lamp with reasonably low repetition rate (~ 30 KHz) is normally used for sample excitation and the start and stop PMTs are used to get the respective signals for the TAC unit.

#### **2.10.1.6. Time Calibration of the MCA channels in a TCSPC Spectrometer**

Time calibration of MCA is done by using a number of accurately calibrated delay lines in the path of the STOP pulses. For this purpose, either the stop or the start signal is bifurcated into two parts, one is fed to the start input of the TAC and the other is routed through the precisely calibrated delay lines and then fed to the stop input of the TAC. For different known delays, the counts are thus collected at different channels of the MCA. The MCA data thus obtained are then transferred to a computer and the time calibration is calculated using a suitable analysis program.

#### **2.10.1.7. Analysis of the Fluorescence Decay Curves Measured in a TCSPC Instrument**

As the light pulses used for the sample excitation in a TCSPC spectrometer has a finite time width and the detection system has also a finite response time, the experimentally measured fluorescence decay curve,  $I(t)$ , is effectively a convolution of the true fluorescence

decay,  $G(t)$ , and the time profile of the excitation pulse,  $P(t)$ . Imagine the excitation pulse to be a combination of large number of  $\delta$ -pulses, it is possible to express the observed decay,  $I(t)$ , as the convolution integral of  $G(t)$  and  $P(t)$  as,

$$I(t) = \int_0^t P(t')G(t - t')dt' \quad (2.12)$$

Both  $I(t)$  and  $P(t)$  can be obtained experimentally. During analysis, a decay function  $G(t)$  is first assumed for the sample and this function is convoluted with the observed  $P(t)$  according to equation 2.12 to obtain a calculated curve  $Y(t)$ . This curve is then compared with the experimentally observed decay curve  $I(t)$ . The variables in the function  $G(t)$  is iteratively changed until a good comparison (best fit) between the  $Y(t)$  and  $I(t)$  is obtained. The function  $G(t)$  is usually assumed to be a sum of exponentials, such that,

$$G(t) = \sum_i B_i \exp - \frac{t}{\tau_i} \quad (2.13)$$

Where  $B_i$  is the pre-exponential factor for the  $i^{\text{th}}$  component and  $\tau_i$  is the corresponding fluorescence lifetime. The success of an analysis and accordingly the acceptance of a fit to the observed decay curve are determined from the judgment of the following statistical parameters.

### 2.10.1.7.1. Reduced Chi-square ( $\chi_r^2$ ) Values

The reduced chi-square ( $\chi_r^2$ ) values are defined as,

$$\chi_r^2 = \frac{\sum_i W_i \{Y(i) - I(i)\}^2}{(n - p)} \quad (2.14)$$

Where  $Y(i)$  is the count at the  $i^{\text{th}}$  channel of the calculated curve,  $I(i)$  is the count at  $i^{\text{th}}$  channel of the experimentally measured curve,  $W_i = 1/I(i)$ , is the weighting factor of the counts in the  $i^{\text{th}}$  channel,  $n$  is the number of channels used for the decay to be analysed and  $p$  is the number

of degrees of freedom in the decay function considered for the analysis (equals to the number of variables in the function  $G(t)$ ). For a good fit, the  $\chi^2$  value should be very close to unity. Normally a  $\chi^2$  value between 1.00 to 1.20 is considered to represent a good fit.

### 2.10.1.7.2. Distribution of Weighted Residuals:

To judge the success of an analysis of a TCSPC data set, the random distribution of the weighted residuals among the data channels is also considered to be an important criterion. The weighted residual for the  $i^{\text{th}}$  channel,  $r_i$ , is defined by equation 2.15.

$$r_i = \sqrt{W_i}\{Y(i) - I(i)\} \quad (2.15)$$

Where  $W_i$ ,  $Y(i)$  and  $I(i)$  are as defined earlier. For a good fit, the weighted residuals should be randomly distributed about the zero line for the whole range of the data channels used in the decay analysis.

In the present study, TCSPC spectrometer from Horiba Jobin Yvon IBH, UK (model Data Station Hub) was used to measure the fluorescence lifetimes of the samples. Different laser sources like 292 nm, 374nm, 406nm, 445nm and 636 nm were used to investigate the charge transfer dynamics. Emission polarizer was set at an angle of  $54.7^\circ$  (with respect to excitation polarization) known as the magic angle to avoid the effect of anisotropy coming from rotational motion of the species. TAC range can be varied from 50 ns to 200 $\mu$ s. Special Hamamatsu PMT, used in combination with a TBX4 module provided by IBH, UK is used with a Peltier cooling. The detector is having a spectral response from  $\sim$ 300 to 800 nm. Also, the measurements were carried out in reverse mode where START pulse is generated by the sample and STOP signal will be given by laser pulse. This was adopted especially for faster data collection and to avoid unnecessary charging of the TAC unit by the high repetition rate excitation pulses. It is important to add here that in the present IBH TCSPC instrument, PMT detector was replaced with an MCP-PMT and the instrument response function of the setup

was improved to ~100ps (FWHM) using diode lasers as the excitation sources and ~1.2 ns (FWHM) with the LED excitation sources. Time-resolved PL decay traces were fitted with non-linear least square analysis supported by instrument fitting program of IBH. All the decay traces are fitted using the software and by using the equation

$$I(t) = \sum_i^n \alpha_i \frac{e^{-t}}{\tau_i} \quad (2.16)$$

where  $I(t)$  is the total intensity remaining at time  $t$ .  $\alpha_i$  and  $\tau_i$  are the amplitude and decay time of  $i^{\text{th}}$  component respectively<sup>157</sup>.

### 2.10.2. Fluorescence Up-Conversion Measurements

TCSPC can provide a time-resolution of about a few tens of picoseconds. However, in certain cases, it is required to achieve a better resolution to understand much faster processes such as electron and hole cooling or charge carrier extraction. In this context femtosecond upconversion is one of the sophisticated techniques that provide a time resolution in sub 100 fs range<sup>167, 168</sup>. Block diagram of the femtosecond fluorescence up-conversion instrument is shown in Figure 2.10. A mode-locked Ti:sapphire oscillator (from CDP Inc. Russia) is optically pumped by a diode pumped solid state laser from Coherent (Verdi, 5W at 532 nm) to produce the ultrashort laser pulses at ~800 nm. The output laser beam from the Ti:sapphire oscillator is first passed through a BBO crystal to generate 2<sup>nd</sup> (around 400nm) or the 3<sup>rd</sup> harmonic (around 266 nm) of the laser light. The higher harmonic light thus produced is separated from the residual fundamental light of the Ti:sapphire laser by using a dichroic mirror and is used for the excitation of the samples. The intensity of the higher harmonic light is normally kept reasonably low to ensure that the fluorescence intensity remains linearly dependent on the excitation laser intensity. This is also required to minimize the photo-degradation of the samples during the measurements of the fluorescence decays. In the actual experimental arrangement, the sample solution is kept in a rotating quartz cell of 1 mm

thickness. The sample cell is rotated continuously during the measurement to prevent localized heating of the sample and to minimize its photo-decomposition. A cut-off filter is used immediately after the sample cell to prevent the residual excitation light and/or Raman light to reach the detection system. The transient fluorescence originating from the sample is then focused onto an up-conversion crystal (0.5 mm thick BBO crystal) using two elliptical mirrors. The residual fundamental beam used as the gate pulse is first directed to an optical

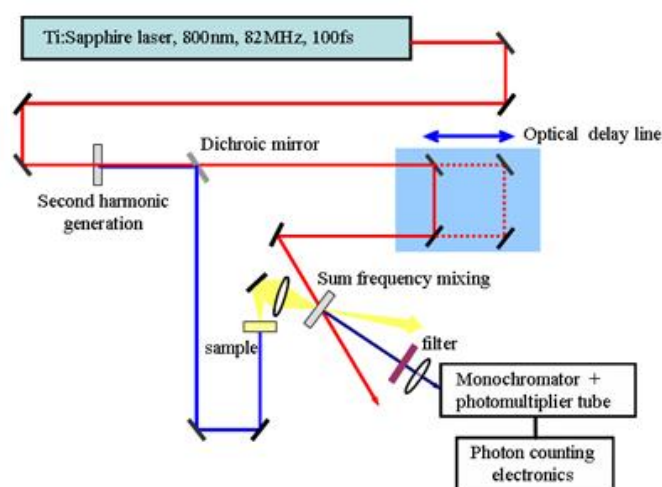


**Figure 2.10:** Layout of femtosecond fluorescence upconversion set up.

delay line and subsequently focused on the up-conversion crystal. A translational stage, driven by a stepper motor with a step size of  $0.1\mu\text{m}$ , is used to change the delay of the gate pulse. Each step of the translational stage changes the optical path length of the gate pulse by  $0.2\mu\text{m}$ , thus delaying the pulse by  $0.66\text{ fs}$  per step. The gate pulse is focused on the up-conversion crystal using a lens to mix with the fluorescence signal and thus to generate the sum-frequency or the up-converted signal. The upconverted light is focused onto a slit of a double monochromator after passing through a UV band pass filter (UG11) that eliminates the gate and the unused fluorescence light but transmits the up-converted light. This up-converted light is finally detected by using a photomultiplier tube connected to a photon counting system (CDP Inc. Russia). A variable wave plate (Berek Compensator) in the path

of the excitation beam is used to control the polarization direction of the excitation pulses relative to the horizontally polarized gate pulses. Fluorescence up-conversion measurements are normally carried out under magic angle condition to avoid the rotational depolarization effect of the probe molecules on the observed fluorescence decays. The fluorescence decay profiles measured for the samples at a given wavelength is a convolution of the sample response with that of the instrument response function (IRF). To extract the true sample response function or the actual fluorescence decay parameters of the sample, the measured fluorescence decay is to be de-convoluted with respect to IRF of the setup. IRF of the instrument can be obtained by mixing the residual excitation light that passes through the sample with the gate pulse in the up-conversion crystal and measuring the concerned sum-frequency light.

In the present thesis, femtosecond optical grating (FOG 100) set up from CDP, Russia was used to determine the hole transfer rate from QDs to catechol and thiol derivatives. The pulse duration of Ti:sapphire laser system is ~100 fs with a repetition rate of 82 MHz. The FWHM of the IRF for the present instrument is ~150 fs.

### **2.11. Femtosecond Transient Absorption (TA) Spectroscopy: Pump-Probe Technique**

As mentioned that both TCSPC and femtosecond fluorescence upconversion give information about excited state and radiative processes. To monitor both ground state and non-radiative processes, femtosecond transient absorption studies were carried out<sup>169, 170</sup>. In TA spectroscopy two pulses are used. One is a pump pulse which is of high intensity and used to excite the sample from ground state to excited state. The other is the probe pulse and is used to excite both ground state and excited state molecules at different time delay. The measured quantity in TA spectroscopy is the change in absorption at different time delay,  $\Delta A$  where  $\Delta A$  is defined as

$$\Delta A = -\log \left( \frac{(I_{\lambda}^{\text{probe}} / I_{\lambda}^{\text{ref}})_{\text{pump}}}{(I_{\lambda}^{\text{probe}} / I_{\lambda}^{\text{ref}})_{\text{No pump}}} \right) \quad (2.17)$$

Where,  $(I_{\lambda}^{\text{probe}} / I_{\lambda}^{\text{ref}})_{\text{pump}}$  is the ratio of the intensity of the transmitted probe pulse to reference pulse after pump excitation and  $(I_{\lambda}^{\text{probe}} / I_{\lambda}^{\text{ref}})_{\text{No pump}}$  is that of an unexcited sample. The intensity of reference signal is introduced in the expression of  $\Delta A$  for the correction of fluctuations within laser light. Data is recorded at different time delay ( $\Delta t$ ), at given wavelength of the probe beam ( $\lambda_i$ ) where,

$$\Delta t = \frac{2\Delta L}{c}$$

$L$  is the optical path length,  $c$  is the velocity of light.

$\Delta A$  gives information about both ground state and excited state properties of a material. The pump pulse excites the sample from the ground state to excited state as shown as process a in Figure 2.11. If the ground state absorption spectrum matches with the probe wavelength then the probe pulse also excites the molecules from the ground state to excited state as shown as process b in Figure 2.11. Because of pump pulse excitation, the number of

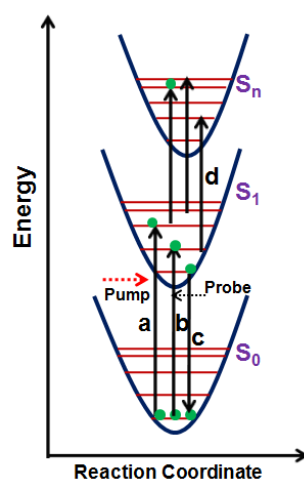


**Figure 2.11.** Scheme of the states involved in a pump-probe experiment (a) excitation of ground state molecules using the pump, (b) excitation of ground state molecules using the probe, (c) stimulated emission from excited state molecules, (d) excited state photoinduced absorption.

molecules available in the ground state for the probe is less as compared to without any pulse excitation, therefore, the term  $(I_{\lambda}^{\text{probe}}/I_{\lambda}^{\text{ref}})_{\text{pump}}$  will be more than  $(I_{\lambda}^{\text{probe}}/I_{\lambda}^{\text{ref}})_{\text{No pump}}$  and consequently  $\Delta A$  will be negative. This negative  $\Delta A$  is referred to as bleach. A similar bleach can also arise if the probe wavelength coincides with emission spectrum (thereby, termed as a stimulated emission) as shown as process c in Figure 2.11. In this condition also  $\Delta A$  will be negative. Excited state molecules can also absorb probe light if suitable states are available as shown as process d in Figure 2.11. In this condition  $(I_{\lambda}^{\text{probe}}/I_{\lambda}^{\text{ref}})_{\text{pump}} < (I_{\lambda}^{\text{probe}}/I_{\lambda}^{\text{ref}})_{\text{No pump}}$ , therefore,  $\Delta A$  will be positive. This positive  $\Delta A$  is referred to as excited state absorption (ESA). Depending on both ground state and excited state properties  $\Delta A$  value will change and information about both ground state and an excited state can be obtained. Since each process is characterized by a definite time constant, TA spectroscopy also gives information about the time constant of different processes in femtosecond time scale resolution by providing a delay between pump and probe pulse following pump pulse excitation.

Femtosecond transient absorption spectrometer consists of Ti-sapphire oscillator, a pulse stretcher, multipass amplifier, pulse compressor and finally pump-probe system. An optical layout of the system is shown in Figure 2.12. A brief description of each component is given below.

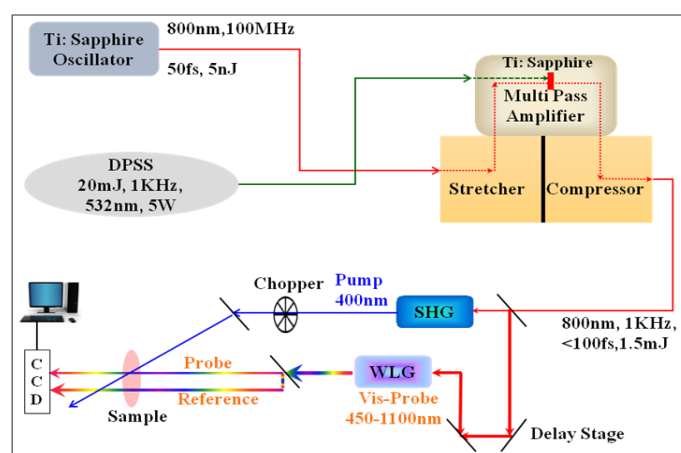


**Figure 2.12.** Schematic layout of femtosecond transient absorption spectrometer.

### 2.11.1. Ultrashort Pulse Generation: Ti-Sapphire Oscillator

In our pump-probe setup, ultrashort pulses are generated from Ti-sapphire oscillator which consists of sapphire ( $\text{Al}_2\text{O}_3$ ) crystal doped with titanium. Ti-Sapphire is a tunable laser where the transition occurs between different levels of  $\text{Ti}^{3+}$  and covers a broad region from 650-1050 nm<sup>168</sup>. As per Heisenberg uncertainty principle because of this broad range emission, ultrashort pulses (<50 fs) can be generated. Ti: Sapphire oscillator is pumped by a diode pump solid state (DPSS) laser (CW mode, 532 nm, 3.8 W). At the very high intensity of the pump laser, the nonlinear index of refraction of the gain medium changes and given as<sup>172</sup>

$$\eta(\nu) = \eta_0(\nu) + \eta_2(\nu)I \quad (2.18)$$

Where the  $\eta_0(\nu)$  is the refractive index in normal condition,  $\eta_2(\nu)$  is the non-linear component which is positive in case of Ti-Sapphire,  $I$  is the light intensity. Again, the refractive index is the function of distance ( $r$ ) as the laser cavity works in the  $\text{TEM}_{00}$  mode in which the intensity of the light beam follow Gaussian distribution [ $I(r) = \exp(-\rho r^2)$ ]<sup>172-174</sup>. Therefore, the refraction index is not homogeneously distributed in the medium and corresponds to a situation as by inserting an additional material in a shape of a Gaussian lens into an optical resonator. This is known as "Kerr effect" and the medium is known as "Kerr medium" (i.e. Ti-Sapphire)<sup>175</sup>. Due to stronger Kerr less focusing in Ti-Sapphire medium the higher intense modes is transmitted through the medium while the lower intense modes can't. During every round trip process, the lost-amplification is repeated. This power dependent loss makes the cavity unstable in CW mode and a slight disturbance of the laser cavity produce a laser pulse. This phenomenon is known as Kerr-lens mode-locking (KLM). This is also referred as "*self mode-locking*" as the Kerr-lens medium is the crystal itself<sup>176-178</sup>. Due to higher bandwidth of the gain medium (Ti-Sapphire, >350 nm) the passive mode locking (Kerr lens is passive object) can give pulse width as short as ~6fs. Since the refractive index

is a function of wavelength, therefore, longer wavelength components travel faster than shorter and it results in group velocity dispersion (GVD). Therefore, the pulse becomes broader. This can be compensated by introducing a chirped mirror or two prisms inside the laser cavity. In the present thesis the oscillator CDP from Avesta, Russia was used. Two prism and high reflector (HR, ~100% of reflection) mirror assembly (for negative GVD) generates ~50 fs pulse with 80-90 MHz pulse repetition rate and 4 nJ/pulse energy from Ti:Sapphire oscillator named as TISSA50 (Ti:Sapphire 50 fs). The optical layout of this oscillator is given in the Figure 2.13. The output from the oscillator is used as a seed pulse for amplification which is demonstrated in the next section.

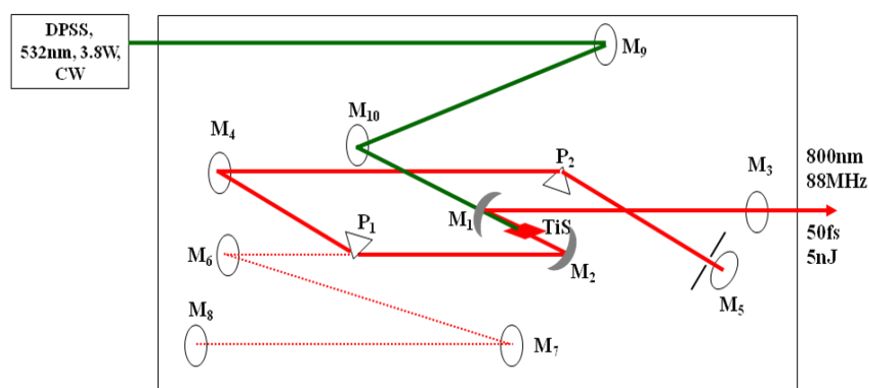


**Figure 2.13.** Optical scheme of TISSA 50 femtosecond Ti:Sapphire oscillator (CDP, Russia).

### 2.11.2. Chirped Pulse Amplification (CPA)

The seed pulse obtained from Ti:Sapphire oscillator has very low energy ~nJ/pulse which is insufficient to carry out a pump-probe measurement. Therefore, it is essential to increase the pulse energy<sup>181</sup>. This is done in three stages. In the first stage, a pulse stretcher is used which stretch the seed fs pulse to several ps. This is essential to avoid the chances of optics damage, as the seed pulse is of fs nature. During the pulse amplification, peak power increases several orders (~GW) which may lead to damage in optics. After stretching, the second step is pulse amplification. This is done by using Ti: Sapphire as an active medium. After amplification, the pulse energy increases ~mJ/pulse. The third step is to again compress

this pulse in fs domain and is done in a pulse compressor. This whole process is known as chirped pulse amplification (CPA)<sup>175, 182, 183</sup>. The output of CPA is fs pulses of mJ/pulse energy. The CPA consists of the following segments:

### 2.11.2.1. Pulse Stretcher:

Pulse stretcher works on the principle of group velocity dispersion (GVD). In a pulse stretcher, the incoming seed pulse can be stretched from <100 fs to few ps<sup>175, 183</sup>. The layout of a pulse stretcher is shown in Figure 2.14 which consists of a diffraction grating, a spherical and a plane mirror. A diffraction grating is placed between two mirrors in such a way that after double pass, the blue frequency has to travel more as compared to red component. As a result, the red component exits the stretcher first which stretches the pulse.

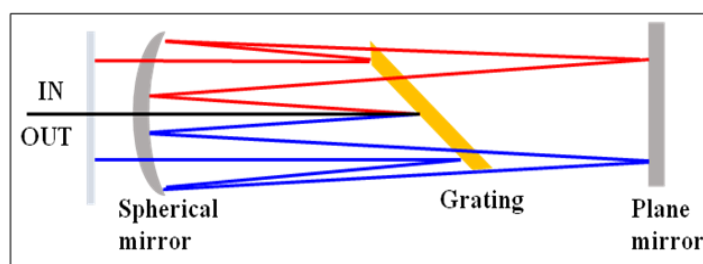


**Figure 2.14.** Illustration of the principle of femtosecond pulse stretcher.

In the MPA50 pulse stretcher (Figure 2.14) the input pulse is dispersed in the horizontal plane. The stretched pulse is directed back to the stretcher with help of vertical retroreflector, and four passes through the stretcher are achieved. Four-pass configuration is necessary to ensure that the stretched beam is spatially reconstructed. Femtosecond pulses with pulse duration ~100 fs are stretched to more than ten ps pulses before amplification. High reflective gold coated holographic grating gives stretcher efficiency higher than 50% for specific wavelength regimes.

### 2.11.2.2. Pulse Picker:

After stretching, the stretched seed pulse is passed through a pulse picker which is installed for one pulse selection from a train of stretched pulse. As a result, seed pulses are qualified for the amplification. The pulse picker utilizes well known electrooptical pockels effect. The pulse train having horizontal polarization goes through the pockels cell. Without applied voltage pulses do not change polarization and exit pulse picker with help of polarizers. When the half wave voltage is applied to the pockels cell, an input pulse changes its polarization from horizontal to vertical, goes through a polarizer and is used as a seed pulse for the amplifier. The applied voltage is synchronized with femtosecond pulse train and Nd:YAG pump pulses. Thus the seed pulses have a pulse repetition rate equal to that of Nd:YAG pump (i.e. 1KHz). Synchronization electronics is designed to trig high voltage applied to pockel cell and to synchronize this with pump pulse and femtosecond pulse train. To select one femtosecond pulse from the train of pulses and to amplify it at maximum pump efficiency is the reason for synchronization.

### 2.11.2.3. Confocal Multipass Ti:Sapphire Amplifier (MPA):

The confocal multipass amplifier has been designed for femtosecond pulse amplification in different media<sup>184</sup>. The 1 KHz stretched pulse is passed into an amplifier which consists of an optically active heavily doped Ti: Sapphire crystal. The gain medium is pumped with another DPSS laser (532 nm) having same repetition rate (1 KHz) and power ~20W. The schematic of the confocal multipass amplifier is shown in Figure 2.15. Ti:Sapphire crystal is placed confocally between two concave mirrors of different radii of curvature having central holes. Due to different focal lengths of the mirrors, the beam cross section is decreased after each pass and slowly it goes towards the centre of the mirror before extraction. To avoid the crystal damage threshold ( $10 \text{ J/cm}^2$ ) typically 8-10 passes is optimized and gain of the order of  $\sim 10^6$  was observed. In the present work, MPA-50 setup

form CDP, Russia was used in multipass amplification. A Q-switched second harmonic Nd:YAG laser (532nm, 1KHz, 5W, ~90s pulse duration) was used for pumping the Ti:Sapphire laser.

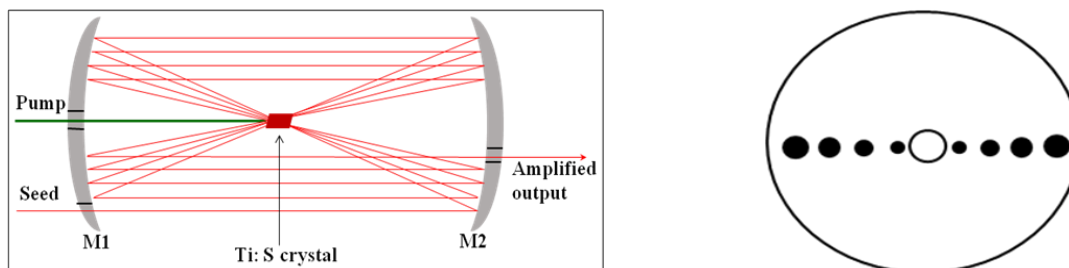


**Figure 2.15.** Optical schematic of two-mirror confocal multipass Ti:Sapphire amplifier. The radiation pattern on the confocal mirror has shown on the right side.

### 2.11.2.3. Pulse Compressor:

The principle of two grating pulse compressor is shown in Figure 2.16. In contrast to the pulse stretcher, red frequency component has to travel more as compared to the blue frequency components<sup>175, 183, 185</sup>. By varying distance between the gratings, the compression can compensate the stretching precisely to almost the same pulse duration as obtained from the seed laser pulse. In the present work, the stretched ps pulses are amplified by MPA50 multipass Ti:Sapphire amplifier and compress to pulses as short as 50-100 fs.

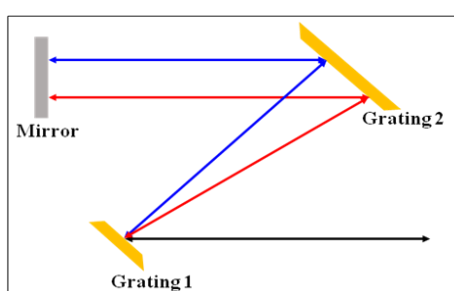


**Figure 2.16.** Illustration of the principle of two grating pulse compressor.

### 2.11.3. Second Harmonic Generation (SHG)

The output pulse after amplification has central wavelength of ~800 nm. In the present work, the samples were excited by 400 nm laser pulse. Therefore, to obtain the 400 nm laser

excitation source from the 800 nm fundamental output of the Ti:Sapphire,  $\beta$ -barium borate (BBO) crystal is used. BBO is used to generate a second harmonic generation (SHG)<sup>175, 183</sup>. The second harmonic generation in BBO crystal works on the principle of non-linear polarization of the crystal. The induced dielectric polarization of a material in presence of an electric field (E) is given by,

$$P = \epsilon_0 (\chi^{(1)}E + \chi^{(2)}E^2 + \chi^{(3)}E^3 + \dots) \quad (2.19)$$

$\chi^{(n)}$  is the susceptibility of  $n^{\text{th}}$  non-linearity. At very high pulse energy the second order susceptibility becomes significant which can be represented as,

$$P^{(2)} = \epsilon_0 \chi^{(2)}E^2 \quad (2.20)$$

E for an electromagnetic wave is given by,

$$E = E_0 \cos(\omega t - kr) \quad (2.21)$$

$$P^{(2)} = \epsilon_0 \chi^{(2)} \cos^2(\omega t - kr) = 1/2 \epsilon_0 \chi^{(2)} E_0^2 (1 + \cos 2(\omega t - kr)) \quad (2.22)$$

The second harmonic is generated only when the phases of two waves match i.e.  $k(\omega) = k(2\omega)$ . This condition is satisfied in a birefringent crystal (e.g. BBO where  $n_o(\omega) = n_e(2\omega)$ ). In the present setup, the amplified pulse (800 nm) is divided into two parts and one of the parts having 100mJ/pulse energy is passed through the BBO crystal to generate the excitation pump laser i.e. 400 nm while other 800 nm light is used to generate white light.

#### 2.11.4. White Light Generation (WLG)

To perform the pump-probe experiment, the probe pulse i.e. the white light continuums (WLC) are needed for detection of transient species. Third-order non-linear interaction of high energy pulse with matter can generate WLC. Self-phase modulation is the phenomenon responsible for WLG. A part of 800 nm amplified pulse with time duration <100 fs having

energy  $\sim 10 \mu\text{J}$  is used for WLG since the peak power is very high ( $\sim 0.1 \text{ GW}$ ). The intensity distribution of a Gaussian pulse is given by

$$I = I_0 \exp(-t^2/\tau^2) \quad (2.23)$$

An intense pulse of Gaussian profile changes the phase of the electric field of the light photon which introduces a frequency chirp and broadens the pulse. The time-dependent frequency chirp is related as,

$$\delta\omega = \delta\phi(t)/\delta t \quad (2.24)$$

For a positive non-linear refractive index leading edge of the pulse is downshifted in frequency. In the present experimental setup a small portion of the 800 nm pulse ( $\sim 2 \mu\text{J}$ ) is focused on a sapphire window of 1.5mm thickness for WLG, the bandwidth of which extends from 450-1100 nm.

### 2.11.5. Pump-probe Transient Absorption Spectrometer

After generation, the WLC, the probe (350-1000 nm) pulse is divided into two parts by a beam splitter. The pump pulse (400 nm) is overlapped on the one of the probe pulses on the sample. This probe is treated as a signal. Another probe beam which does not overlap with the pump pulse but passing through the sample is providing the reference signal. The experimental sample solutions are circulating to avoid the photo-bleaching. The pump pulse is passed through a polarizer having an angle of  $54.7^\circ$  to avoid the effect of anisotropy. A mechanical chopper operating at 500Hz is placed after the pump pulse but before the sample, which blocks every alternate pump pulses so that ratio of transmitted intensities of consecutive probe pulses corresponds to transient absorbance. In the present set up we use the Exipro transient absorption spectrometer where we use a retroreflector for delay stage and CCD (charge coupled device) to detect the signal. The excited state kinetics of the samples can be measured in 0.66fs-4 ns time resolution providing the time delay in the probe pulse

using retroreflector. Typical temporal resolution of this pump-probe set up is measured by bleach signal of meso-tetrakis-(4-sulphanatophenyl) porphyrin dianion (TPPS) at 710 nm ( $\lambda_{\text{pump}}$  400 nm, aqueous solution at pH 1) and found to be  $\sim 100\text{fs}$ . Finally, the data are analyzed with the help of Lab-view programme. A typical layout of pump-probe set up is shown in Figure 2.17.

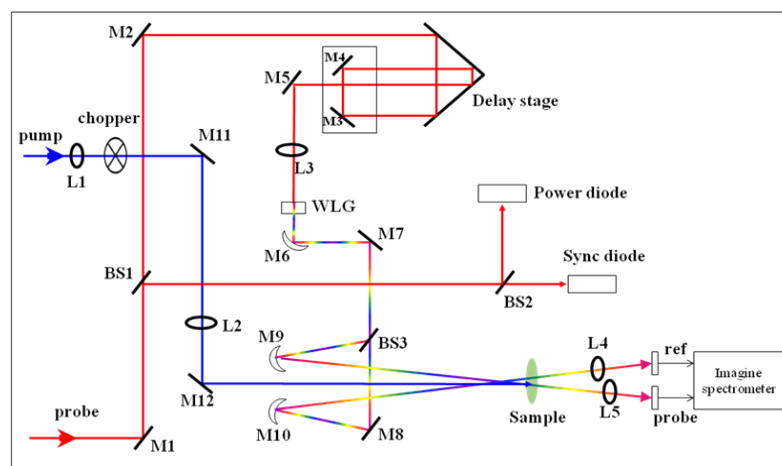
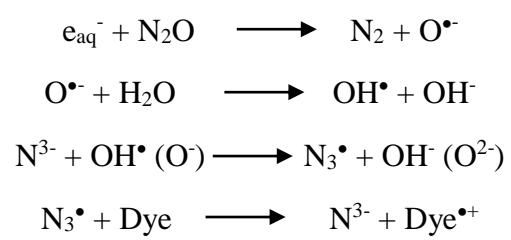


**Figure 2.17.** Optical layout of pump-probe set up.

## 2.12. Pulse Radiolysis

Pulse radiolysis technique is a complementary technique for detecting dye cation (formed after injecting electron to the semiconductor) in solution phase. Electron pulses of 50 ns duration from a 7 MeV linear accelerator were used for irradiation. The transients produced were detected by kinetic spectrophotometer using 450W pulsed xenon lamp along with monochromator, photomultiplier, and digital oscilloscope. A one-electron oxidation reaction is carried out in pulse radiolysis experiments of dye solution ( $10^{-4} \text{ mol dm}^{-3}$ ). Solution saturated with  $\text{N}_2\text{O}$  and  $\text{NaN}_3$  ( $5 \times 10^{-2} \text{ mol dm}^{-3}$ ) was added. The dyes were oxidized to the cation radical by reacting with azide ion in a one-electron oxidation reaction as given below:

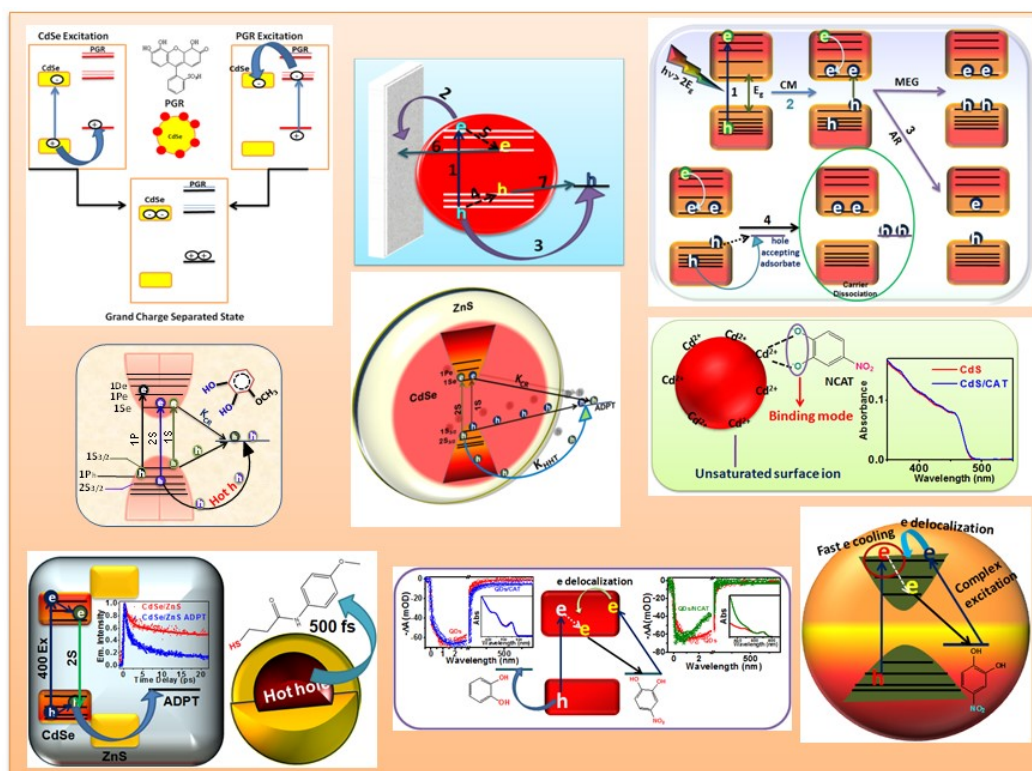






# CHAPTER-3

## Ultrafast Charge Carrier Dynamics in QDs/Molecular Adsorbate System: An Implication to High Efficiency Quantum Dot Solar Cell

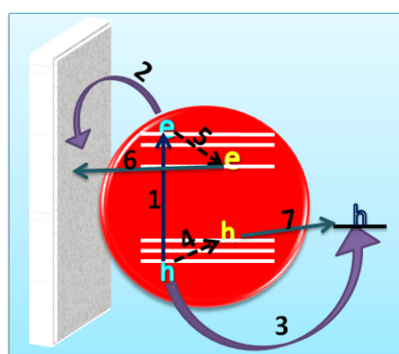


- *J. Phys. Chem. C*, 2014, 118 (30), 16358–16365
- *Chemistry–A European Journal*, 2015, 21 (11), 4405-4412.
- *Nanoscale*, 2016, 8 (4), 1823-1833.
- *Chemistry–A European Journal*, 2017, 23 (44), 10590-10596.
- *J. Phys. Chem. C (Feature Article)*, 2018, 122 (31), 17586-17600.



### 3.1. Introduction

Quantum dots (QDs) are known to be a good candidate for solar cell application due to their exciting properties such as band-gap tunability<sup>11, 121, 186-188</sup>, multiexciton generation (MEG)<sup>120, 189-192</sup>, larger extinction coefficient and longer exciton lifetime<sup>193</sup>. In QDs materials, absorption of high energy photon creates hot electrons and hot holes which quickly gets cooled down to the band edges with sequential emission of phonons (Scheme 3-1). On efficient extraction of these band-edge, charge carriers efficiency of QDSC can reach up to 31%<sup>13</sup>. However, if hot charge carriers can be extracted prior to cooling then efficiency can reach to as high as 66%<sup>14</sup> (Scheme 3-1). Till date the highest photoconversion efficiency of QDSC is reported to be 13.43%<sup>193</sup>, which is much lower than conventional DSSC<sup>195</sup>. This clearly shows that QDSC has a lot of potential to increase their efficiency and factors which leads to its lower efficiency needs to be understood clearly. One of the main processes which



**Scheme 3-1.** Basic processes involved in hot carrier quantum dot solar cell: 1) photo-excitation of QD, 2) hot electron transfer, 3) hot hole transfer, 4) hole cooling, 5) electron cooling, 6) thermalized electron transfer and 7) thermalized hole transfer.

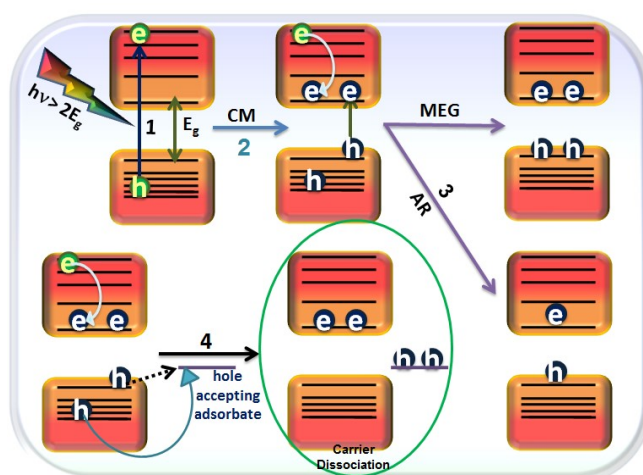
decide the efficiency of any QDSC is the extraction rate of photo-generated charge carriers from QDs (Scheme 3-1). It has been widely reported that electron transfer (ET) rate is much faster<sup>196, 197</sup>  $\sim 10^{10}$ - $10^{12}$   $S^{-1}$  and a number of reports are available on the same in different QDs/molecular adsorbate and QDs/semiconductor nanoparticle ( $TiO_2$ ,  $ZnO$  etc) systems<sup>198-</sup>  
<sup>210</sup>. However, not many reports are available on hole transfer (HT) dynamics

from photoexcited QDs to molecule. One of the main reasons is that holes are not characterized properly due to featureless weak absorption in near IR region and also nature of transition in transient absorption is not well understood<sup>121, 211, 212</sup>. Also the hole extraction rate is slow<sup>213, 214</sup>  $\sim 10^8$ - $10^9$  s<sup>-1</sup> and is one of the main reasons for low efficiency of QDSC as it increases the recombination probability between photo-generated electron and hole. Therefore, it is very important to extract hole at much faster rate. Also the size of the QDs is higher (more than 2-3 nm sometimes larger) as compared to dye molecule (size is less than 1 nm) as a result QDs loading on TiO<sub>2</sub> electrode is much less as compared to dye loading in DSSC. Due to lower loading, injected electrons in QDSC are in direct contact with the electrolyte which is undesirable and also a reason for lower efficiency of QDSC. The present chapter deals with the composite system of QDs with different molecular adsorbate where the main focus is to extract hole at a comparable rate as of electron so that a higher efficiency QDSC can be realized.

The first part of this chapter explains the concept of super sensitization in solar cell<sup>215-217</sup>. In super sensitization, QDs and molecular adsorbate can exchange charge carriers where molecular adsorbate in addition to photosensitizing the QDs material can also act as a hole transporting materials, where holes are generated out of photo-excitation of QDs. As a result grand charge separation can take place in the QDs-molecular composite material and can be used as a super sensitizer. Till now not many reports are available in literature on charge transfer (CT) dynamics of super-sensitizer materials in ultrafast time scale, except the work reported by Kamat and coworkers<sup>215</sup> in CdS QDs sensitized squaraine dye molecules. However, the dynamics of hole and electron transfer process in super-sensitizer (QDs-dye composite) are not reported precisely in literature. This was demonstrated in a coupled system of CdSe QDs and pyrogallol red (PGR). Redox energy level of CdSe QDs and PGR molecule suggest that CB of CdSe lies below LUMO level (both S2 and S1 states) of PGR

and HOMO level of PGR lies above the VB of CdSe QDs. In this situation, photo-excited hole in CdSe QDs can be captured by PGR molecules and photo-excited PGR can inject electron in the CB of CdSe QDs. Steady state and time-resolved emission measurements were carried out to confirm HT process in the above system. Femtosecond transient absorption spectroscopy has been employed to monitor the CT (both electron and hole) dynamics in CdSe/PGR composite system in ultrafast time scale and grand charge separation has been demonstrated.

As mentioned above that efficiency of QDSCs can reach to 66%<sup>14</sup> if hot charge carriers can be extracted prior to their cooling. Also, it is widely reported in the literature while exciting QDs materials with energy more than  $2E_g$  (band gap) (Scheme 3-2, Process 1) multi exciton generation (MEG) can be realized<sup>120</sup> (Scheme 3-2, Process 2). However, the main competing process with MEG is the Auger assisted charge recombination process (Scheme 3 2, Process 3) which leads to the non-radiative recombination of generated exciton. The

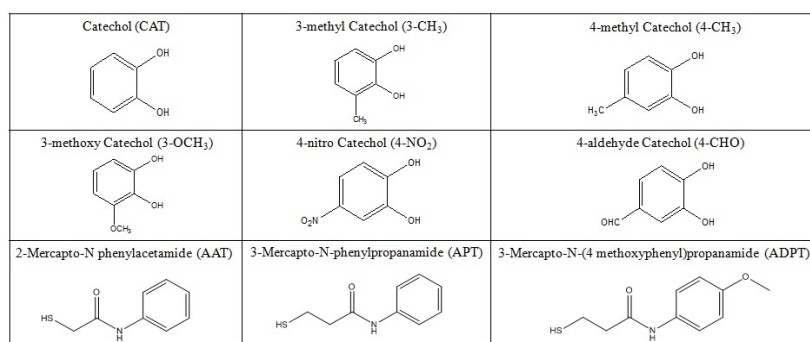


**Scheme 3-2.** Different processes involved after photo-excitation of QD materials with photon energy  $> 2E_g$ . **Process 1.** Generation of hot charge carriers, **Process 2.** Carrier multiplication (CM) followed by multiple exciton generation (MEG), **Process 3.** Non radiative auger recombination, **Process 4.** Charge carrier dissociation in presence of hole accepting adsorbate.

probability of auger recombination can be reduced if the coupling between electron and hole can be reduced. In addition to this, another process can be proposed by which the efficiency of QDSC can be increased where advantage of MEG and hot charge carrier extraction can be combined together as shown in Scheme 3-2. A suitable hole transporting molecule can be used which can extract hot hole at a faster rate before its relaxation to band edge level (Scheme 3-2, process 4). Due to this process, both electron – hole recombination probability and hence auger recombination can be reduced drastically which will eventually increase the carrier multiplication (CM) probability. Researchers have demonstrated the hot electron extraction<sup>197, 215-218</sup> from QDs materials using different adsorbates however, till date no report is available on hot hole extraction.

The second part of this chapter focus on this issue where hot hole extraction processes from QDs and core shell quantum dots (CSQDs) to catechols and newly synthesized thiols was monitored. Thiols and catechols are known to be good binder for QDs surface and many researchers have studied their interaction with different QDs<sup>222-224</sup>. However very few reports are available in literature which demonstrates charge carrier extraction from QDs to catechols and thiols in fast and ultrafast time scale. In the present thesis, CT dynamics of CdSe QDs with different catechol (Chart 3-1) and thiol derivatives (Chart 3-1) was investigated. Along with this, effect of electron withdrawing and electron donating groups on CT dynamics was also studied.

**Chart 3-1.** Structure of different catechol and thiol derivatives used in the study



As described above that it is very important to extract the charge carriers at a much faster rate before their recombination. For this, a number of composite systems of QDs have been explored with an aim to extract charge carriers at much faster rate and to get a higher efficient QDSC<sup>225-230</sup>. For this purpose, Sykora et al.<sup>231</sup> demonstrated hole transfer from photo-excited CdSe QDs to Ru-Polypyridine complexes in a time scale of  $\sim 5$  ps. Huang et al.<sup>208</sup> have demonstrated multiple exciton dissociation in CdSe QDs through electron transfer to adsorbed methylene blue with an average time scale of 2 ps. Jin et al.<sup>232</sup> have studied the charge separation in zinc porphyrin–QDs complexes where they have shown electron transfer from zinc porphyrin to QDs. In all the above stated reports different molecules were chosen that acts as either hole or electron transporting molecules for QDs with an aim to get better charge separation. Interestingly in some of the cases CT complex formation between QDs and molecular adsorbates was also observed<sup>233-236</sup>. Here the advantage is higher solar radiation absorption and faster charge carrier extraction can be coupled in a single system This was observed earlier in binary system of CdS QDs and dibromofluorescein (DBF)<sup>236</sup> where CdS QDs and DBF form a strong CT complex and on photo-excitation all the electrons are localized in QDs while hole are localized in DBF resulting in grand charge separation. Similar features were also observed by Dworak et al.<sup>235</sup> in a composite system of CdSe QDs and alizarin where they have observed a CT complex formation and electron transfer from alizarin excited state to QDs in a time scale of  $\sim 19$  ps. In both the above reports CT complex formation was observed from HOMO of the adsorbate to the conduction band (CB) of QDs resulting in solar radiation absorption in red region of solar spectrum. However, in any hybrid system the interface between inorganic semiconductor and the organic moiety is very important and controls various processes such as charge trapping, charge transfer and recombination pathways<sup>235, 237</sup>. Therefore, a detailed understanding about the interface and its effect on the above processes is important to understand the processes at fundamental level. In this context, Peterson et al.<sup>237</sup> have used CdS QDs and changed its surface

composition from Cd rich to Cd deficient by varying Cd:S ratio and monitored the effect of this change on charge transfer dynamics in CdS QDs sensitized methyl viologen (MV). They have observed that the interaction between CdS QDs and MV depends on the surface stoichiometry and found that interface play an important role in charge transfer processes. In above stated reports binding of ligands with metal ions at QDs surface and its effect on charge transfer dynamics has been demonstrated however nobody has discussed the complex formation at QDs/ligand interface and its effect on charge carrier relaxation and charge transfer dynamics within QDs/molecular adsorbates system.

In the third part of this chapter, effect of interface on charge carrier dynamics of CdX (X = S, Se, Te) QDs was studied. A composite system of CdX QDs with nitro catechol (NCAT) was chosen where both form a complex. Interestingly the complex formation was observed due to the interaction between surface Cd<sup>2+</sup> ions on QDs surface and NCAT. Steady state absorption, luminescence, time resolved luminescence and femtosecond transient absorption techniques were used to monitor different processes and effect of this complex on charge carrier dynamics of CdX/NCAT system.

### ***3.2. Experimental***

#### **3.2.1. Chemicals**

Cadmium oxide (CdO, 99.5%), Zinc acetate (ZnAc<sub>2</sub>, 99.9%), PGR, cadmium acetate dihydrate, selenium (Se, 99.99%), sulphur powder (S, 99.99%), tellurium powder (Te, 99.99%), oleic acid (90%), tri-octly phosphine (TOP, 90%), octadecene (ODE) (90%), catechol, 4-nitro catechol, 3- hydroxy nitro benzene and nitro benzene were purchased from Aldrich. All the chemicals used as received without further purification. AR grade chloroform and AR methanol were used for precipitation.

#### **3.2.2. Synthesis of CdX QDs**

Oleic acid capped CdX (X= S, Se and Te) QDs were synthesized by hot injection route with slight modification<sup>153</sup>. In brief stock cadmium oleate solution was prepared by heating 0.51 g cadmium oxide (4.0 mmol), 3.4ml oleic acid (10.6 mmol), and 11.6 ml octadecene at 180°C under the flow of Ar gas. Once the solution becomes clear the temperature was increased to 260-270 °C. A stock solution of X was prepared by mixing 1.1 ml of TOP (2.5mmol) with required amount of X (2 mmol) and 4.4 ml octadecene. This TOPX solution was quickly injected to the reaction mixture. Rapid color change indicates the formation of QDs. Optical absorption spectra was recorded at different time interval to monitor the growth of QDs. Once a desired size was obtained the temperature was decreased and the reaction mixture was allowed to cool. The solution was dissolved in chloroform and then re-precipitated with methanol for 3 times. Size of the QDs were determined using sizing curve<sup>150</sup>.

### 3.2.3. Synthesis of CdSe/ZnS Type-I CSQDs

For the preparation of CdSe/ZnS core-shell QD, previously prepared CdSe QDs was used as a core. For the preparation of ZnS shell, Zn-oleate was used as Zinc precursor and Sulphur powder as Sulphur precursor. Zn-oleate was prepared by taking 0.109g of Zn-acetate (0.5 mmol) and 0.425 ml oleic acid (1.3 mmol) in 1.5 ml octadecene. This mixture is refluxed at 180 °C into a three-neck round bottom flask in inert atmosphere. This Zn-oleate was added to a 5µmole CdSe QD solution. To prepare the stock sulphur solution, 0.16 g sulphur powder (2 mmol) was reacted with 1.1 ml TOP (2.5mmol) in 4.4 ml octadecene. TOPS was added drop wise to the solution of Zn-oleate in CdSe through a syringe at 180°C. Different amount of Zn and S precursor were added sequentially to get the desired monolayer thickness of ZnS over CdSe core. A colour change from yellow to red to dark red colour solution was obtained after addition of TOPS. The temperature was allowed to fall below 100 °C and the solution was dissolved in chloroform. The prepared CdSe/ZnS CSQDs was re-precipitated with methanol for 3 times.

### 3.3. Results & Discussions

#### 3.3.1. Ultrafast Hole/Electron Transfer Dynamics in CdSe QDs Sensitized by PGR: A Super-Sensitization System

Main aim of this investigation is to find the suitability of CdSe/PGR composite materials as a super-sensitizer. As a super-sensitizer it is expected that on photo-excitation of CdSe/PGR composite materials charge (electron/hole) separation will take place within the materials. To understand the CT behavior between PGR and CdSe QDs, it is very important to study steady state optical absorption and photoluminescence behavior of the composite system. Figure 3-1 shows the steady state absorption spectrum of CdSe QDs after adding different concentration of PGR. CdSe QDs used in the present studies has the exciton peak at 463 nm (Figure 3-1a). Optical absorption spectra of free PGR (Figure 3-1f) at highest

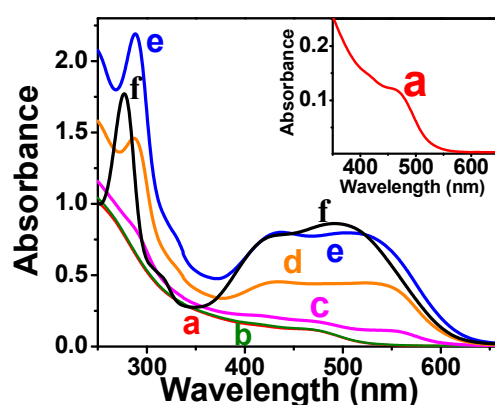


**Figure 3-1.** Optical absorption spectra of CdSe QDs (1  $\mu\text{M}$ ) with different concentration of PGR. PGR concentrations are (a) 0.0, (b) 1  $\mu\text{M}$ , (c) 10  $\mu\text{M}$ , (d) 50  $\mu\text{M}$ , (e) 100  $\mu\text{M}$ ; (f) 100  $\mu\text{M}$  PGR without CdSe QDs. **Inset:** Absorption spectra of pure CdSe QDs.

concentration (100  $\mu\text{M}$ ) was also recorded which clearly shows two absorption bands, one in UV region peaking at 278 nm and another broad absorption band with two humps in the visible region (400 – 650 nm). It is reported in the literature<sup>238</sup> that many triphenyl methane dyes have two absorption bands: one in the UV region is attributed to  $S_0 \rightarrow S_2$  transition and

another in the visible region which has been attributed to  $S_0 \rightarrow S_1$  transition. On addition of different concentration of PGR in CdSe QDs, it is clearly seen from Figure 3-1 that no CT interaction takes place between CdSe QDs and PGR molecule in the ground state. Steady state emission and excitation spectra of the composite were also recorded to monitor the CT behavior in the excited state and are shown in Figure 3-2. It is clearly seen that pure CdSe

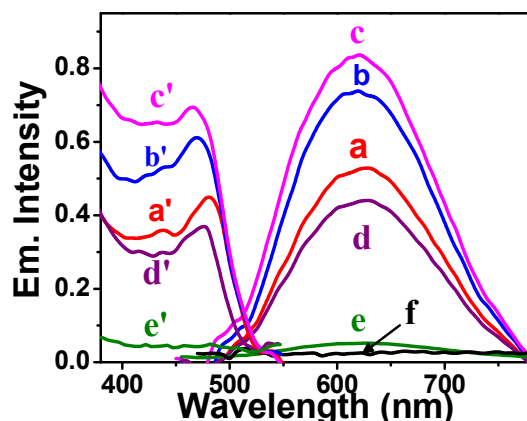
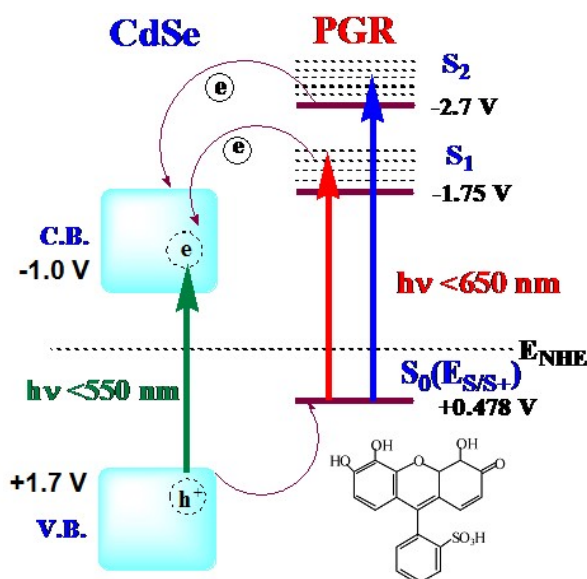


**Figure 3-2.** Emission (right side) and excitation (left side) spectra of CdSe QDs with different concentration of PGR. PGR concentrations are (a) 0.0, (b) 1  $\mu\text{M}$ , (c) 10  $\mu\text{M}$ , (d) 50  $\mu\text{M}$ , (e) 100  $\mu\text{M}$  and (f) emission spectra of pure PGR at 100  $\mu\text{M}$  concentrations. Both emission and excitation spectra of CdSe QDs are shown in the composite system after doing OD correction at exciting wavelength ( $\lambda_{\text{ex}} = 400\text{nm}$ ,  $\lambda_{\text{em}} = 620\text{nm}$ ,) for CdSe QDs absorption.

$$[\text{CdSe}] - 2\mu\text{M}.$$

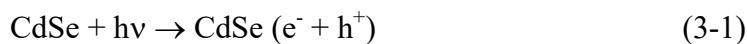
QDs emit in the wavelength region 500-800 nm region with a peak at 625 nm (Figure 3-2a) which can be attributed to emission due to surface state. Figure 3-2 a-e shows the emission spectrum of CdSe QDs in presence of various concentration of PGR after exciting the samples at 400 nm. The emission spectra are shown by incorporating OD (optical density) correction for CdSe QDs at exciting wavelength ( $\lambda_{\text{ex}} = 400\text{nm}$ ). Interestingly the emission intensity increases till the concentration of PGR is 10  $\mu\text{M}$  (Figure 3-2c). On further increment of PGR concentration the emission intensity of CdSe QDs gradually decreases and

completely quenched at 100  $\mu\text{M}$  of PGR concentration (Figure 3-2e). Excitation spectra of CdSe/PGR system (Figure 3-2, left side) also suggest that on PGR addition at low concentrations emissive state of CdSe QDs improve quite dramatically while at higher concentrations they are quenched. Figure 3-2f shows the emission spectrum of PGR at 100  $\mu\text{M}$  concentration in water after exciting at 400 nm light. No emission was observed from PGR molecule in water due to presence of pyrogallol moiety (three consecutive OH group) that form H-bond with water molecules and thus non-radiative transitions can take place very efficiently<sup>239</sup>. Scheme 3-3 suggests that on photo-excitation of CdSe QDs electron and holes are generated and in presence of PGR, HT process from CdSe QDs to PGR is thermodynamically favourable. Therefore, in presence of PGR it is expected that emission intensity of CdSe QDs will decrease due to HT process. However, an initial increment in emission intensity of CdSe QDs on addition of low concentration of PGR suggests surface



**Scheme 3-3.** Charge transfer processes in CdSe/PGR composite materials are depicted in the Scheme. Photoexcitation of CdSe QDs below 550 nm radiation generates electron ( $e^-$ ) and hole ( $h^+$ ) pairs where hole ( $h^+$ ) is captured by PGR molecule, on the other hand photoexcited PGR by below 650 nm radiation injects electron in the CB of CdSe. Molecular structure of PGR is shown in the scheme.

modification of CdSe QDs. Here the pyrogallol moiety of PGR might be having the affinity to bind with CdSe QDs and thus creating more emitting surface state defect. Earlier Baker and Kamat<sup>240</sup> reported increment of surface state emission in trioctylphosphineoxide/dodecylamine-capped CdSe QDs by addition of MPA as another modifier molecule. Also, ~10 nm blue shift in surface state emission and ~14 nm shift in excitation spectrum of CdSe QDs were observed on addition of 1-10  $\mu\text{M}$  of PGR. A similar hypsochromic shift was also observed by Hines and Kamat<sup>241</sup> in CdSe QDs passivated by  $\beta$ -alanine ( $\beta$ -Ala). According to them, excitonic wavefunction of QDs are influenced on binding of  $\beta$ -Ala to the QDs surface. On further increment of PGR concentration, HT channel from photoexcited CdSe QDs to PGR dominates, as a result decrement in CdSe QDs emission intensity was observed. Since the oxidation potential of PGR is 0.478 V vs NHE, it can effectively scavenge the photo-generated holes from the CdSe surface. Note that VB edge of CdSe QDs is expected to be around +1.7 V vs NHE. HT reaction can be expressed by the equations below:



Time resolved emission studies of CdSe QDs were performed after addition of different concentration of PGR to monitor the above processes and are shown in Figure 3-3. The emission decay trace of CdSe QDs at 625 nm can be fitted multi-exponentially with time constants  $\tau_1 = 0.73$  ns (38.4%),  $\tau_2 = 7.4$  ns (41%),  $\tau_3 = >30$  ns (20.6%) with  $\tau_{\text{avg}} = 6.8$  ns (where  $\tau_{\text{avg}} = (a_1\tau_1 + a_2\tau_2 + a_3\tau_3)/(a_1 + a_2 + a_3)$  where  $a_1$ ,  $a_2$  and  $a_3$  are the amplitudes of emission decay components corresponding to  $\tau_1$ ,  $\tau_2$  and  $\tau_3$  respectively). On addition of 50  $\mu\text{M}$  PGR, the emission decay is found to be much faster and can be fitted with time constants of  $\tau_1 = 0.2$  ns (63%),  $\tau_2 = 1.8$  ns (30%),  $\tau_3 >30$  ns (7%) with  $\tau_{\text{avg}} = 2.14$  ns. On further addition of PGR, emission decay becomes extremely fast with pulse-width limited decay ( $\tau_{\text{avg}} \sim 0.12$  ns). This

confirms HT process from QDs to PGR. However, with nanosecond time scale resolution it is difficult to determine the HT time correctly.

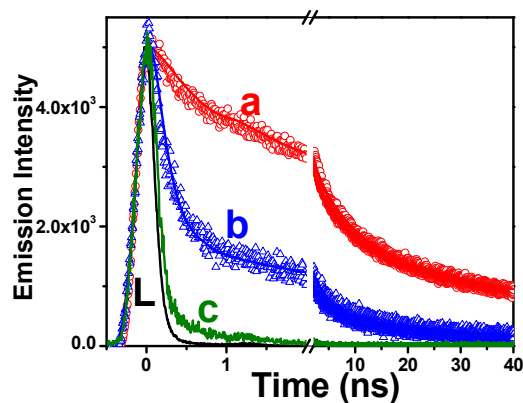


**Figure 3-3.** Time-resolved emission decay traces of CdSe QDs at 625 nm on addition of a) 0.0  $\mu\text{M}$ , b) 50  $\mu\text{M}$  and c) 100  $\mu\text{M}$  PGR molecules after exciting the QDs at 406 nm.

As described in Scheme 3-3 that at 400 nm both QDs and PGR will be excited. On photoexcitation of CdSe QDs, hole can be transferred to PGR. At the same time, photoexcited PGR can also inject electron into the CB of CdSe. Time resolved emission studies suggests only HT process from CdSe QDs to PGR and there also HT time was not determined correctly. Therefore, to determine HT time in early time scale and to monitor the ET dynamics in above-system, femtosecond transient absorption spectroscopic measurements have been carried out. Figure 3-4A shows the transient absorption spectra of photoexcited CdSe QDs in different time delay, which comprises a broad positive absorption band in 500-900 nm regions. The first exciton position for the CdSe (Figure 3-1a) appears at  $\sim 463$  nm however, in the transient spectrum we could show only from 490 nm due to low intensity of probe light below 490 nm in our experimental setup. The transient positive absorption beyond 500 nm region can be attributed to absorption of light by photo-generated charge carriers (both electrons and holes) in free or in trapped surface states. Figure 3-4B shows the transient absorption spectra of photoexcited PGR at different time delay, which comprises a negative absorption band in 500-600 nm regions and a broad positive absorption band in 620-900 nm

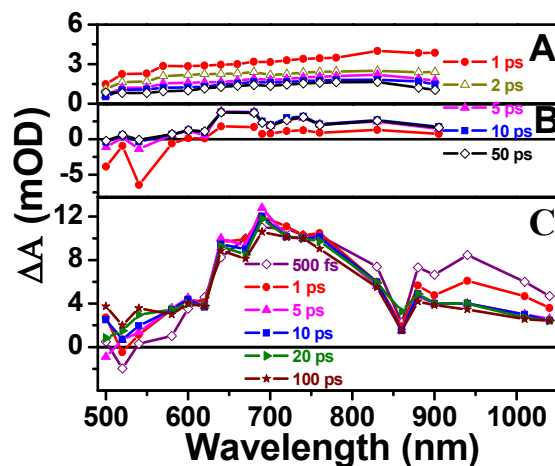


**Figure 3-4.** Transient absorption spectra of (A) CdSe (top panel), (B) PGR (middle panel) and (C) CdSe/PGR composite materials (bottom panel) in water at different time delay after excitation at 400 nm laser light.

regions. The negative absorption (bleach) appears due to photoexcitation of the ground state molecules, where the molecules have optical absorption in the same spectral region (Figure 3-1f). The transient absorption signal of PGR can be attributed to the excited singlet ( $S_1$ ) state absorption. Now to understand the CT dynamics in CdSe/PGR composite system, transient absorption spectra was recorded and is shown as Figure 3-4C. Transient absorption spectrum of CdSe/PGR comprises small bleach at 510 nm and two broad absorption bands at 600-850 nm and 850-1000 nm respectively. The broad spectral absorption in 850-1000 nm regions can be attributed to the electrons in the CB of CdSe QDs. As already reported that electrons in the CB of QDs materials can be detected by visible and near IR absorption band<sup>244, 245</sup>. The transient absorption peak at 600-800 nm can be attributed to PGR cation radical<sup>246</sup>. The band having maximum at 690 nm is assigned to PGR cation radical ( $\text{PGR}^{\cdot+}$ ). Assignment of this band has been made on the basis of the results obtained in pulse radiolysis experiments as shown as Figure 3-5, where  $\text{PGR}^{\cdot+}$  was generated selectively by the reaction of  $\text{N}_3^{\cdot-}$  Radical with PGR molecule in  $\text{N}_2\text{O}$  saturated aqueous solution. It was also reported earlier<sup>246</sup> that  $\text{PGR}^{\cdot+}$  cation radical has transient absorption band at 690 nm.

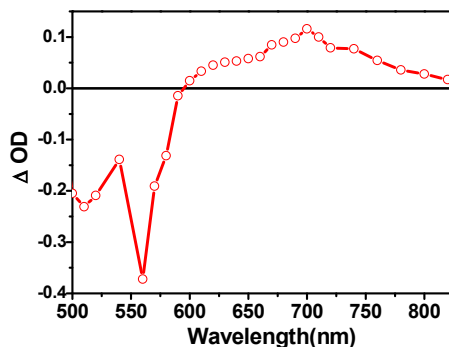


**Figure 3-5.** Transient absorption spectrum of the cation radical of PGR obtained from one-electron oxidation in pulse radiolysis.

Now to understand the CT dynamics in CdSe/PGR composite system kinetics decay traces at 690 nm and 900 nm were monitored and are shown in Figure 3-6C. To compare, kinetic decay traces of pure CdSe QDs and PGR were also monitored and are shown as Figure 3-6A and 3-6B respectively. The kinetic traces for CdSe QDs can be fitted at 690 nm with time constants  $\tau_1 = 0.5$  ps (33%),  $\tau_2 = 2.5$  ps (36%) and  $\tau_3 > 200$  ps (31%) (Figure 3-6a) and at 900 nm with time constants  $\tau_1 = 0.3$  ps (42%),  $\tau_2 = 2$  ps (44%) and  $\tau_3 > 200$  ps (14%) (Figure 3-6b). The shorter components at both the wavelengths can be attributed to trapping of charge carriers and the longer component ( $>200$  ps) can be attributed to recombination dynamics of photo excited carriers. On the other hand the kinetics for PGR at 690 nm can be fitted with 0.5 ps (60%) and 2.5 ps (40%) growth components and with decay of  $> 200$  ps (Figure 3-6c) and the kinetic trace at 900 nm can be fitted with 3.6 ps growth and  $> 200$  ps decay components (Figure 3-6d). The growth time constants 2-3 ps can be attributed to vibrational relaxation. The kinetic trace at 690 nm can be fitted with bi-exponential growth with time constants of 150 fs (85%) and 500 fs (15%) and eventually decays with time constants  $\tau_1 = 4$  ps (15%) and  $\tau_2 = >200$  ps (85%) (Figure 3-6e). However, the kinetic trace at 900 nm can be fitted with  $\sim 150$  fs growth time and multi-exponential decay with time constants of  $\tau_1 = 600$  fs (38%),  $\tau_2 = 2$  ps (26%),  $\tau_3 = >200$  ps (36%) (Figure 3-6f). It's very

interesting to see that growth and decay dynamics is completely different at 690 and 900 nm in CdSe/PGR composite system. This observation clearly suggests that generation of electron in the CB and formation of PGR cation radical might be taking place through more than one process. Scheme 3-3 shows the energy level diagram of CdSe/PGR composite. It is clearly

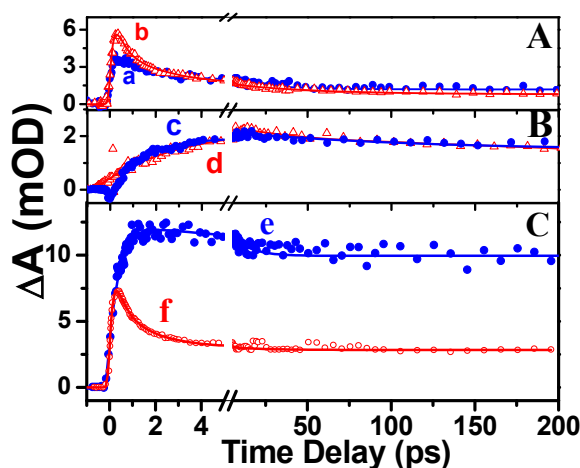


**Figure 3-6:** Kinetic decay traces at (A) (a) 690 nm and b) 900 nm for CdSe, at (B) (c) 690 nm and (d) 900 nm for PGR and at (C) (e) 690 nm and f) 900 nm for CdSe/PGR system in water after exciting the samples at 400 nm laser light.

seen that VB and CB of CdSe lies below HOMO and LUMO (both  $S_1$  and  $S_2$ ) level of PGR respectively. So on photo-excitation of CdSe QDs by radiation below 550 nm (Figure 3-1a) light electrons and holes are generated where holes can be transferred to PGR as it is thermodynamically viable. On the other hand photo-excitation of PGR molecule below 650 nm light (Figure 3-1f) can inject electron into the CB of CdSe QDs. As a result on photo-excitation of either PGR or CdSe QDs lead to charge separation in CdSe/PGR composite system, where in both cases electrons are localized in CdSe QDs and holes are localized in PGR with the formation of PGR cation radical. In femtosecond time resolved absorption studies we can clearly see the appearance of electron at 900 nm (near IR region) in  $\sim 150$  fs time scale, however PGR cation radical appears at 690 nm bi-exponentially with time constants of 150 fs (85%) and 500 fs (15%). Longer growth time (500 fs) of PGR cation

radical is attributed to HT time from CdSe QDs to PGR molecule and shorter growth time (150 fs) has been attributed to the electron injection from excited PGR to CdSe. Figure 3-1 suggests that in CdSe/PGR composite system both CdSe and PGR can absorb 400 nm laser light where ~75% light is absorbed by PGR and 25% light is absorbed by CdSe QDs. In the present studies major charge separation process in CdSe/PGR composite system take place by electron injection from photo-excited PGR to CdSe QDs which is clearly seen from the growth kinetics of PGR cation radical. Now it is very interesting to see that in addition to difference in growth dynamics of the transients at 690 nm and 900 nm, decay dynamics is also different. Decay kinetics at 690 nm can be fitted bi-exponentially with time constant of  $\tau_1 = 4$  ps (15%) and  $\tau_2 = >200$  ps (85%) and can be attributed to the recombination reaction between PGR cation radical and electron in CdSe QDs. The 900 nm transient which has been attributed to electron in CdSe QDs decays with time constants  $\tau_1 = 600$  fs (38%),  $\tau_2 = 2$  ps (26%) and  $\tau_3 = >200$  ps (36%). The faster components like 600 fs and 2 ps at 900 nm can be attributed to electron trapping dynamics in CdSe QDs. However, the long time component (>200 ps) can be attributed to recombination dynamics between PGR cation radical and electron in CdSe QDs. As already mentioned that CdSe QDs have defect states, so it is quite obvious once the electrons are excited from VB or injected into the CB, it will go for trapping process. It is interesting to see that early time dynamics in CdSe/PGR composite at 900 nm (Figure 3-6f) is quite similar to pure CdSe QDs (Figure 3-6b). However, in longer time scale it is clear that the kinetic trace for pure CdSe QDs decay much faster as compared to that of CdSe/PGR composite. The most interesting observation in the present investigation is the slow recombination dynamics between electron in CdSe QDs and PGR cation radical. Both grand charge separation and slow charge recombination in this system promotes its application in high efficiency QDSC.

### 3.3.2. Hot Hole Extraction in QDs/Catechol and QDs/Thiol composite System

#### 3.3.2.1. Hot hole extraction dynamics in CdSe QDs/Catechol composite system

To monitor interaction between CdSe QDs and catechols, steady state absorption studies have been carried out. Steady state absorption studies shows that the first excitonic absorption peak for CdSe QDs appeared at 590 nm corresponding to 1S ( $1S_{3/2}-1S_e$ ) transition (Figure 3-7A). The size of these QDs was determined to be 4.5 nm using sizing curve<sup>153</sup>. For this size of quantum dot the other two excitonic absorption peaks appeared at 530 and at 490

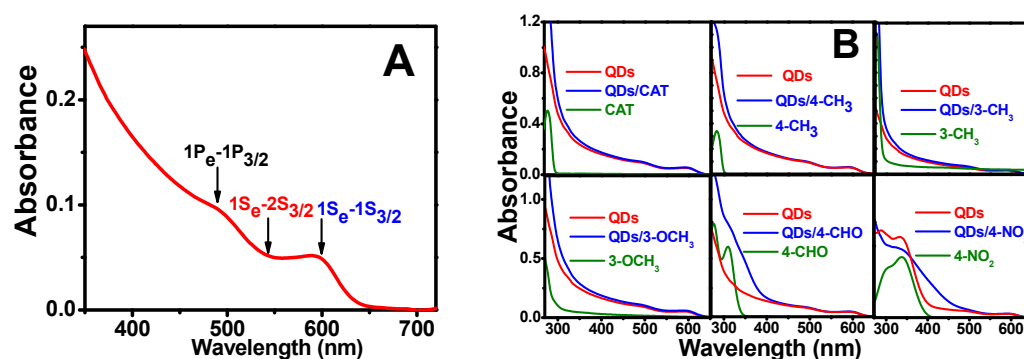


**Figure 3-7 (A).** Steady state absorption spectrum of CdSe QDs. **(B)** Steady state absorption spectrum of CdSe QDs with different catechol derivatives. QDs/Catechol concentration is 1:1000.

nm which corresponds to 2S ( $2S_{3/2}-1S_e$ ), and IP ( $1P_h-1P_e$ ) transitions respectively<sup>247</sup> (Figure 3-7A). To follow CT reaction in the excited state, ground state interaction between CdSe QDs and catechols was monitored using steady state absorption studies and is shown in Figure 3-7B. It is clearly seen that CAT, 3-CH<sub>3</sub>, 4-CH<sub>3</sub> and 3-OCH<sub>3</sub> do not form any CT complex with CdSe QDs (Figure 3-7B). However 4-NO<sub>2</sub> and 4-CHO form CT complex with CdSe QDs (Figure 3-7B).

To monitor CT interaction in the excited state, steady state emission spectroscopy of CdSe QDs has been carried out in absence and in presence of the catechols. Steady state emission spectrum of CdSe QDs shows sharp excitonic emission at 620 nm with quantum

yield of 16% and is shown in Figure 3-8A, curve a. On addition of catechol derivatives a complete quenching in CdSe QDs luminescence has been observed as shown in Figure 3-8A, curve b. This quenching in CdSe QDs luminescence could be either due to energy transfer or due to CT from photo-excited QDs to the catechols. Energy transfer in these systems is not possible because there is no overlap between QDs emission and catechols absorption as the all catechols absorb below 400 nm (Figure 3-7B). So the only viable process might be due to CT from photo-excited CdSe QDs to the catechols. To determine whether the quenching occurs due to ET or HT, redox level of catechols in chloroform were determined using CV by taking ferrocene as standard. CV curve of CAT is shown in Figure 3-8B. Redox levels of different catechols with respect to NHE are given in Table 3-1. VB ( $1S_h$ ) level of CdSe QDs reported to be 1.63 V<sup>196</sup>, while CB ( $1S_e$ ) is determined to be -0.47 V after adding band gap energy with VB energy ( $E_{BG} = 2.1$  eV). The above experimental results and literature value clearly suggest that both HOMO and LUMO levels of the catechols lie above the VB level and CB level of CdSe QDs. So, the luminescence quenching of CdSe QDs in presence of catechols can be attributed to HT from photo-excited CdSe QDs to the catechols as the process is thermodynamically viable. In the present investigation HT reaction can be expressed by the equations below:

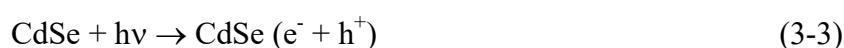


**Table 3-1:** Redox levels of different catechol derivatives with respect to NHE. Values are corrected by taking ferrocene as an internal standard.

	$E_{ox}/\text{NHE}$
3-OCH <sub>3</sub>	0.9
Cat	0.98
4-CH <sub>3</sub>	1.082
3-CH <sub>3</sub>	1.087
4-CHO	1.23
4-NO <sub>2</sub>	1.27

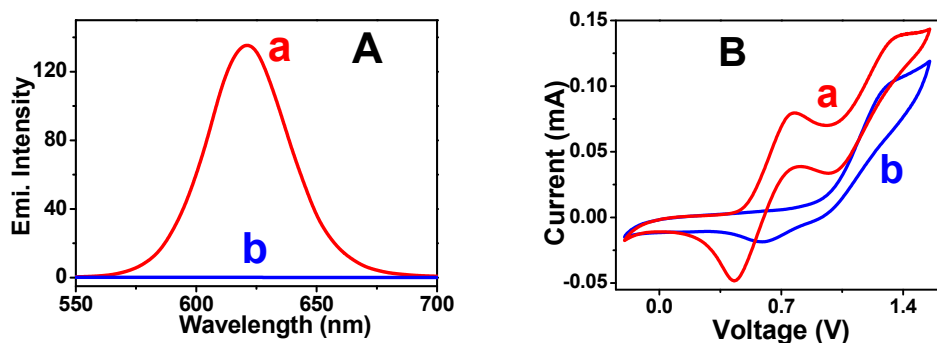


**Figure 3-8 (A)** Steady state emission spectrum of CdSe QDs in absence (a) and in presence of CAT (b), QDs/CAT concentration is 1:1000. **(B)** CV curve of CAT (a) with ferrocene and (b) without ferrocene in chloroform.

To understand the effect of molecular structure on HT reaction, concentration dependent emission studies have been carried out for CdSe QDs in presence of different catechols derivatives. Figure 3-9A shows change in quantum yield of CdSe QDs in presence of different catechols derivatives at different concentration of catechol. It is seen from Figure 3-9A that at 1:1 concentration ratio of catechols vs CdSe QDs decrement in emission QY found to be low and is very close to 16% for all the catechols derivatives. However with increasing catechols concentration emission QY gradually decreases and completely quenches at catechol to QDs concentration ratio of 1000:1. It is interesting to see that decrement of CdSe QY is different for different catechol derivatives at same catechol to QDs ratio. However the quenching efficiency is much higher for 4-NO<sub>2</sub> and 4-CHO as compared to other catechols derivatives. In order to find whether higher luminescence quenching is due to higher adsorption of 4-NO<sub>2</sub> and 4-CHO on CdSe QDs or due to their higher HT rate, time resolved emission studies have been carried out in nanosecond time resolution by exciting the samples at 406 nm laser light and monitoring the emission at 620 nm (Figure 3-9B). Interestingly in time resolved studies at lower concentration ratio of catechols and CdSe QDs (10:1), different emission quenching rate is observed in different catechols derivatives. This observation

clearly suggests that HT rate is different in different composite systems and is maximum in case of CdSe/3-OCH<sub>3</sub> system. It also suggests that although 4-NO<sub>2</sub> and 4-CHO derivatives of catechol form CT complex with CdSe QDs (Figure 3-7B) still HT rate is higher in CdSe/3-OCH<sub>3</sub> system. This might be due to either higher free energy (-ΔG) for HT reaction or higher electron donating ability of 3-OCH<sub>3</sub> which facilitates HT reaction. We have also carried out luminescence quenching studies at higher catechol concentration (~1000:1) and shown in Figure 3-9B, inset. It has been observed that HT process in all the QDs/ catechols composite systems are too fast to monitor with nano-second time resolution.

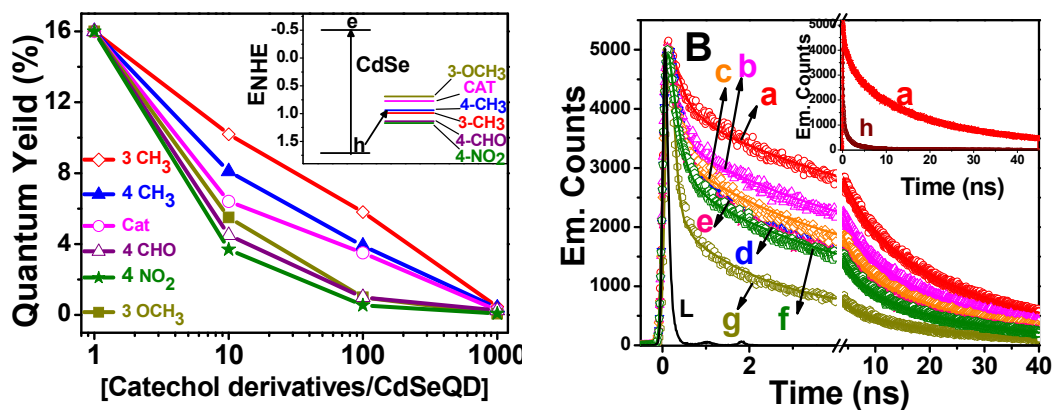


**Figure 3-9 (A)** Change in quantum yield of CdSe QDs in presence of different catechols derivatives at different concentration of catechols. **Inset:** Energy levels of VB and CB of CdSe QD and HOMO levels of different catechol derivatives. **(B)** Time resolved emission studies of CdSe QDs with different catechol derivatives (a) CdSe (b) CdSe/4-CH<sub>3</sub> (c) CdSe/3-CH<sub>3</sub> (d) CdSe/Cat (e) CdSe/4-CHO (f) CdSe/4-NO<sub>2</sub> (g) CdSe /3-OCH<sub>3</sub> ( $C_{\text{CdSe}}=0.16 \mu\text{M}$ ,  $C_{\text{Catechols}}=1.6 \mu\text{M}$ ). **Inset** (a) CdSe (h) CdSe/3-OCH<sub>3</sub> ( $C_{\text{CdSe}}=0.16 \mu\text{M}$ ,  $C_{\text{Catechols}}=0.16 \text{mM}$ ).

As mentioned above that HT process is too fast to monitor with nano-second time scale resolution. To determine HT rate correctly and to see the effect of molecular structure on HT rate, fluorescence upconversion studies have been carried out by exciting the CdSe QDs at 400 nm and monitoring its luminescence at 620 nm in absence and presence of catechols

derivatives and shown in Figure 3-10. In all QDs/catechols composite system catechols: QDs ratio was kept ~1000:1 where no luminescence was observed from the composite systems. It is clearly seen that in presence of catechols the emission kinetics decays much faster as compared to pure CdSe QDs. Decay trace of pure QDs can be fitted multi-exponentially with different time constants and shown in Table 3-2. It is evident from Table 3-2 that the average lifetimes of CdSe/catechol composite systems are 20-50 times shorter as compared to that of CdSe QDs which confirms HT process in the composite materials as suggested in equation 3-5. HT rate constants in different composite systems can be determined through the following expression:

$$k_{HT} = 1/\tau_{CdSe/Catechols} - 1/\tau_{CdSe} \quad (3-5)$$

Using the average lifetime values of CdSe QDs and CdSe/catechol composites the HT rate constants have been determined and shown in Table 3-2. It is interesting to see that HT rate is different for different catechols derivatives depending on their redox energy level. Here the free energy of HT reaction is directly proportional to the redox energy level of VB of CdSe QDs and ground state potentials of catechol derivatives. In the present situation free energy of charge separation can be determined as

$$\Delta G_{HT}^{\circ} = E_{VB}^{CdSe} - E_{Cat/Cat+} - e^2/\epsilon r_{DA} \quad (3-6)$$

Where  $E_{VB}^{CdSe}$  is the VB energy level of CdSe QDs,  $E_{Cat/Cat+}$  is the oxidation potential of catechols, and  $e^2/\epsilon r_{DA}$  is the stabilization energy of the product ion pair state in chloroform (where  $e$  is the charge of an electron,  $\epsilon$  is the dielectric constant of the solvent, and  $r_{DA}$  is the distance between donor-acceptor pair). Since  $e^2/\epsilon r_{DA}$  value will be approximately same for all the composite systems of CdSe with catechol derivatives we can write equation 3-6 as

$$\Delta G_{HT}^{\circ} \propto E_{VB}^{CdSe} - E_{Cat/Cat+} = \Delta G_{HT}^{\dagger} \quad (3-7)$$

Using equation 3-7,  $\Delta G_{HT}^\ddagger$  for all the QDs/catechol pairs was calculated and shown in Table 3-2. One of the main aim of present investigation is to monitor systematic charge separation reaction in CdSe QDs/catechol derivatives with changing molecular structure of the adsorbate. Earlier Kathryn et al.<sup>248</sup> reviewed charge separation (both electron and hole transfer) reaction for different QDs and acceptor systems, where it has been observed CT rate increases with free energy for charge separation reaction. Frederick et al.<sup>222</sup> have

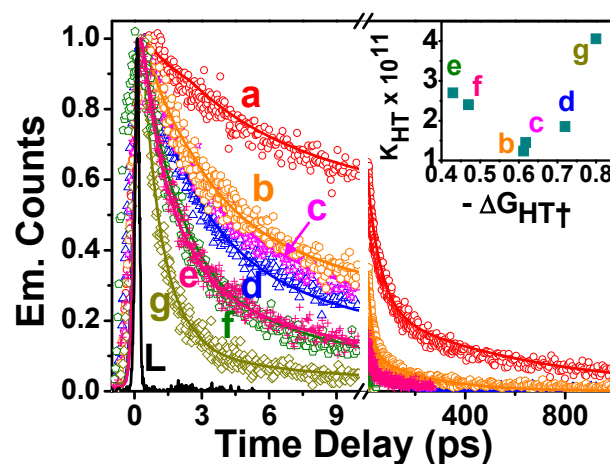


**Figure 3-10:** Fluorescence upconversion decay traces of CdSe QDs ( $\lambda_{ex}$  - 400 nm and  $\lambda_{em}$  - 620 nm) with and without catechol derivatives. (a) pure QDs (b) CdSe/3-CH<sub>3</sub> (c) CdSe/4-CH<sub>3</sub> (d) CdSe/Cat (e) CdSe/4-CHO (f) CdSe/4-NO<sub>2</sub> (g) CdSe/3-OCH<sub>3</sub>. **Inset:** Plot of change of HT rate with Gibbs free energy of CT reaction.

**Table 3-2:** Parameters for multi-exponential fit of emission decay traces for CdSe QDs in absence and in presence of different catechol derivatives.  $\lambda_{em}$  = 620 nm,  $\lambda_{ex}$  = 400 nm.

System	$\tau_1$ (ps)	$\tau_2$ (ps)	$\tau_3$ (ps)	$\tau_{avg}$ (ps)	$-\Delta G_{HT}^\ddagger$	$k_{HT} \times 10^{11}$
CdSe	4.7 (39%)	55 (40%)	>500 (21%)	110		
CdSe/Cat	1.5 (36%)	7.42 (63%)	>50 (1%)	5.5	0.72	1.85
CdSe/4-NO <sub>2</sub>	1.42 (63%)	8.8 (36%)	>50 (1%)	3.7	0.43	2.7
CdSe/3-CH <sub>3</sub>	2.4 (58%)	18 (41%)	>50 (1%)	8.15	0.61	1.23
CdSe/4-CH <sub>3</sub>	1.8 (46%)	10.5 (53%)	>50 (1%)	6.9	0.62	1.45
CdSe/3-OCH <sub>3</sub>	0.8 (89%)	12.8 (10%)	>50 (1%)	2.5	0.80	4.0
CdSe/4-CHO	1.16 (68%)	9.25 (31%)	>50 (1%)	4.16	0.47	2.4

demonstrated control of hole delocalization in a series of para substituted phenyldithiocarbamate (PTC) sensitized CdSe QDs. However in the above reports systematic studies of HT dynamics with changing molecular structure and rate of HT was never discussed. In the present work, both HT time and free energy of charge separation reaction was determined and tried to correlate with Marcus electron transfer theory. It is clear from Table 3-2 and Figure 3-10 inset that HT rate increases with free energy of HT reaction except for 4-CHO and 4-NO<sub>2</sub>. It is interesting to see that HT rate for 4-CHO and 4-NO<sub>2</sub> is higher as compared to other catechols (except 3-OCH<sub>3</sub>) where free energy of HT reaction is lower for both the systems as compared to other QD/catechol derivatives (Table 3-2). In steady state absorption studies it was observed that both 4-CHO and 4-NO<sub>2</sub> form CT complex (Figure 3-7B) which suggest that the coupling matrix for CT reaction will be higher for both the systems as compared to other composites. As a result, higher HT rate for both 4-CHO and 4-NO<sub>2</sub> sensitized CdSe QDs systems was observed. However the most remarkable observation is that the HT rate is much higher in case of CdSe/3-OCH<sub>3</sub> system as compared to other composite systems. Due to strong electron donating property of 3 methoxy group in 3-OCH<sub>3</sub> hole capturing ability increases, as a result, faster HT reaction was observed as compared to other systems.

In view of the fact that thermalized HT rate is very fast in catechol derivatives, possibility to extract hot hole from upper excitonic state ( $2S_{3/2}$ ) of CdSe QDs was explored. To investigate hot hole extraction process it was important to monitor hot exciton luminescence from the QDs materials. Luminescence from hot excitonic state is not widely reported due to ultrafast excitonic decay and low QY<sup>249</sup>. However Cho et al.<sup>250</sup> and Mondal et al.<sup>251</sup> have reported hot luminescence from QDs materials. Although, in our present work no emission band from hot states was observed still the emission at 560 nm was recorded which is expected to be emissive wavelength due to 2S excitonic state of CdSe QDs and are shown

in Figure 3-11A. It is clear from Figure 3-11A that emission decay trace of CdSe QDs in absence or in presence of different catechol derivatives is almost similar except for 3-OCH<sub>3</sub>. A separate emission decay trace of CdSe QDs and CdSe/3-OCH<sub>3</sub> derivative was also plotted and shown in Figure 3-11B. Faster decay trace at 2S excitonic position in presence of 3-OCH<sub>3</sub> clearly suggests that 3-OCH<sub>3</sub> can be used to extract hot hole from photo-excited CdSe QDs. Emission decay trace of CdSe QDs can be fitted multi-exponentially however major component can be fitted with 400 fs (60%) time constant, Table 3-3. This faster time constant of 400 fs can be attributed to radiative or non-radiative recombination time between hole in 2S<sub>3/2</sub> state and electron in 1S<sub>e</sub>, or may be non radiative relaxation of hole from 2S<sub>3/2</sub> to 1P<sub>h</sub> or 1S<sub>3/2</sub> state (Figure 3-11 and Scheme 3-4). Now it is interesting to see that emission decay trace for 2S exciton in presence of 3-OCH<sub>3</sub> (Figure 3-11B) decay much faster as compared to pure CdSe QDs (Figure 3-11B). This faster decay at 2S exciton position shows the extraction of hole from 2S<sub>3/2</sub> state to 3-OCH<sub>3</sub>. This observation clearly suggests that 3-OCH<sub>3</sub> can be used to extract hot hole as compared to any other catechol derivatives which might be due presence of methoxy (electron donating) group in 3-OCH<sub>3</sub>. As observed in Table 3-3 that major component in the emission decay trace of pure CdSe QD at 560 can be fitted with

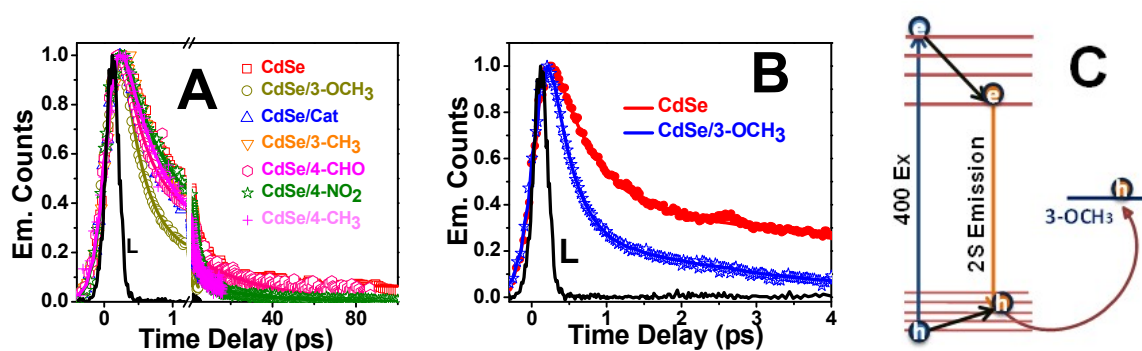


**Figure 3-11A:** Fluorescence upconversion decay traces of CdSe QDs in absence and in presence of catechol derivatives. **B:** Fluorescence upconversion decay traces of CdSe QDs in absence and in presence 3-OCH<sub>3</sub>.  $\lambda_{\text{ex}}$ - 400 nm,  $\lambda_{\text{em}}$ - 560 nm. **C:** Mechanistic scheme of HT reaction from hot excitonic state of CdSe QDs to 3-OCH<sub>3</sub>.

**Table 3-3:** Parameters for multi-exponential fit of emission decay traces for CdSe QDs in absence and in presence of different catechol derivatives monitoring at 560 nm after exciting at 400 nm.

Sample	$\tau_1$ (ps)	$\tau_2$ (ps)	$\tau_3$ (ps)	$\tau_{avg}$ (ps)
CdSe	0.4 (63%)	7 (30%)	>20(7%)	3.75
CdSe/4-NO <sub>2</sub>	0.35 (60)	5 (38.5%)	>20 (1.5%)	2.43
CdSe/3-CH <sub>3</sub>	.32 (60%)	6 (38.5%)	>20 (1.5%)	2.8
CdSe/4-CHO	0.32 (63%)	6.5 (35.5%)	>20 (1.5%)	2.8
CdSe/4-CH <sub>3</sub>	0.32 (63%)	6 (35.5%)	>20 (1.5%)	2.63
CdSe/Cat	0.32 (63%)	6 (35.5%)	>20 (1.5%)	2.63
CdSe/3-OCH <sub>3</sub>	0.25 (75%)	4 (24.5%)	>20 (0.5%)	1.25

400 fs (60%) time constant. However in presence of 3-OCH<sub>3</sub> major component can be fitted with 250 fs time constant (75%). From this observation, hot hole extraction time from CdSe QDs to 3-OCH<sub>3</sub> can be attributed to ~ 250 fs. To the best of our knowledge this is first experimental observation on hot hole transfer from photo-excited QDs materials to molecular adsorbate.

To comprehend the above processes and to monitor the charge recombination (CR) reaction between electrons in CdSe QDs and holes in the catechols another complimentary technique, ultrafast transient absorption spectroscopy was used. Ultrafast transient absorption studies were carried out after exciting the samples at 400 nm and monitoring the transients in 460-700 nm regions. Figure 3-12A shows the transient absorption spectra of pure CdSe QDs which show two distinct negative absorption bands peaking at 490 nm (1P) and at 590 nm (1S). No positive absorption in the 640-700 nm regions was observed suggesting minimum defect states in the QDs materials. Figure 3-12B shows the transient absorption spectra of CdSe/3-OCH<sub>3</sub> which looks very similar to that of pure CdSe QDs with two negative absorption bands peaking at 490 and 590 nm respectively. Interestingly in CdSe/3-OCH<sub>3</sub> system relative bleach intensity at upper excitonic states (470-550 nm region, 2S and 1P excitons) is less as compared to that of lower excitonic state (550-630 nm region, 1S exciton).

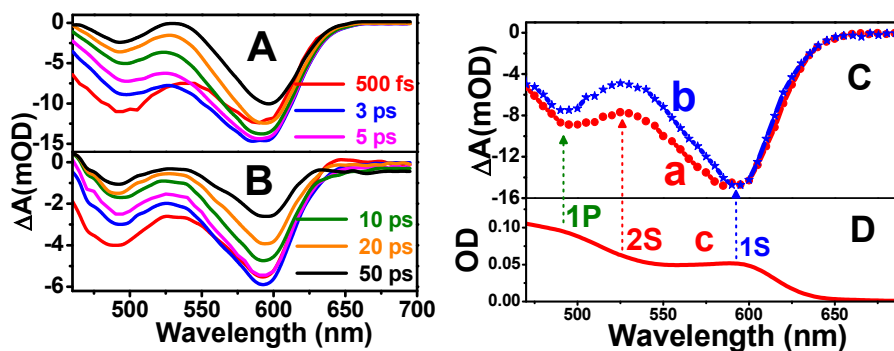


**Figure 3-12.** Transient absorption spectra of (A) CdSe QDs and (B) CdSe QDs in presence of 3-OCH<sub>3</sub> at different time delay after exciting the samples at 400 nm laser light. (C) Transient spectra at 3 ps time delay for CdSe QDs (a) in absence and (b) in presence of 3-OCH<sub>3</sub> after normalizing the bleach at 590 nm (1S exciton). (D) Steady state optical absorption spectra of pure CdSe QDs showing different excitonic position.

To understand CT behavior in CdSe/3-OCH<sub>3</sub> system, transient spectra of CdSe QDs in absence and in presence of 3-OCH<sub>3</sub> at 3 ps time delay is shown in Figure 3-12C. It is clearly seen that in case of CdSe/3-OCH<sub>3</sub> system intensity of transient bleach in 470-550 nm region is much less as compared to that in CdSe QDs system. As already mentioned in steady state optical absorption studies that for CdSe QDs of size  $\sim 4.5$  nm the second excitonic peak comes in the region of 520-540 nm and has been marked as 2S exciton in Figure 3-12D. So it is clear from transient absorption studies that intensity of 2S excitonic absorption bleach in CdSe QDs is much less in presence of CdSe/3-OCH<sub>3</sub> system which suggest that hole from 2S<sub>3/2</sub> state is transferred to 3-OCH<sub>3</sub> before relaxing to either 1P<sub>h</sub> state or to 1S<sub>3/2</sub> state (Figure 3-12C) (Scheme 3-4). Transient absorption spectra of CdSe QDs in presence of other catechol derivatives was also recorded however, no indication of hot hole extraction was observed.

To understand charge carrier relaxation and CT dynamics in CdSe QDs in absence and in presence of 3-OCH<sub>3</sub>, bleach growth and recovery dynamics at two different excitonic

positions, 490 nm (1P) and at 530 nm (2S) (hot states) was monitored and are shown in Figure 3-13. To compare the effect of electron donating group on hot hole extraction, bleach recovery dynamics of CdSe QDs with CAT at both the wavelengths was also monitored. Bleach kinetics can be fitted multi-exponentially with different time constants and is shown in Table 3-4. The growth kinetics of CdSe QDs at 490 nm (1P excitonic bleach) can be fitted single exponentially with time constants 200 fs. This 200 fs time constant can be attributed to the electron cooling from upper excitonic state to  $1P_e$  state (Scheme 3-4). However at 530 nm (2S) bleach growth can be fitted bi-exponentially with time constants of 100 fs and 700-800 fs. Here the slower time constant of 800 fs can be attributed to electron cooling from  $1P_e$  to  $1S_e$  state (Scheme 3-4). Now it will be interesting to monitor the charge carrier dynamics in presence of CAT and 3-OCH<sub>3</sub>. It is clearly seen that bleach growth and recovery kinetics of CdSe QDs in presence of CAT is very similar to that of pure QDs at both the wavelengths. However, in presence of 3-OCH<sub>3</sub> both growth and recovery time at 490 nm for CdSe QDs become faster (Figure 3-13, Table 3-4) but major changes were observed at 530 nm which corresponds to 2S bleach dynamics. Bi-exponential growth at 530 nm for CdSe QDs become single exponential with pulse width limited time (<100 fs) and in early time bleach recovers

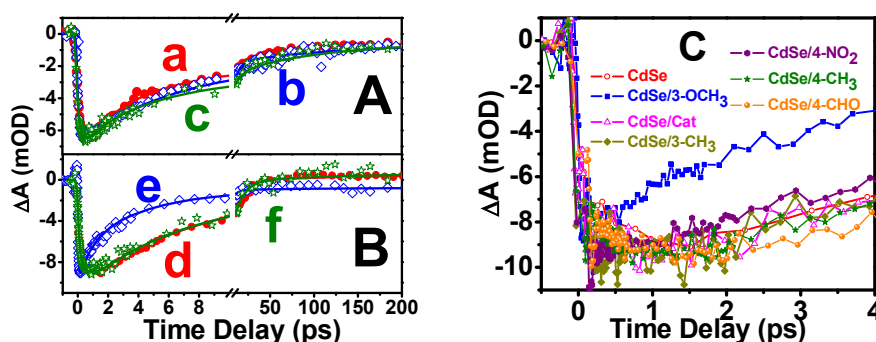
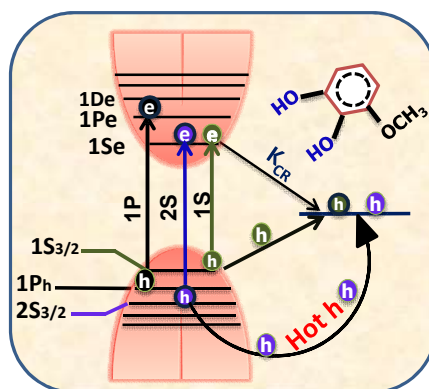


**Figure 3-13** (A) Bleach recovery kinetics of (a) CdSe (b) CdSe/3-OCH<sub>3</sub> (c) CdSe/Cat at 490 nm; (B) Bleach recovery kinetics of (d) CdSe (e) CdSe/3-OCH<sub>3</sub> (f) CdSe/Cat at 530 nm after exciting the sample at 400 nm. (C) Bleach recovery kinetics of CdSe QD at 530 nm monitored in absence and in presence of different catechol derivatives.



**Scheme 3-4.** Energy level diagram of CdSe QDs showing different discrete states of both CB and VB. HOMO level of 3-OCH<sub>3</sub> is also shown. The scheme demonstrate both thermalized and hot hole extraction by 3-OCH<sub>3</sub> from CdSe QDs.

with a faster component of 250 fs. This change in bleach recovery kinetics can be attributed to hot hole extraction from 2S<sub>3/2</sub> state of CdSe QDs to 3-OCH<sub>3</sub> (Figure 3-13 and Scheme 3-4). Bleach dynamics of CdSe QDs at 530 nm was also monitored in presence of CAT (Figure 3-13B) and with other catechol derivatives (Figure 3-13C) however, bleach recovery kinetics almost matched with pure CdSe QDs at 530 nm. This observation clearly suggest that hot hole transfer reaction is only observed in CdSe/3-OCH<sub>3</sub> system which is also confirmed in fluorescence up-conversion measurements.

**Table 3-4:** Multi-exponential fitting parameters for bleach recovery kinetics at different excitonic wavelengths (490 nm and 530 nm) of CdSe QDs in absence and in presence of catechol (CAT) and 3-OCH<sub>3</sub> after exciting the samples at 400 nm.

Sample/ $\lambda_{\text{probe}}$	$\tau_1$ (fs) (Growth)	$\tau_2$ (ps) (Growth)	$\tau_1$ (ps)	$\tau_2$ (ps)	$\tau_3$ (ps)	$\tau_4$ (ps)	$\tau_{\text{avg}}$ (ps)
CdSe 490	200		2.1 (40%)	8.5 (41%)	120 (15.3%)	>1000 (3.7%)	59.7
CdSe/CAT 490	200		2.1 (25.2%)	8 (39.4%)	100 (26.8%)	>1000 (8.6%)	116.2
CdSe/3-OCH <sub>3</sub> 490	<100		0.8 (0.3%)	6 (69.5%)	100 (20.3%)	>1000 (9.9%)	100.9
CdSe 530	<100 (46.4%)	0.7 (53.6%)	2.7 (31.8%)	11 (65.3%)	100 (2.9%)		10.9
CdSe/Cat 530	<100 (61.5%)	0.7 (38.5%)	2.5 (25.4%)	11 (67.4%)	150 (7.2%)		67.2
CdSe/3-OCH <sub>3</sub> 530	<100		0.25 (30.4%)	3.5 (58.2%)	100 (8.7%)	>1000 (2.7%)	37.8

Now to observe the charge recombination (CR) dynamics, bleach recovery kinetics at 1S excitonic position (590 nm) of CdSe QDs in presence of different catechol derivatives was monitored and is shown in Figure 3-14. The bleach recovery kinetics for CdSe QDs can be fitted multi-exponentially with time constants of  $\tau_1 = 5.8$  (21%),  $\tau_2 = 60$  (37.3%),  $\tau_3 = 180$  (21%),  $\tau_4 = >1$ (20.7%) with  $\tau_{avg} = 268$  ps (Table 3-5). This dynamics can be attributed to CR between electron in the CB and hole in the VB of CdSe QDs. However in presence of catechol derivatives bleach recovery kinetics are different depending on the molecular structure of the catechol derivatives and are shown in Table 3-5. It is interesting to see that CR dynamics of CdSe/4-CHO and CdSe/4-NO<sub>2</sub> is much slower as compared to rest of the QDs/catechol derivative composite system. Average time constants ( $\tau_{avg}$ ) have been calculated in all the composite systems and are shown in Table 3-5. CR rate ( $k_{CR}$ ) for different composite systems can be determined as  $k_{CR} = 1/\tau_{avg}$ . Now it's important to monitor the CR dynamics with free energy of CR reaction. To do so free energy of CR reaction ( $-\Delta G_{CR}$ ) was calculated after following the equation below.

$$\Delta G_{CR}^{\circ} = E_{CB}^{CdSe} - E_{Cat/Cat+} \quad (3-8)$$

where  $E_{CB}^{CdSe} = E_{VB}^{CdSe} - E_{00}$  and  $E_{00}$  is the band gap of the QDs.

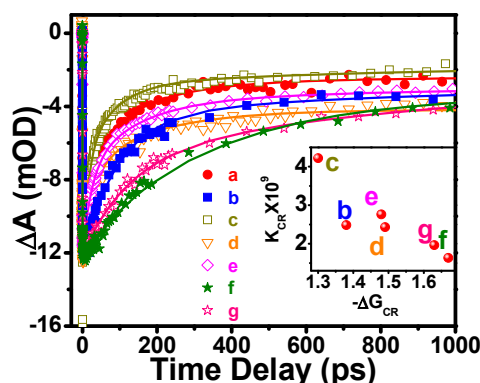


**Figure 3-14.** Bleach recovery kinetics of CdSe QDs at 590 nm (a) in absence and in presence of (b) CAT (c) 3-OCH<sub>3</sub> (d) 3-CH<sub>3</sub> (e) 4-CH<sub>3</sub> (f) 4-NO<sub>2</sub> (g) 4-CHO. **Inset:** Variation of CR reaction rate with Gibbs free energy ( $-\Delta G_{CR}$ ) of reaction.

**Table 3-5:** Multi-exponential fitting parameters for the bleach recovery kinetics of CdSe QDs/catechol derivatives. Change in CR rate with free energy of CR reaction in different CdSe QDs/catechol derivatives composites.

Sample	$\tau_1$ (ps)	$\tau_2$ (ps)	$\tau_3$ (ps)	$\tau_4$ (ns)	$\tau_{avg}$ (ps)	$-\Delta G_{CR}$	$K_{CR} \times 10^9$
CdSe	5.8 (21%)	60 (37.3%)	180 (21%)	>1 (20.7%)	268		
CdSe/-OCH <sub>3</sub>	5 (2.4%)	27 (59.2%)	150 (19.2%)	>1 (19.2%)	237	1.3	4.22
CdSe/CAT	60 (16.5%)	110 (47.7%)	>1000 (35.8%)		420	1.38	2.48
CdSe/4-CH <sub>3</sub>	25 (37.5%)	140 (31.7%)	1000 (30.8%)		362	1.48	2.76
CdSe/3-CH <sub>3</sub>	6 (12.1%)	40 (28.2%)	200 (24.2%)	>1 (35.1%)	412	1.49	2.43
CdSe/4-CHO	70 (6.9%)	330 (62.2%)	1000 (30.9%)		519	1.63	1.93
CdSe/4-NO <sub>2</sub>	50 (1.6%)	130 (42.8%)	1000 (55.6%)		612	1.67	1.63

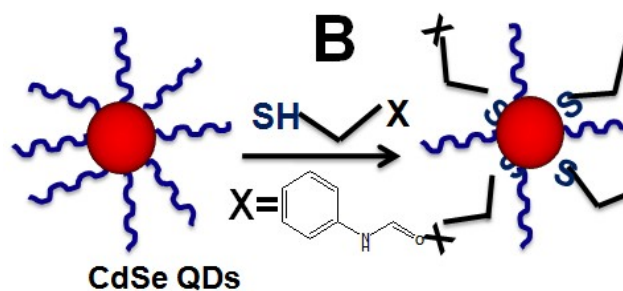
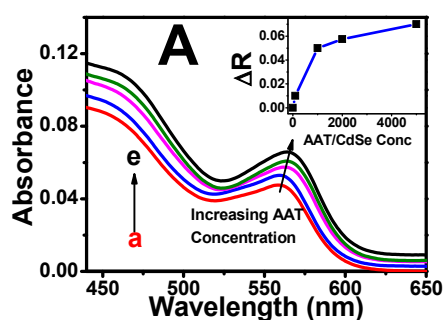
Following the above equation ( $-\Delta G_{CR}$ ) was determined and shown in Table 3-5. It is interesting to see that rate of CR reaction decreases with increase in free energy of reaction ( $-\Delta G_{CR}$ ). It clearly indicates that CR reaction in CdSe QDs/Catechol derivatives falls in the inverted region of the ET reaction of Marcus theory.

### 3.3.2.2. Hot hole extraction dynamics in CdSe QDs/thiols composite system

As mentioned above that hot hole extraction is possible in a composite system of CdSe QDs with 3-methoxy catechol, this possibility was explored further by designing and synthesizing three thiol molecules (Chart 3-1) and monitoring their interaction with CdSe QDs. It has also been reported that over coating a wide band gap shell (such as ZnS) on bare CdSe QDs can greatly enhance photostability of bare QDs<sup>252, 253</sup>. Therefore experiments were also carried out with CdSe/ZnS type I CSQD to understand whether hot hole extraction is still possible in presence of type I shell or not.

Figure 3-15A shows the optical absorption spectra of CdSe QDs in absence and in presence of different concentrations of AAT. Absorption spectra of pure CdSe QDs (Figure 3-15a) shows the first excitonic peak at 559 nm corresponding to 1S ( $1S_e-1S_{3/2}$ ) transition and another peak at 470 nm corresponding to 1P ( $1P_e-1P_h$ ) transition<sup>244</sup>. Optical absorption spectra of CdSe QDs in presence of different concentration of AAT shows that no CT

complex are formed between them, however interestingly the first excitonic peak (1S) position shifts to the red region of the spectrum with increasing AAT concentration (559 to 564 nm) (Figure 3-15e). On addition of the thiols, ligand exchange process on QDs surface takes place (Figure 3-15B) which results in mixing of VB orbital of QDs with the HOMO of thiol ligands. Due to this mixing hole can delocalize into the ligand shell and a red shift in absorption spectra was observed. To demonstrate exciton delocalization in CdSe/AAT system, change in excitonic radius<sup>224</sup> ( $\Delta R$ ) with an increase in AAT concentration was also plotted and is shown in Figure 3-15A inset. It is clearly seen from Figure 3-15A inset that with an increase in AAT concentration an increment in excitonic radius was observed. The similar results were found with other two thiols, ADPT and APT also and shown in Figure 3-15C and Figure 3-15D respectively. Similar exciton delocalization and red shift in absorption spectra was also reported earlier by Weiss and coworkers<sup>222</sup> where they have shown that ligand exchange on CdSe QDs with phenyldithiocarbamate (PTC) ligand can delocalize hole from QDs to PTC. It is interesting to note that with all three thiols almost similar degree of exciton delocalization was observed despite the difference in their molecular structures. It suggests that the binding of  $S^-$  ion of the thiols to the  $Cd^{2+}$  ions on the QDs surface is responsible for the exciton delocalization. Since this  $S^-$  ion is not in conjugation with the main molecule therefore the charge carriers will be localized only on  $S^-$  ion of the thiols. As a result similar degree of exciton delocalization was observed in all the systems.



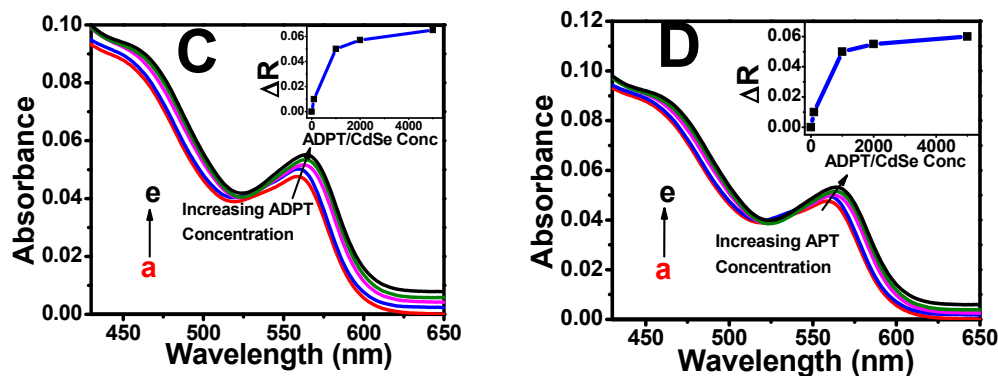


**Figure 3-15** (A) Steady state optical absorption spectra of CdSe QDs with different concentration of (A) AAT (C) ADPT (D) APT, (a) Pure QD, (b) QD:Thiol= 1:10, (c) QD:Thiol = 1:100 (d) QD:Thiol = 1:1000, (e) QD:Thiol = 1:5000. **Inset:** change in  $\Delta R$  value with increase in concentration of Thiol. **(B)** Schematic diagram of ligand exchange of oleic acid with thiols on QD surface in presence of large concentration of thiols.

Now to monitor the effect of shell on exciton delocalization, steady state absorption studies of CdSe/ZnS CSQDs has been carried out in absence and in presence of different derivatives of thiol and are shown in Figure 3-16A. Steady state absorption spectra of CdSe/ZnS CSQDs (Figure 3-16A) shows the presence of 1S and 1P excitons at 570 and 475 nm in contrast to 559 and 470 nm (Figure 3-15A) for CdSe QDs. This red shift in absorption spectra of CSQDs as compared to pure core QDs has been observed earlier also and assigned

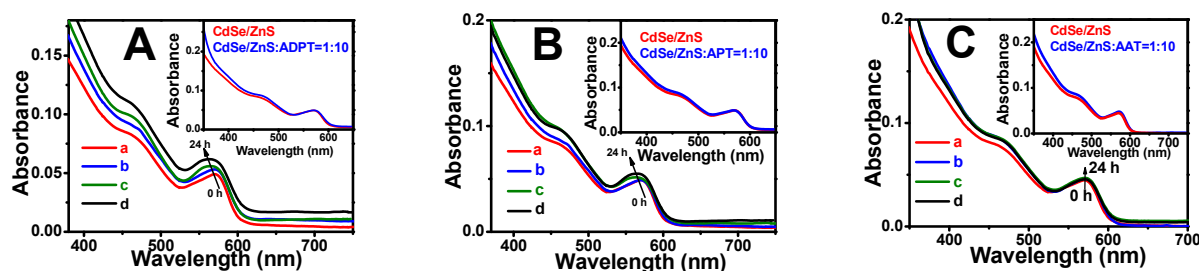


**Figure 3-16.** Steady state optical absorption spectra of CdSe/ZnS CSQD at different time in presence of (A) ADPT (B) APT and (C) AAT. (Thiol:CdSe/ZnS=1000:1) (a) Pure CSQD, (b) CSQD/Thiol at 4 h, (c) CSQD/Thiol at 16 h, (d) CSQD/Thiol at 24 h. **Inset:** Steady state optical absorption spectra of CSQD after 24 h in presence of thiols (Thiol:QD=10:1).

to the leaking of charge carriers from core to shell<sup>254</sup>. Steady state absorption studies of CdSe/ZnS CSQDs in presence of all the three thiols show no red shift in absorption spectra (Figure 3-16) as observed for CdSe QDs (Figure 3-15A). However, with time the exciton peak becomes broader in case of both ADPT and APT at higher thiol concentration (QD:Thiol = 1:1000) (Figure 3-16A and Figure 3-16B respectively) but not in case of AAT (Figure 3-16C). At the same time no such features were observed at lower concentration of thiols (Figure 3-16, inset). To understand this peculiar behaviour and difference in interaction mechanism of AAT as compared to both APT and ADPT, experiments in presence of added  $Zn^{2+}$  ions to the CSQDs solution with thiols were carried out. First a solution of QDs with thiols was prepared and to this solution 50  $\mu$ L of methanol containing 1.5 mg of  $Zn^{2+}$  ion was added. The mixture was sonicated for 1 hr to allow proper mixing of all the constituents. Absorption studies were carried out in above system at different time and changes in spectra were monitored. Absorption spectra of QDs with three thiols suggests that in case of AAT spectra is almost similar at two different times (after 4 hrs and 24 hrs, Figure 3-17A) however in case of both ADPT and APT there is an appreciable change in absorption spectra at different time (Figure 3-17A). Interestingly the absorption spectra of CSQDs/Thiols in presence of added  $Zn^{2+}$  ions at 4 hrs is matching with the spectra of CSQDs with respective thiols after one day (Figure 3-17A). This observation suggests the formation of  $Zn^{2+}$ /thiol complex and its interaction with CSQDs surface is responsible for the change in absorption spectra. When extra added  $Zn^{2+}$  ions is present in the system, the formation of  $Zn^{2+}$ /thiol complex is fast and consequently change in absorption spectra is observed even in 4 hrs. In case of pure CSQDs with thiols, some of the  $Zn^{2+}$  ions will be etched from the QDs surface but this process is slow and therefore change in absorption spectra is observed after one day (Figure 3-17B). This observation was also confirmed by carrying out experiment in presence of excess  $Cd^{2+}$  ions where no change in absorption spectra is observed even after one day in

case of all three thiols. This suggests that all three thiols has high affinity to bind with  $\text{Cd}^{2+}$  ions as compared to  $\text{Zn}^{2+}$  ions and during the interaction of thiols with CSQDs, thiols try to approach  $\text{Cd}^{2+}$  ions of CdSe/ZnS CSQDs and in this process some of the  $\text{Zn}^{2+}$  ions can be

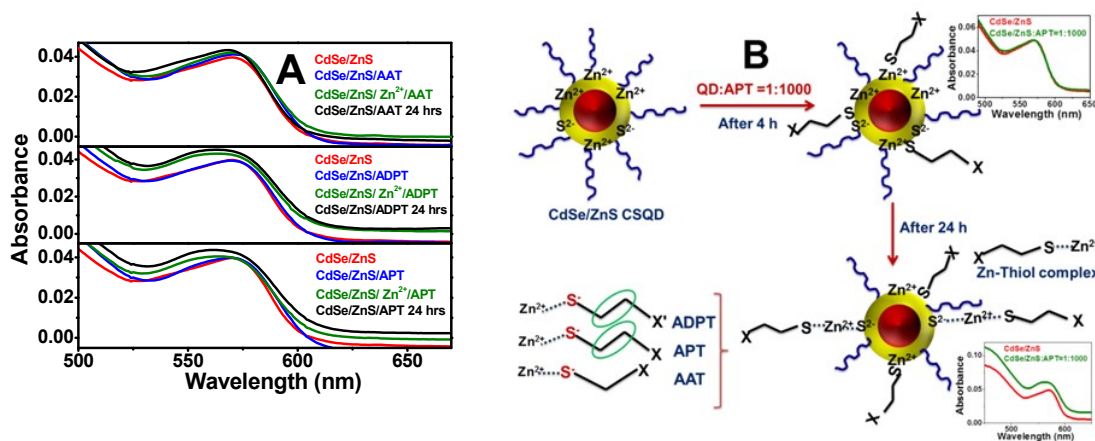


**Figure 3-17A:** Steady state absorption spectra of CSQDs in presence and absence of  $\text{Zn}^{2+}$  ions and thiols. **B:** Schematic diagram of interaction of thiols with CSQDs.

etched from the surface forming  $\text{Zn}^{2+}$ /thiol complex. In case of both APT and ADPT this  $\text{Zn}^{2+}$ /thiol complex is able to interact with the CSQDs surface thereby changing absorption spectrum. However in case of AAT, it is not able to interact with the CSQDs surface and no change in absorption spectra is observed. This is due to the presence of extra  $\text{CH}_2$  group in both APT and ADPT due to which steric hindrance for the interaction with CSQDs surface from the oleic acid molecule present on the surface will be less (Figure 3-17B). Experiment were also carried out with low concentration of thiols (QD:Thiol = 1:10) where no such features was observed.

As thiols are known to be good binder as well as good hole transporting molecules, HT dynamics in CdSe/thiol and CdSe/ZnS/thiol systems was studied. To verify HT processes, steady state emission studies have been carried out for both QDs and CSQDs in absence and in presence of the thiols. Figure 3-18A and 3-18B indicate the emission spectra of CdSe QDs and CdSe/ZnS CSQDs in absence and in presence of AAT, APT and ADPT at the

concentration ratio of thiols:QD = 1000:1. The emission peak for CdSe QDs appears at 580 nm ( $\phi_f = 20\%$ ) and for CdSe/ZnS CSQDs ( $\phi_f = 30\%$ ) appears at 590 nm. It is interesting to observe that in presence of all the thiols the emission intensity of CdSe QDs is drastically reduced (Figure 3-18A). This quenching in CdSe QDs emission cannot be attributed to the energy transfer from photo-excited CdSe QDs to the thiols as there is no overlap between optical absorption spectra of the thiols and emission spectra of CdSe QDs. Now to confirm that the quenching of CdSe QDs emission is due to HT, the redox level of the thiols and QDs were determined. The VB ( $1S_h$ ) level of CdSe QDs was reported to be  $1.65 \text{ V}^{193}$ , whereas the CB ( $1S_e$ ) was determined to be  $-0.56 \text{ V}$  after adding the band gap energy to the VB energy ( $E_{BG}=2.21 \text{ eV}$ ). Redox level of ADPT was determined using differential pulse voltammetry

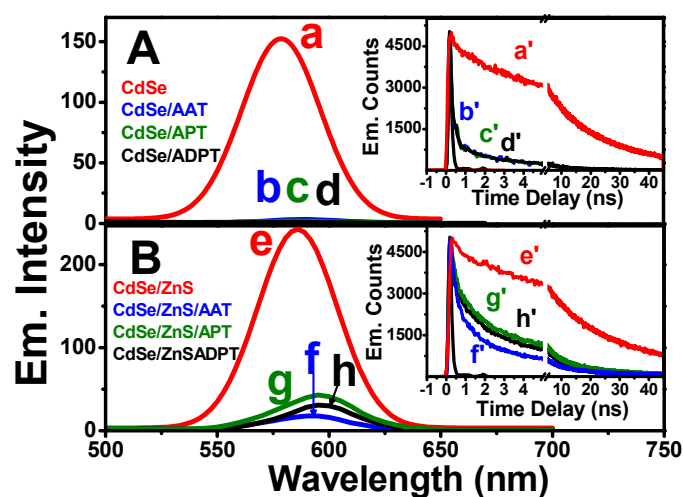


**Figure 3-18 (A):** Steady state emission spectra of CdSe QDs (a) in absence and in presence of the thiols (b) AAT, (c) APT and (d) ADPT. **Inset:** Time-resolved emission spectra of CdSe QDs (a') in absence and in presence of the thiols (b') AAT, (c') APT and (d') ADPT. **(B)** Steady state emission spectra of CdSe/ZnS CSQDs (e) in absence and in presence of thiols (f) AAT, (g) APT and (h) ADPT. **Inset:** Time-resolved emission spectra of CdSe/ZnS CSQDs (e') in absence and in presence of the thiols (f') AAT, (g') APT and (h') ADPT. Concentration ratio for thiol:QDs and thiol:CSQDs were 1000:1.

(DPV) studies and found to be 1.56 V vs NHE (Figure 3-19). The VB level of QD and HOMO of ADPT suggests that the HT from photo-excited CdSe QDs to ADPT is thermodynamically favourable process. At this point, it is important to mention that the redox level of other two thiols, APT and AAT could not be measured, however keeping in mind that the molecular structure of all three thiols are almost similar, it is expected that redox level of both APT and AAT will be almost similar as that of ADPT and therefore the

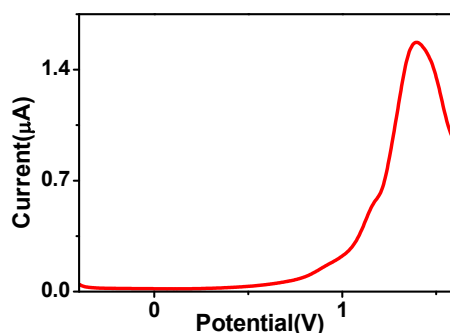


**Figure 3-19:** Differential pulse voltammetry curve of ADPT.

quenching in emission can be attributed to the HT. Steady state emission studies of CdSe/ZnS CSQDs have also been carried out in presence of the thiols and there also an appreciable quenching in emission was observed. Earlier<sup>255</sup> emission quenching of CdSe/ZnS CSQDs in presence of aurin-tricarboxylic acid (ATC) was reported and has been assigned to the HT from CSQDs to ATC. Similarly in the present investigation also the quenching in CSQDs emission on addition of thiols has been assigned to the HT from CSQDs to thiols (Scheme 3-5). To determine HT dynamics, time resolved emission studies of CdSe QDs and CdSe/ZnS CSQDs have been carried out in absence and presence of thiols and are shown in Figure 3-18A and 3-18B Inset. Emission decay trace of CdSe QDs and CdSe/ZnS CSQDs can be fitted multi-exponentially with average life time of  $\sim 10$  ns and  $\sim 15$  ns respectively (Table 3-6). However, it is interesting to see that in presence of the thiols the emission trace of QDs decays with pulse width limited time constant ( $< 100$  ps). Similarly in case of CSQDs the

emission trace decays very fast with the fastest component of  $\sim 150$  ps (Table 3-6). These observations again confirm the HT process from QDs and CSQDs to the thiols.

**Table 3-6:** Time resolved emission decay parameters in nanosecond time scale resolution

$$(\lambda_{\text{ex}}\text{-}400\text{nm}, \lambda_{\text{em}}^{\text{CdSe}}\text{-}580\text{ nm}, \lambda_{\text{em}}^{\text{CdSe/ZnS}}\text{-}590\text{ nm})$$

Sample	$\tau_1(\text{ns})$	$\tau_2(\text{ns})$	$\tau_3(\text{ns})$	$\tau_{\text{avg}}(\text{ns})$
CdSe	0.5 (28%)	10 (60%)	40 (12%)	10.9
CdSe/ZnS	0.6 (22%)	12 (58%)	40 (20%)	15
CdSe/ZnS/APT	0.15 (50%)	3.5 (40%)	15 (10%)	3
CdSe/ZnS/ADPT	0.15 (52%)	3.5 (38%)	15 (10%)	2.9
CdSe/ZnS/AAT	0.15 (60%)	3.5 (32%)	15 (8%)	2.4

By employing steady state absorption, emission and time-resolved emission studies, exciton delocalization and HT processes from both QDs and CSQDs was demonstrated. Now to further reconfirm HT processes, exciton delocalization and their impact on charge carrier dynamics ultrafast transient absorption spectroscopy was carried out after exciting samples at 400 nm and monitoring the transients in 460-650 nm regions. Transient absorption spectra of pure CdSe QDs shows the presence of two distinct negative absorption bands peaking at 470 nm (1P) and at 558 nm (1S) with a hump at 525nm (2S) (Figure 3-20). Interestingly in presence of thiols the transient peak appears at 475 nm and at 564 nm respectively (Figure 3-21). This red shift (558 nm to 564 nm) in transient absorption spectrum of QDs/thiol confirms the exciton delocalization into the ligand shell. Transient absorption spectra of CSQDs also show two transient bleach peaks at 575 (1S) and at 480 nm (1P) (Figure 3-20). However, in presence of both ADPT and APT the exciton peak becomes broader but not with AAT (Figure 3-21). The similar observation was also found in our steady state measurements also.

To summarize the above mentioned features, transient spectrum at 2 ps time delay was plotted for both CdSe QDs and CdSe/AAT along with their absorption spectra and are shown in Figure 3-22A and 3-22B respectively. It is interesting to see that in the transient

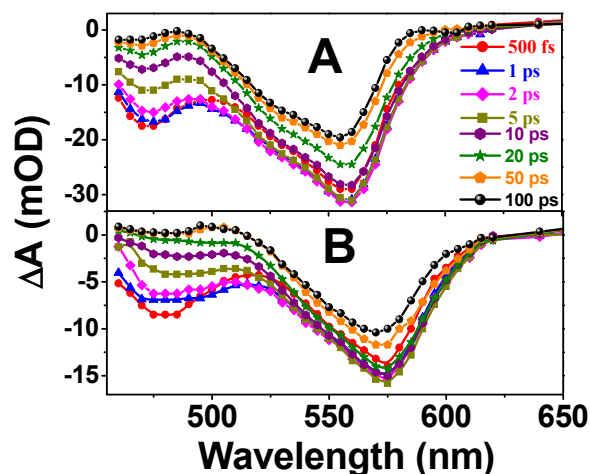


**Figure 3-20.** Transient absorption spectra of (A) CdSe QDs (B) CdSe/ZnS CSQDs at different time delay after exciting at 400 nm.

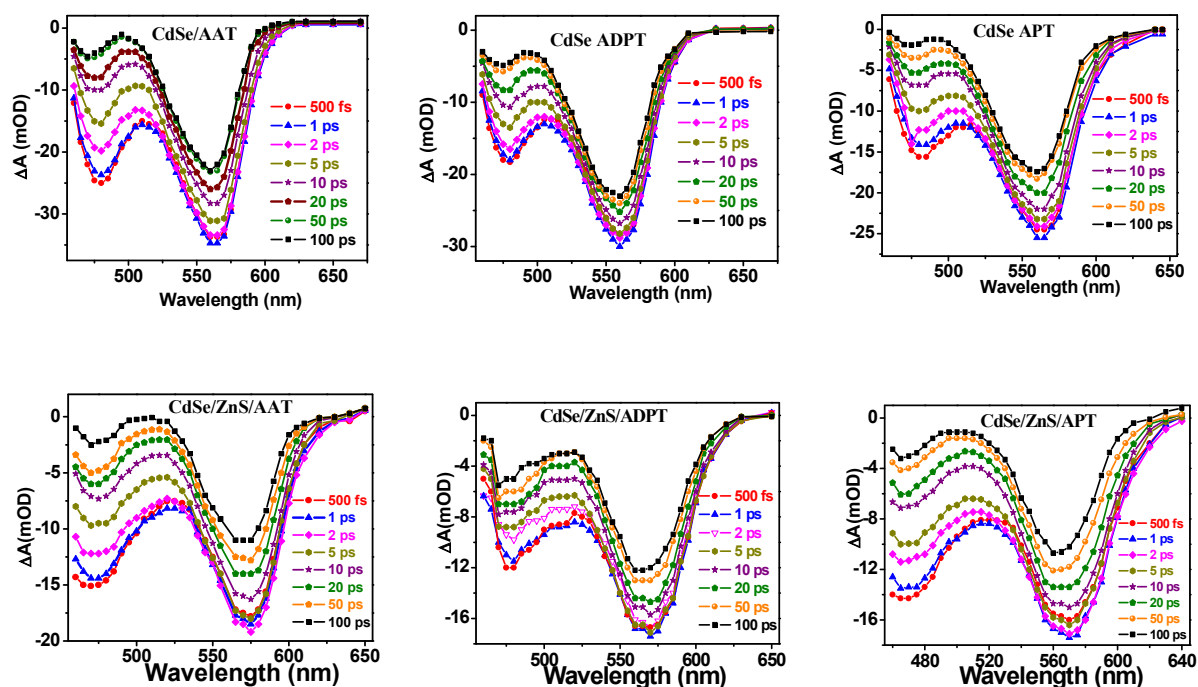


**Figure 3-21.** Transient absorption spectra CdSe QDs and CdSe/ZnS CSQDs with Thiols at different time delay after exciting at 400 nm.

spectra of CdSe/AAT both 1P and 1S excitonic bleach of CdSe QDs moves to the red region. Earlier many authors<sup>41, 43</sup> have demonstrated the carrier delocalization using steady state absorption and emission studies. However nobody has established the same through transient

absorption spectroscopy and to the best of our knowledge, it is confirmed for the first time through our studies. Transient spectra of CdSe/ZnS CSQDs in presence of thiols at 2 ps time

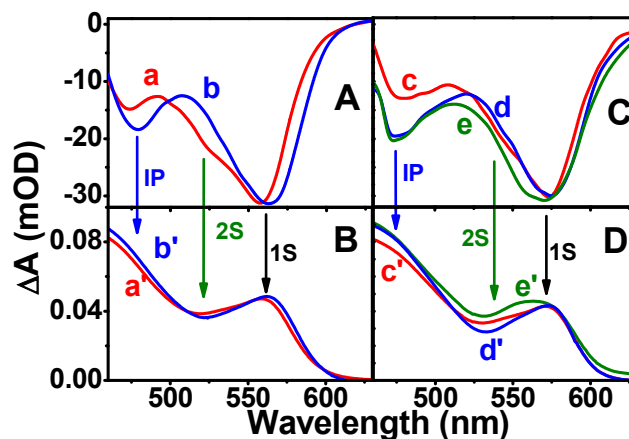


**Figure 3-22 (A).** Transient spectra at 2 ps time delay for CdSe QDs (a) in absence and (b) in presence of AAT after normalizing the bleach at 558 nm (1S exciton). **(B)** Steady state optical absorption spectra of CdSe QDs (a') in absence and (b') in presence of AAT showing different excitonic position. **(C)** Transient spectra at 2 ps time delay for CdSe/ZnS CSQDs (c) in absence and in presence of (d) AAT and (e) APT after normalizing the bleach at 575 nm (1S exciton). **(D)** Steady state optical absorption spectra of CdSe/ZnS CSQDs (c') in absence and in presence of (d') AAT and (e') APT showing different excitonic position.

delay were also plotted. Interestingly transient bleach due to 1S exciton for CSQDs does not change in presence of AAT (Figure 3-22d) but become broader in presence of both APT (Figure 3-22e). Similar broadening was also observed with ADPT. Another interesting observation we made is that in CdSe/thiol the bleach due to 2S excitonic absorption decreases as compared to CdSe QD. This can be attributed to the extraction of hole from 2S state to thiols. Similar features were not observed with CSQDs which might be due to the broadening of transient spectra in presence of the thiols.

To understand hot hole transfer processes, bleach recovery kinetics at 2S excitonic position was monitored for both CdSe QDs and CdSe/ZnS CSQDs in absence and in presence thiols and are shown in Figure 3-23. All the kinetics can be fitted multi-exponentially and are given in Table 3-7. It is interesting to see that the bleach recovery kinetics is faster in presence of the thiols. In our earlier section, transient spectra of CdSe QDs in presence of 3-methoxy catechol (3-OCH<sub>3</sub>) were shown where a faster bleach recovery at 2S excitonic position was observed as compared to pure CdSe QDs. This was attributed to the hot hole transfer reaction from 2S<sub>3/2</sub> state of photo-excited CdSe QDs to HOMO of 3-OCH<sub>3</sub>. Similarly in the present studies faster bleach recovery kinetics can also be attributed to hot hole transfer from photo-excited CdSe QDs and CdSe/ZnS CSQDs to the thiols.

**Table 3-7:** Transient absorption fitting parameters ( $\lambda_{\text{ex}}$ -400nm,  $\lambda_{\text{monitoring}}^{\text{CdSe}}$  -525 nm,  $\lambda_{\text{monitoring}}^{\text{CdSe/ZnS}}$  - 530 nm).

	$\tau_1$ (growth) (ps)	$\tau_2$ (growth) (ps)	$\tau_1$ (decay) (ps)	$\tau_2$ (decay) (ps)	$\tau_3$ (decay) (ps)
CdSe	0.15 (57.5%)	0.45 (42.5%)	8 (35%)	17 (15%)	>400(50%)
CdSe/AAT	0.12 (100%)		3 (22.3%)	8 (37.7%)	>400(40%)
CdSe/ADPT	0.18 (100%)		5 (10%)	20 (40%)	>400 (50%)
CdSe/APT	0.15 (100%)		3.4 (15%)	10 (40%)	>400 (45%)
CdSe/ZnS	0.15 (53.5%)	0.8 (46.5%)	3 (30.3%)	50 (33.3%)	>400 (36.4%)
CdSe/ZnS/AAT	0.3 (100%)		3.5 (50%)	17 (24%)	>400 (26%)
CdSe/ZnS/APT	0.35 (100%)		4 (42.5%)	17 (21.5%)	>400 (36%)
CdSe/ZnS/ADPT	0.3 (100%)		4 (44%)	17 (26%)	>400 (30%)

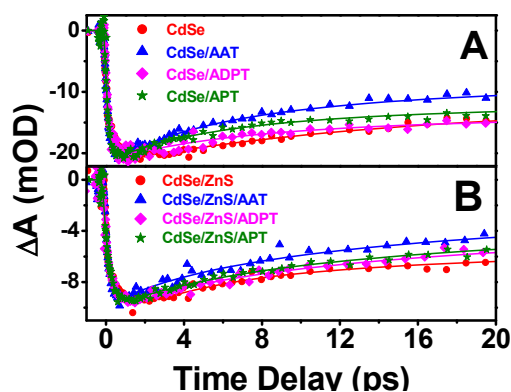


**Figure 3-23:** Bleach recovery kinetics of (A) CdSe QDs and (B) CdSe/ZnS CSQDs in absence and in presence of the thiols at 525 nm and 535 nm respectively (2S excitonic position).

As mentioned above that thiols interact with both QDs and CSQDs leading to hole transfer. However the HT rate was too fast to monitor with nanosecond time scale resolution. At the same time signature of hot hole extraction was also observed through ultrafast transient absorption spectroscopy but time scale of hot hole transfer reaction could not be determined due to overlap of different transients in the transient absorption spectra. To determine HT rate (both hot and thermalized) precisely in the above systems femtosecond fluorescence upconversion studies have been carried out by exciting the samples at 400 nm laser light. Figure 3-24 shows the fluorescence upconversion decay traces of pure CdSe QDs at 580 nm and CdSe/ZnS CSQDs at 590 nm in absence and in presence of the thiols. In all QDs/thiols and CSQDs/thiols composite systems, the thiol/QDs concentration ratio was kept at approximately 1000:1, where complete quenching of luminescence was observed. It is clearly seen that the emission decay traces of QDs/thiols and CSQDs/thiols composite systems decay much faster as compared to both pure QDs and CSQDs respectively. For CdSe QDs the kinetic decay trace at 580 nm can be fitted multi-exponentially with time constants of  $\tau_1 = 3.2$  ps (33%),  $\tau_2 = 22.7$  ps (45%), and  $\tau_3 = > 1$  ns (22%), with  $\tau_{\text{avg}} = 231.3$  ps.

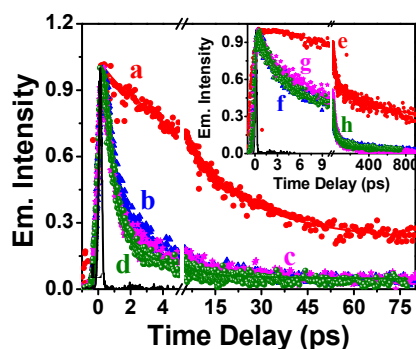


**Figure 3-24.** Fluorescence upconversion decay traces of (a) CdSe QDs (b) CdSe/AAT (c) CdSe/ADPT (d) CdSe/APT at 580 nm. **Inset:** Fluorescence upconversion decay traces of (e) CdSe/ZnS (f) CdSe/ZnS/AAT (g) CdSe/ZnS/ADPT (h) CdSe/ZnS/APT at 590. Excitation wavelength was kept at 400 nm in all the systems. Concentration ratio for both thiols:QDs and thiols:CSQDs were kept 1000:1.

**Table 3-8:** Femtosecond fluorescence upconversion fitting parameters ( $\lambda_{\text{ex}}=400\text{nm}$ ,  $\lambda_{\text{em}}^{\text{CdSe}}$ -580 nm,  $\lambda_{\text{em}}^{\text{CdSe/ZnS}}$  - 590 nm).

	$\tau_1$ (ps)	$\tau_2$ (ps)	$\tau_3$	$\tau_{\text{avg}}$ (ps)
CdSe	3.2 (33%)	22.7 (45%)	>1 ns (22%)	231.3
CdSe/AAT	0.82 (78.3%)	4.8 (16.3%)	105.6 ps (5.4%)	5.75
CdSe/APT	0.7 (88.2%)	6.6 (7.3%)	100 ps (4.5%)	5.03
CdSe/ADPT	0.6 (72%)	1.8 (20.3%)	62.6 ps (7.7%)	4.85
CdSe/ZnS	26.4 (43.2%)	373 (21.2%)	>1 ns (35.6%)	385
CdSe/ZnS/AAT	2 (50.4%)	20.5 (38.4%)	>100 ps (11.2%)	19.4
CdSe/ZnS/APT	3 (58.7%)	32.3 (33.3%)	>100 ps (8%)	19.3
CdSe/ZnS/ADPT	2.5 (47%)	31.45 (44.2%)	>100 ps (8.8%)	23.2

However, in presence of ADPT, the kinetic decay trace becomes much faster and can be fitted multi-exponentially with time constants of  $\tau_1 = 0.6$  ps (72%),  $\tau_2 = 1.8$  ps (20.3%), and  $\tau_3 = 62.6$  ps (7.7%), with  $\tau_{\text{avg}} = 4.85$  ps. It is interesting to see that in presence of all three thiols, the emission decay trace is almost similar with marginal difference in time constants (Table 3-8) and the average lifetime of CdSe/thiol system is  $\sim 50$  times faster as compared to that of pure CdSe QDs. Now using equation 3-5 the HT rate constant and HT time has been determined to be  $2 \times 10^{11} \text{ S}^{-1}$  and  $\sim 5$  ps respectively.

The fluorescence upconversion decay trace of CdSe/ZnS CSQDs is also found to decay faster in presence of the thiols suggesting HT reaction from photo-excited CSQDs to the thiols. Upconversion decay trace at 590 nm for CdSe/ZnS CSQDs can be fitted multi-exponentially with time constants of  $\tau_1 = 26.3$  ps (43.2%),  $\tau_2 = 373$  ps (21.2%), and  $\tau_3 = > 1$  ns (35.6%), with  $\tau_{\text{avg}} = 385$  ps (Table 3-8). However, in presence of ADPT the kinetic decay trace of CdSe/ZnS CSQDs can be fitted multi-exponentially with time constants of  $\tau_1 = 2.5$  ps (47%),  $\tau_2 = 31.45$  ps (44.2%), and  $\tau_3 = > 100$  ps (8.8%), with  $\tau_{\text{avg}} = 23.2$  ps (Table 3-8). Using equation 3-5 the HT rate and HT time is determined to be  $\sim 4.3 \times 10^{10} \text{ S}^{-1}$  and  $\sim 23$  ps respectively. With other two thiols also the HT rate is found to be almost similar. This slow

HT rate for CdSe/ZnS/thiol composite as compared to CdSe/thiol can be attributed due to the presence of ZnS shell over CdSe core. The presence of a wider band gap material (ZnS) over CdSe core creates an energetic barrier for HT reaction as a result HT rate is found to be slow. It's noteworthy to mention that in both the CdSe QDs and CdSe/ZnS CSQDs systems HT rate does not change appreciably with the change in molecular structure of the adsorbate.

As observed that HT rate is very fast in case of QDs/thiol system, this leads us to explore the possibility of hot hole extraction from photo-excited CdSe QDs to the thiols. At the same time in transient absorption studies also signature of hot hole extraction was observed however, hot hole extraction time could not be determined. Therefore to explore the hot hole extraction possibility and to determine hot hole transfer rate, fluorescence upconversion studies have been carried out by exciting the samples at 400 nm and monitoring the luminescence at hot excitonic position. Luminescence from hot excitonic state is not widely reported due to low QY<sup>249</sup> and ultrafast excitonic decay, however Mondal et al.<sup>251</sup> and Cho et al.<sup>250</sup> have reported hot luminescence from QDs materials. Although in the earlier part of this chapter, hot hole extraction from CdSe QDs to 3 methoxy catechols after monitoring 2S luminescence was demonstrated however, effect of type I shell on hot hole extraction dynamics was not discussed. As mentioned that it is difficult to get hot exciton luminescence from QDs materials, in present study also no emission band corresponding to 2S excitonic state from both CdSe QDs and CdSe/ZnS CSQDs was observed. From transient absorption spectra of CdSe QDs, 2S excitonic absorption band appears at 525 nm (Figure 3-25A), so 2S excitonic luminescence band is expected to appear at ~540 nm. Similarly for CdSe/ZnS CSQDs 2S excitonic luminescence band is expected to appear at ~550 nm. Figure 3-25 shows the fluorescence upconversion decay trace of both CdSe QDs and CdSe/ZnS CSQDs in absence and in presence of different thiols at 540 nm and 550 nm respectively. It is interesting to see that the emission decay trace at 2S excitonic position decays much faster as compared

to that of at 1S excitonic position (Figure 3-24) for both CdSe QDs and CdSe/ZnS CSQDs. Emission decay trace of CdSe QDs can be fitted multi-exponentially with major component of 600 fs (60%) time constant (Table 3-9). This faster component can be attributed to relaxation of hole from  $2S_{3/2}$  state to  $1S_{3/2}$  state or due to radiative and nonradiative recombination of electron in  $1S_e$  state and hole in  $2S_{3/2}$  state (Scheme 3-5). In presence of the thiols, this decay becomes much faster as compared to pure QD as shown in Figure 3-25A. This observation clearly suggests that in presence of thiols additional decay channel is available for photo-generated charge carriers, which is much faster as compared to the relaxation processes of the pure QDs. This faster relaxation channel can be assigned to the hot hole transfer from photo-excited QDs to the thiols (Figure 3-25A, centre scheme). The emission decay trace of CdSe QDs in presence of thiols can be fitted multi-exponentially with major component as 300 fs (>90%) (Table 3-9). This 300 fs time constant can be attributed to hot hole transfer from photo-excited CdSe QDs to the thiols. In the earlier part of this chapter, it was observed that hot hole extraction depends on the electron donating and withdrawing ability of adsorbates. However, interestingly in the present investigation hot hole transfer rate is found to be independent of the molecular structure of the thiols.

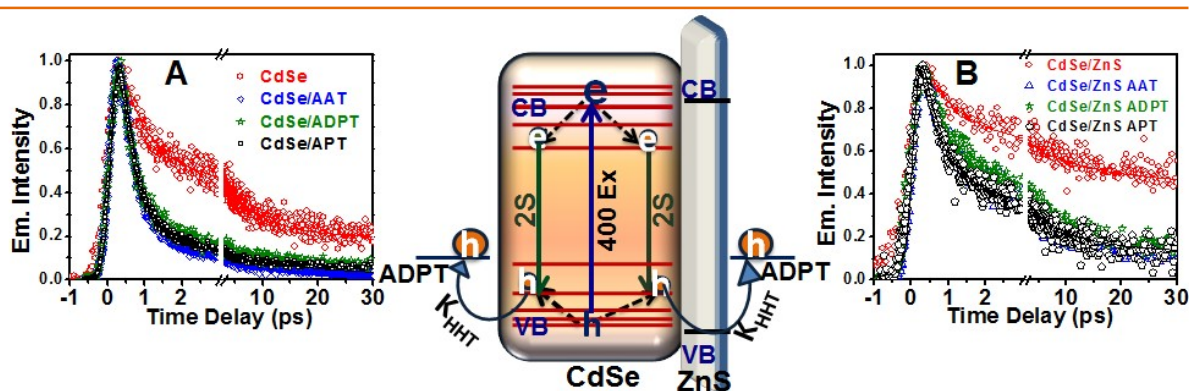


**Figure 3-25.** Fluorescence upconversion decay traces of (A) CdSe QDs (B) CdSe/ZnS CSQDs with different thiols at 2S luminescence position ( $\lambda_{\text{ex}}$ - 400 nm,  $\lambda_{\text{em}}$ - 540 nm for CdSe QDs and 550 nm for CdSe/ZnS CSQDs).

One of the most important aim in the present investigation is to find out whether it is possible to extract hot hole from CdSe QDs core even in presence of type 1 shell ZnS over it or not. To find out this fluorescence upconversion decay trace for CSQDs was monitored at 2S excitonic position in presence and in absence of the thiols and is shown in Figure 3-25B. The emission decay trace of CdSe/ZnS CSQDs can be fitted multi- exponentially with major component of 1ps (44%) time constant (Table 3-9). However, interestingly in presence of the thiols emission decay traces become faster with the time constant of 500 fs as major component with higher contribution (~65%). This 500 fs time constant can be assigned to the hot hole extraction time from CdSe/ZnS CSQDs to the thiols. Due to the presence higher band gap ZnS shell over CdSe core HT is thermodynamically not viable. As already mentioned above that leaking of hole is possible from core to thiols. From our experimental observation it is clear that like thermalized hole, hot hole can also leak from CdSe core to the thiol molecules through ZnS shell. This might be due to higher coupling of thiols with QDs which facilitates hot hole extraction.

**Table 3-9:** Femtosecond fluorescence upconversion fitting parameters ( $\lambda_{\text{ex}} = 400\text{nm}$ ,  $\lambda_{\text{em}}^{\text{CdSe}} = 540\text{ nm}$ ,  $\lambda_{\text{em}}^{\text{CdSe/ZnS}} = 550\text{ nm}$ ).

	$\tau_1$ (ps)	$\tau_2$ (ps)	$\tau_3$ (ps)
CdSe	0.6 (56.1%)	6.6 (28.4%)	>100 ps (15.5%)
CdSe/AAT	0.3 (93.2%)	20.5 (6.8%)	
CdSe/APT	0.3 (92.2%)	20.7 (7%)	
CdSe/ADPT	0.3 (90%)	21.7 (10%)	
CdSe/ZnS	1 (44.3%)	13.1(18.8%)	>1 ns (36.9%)
CdSe/ZnS/AAT	0.5 (62.2%)	6 (26.7%)	>100 ps (11.1%)
CdSe/ZnS/ADPT	0.5 (63%)	6.7 (22.8%)	>100 ps (14.2%)
CdSe/ZnS/APT	0.5 (68.4%)	6.5 (20.5%)	>100 ps (11.1%)

Finally to determine the CR dynamics between electrons in QDs and hole in thiols (Scheme 3-5), bleach recovery kinetics was monitored at 1S excitonic position (560 nm for CdSe QDs and at 570 nm for CdSe/ZnS CSQDs) for CdSe/Thiol and CdSe/ZnS/Thiol

systems using ultrafast transient absorption spectroscopy and are shown in Figure 3-26. The bleach recovery kinetics for pure CdSe QDs and CdSe/ZnS CSQDs can be fitted multi-exponentially with time constants of  $\tau_1 = 10$  ps (39%),  $\tau_2 = 50$  ps (6%),  $\tau_3 \Rightarrow >400$  ps (55%) and  $\tau_1 = 15$  ps (33.3%),  $\tau_2 = 60$  ps (10%),  $\tau_3 \Rightarrow >400$  ps (56.7%) respectively (Table 3-10).

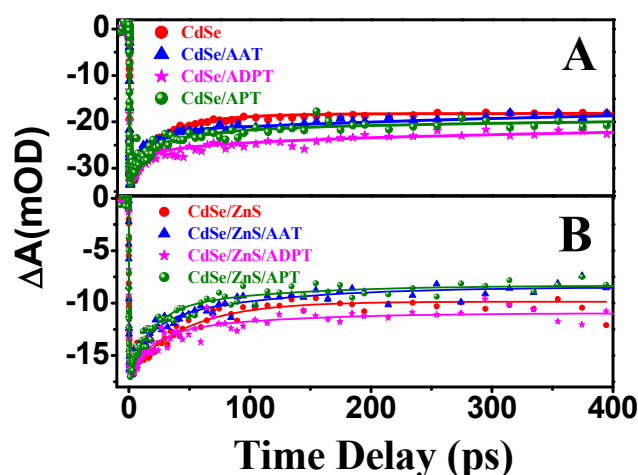
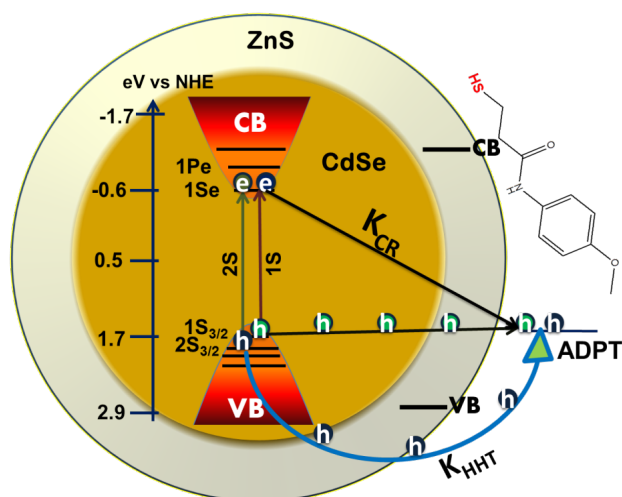


**Figure 3-26.** Bleach recovery kinetics of (A) CdSe QDs and (B) CdSe/ZnS CSQDs in absence and in presence of the thiols. Bleach kinetics was monitored at 560 nm and at 570 nm for CdSe QDs and for CdSe/ZnS CSQDs respectively.



**Scheme 3-5:** Energy level diagram of CdSe/ZnS CSQDs showing different discrete states of both CB and VB. HOMO level of ADPT is also shown. The scheme demonstrate both thermalized and hot hole extraction by ADPT from CdSe QDs.

**Table 3-10:** Transient absorption fitting parameters ( $\lambda_{\text{ex}}=400\text{nm}$ ,  $\lambda_{\text{monitoring}}^{\text{CdSe}}=560\text{ nm}$ ,  $\lambda_{\text{monitoring}}^{\text{CdSe/ZnS}}=570\text{ nm}$ ).

	$\tau_1$ (growth) (ps)	$\tau_2$ (growth) (ps)	$\tau_1$ (decay) (ps)	$\tau_2$ (decay) (ps)	$\tau_3$ (decay) (ps)
CdSe	0.15 (57.5%)	0.45 (42.5%)	10 (39%)	50 (6%)	>400(55%)
CdSe/AAT	0.12 (60%)	0.4 (40%)	9.5 (40%)	52 (5%)	>400(55%)
CdSe/ADPT	0.12 (60%)	0.4 (40%)	12(25.4%)	60 (7.6%)	>400 (67%)
CdSe/APT	0.12 (60%)	0.4 (40%)	11 (31.3%)	55 (8.7%)	>400 (60%)
CdSe/ZnS	0.15 (53.5%)	0.9 (46.5%)	15 (33.3%)	60 (10%)	>400 (59.7%)
CdSe/ZnS/AAT	0.15 (53.5%)	0.3(46.5%)	9.5 (36%)	50 (14%)	>400(50%)
CdSe/ZnS/APT	0.15 (53.5%)	0.35 (46.5%)	17(30%)	60 (4.4%)	>400 (65.6%)
CdSe/ZnS/ADPT	0.15 (53.5%)	0.32 (46.5%)	8 (35%)	50 (15%)	>400 (50%)

These dynamics can be attributed to CR between electron in the CB and hole in the VB of the QDs. Bleach recovery kinetics for both QDs and CSQDs in presence of thiols was also monitored and is shown in Figure 3-26. It is interesting to see that although no appreciable change was observed on both hot and thermalized HT dynamics, bleach recovery kinetics in QDs/thiols and CSQDs/thiols are different for different thiol derivatives depending on the molecular structure of the thiol derivatives (Table 3-10). It is clear from Figure 3-26 and Table 3-10 that CR dynamics is relatively faster in QDs/AAT as compared to that in QDs/ADPT for both QDs and CSQDs. This might be due to the difference in molecular size of AAT and ADPT (Chart 3-1). As mentioned above that thiols interact with QDs through S atom so after the HT, initially the hole will be localized on the S atom of thiols and then it will be delocalized in the benzene ring. Since ADPT have larger molecular structure as compared to AAT, the delocalization of hole should be more in ADPT as compared to that in AAT. This implies that the CR rate will be slower in QDs/ADPT and CSQDs/ADPT system as compared to that in QDs/AAT and CSQDs/AAT as observed also.

### 3.3.3. Metal-Ligand Complex Induced Ultrafast Charge Separation and Electron Relaxation Dynamics in CdX (X = S, Se, Te) Quantum Dots Sensitized Nitro Catechol

It is well reported in literature that HT from QDs is a difficult task<sup>252, 253</sup> because of its limited wavefunction overlap. To address this issue, a composite system of nitro catechol (NCAT) with CdS QDs was chosen where NCAT serve as a hole transporting molecule for CdS QDs. Before monitoring the excited state interaction, ground state interaction between CdS QDs and NCAT was monitored. Figure 3-27A shows the steady state optical absorption spectrum of CdS QDs in absence and presence of NCAT. Absorption spectrum of CdS QDs shows the excitonic peak at 460 nm (Figure 3-27A, a). Figure 3-27A, c shows the optical absorption spectrum of NCAT that absorbs <400 nm. Now on addition of NCAT in CdS QDs, a CT complex formation was observed in blue region of solar spectrum and is shown in Figure 3-27A, b. To find the exact position of the complex, spectrum 3-27A, a and 3-27A, c were added and shown as Figure 3-27A, d. This spectrum was subtracted (Figure 3-27A, d) from Figure 3-27A, b and after subtraction the CT complex spectrum is shown as Figure 3-27A, e peaking at ~390 nm. Earlier many researchers have reported the CT complex formation between QDs and different molecular adsorbates where the CT complex formation was observed from HOMO of ligand to the CB of QDs leading to solar radiation absorption in red region of solar spectrum<sup>208, 231, 236, 257</sup>. But here surprisingly CT complex formation was observed in the blue region of solar spectrum that was not observed so far. To investigate

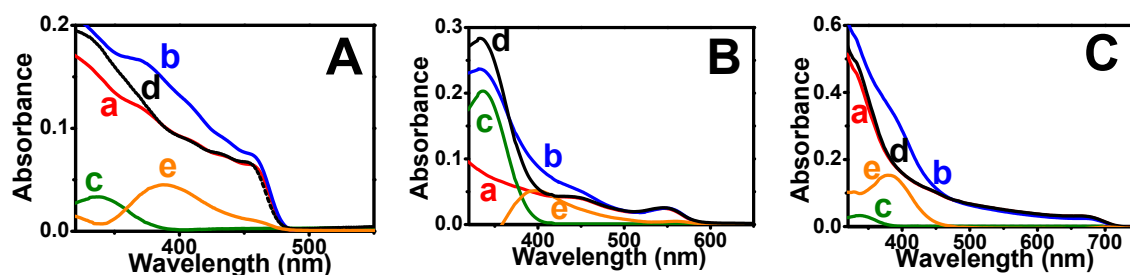


**Figure 3-27.** Steady state absorption spectra of QDs with NCAT. (A) CdS QDs, (B) CdSe QDs, (C) CdTe QDs (a) pure QDs (b) QDs/NCAT (c) NCAT (d) QDs+NCAT (e) b-d.

this feature further, CdSe and CdTe QDs were also synthesized and their interaction with NCAT was monitored and shown in Figure 3-27B and 3-27C respectively. Interestingly with both of these QDs also, CT complex formation was observed which appears at almost same position as in case of CdS/NCAT system (Figure 3-28). Here it is important to mention that during the synthesis of QDs, 2:1 ratio of  $\text{Cd}^{2+}$  and  $\text{X}^{2-}$  ( $\text{X} = \text{S}, \text{Se}, \text{Te}$ ) precursor were used thereby, surface of QDs will be rich in  $\text{Cd}^{2+}$  ions as compared to  $\text{X}^{2-}$  ions. Since in all three QDs complex formation was observed at almost same position, this observation lead us to think that this might be due to the interaction of excess  $\text{Cd}^{2+}$  ions on the surface of QDs with NCAT. To investigate this, interaction between pure  $\text{Cd}^{2+}$  ions and NCAT was monitored. Figure 3-29A shows the steady state absorption spectra of pure cadmium acetate dihydrate

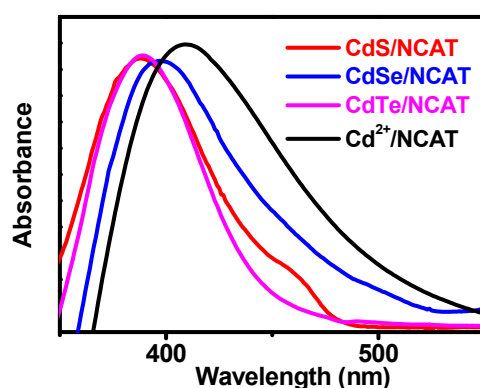


**Figure 3-28:** Complex spectrum of CdS QDs, CdSe QDs, CdTe QDs and  $\text{Cd}^{2+}$  ion with NCAT.

(CAD) (Figure 3-29A, a), NCAT (Figure 3-29A, c), and CAD/NCAT (Figure 3-29A, b) in chloroform. It is clear from Figure 3-29A that both pure  $\text{Cd}^{2+}$  ions and NCAT do not show any absorption beyond 400 nm however, their composite shows a strong absorption band at ~400 nm (Figure 3-29A, b) that extends till 600 nm. This has also been observed visually by strong coloration of the sample on addition of NCAT to CAD (Figure 3-29A, c'). CT complex spectrum was determined by subtracting Figure 3-29A, d from Figure 3-29A, b and is shown

as Figure 3-29A, e peaking at  $\sim 400$  nm. From spectrum 3-29A, e it is clear that the interaction between pure  $\text{Cd}^{2+}$  ion and NCAT leads to the CT complex formation peaking at  $\sim 400$  nm and is almost at the similar position as in the composite systems of CdX QDs and NCAT. This observation clearly suggests that the complex formation of CdX QDs and NCAT is due to the interaction between excess  $\text{Cd}^{2+}$  ions on the QDs surface and NCAT ligand. This is shown schematically in Figure 3-29B where all three QDs have different VB and CB

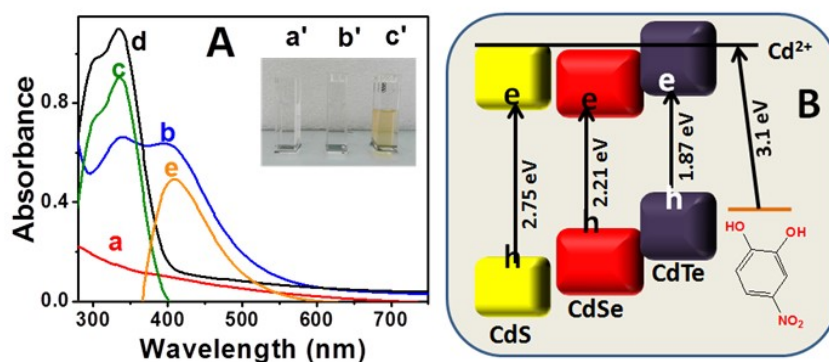


**Figure 3-29 (A).** Steady state absorption spectra of (a) CAD (b) CAD/NCAT (c) NCAT (d) CAD+NCAT (e) b-d. **Inset:** (a') C (b') NCAT (c') CAD/NCAT in  $\text{CHCl}_3$ . **(B)** Schematic diagram for the QDs/NCAT complex formation.

levels. A black line has been drawn to show the  $\text{Cd}^{2+}$  ion level on surface of QDs. The peak position of complex in all three QDs/NCAT composite systems suggests the direct transition from NCAT to  $\text{Cd}^{2+}$  levels leads to complex formation at  $\sim 400$  nm. Earlier many studies have been done where researchers have demonstrated the binding of ligands with metal ions on QDs surface<sup>222, 258</sup>. However, to the best of our knowledge no reports were available where a direct CT complex formation between metal ion on QDs surface and ligands has been reported as observed in our present study.

As mentioned that the complex formation between QDs and NCAT is due to metal-ligand interaction on QDs surface. To understand this behavior further and the reason for complex formation, interaction of QDs with CAT was monitored and shown in Figure 3-30.

Interestingly no complex formation was observed between QDs and CAT. Similar studies were also carried out with CAD ( $\text{Cd}^{2+}$  ion) and there also no complex formation was observed (Figure 3-30). This observation suggests that the presence of nitro group in NCAT is necessary for complex formation. As mentioned above that the QDs surface has excess unsaturated  $\text{Cd}^{2+}$  ions. In presence of CAT and NCAT these surface metal ions bind

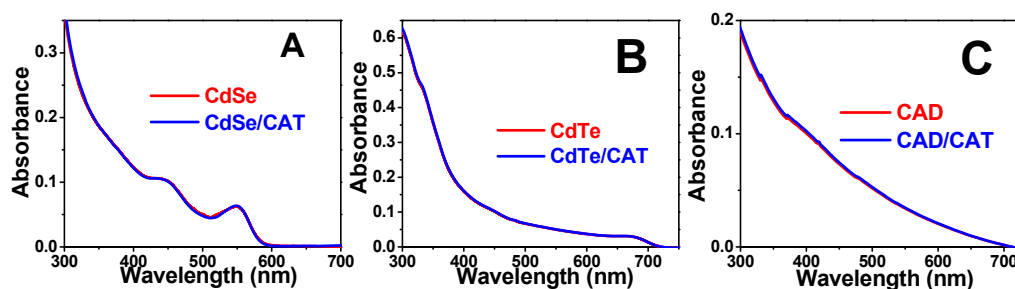


**Figure 3-30.** Steady state absorption spectra of (A) CdSe QDs, (B) CdTe QDs and (C) CAD in absence and presence of CAT.

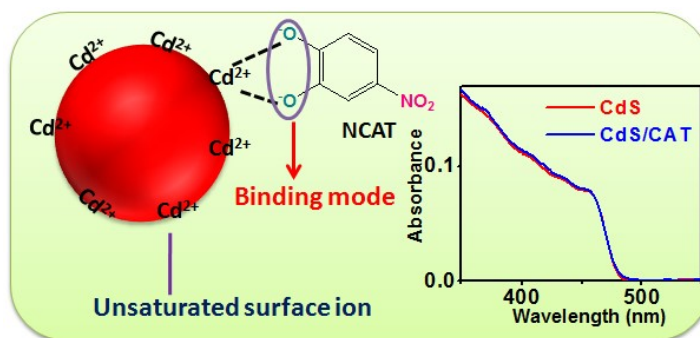


**Figure 3-31.** Schematic diagram for the interaction of NCAT with QDs surface. **Inset:** Steady state absorption spectra of CdS QDs in absence and presence of CAT.

with catecholate moiety as reported earlier also<sup>196, 257</sup>. The formation probability of catecholate will be more in NCAT as compared to CAT because of electron withdrawing nitro group. This stabilizes catecholate moiety thereby leading to a better interaction of surface  $\text{Cd}^{2+}$  ions with catecholate (Figure 3-31) in NCAT.

As discussed above that metal ligand complex formation on QDs surface was observed, steady state luminescence studies were carried out to find whether this complex

effects the luminescence properties of QDs or not. For this, samples were excited at different wavelengths and emission was monitored. Figure 3-32A shows the steady state luminescence spectrum of CdS QDs in presence and absence of NCAT by exciting at two different wavelengths, 400 and 430 nm. It is clearly shown from Figure 3-32A that in presence of NCAT, luminescence intensity of CdS QDs decreases drastically. However, the decrement in luminescence intensity is much faster at 400 nm excitation (Figure 3-32A, e, Figure 3-33A,) as compared to 430 nm excitation (Figure 3-32A, d, Figure 3-33A). As observed in steady state optical absorption studies that on addition of NCAT, a complex formation of CdS QDs was observed in blue region of solar spectrum peaking at ~390 nm. A faster decrement in luminescence intensity on addition of NCAT at 400 nm as compared to at 430 nm suggests the effect of complexation on luminescence quenching where complex formation favors faster luminescence quenching. This has been further validated by carrying out experiment on addition of CAT, where the extent of quenching is same at both the excitation wavelengths (Figure 3-32A, b and 3-32A, c, Figure 3-33A). This clearly indicates that complex formation favors faster luminescence quenching. To extent it further, similar studies were carried out with CdSe QDs and there also faster luminescence quenching in CdSe/NCAT at 400 nm excitation (Figure 3-32B, e') as compared to at 500 nm excitation (Figure 3-32B, d') was observed. However, no such features were observed in CdSe/CAT and the extent of luminescence quenching was almost same at both the excitation wavelengths (Figure 3-32B, b' and 3-32B, c', Figure 3-33B). This observation further shows that complex formation favors faster luminescence quenching. Similar studies were also carried out with CdTe QDs where interestingly no quenching in luminescence intensity was observed at both 600 nm and 400 nm excitation however, an increment in luminescence intensity was observed (Figure 3-32C, b'' and 3-32C, c'' respectively). This might be due to the surface modification of CdTe QDs with CAT that might reduce some of the trap states. Similar studies were also carried out

with NCAT where interestingly no appreciable luminescence quenching was observed at 600 nm excitation (Figure 3-32C, d'', Figure 3-33C) however, at 400 nm excitation a quenching in luminescence intensity was observed (Figure 3-32C, e''). To understand these peculiar behaviors, energetic of the processes were calculated in above systems. In our earlier section

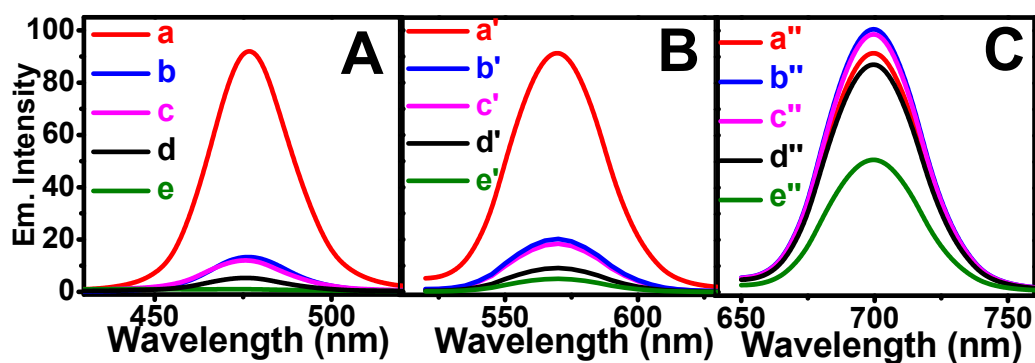


**Figure 3-32.** Change in luminescence intensity of (A) CdS QDs (B) CdSe QDs (C) CdTe QDs in absence and presence of CAT and NCAT at CAT/NCAT to QDs ratio 100:1. (a) CdS QDs, (b) CdS/CAT,  $\lambda_{\text{ex}}$ - 430 nm, (c) CdS/CAT,  $\lambda_{\text{ex}}$ - 400 nm, (d) CdS/NCAT,  $\lambda_{\text{ex}}$ - 430 nm, (e) CdS/NCAT,  $\lambda_{\text{ex}}$ - 400 nm, (a') CdSe QDs, (b') CdSe/CAT,  $\lambda_{\text{ex}}$ - 500 nm, (c') CdSe/CAT,  $\lambda_{\text{ex}}$ - 400 nm, (d') CdSe/NCAT,  $\lambda_{\text{ex}}$ - 500 nm, (e') CdSe/NCAT,  $\lambda_{\text{ex}}$ - 400 nm, (a'') CdTe QDs, (b'') CdTe/CAT,  $\lambda_{\text{ex}}$ - 600 nm, (c'') CdTe/CAT,  $\lambda_{\text{ex}}$ - 400 nm, (d'') CdTe/NCAT,  $\lambda_{\text{ex}}$ - 600 nm, (e'') CdTe/NCAT,  $\lambda_{\text{ex}}$ - 400 nm.

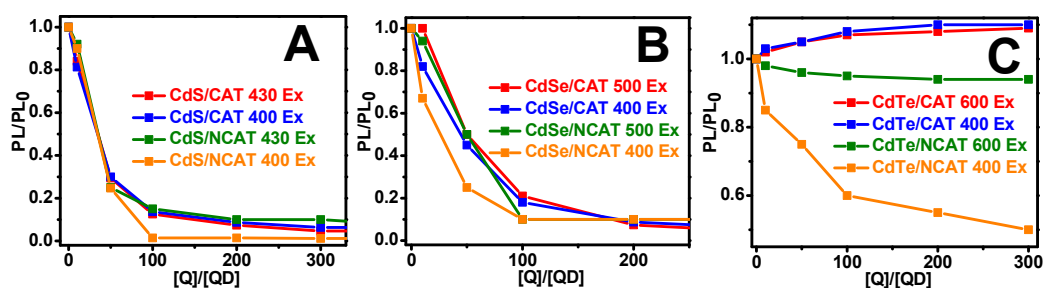


**Figure 3-33.** Change in luminescence intensity of (A) CdS QDs, (B) CdSe QDs, (C) CdTe QDs in presence of CAT and NCAT at two different excitation wavelengths at different concentration of CAT/NCAT to QDs ratio.

redox levels of both CAT and NCAT was mentioned. Redox levels of CdSe QDs were available in literature<sup>193</sup>. Redox level of CdS and CdTe QDs was calculated by adding the difference in VB offset energy of CdSe and CdS QDs to CdSe QDs levels<sup>256</sup> and CdSe and CdTe QDs to CdSe QDs levels<sup>259</sup> respectively (Figure 3-34D). Redox level of both CdS and CdSe QDs and CAT and NCAT suggests that HT process from QDs to CAT/NCAT is thermodynamically favorable. Free energy of HT process was calculated using equation 3-6

**Table 3-11:**  $G_{HT}^{\dagger}$  value for QDs/CAT/NCAT pairs.

System	$\Delta G_{HT}^{\dagger}$
CdS/CAT	-1.32
CdS/NCAT	-1.03
CdSe/CAT	-0.72
CdSe/NCAT	-0.43
CdTe/CAT	-0.12
CdTe/NCAT	0.20

and is shown in Table 3-11. It is clear from Table 3-11 that although  $\Delta G_{HT}^{\dagger}$  for HT is less in case of QDs/NCAT as compared to QDs/CAT however, luminescence quenching is much more in case of former as compared to later when the sample were excited at complex position (400 nm excitation). This observation again suggests that the complex formation favors faster luminescence quenching even if process is less energetically driven. Now it is interesting to observe from Table 3-11 that in case of CdTe QDs the HT process is very less energetically favorable with CAT and with NCAT the process is not favorable. However, steady state luminescence studies suggests quenching in CdTe QDs luminescence only with NCAT at 400 nm excitation (Figure 3-32C, e") while no luminescence quenching was observed in other conditions and with CAT (Figure 3-32C, d", 3-32C, a" and 3-32C, b"). This particular observation further confirms that because of complex formation charge separation occurs in systems that otherwise was not thermodynamically favorable.

As described that luminescence quenching is maximum in QDs/NCAT composite system at 400 nm excitation as compared to at other wavelengths. To investigate this feature

further and the effect of metal-ligand complex on charge separation dynamics, time resolved emission studies in nanosecond time scale resolution were carried out by exciting the samples at different wavelengths and monitor their decay. Figure 3-34A and 3-34B shows the luminescence decay trace of CdS and CdSe QDs respectively in presence and absence of CAT and NCAT by exciting the samples at 406. It is clear from Figure 3-34A and 3-34B that the luminescence decay trace of QDs is much faster with CAT and NCAT as compared to pure QDs decay. The faster luminescence decay in presence of CAT and NCAT is due to HT process from QDs to CAT and NCAT. Another interesting observation that is clear from Figure 3-34A and 3-34B is that the decay dynamics is much faster in QDs/NCAT composite system as compared to QDs/CAT composite. As mentioned above that  $-\Delta G_{HT}^{\ddagger}$  value for HT is less in case of QDs/NCAT composite system as compared to QDs/CAT however, the faster decay dynamics in QDs/NCAT as compared to QDs/CAT again suggest that complex formation favors better charge separation. Similar experiments were also carried out by exciting the samples at 445 nm and are shown in Figure 3-34A and 3-34B, inset. There also faster luminescence decay in QDs/NCAT composite system was observed as compared to QDs/CAT. It is interesting to observe from steady state absorption studies that although complex formation peaks at  $\sim 390$  nm however, it extends till 500 nm (Figure 3-27). Therefore even at 445 nm excitation the effect of complexation will be there that might lead to faster luminescence decay in QDs/NCAT as compared to QDs/CAT. Similar studies were also carried out in CdTe/CAT and CdTe/NCAT composite systems by exciting the samples at 406 nm and 636 nm. Figure 3-34C' shows the luminescence decay trace of CdTe QDs in absence and presence of CAT and NCAT after exciting the samples at 636 nm. It is clear from Figure 3-34 C' that there is no change in luminescence decay trace of CdTe QDs on addition of both CAT and NCAT suggesting very less possibility of HT process. As described above that the  $\Delta G_{HT}^{\ddagger}$  value for HT is very less in case of CdTe/CAT (-0.12 eV) therefore the

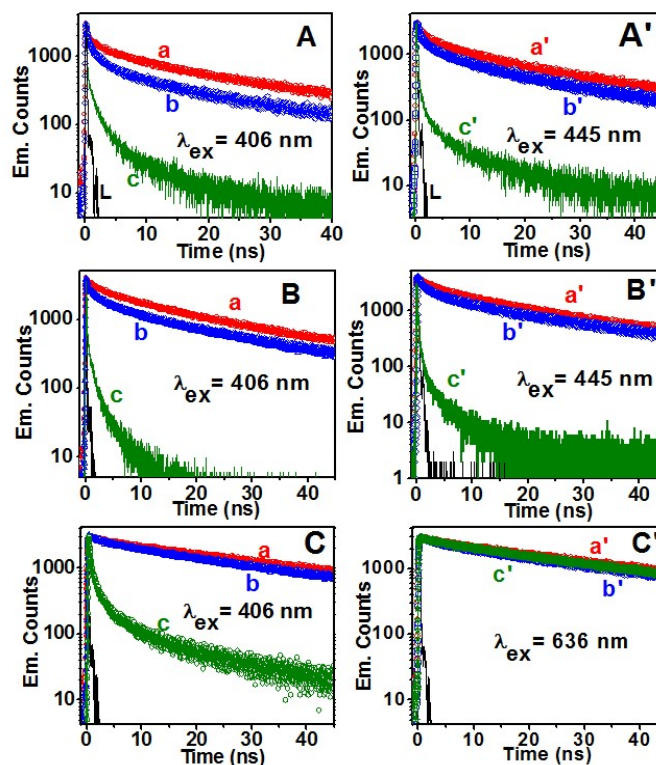
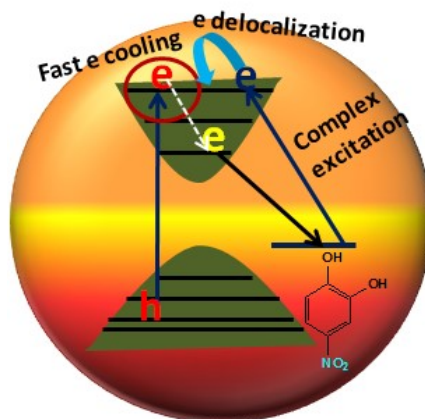


**Figure 3-34.** Time resolved emission decay traces of QDs in absence and presence of CAT and NCAT. **(A)** CdS QDs,  $\lambda_{ex}$ - 406 nm,  $\lambda_{em}$ - 475 nm, **(A')** CdS QDs,  $\lambda_{ex}$ - 445 nm,  $\lambda_{em}$ - 475 nm, **(B)** CdSe QDs,  $\lambda_{ex}$ - 406 nm,  $\lambda_{em}$ - 575 nm, **(B')** CdSe QDs,  $\lambda_{ex}$ - 445 nm,  $\lambda_{em}$ - 575 nm, **(C)** CdTe QDs,  $\lambda_{ex}$ - 406 nm,  $\lambda_{em}$ - 735nm. **(C')** CdTe QDs,  $\lambda_{ex}$ - 636 nm,  $\lambda_{em}$ - 735nm. (a, a') Pure QDs, (b, b') QDs/CAT, (c, c') QDs/NCAT.

probability of HT is less and no appreciable change in decay dynamics of CdTe QDs on addition of CAT was observed. Similar behaviors have also been observed when the samples were excited at 406 nm and there also the decay trace of CdTe QDs on addition of CAT was almost similar as that without CAT (Figure 3-34C). Interestingly when the similar studies were carried out on addition of NCAT the behaviors were different and faster luminescence decay was observed at 406 nm excitation while no changes were observed at 636 nm excitation. As per  $\Delta G_{HT}^{\dagger}$  value, HT from CdTe QDs to NCAT is not thermodynamically favorable ( $\Delta G_{HT}^{\dagger}$  value for HT is 0.20 eV) therefore, no change in decay dynamics of CdTe

QDs on addition of NCAT at 636 nm excitation was observed and decay dynamics of CdTe/NCAT composite was almost similar to that of pure CdTe QDs. However, at 406 nm a strong complexation between CdTe QDs and NCAT (Figure 3-27C) was observed and because of this faster luminescence decay trace was observed. This observation clearly



**Scheme 3-6:** Different processes involved on photo-excitation of QDs with NCAT.

demonstrates that complex formation favors charge separation even if the process is not thermodynamically favorable. As it is clear from steady state optical absorption studies that there is no complex formation at 636 nm (Figure 3-27C) therefore, the decay dynamics at 636 nm excitation will be governed by the interaction of NCAT with pure QDs (Figure 3-27C). However at 406 nm excitation a strong CT complex formation occurs (Figure 3-27C) and decay dynamics will be affected by this complexation. Our experiment of CdTe QDs with NCAT clearly confirms that complex formation favors faster charge separation. This has been shown schematically in Scheme 3-6 where at 400 nm both QDs and complex will be excited. On excitation of complex, the electron will be excited to  $\text{Cd}^{2+}$  levels that further delocalized into the CB of QDs as shown in Scheme 3-6. At the same time, QDs excitation will also create electron and hole in the CB and VB of QDs. Because of strong coupling between NCAT and QDs, the electron in CB of QDs can combine with the  $\text{NCAT}^+$  before its recombination with the hole lying in the valance band (VB) of the QDs (Scheme 3-6). This

---

suggests that electron- hole can be decoupled within the QDs material before their recombination and higher efficiency solar cell can be realized.

To demonstrate the above processes further and to see the effect of complexation on CR dynamics, femto-second transient absorption studies has been carried out by exciting the samples at 400 nm and monitoring the transients at excitonic position. Figure 3-35A shows the transient absorption spectrum of CdS QDs. Transient absorption spectrum of CdS QDs shows the excitonic bleach at 460 nm that matches well with the steady state optical absorption spectrum of CdS QDs (Figure 3-27A, a). Bleach recovery kinetics of CdS QDs in absence and in presence of CAT and NCAT at 460 nm was monitored and are shown in Figure 3-35B. It is interesting to observe from Figure 3-35B that bleach recovery kinetics of CdS QDs becomes relatively slower on addition of CAT. At 400 nm excitation electron will be transferred from VB to CB of QDs leaving hole in VB. As HT from CdS QDs to CAT is thermodynamically favorable process, this will leave electron in QDs while hole will be transferred to CAT. This results in weak coulomb interaction between electron and hole thereby CR is slower in CdS/CAT composite system (Figure 3-35B, b) as compared to CdS QDs (Figure 3-35B, a). Similar features have been observed earlier also<sup>209, 260</sup>. Now in case of CdS/NCAT composite system where at 400 nm both QDs and complex will be excited (Figure 3-27A, b), CR dynamics is different as compared to pure CdS QDs as shown in Figure 3-35B, c. It is interesting to observe from Figure 3-35B, c that the bleach recovery dynamics is faster in CdS/NCAT as compared to pure CdS QDs. This might be due to the strong coupling between QDs and NCAT that favors faster CR. Similar studies were also carried out in CdSe QDs and are shown in Figure 3-35C and 3-35D. Transient absorption spectrum of CdSe QDs shows the presence of first excitonic bleach at 550 nm (Figure 3-27) that matches well with the steady state absorption spectrum (Figure 3-27B, a). Bleach recovery kinetics of CdSe QDs in absence and in presence of CAT and NCAT at first

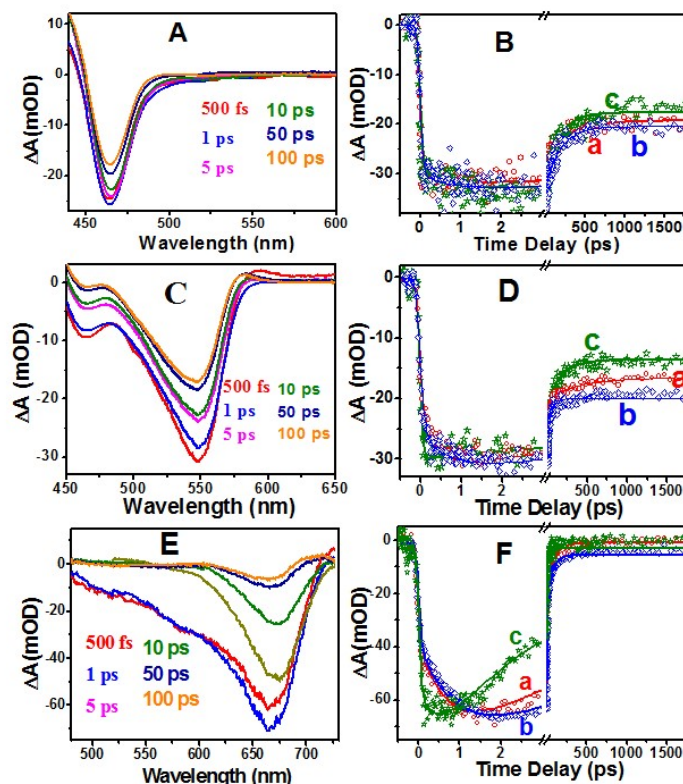


**Figure 3-35.** Transient absorption spectrum of (A) CdS QDs (C) CdSe QDs (E) CdTe QDs.

Bleach recovery dynamics of (B) CdS QDs,  $\lambda_{\text{mon}}$ -460 nm (D) CdSe QDs,  $\lambda_{\text{mon}}$ -550 nm (F) CdTe QDs,  $\lambda_{\text{mon}}$ -670 nm in presence and absence of CAT and NCAT (a) pure QDs, (b) QDs/CAT, (c) QDs/NCAT.

**Table 3-12:** Multi-exponential fitting parameters for the bleach recovery kinetics of CdX QDs in absence and in presence of CAT and NCAT.

Sample	$\tau_1$ (Growth) (fs)	$\tau_2$ (Growth) (ps)	$\tau_1$ (Recovery) (ps)	$\tau_2$ (Recovery) (ps)	$\tau_3$ (Recovery) (ns)
CdS	<100 (90%)	0.4 (10%)	22 (18.5%)	300 (20.7%)	>1.5 (60.8%)
CdS/CAT	<100 (90%)	0.5 (10%)	22 (18%)	300 (20%)	>1.5 (62%)
CdS/NCAT	<100 (90%)	0.35 (10%)	22 (19%)	300 (22%)	>1.5 (59%)
CdSe	<100 (80%)	0.8 (20%)	10 (20%)	100 (25%)	>1.5 (55%)
CdSe/CAT	<100 (70%)	0.8 (30%)	10 (20%)	100 (18%)	>1.5 (62%)
CdSe/ NCAT	<100 (100%)		3.8 (10%)	50 (40%)	>1.5 (50%)
CdTe	<100 (60%)	0.8 (40%)	5 (80%)	100 (19%)	>1.5 (1%)
CdTe/CAT	<100 (58%)	0.95 (42%)	6.5 (73%)	100 (22%)	>1.5 (5%)
CdTe/ NCAT	<100 (65%)	0.4 (35%)	2.8 (80%)	40 (19%)	>1.5 (1%)

excitonic position was monitored and are shown in Figure 3-35D. It is interesting to observe from Figure 3-35D, a that for CdSe QDs bleach growth kinetics can be fitted with two time constants (<100 fs and 800 fs) followed by slow bleach recovery (Table 3-12). The two time constants have been assigned to the electron cooling from upper states to the CB edge level. The similar features were also observed in CdSe/CAT composite system (Figure 3-35D, b) but both bleach growth and bleach recovery kinetics are slower as compared to CdSe QDs. This is again due to HT from CdSe QDs to CAT as mentioned above. Due to HT process, electron and hole decoupled within the QDs material that result in slow electron cooling from the upper states as well as slow electron – hole recombination. Now interestingly in case of CdSe/NCAT composite system (Figure 3-35D, c), bleach growth is much faster as compared to pure QDs material and can be fitted with single life time of <100 fs (Table 3-12). Faster bleach growth in CdSe/NCAT composite system suggests faster electron cooling from upper states to CB edge. Also the bleach recovery is much faster in CdSe/NCAT composite system as compared to pure CdSe QDs that again might be due to higher coupling of CdSe QDs with NCAT. Here it is important to mention that at 400 nm both complex and QDs will be excited (Scheme 3-6). On complex excitation, electron will be excited from NCAT to Cd<sup>2+</sup> levels leaving NCAT positively charged. At the same time excitation within the QDs material will also create electron in CB and hole in VB (Scheme 3- 6). Since NCAT is already an electron deficient moiety because of electron withdrawing nature of nitro group present, it cannot hold positive charge. This result in an increase in coulomb interaction between electron in CB and NCAT<sup>+</sup>. Therefore the electron relaxation within the CB will be very fast leading to faster bleach growth (Scheme 3-6). At the same time strong coupling between QDs and NCAT results in faster recombination of electron in CB and NCAT<sup>+</sup> (Scheme 3-6). In case of CdS QDs/NCAT composite no appreciable change in bleach growth kinetics was observed as observed in CdSe/NCAT composite. In this case the excitonic bleach is at 460 nm and at 400

nm excitation electrons are not excited to much upper states as in case of CdSe QDs. Therefore no observable change in bleach growth dynamics of CdS/NCAT composite system was observed as observed in CdSe/NCAT composite. Similar study was also carried out in CdTe QDs and shown in Figure 3-35E. Bleach recovery kinetics of CdTe QDs in absence and in presence of CAT and NCAT was monitored and are shown in Figure 3-35F. It is interesting to observe from Figure 3-35F, b that bleach recovery kinetics of CdTe QDs is slower in presence of CAT. This observation suggests HT process from CdTe QDs to CAT.  $G_{HT}^{\dagger}$  value for HT from CdTe QDs to CAT suggests that the process is thermodynamically favorable. Although, no HT process in steady state and time resolved measurements was observed but transient absorption studies clearly indicates the signature of HT process. Similar studies have also been carried out with NCAT and are shown in Figure 3-35F, c. It is interesting to observe from Figure 3-35F, c that on addition of NCAT bleach growth is much faster as compared to pure CdTe QDs (Figure 3-35F, a). The similar observation has been observed for CdSe/NCAT composite system also and assigned to the faster relaxation of electron from upper states to CB edge. Here also similar behaviors were observed and assigned to the faster relaxation of electron from upper states to CB edge because of strong interaction between electron and NCAT<sup>+</sup>. Bleach recovery kinetics was also found to be faster in CdTe/NCAT composite system as compared to pure CdTe QDs because of strong coupling between QDs and NCAT. This observation suggests that the recombination between electron and NCAT<sup>+</sup> is much faster as compared to recombination between electron and hole lying within QDs material. Because of this electron-hole decoupling in QDs material hole can be extracted at a much faster rate and a higher efficient solar cell can be realized. The similar observation has been observed earlier by Huang et al.<sup>208</sup> also where they have observed faster bleach recovery on addition of electron transporting molecule.

### 3.4. Conclusions

In the present chapter, binary system of QDs with different molecular adsorbates were demonstrated where the main aim was to extract hole at a comparable rate as that of electron so that higher efficient QDSC can be realized. During this study a number of exciting observations such as grand charge separation, hot hole extraction and metal-ligand complex formation was revealed and their effect on charge carrier dynamics within QDs/molecular adsorbate system was studied.

The first part of this chapter demonstrated a coupled system of CdSe QDs with PGR, where energy level diagram suggest that hole can be transferred from photo-excited CdSe QDs to PGR molecule and photo-excited PGR can inject electron into the CB of CdSe QDs. At lower concentration range ( $\leq 10 \mu\text{M}$ ) PGR molecule found to modify the CdSe QDs surface resulting in increase in photoluminescence of QDs. However, at higher concentrations photoluminescence of CdSe QDs gets completely quenched indicating HT from photo-excited CdSe QDs to PGR molecule. Femto-second transient absorption studies in CdSe/PGR composite shows transient absorption band at 600-850 nm peaking at 690 nm due to PGR cation radical and 850-1000 nm region due to electron in the CdSe QDs. The formation of PGR cation radical is found to be bi-exponential process with time constants of 150 fs and 500 fs, where 500 fs component is attributed to the transfer of hole from photoexcited CdSe to PGR and 150 fs component is attributed to electron injection time from photo-excited PGR to CdSe QD. Charge recombination dynamics found to be extremely slow ( $\gg 200$  ps) confirming grand charge separation in CdSe/PGR composite system.

In the second part of this chapter, hole transfer and hot hole transfer dynamics from CdSe QDs to a series of catechol and thiol derivatives were demonstrated using Femtosecond fluorescence upconversion and Femtosecond transient absorption techniques. Experiments

were also carried out in presence of ZnS shell to understand the effect of shell on hot hole extraction dynamics in CdSe/Thiol composite system. Steady state absorption and ultrafast transient absorption studies demonstrate exciton delocalization from CdSe QDs to thiols. However similar features were not observed in presence of ZnS layer over CdSe core but a broadening in excitonic absorption was observed for ADPT and APT but not for AAT. Steady state and time resolved luminescence studies confirm HT process from photo-excited CdSe QDs to catechols and thiols. Thermalized HT time from CdSe QDs to catechol derivatives is found to be 2-10 ps depending on the molecular structure of the catechols while for thiols it is found to be ~5 ps. Thermalized HT rate in presence of ZnS shell suggests that HT rate is ~20 ps in CdSe/ZnS/Thiol composite system. Interestingly hot hole transfer from the  $2S_{3/2}$  state of CdSe QDs found to take place only to 3-OCH<sub>3</sub> with time scale of ~250 fs. Higher electron donating ability of methoxy group in 3-OCH<sub>3</sub> facilitate hot hole extraction process. Similar features were also observed in CdSe/Thiol and CdSe/ZnS CSQDs composite and hot hole extraction time was observed to be ~300 fs and ~500 fs respectively. CR reaction was also monitored in photo-excited CdSe/catechol composite systems and found to follow rate law of Marcus electron transfer theory. To the best of our knowledge this is the first work where hot hole extraction from photo-excited QDs material and type 1 CSQDs material has been demonstrated. Result indicates hot hole transfer from QDs even in presence of type 1 shell to technologically relevant hole acceptor is possible, minimizing the unnecessary heat loss and eventually highly efficient hot-carrier QDSC cell can be realized.

In the third part of this chapter, an interfacial complex between CdX QDs (X=S, Se and Te) and NCAT was observed and was not reported so far. From steady state absorption studies, it was observed that the complex is due to interaction of Cd<sup>2+</sup> ions on QDs surface with NCAT. Steady state luminescence and time resolved emission studies have been carried out to understand the effect of this complex on CT dynamics. Interestingly faster

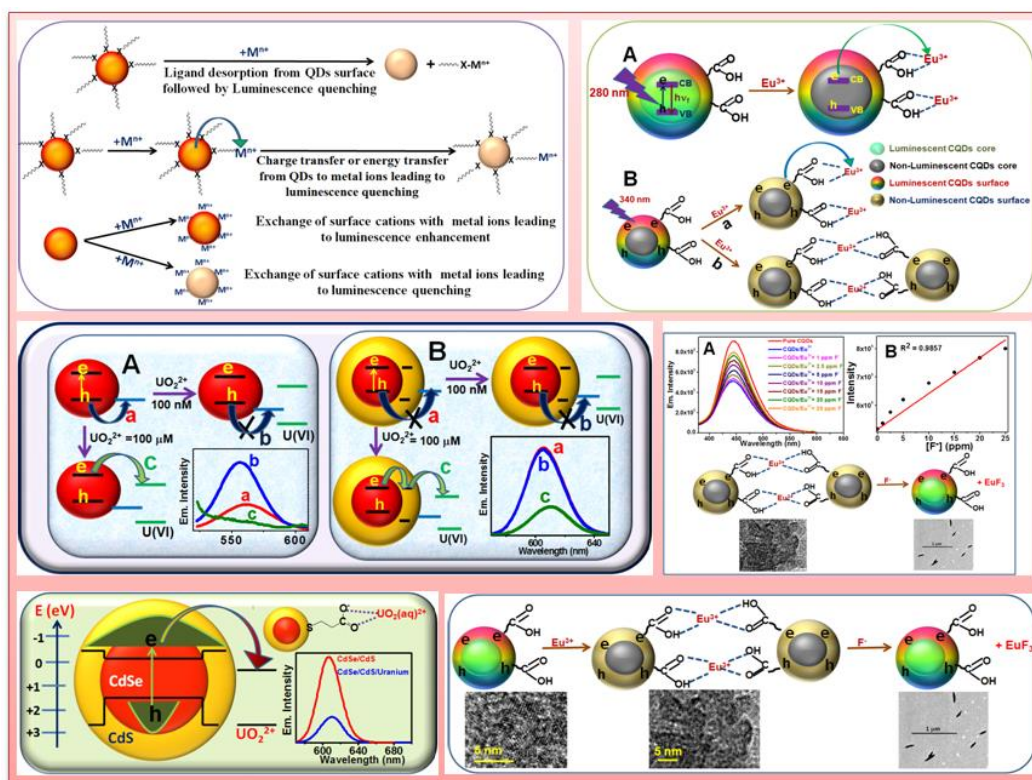
luminescence quenching and luminescence decay was observed in QDs/NCAT as compared to QDs/CAT even though  $-\Delta G_{HT}^{\dagger}$  value for HT is less in the former as compared to later. This suggests that complex formation favors faster charge separation. This has been subsequently validated by carrying out experiment with CdTe QDs where thermodynamically HT processes were not favorable in CdTe/NCAT composite system however CT and luminescence quenching was observed because of complex formation. This suggests that due to complex formation, charge separation can be realized in such systems that otherwise was not thermodynamically favorable. Femto-second transient absorption studies have been carried out that suggests faster bleach growth and recovery in case of QDs/NCAT composite system as compared to pure QDs. This suggests faster electron relaxation from upper states to CB edge and faster electron-NCAT<sup>+</sup> recombination in QDs/NCAT composite system as compared to pure QDs. This results in electron-hole decoupling within the QDs material and charge can be extracted before their recombination. Higher solar radiation absorption and better charge separation coupled in a single system due to metal-ligand complex formation has not been reported in literature and to the best of our knowledge this is the first report. Both of these processes can lead to an increase in solar cell efficiency and finally a higher efficient QDSC can be realized.





# CHAPTER-4

## Quantum Dots as a Probe to Detect Uranium and Fluoride Ions



➤ *Langmuir*, 2017, 33 (33), 8114-8122

➤ *ACS Applied Material & Interfaces*, 2017, 9 (24), 20536–20544.

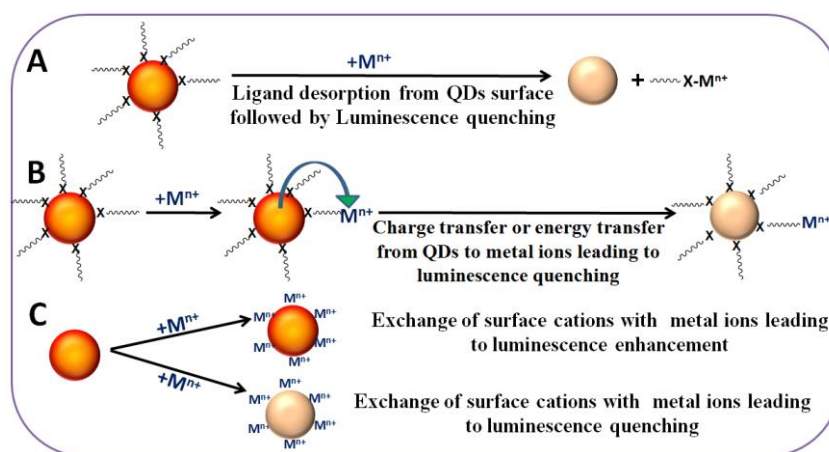


#### 4.1. Introduction

Uranium is one of the most toxic heavy elements<sup>261-263</sup> with a maximum permissible contamination level in drinking water ~30 ppb<sup>30</sup> as per WHO guidelines. +6 is the most stable oxidation state for uranium with maximum bioavailability in aerobic environment<sup>264-266</sup>. With this perspective, there is a great need to design systems which can quickly detect uranium at trace concentrations and can confine if the concentration is more than the prescribed limit. A number of techniques have been developed in past that can measure the trace concentrations of uranium in different samples. It includes atomic absorption spectroscopy<sup>267</sup>, electrochemical methods<sup>268, 269</sup>, total reflection X-ray fluorescence spectrometry<sup>270</sup>, cold-vapour atomic spectrometry<sup>271</sup> etc. However, all these techniques are expensive and involve sophisticated instrumentation. Most of the above techniques need pre-treatment of the samples which makes the process tedious and time consuming. Therefore it is essential to develop a simple and in-situ method for detection of uranium in environmental samples.

High luminescent QDs<sup>272</sup> find applications in number fields that includes photocatalysis<sup>273, 274</sup>, solar energy conversion<sup>275</sup>, bio-imaging<sup>276, 277</sup> and environmental science<sup>258</sup>. Recently trace element detection by luminescence quenching of different QDs have been reported by many research groups<sup>44-55</sup>. However further work needs to be carried out in this direction, as most of the metal ion detection is done in aqueous solution where stability of the bare QD materials is one of the major issues. So it's extremely important to stabilize the QDs in aqueous solution and to understand the mechanism behind the detection. QDs interact with metal ions by three different pathways<sup>54</sup> as shown in Scheme 4-1. The first mechanism of interaction is ligand desorption from QDs surface in presence of foreign metal ions and is shown in Scheme 4-1A. This is a predominant mechanism on interaction when added metal ions have strong binding toward ligands as compared to cations on QDs surface. This leads to the generation of trap states on the surface of QDs resulting in luminescence quenching. This

mechanism of interaction has been shown earlier by different research groups and applied successfully for the detection of trace level of metal ions<sup>47, 53</sup>. The second process by which luminescence of QDs can be quenched is either CT or energy transfer from QDs to metal ion as depicted in Scheme 4-1B. Photo-excitation in QDs material generates e-h pair. The electron from QDs can be transferred to metal ions resulting in luminescence quenching<sup>48</sup>. Here the distance between QDs and metal ion and energetic of the process are two important



**Scheme 4-1:** Different processes involved during the interaction of metal ions with QDs surface. (A) Ligand desorption from QDs surface. (B) Energy transfer or CT from QDs to a metal ion. (C) Cation exchange on QDs surface leading to both luminescence enhancement and quenching.

factors to be considered<sup>258</sup>. Although many reports available where trace level detection following this mechanism has been proposed<sup>50-52</sup> but clear evidence and complete understanding is still lacking in the literature. The alternative of this is luminescence quenching by energy transfer. This mechanism is favourable when the emission spectra of QDs overlap with the absorption spectra of metal ions however very few reports are available on this mechanism<sup>46</sup>. The third mechanism of interaction which can lead to both luminescence enhancement and quenching is depicted in Scheme 4-1C. Here foreign metal ion can displace QDs cation and occupy its position<sup>44, 49</sup>. This might lead to both luminescence enhancement and quenching depending on material properties. This type of

interaction mechanism has been reported in the literature and can be used as a tool to detect different metal ions<sup>44, 49</sup>. A number of reports are available where researchers have demonstrated the application of QDs for detection of different metal ions<sup>44-55</sup>. Interestingly not many reports are available in the literature on detection of uranium metal ion through luminescence quenching of QDs except the report by Dutta and Kumar<sup>51</sup> in amine modified CdS QDs. Although they have shown trace level detection of uranium using these QDs, however clear mechanism of QDs luminescence quenching by uranium ion is not been discussed which is extremely important for making efficient detection methodology.

The first part of this chapter focus on this issue where high luminescent MPA capped CdSe QDs and CdSe/CdS CSQDs with different thickness of CdS shell were synthesized and used for detection of uranium. Steady state absorption and luminescence studies were performed to monitor ground state interaction. Experiments were also carried out with different concentrations of uranium to determine the sensitivity and limit of detection (LOD) of the method. Time resolved studies have been carried out to understand the mechanism of interaction and based on the experimental results mechanism of uranium interaction with QDs has been proposed.

Along with uranium detection, the design of fluoride ion sensors is also an active area of investigation<sup>38-41, 56-63</sup> because of its high toxicity<sup>64</sup> and widespread availability in drinking water, toothpaste, and osteoporosis drugs<sup>43, 56</sup>. It is considered as one of the major water pollutants and excess intake can harm different organs of human body<sup>64, 278</sup>. It has also been realized that the prolonged exposure to fluoride ion can inhibit IQ development in children<sup>66, 279, 280</sup> and as per World Health Organization (WHO) it can permanently damage bones, kidney and even leads to death<sup>65, 281</sup>. Due to its severe health side effects, WHO limits the fluoride ion concentration in drinking water ~ 1.5 mg/L<sup>64, 65</sup>. Hence it is very important to develop methods for fluoride ion detection that is highly sensitive, selective, cost-effective,

simple and allow real-time detection. A number of commercially developed methods are available for this purpose that includes ion selective electrode<sup>278</sup>, nuclear magnetic resonance spectroscopic analysis<sup>56</sup> and colorimetric (UV) methods<sup>58, 60</sup>. Among them, ion selective electrode methods are most widely used. However, both ion selective electrode and nuclear magnetic resonance spectroscopic methods have the limitations such as requirement of complex instrumentation, well-equipped laboratories, and trained personnel. Hence both the methods cannot be used in minimally resourced laboratories. To overcome these limitations, photoluminescence based detection methods are emerging as an alternate<sup>41, 59, 62-66, 278-284</sup>. The method has advantages such as low cost, high sensitivity, low detection limit, ease of handling, and real-time detection. Considerable efforts have been made to develop this method by exploiting different strategies such as supramolecular recognition<sup>38-40</sup>, hydrogen bonding<sup>38, 41</sup>, Lewis acid–base interactions<sup>38, 42, 43</sup>. However, in most of the above stated strategies, organic molecules are being utilized<sup>40, 42, 43</sup> and the synthesis of these molecules is a challenging task<sup>39</sup>. More importantly, most of these molecules are water insoluble<sup>39, 42, 43</sup>. Hence, the detection of the fluoride ions using these molecules cannot be done directly in water and further treatment is required to make them water dispersible. At the same time interference from other competing anions is an issue that has to be resolved. Therefore, there is a need to develop new methods for fluoride ion detection that are much simpler and can overcome most of the above stated limitations.

Recently, semiconductor quantum dots (SQDs) are emerging as an alternative to organic molecules and attains a lot of attention. However, most of the studied semiconductors use cadmium, selenium, and lead as constituent elements and owing to their high toxicity, their application in a real environment is a question of debate. It is therefore utmost important to find alternate materials that are environmentally more benign and less toxic. In view of this, carbon based quantum dots (CQDs) attains a lot of attention<sup>285-287</sup>. The superior

properties of CQDs, such as high aqueous stability, high biocompatibility, and low toxicity make them an ideal candidate over cadmium and lead based SQDs to explore their applications in a number of fields such as bioimaging<sup>65, 288, 289</sup>, biosensors<sup>288, 290</sup> and drug delivery<sup>291</sup>. Recently CQDs and their composites are also being utilized as chemo-sensors and their application to detect a wide range of cations and anions have been demonstrated<sup>50, 64, 66, 292-296</sup>. The detection application of CQDs involves a change in its photoluminescence intensity on interaction with foreign ions<sup>64, 65</sup>. Dong et al.<sup>50</sup> have utilized the photoluminescence property of polyamine functionalized CQDs for selective and sensitive detection of copper ions. They have shown that 6 nM copper ions can be detected using these CQDs. Xu et al.<sup>293</sup> have demonstrated the application of these dots for detection of tartrazine in food samples. Gogoi et al.<sup>294</sup> have utilized these dots for detection of a number of heavy metals such as chromium, copper, iron, lead, and manganese. It shows that a lot of work is going on where the application of these dots as a detection probe has been explored. However, very few reports are available where its application for fluoride ion detection has been demonstrated<sup>64-67</sup>. Mohapatra et. al.<sup>65</sup> have used a composite system of CQDs and magnetically separable nickel ethylenediaminetetraacetic acid complex bound-silica coated magnetite NPs for fluoride ion detection. The method shows a high selectivity but the synthesis of the material involves a number of steps. At the same time, a clear understanding of the detection mechanism has not been given which is equally important to design and understand better detection methods. Liu et. al.<sup>64</sup> have designed a novel fluorescent probe for fluoride ion detection based on zirconium complexed CQDs. They have shown the application of their materials in real samples however, the experimental condition required a little higher temperature that makes the process tedious. Basu et. al.<sup>66</sup> have also used CQDs for fluoride ion detection. They have demonstrated a ready to use detection device. However, they have not shown its applicability in real environmental samples. All the above reports

suggest that a number of materials have been developed for fluoride ion detection but still more improvement is needed. At the same time to design and develop better detection probes, it is very important to understand the working mechanism of the probe and its applicability in real environmental samples which is still lacking in the literature.

In the second part of this chapter, a new method for fluoride ion detection has been demonstrated. In spite of difficult synthesis and methodology adopted so far, the method chosen is simple, selective, sensitive, green and can be used directly in an aqueous medium. A composite system of CQDs and europium were chosen where the photoluminescence property of CQDs was used for fluoride ion sensing. A clear mechanism on working on this probe has been demonstrated which will help in future to design and develop better detection probes. Experiments with other competing ions suggest that the probe is selective in nature and can be used for real sample analysis.

## **4.2. Experimental**

### **4.2.1. Materials**

Cadmium oxide (CdO), oleic acid (OA), 1-octadecene (ODE), trioctylphosphine (TOP, 90%), selenium, sulphur, 3-mercaptopropionic acid (MPA), uranyl nitrate hexahydrate salt, Ethylenediaminetetraacetic acid (EDTA), Citric acid, europium (III) nitrate pentahydrate, dialysis membranes (1 kDa cut off), ammonium hydrogen fluoride, potassium chloride, potassium bromide, potassium iodide, ammonium nitrate, ammonium acetate, ammonium carbonate were purchased from Sigma-Aldrich and used without further purification. Analytical grade sodium hydroxide was used. Chloroform and methanol (AR grade) were used to disperse and precipitate the nanocrystals, respectively. Ultrapure water used in this study was obtained from a Milli-Q ion exchange column (Millipore) with a resistivity of 18.2 M $\Omega$ cm.

#### 4.2.2. Synthesis of CdSe/CdS Quasi Type-II CSQDs

CdSe/CdS CSQDs were synthesized by following previously reported literature method<sup>297</sup> with minor modification. To synthesize CdSe/CdS CSQDs, previously prepared CdSe QDs was used as a core. Synthesis of OA capped CdSe QDs was mentioned in detail in chapter 3. CdS shell growth over CdSe core has been carried out by using Cd-oleate as the cadmium precursor and sulphur powder as the S precursor. The desired amount of cadmium and sulphur precursors was injected into CdSe core at 180°C in inert Ar gas atmosphere. The mixture was heated for 1 h followed by quenching using methanol and finally dispersed in chloroform. Three CSQDs with different thickness of CdS shell has been synthesized. These particles were abbreviated as CdSe/CdS 1, CdSe/CdS 2, and CdSe/CdS 3 with ascending order CdS shell thickness.

#### 4.2.3. Synthesis of water dispersible MPA capped QDs and CSQDs via ligand exchange

Water dispersible MPA capped CdSe QDs and CdSe/CdS CSQDs were synthesized by replacing initial hydrophobic surfactants, OA with MPA after following reported literature method<sup>297</sup>. Typically, MPA (0.123 g, 0.4 mmol) was dissolved in 0.3 mL of deionized water. The solution was then adjusted to pH 12 with 40% NaOH. This solution was then added into 5.0 mL QDs and CSQDs chloroform solution (0.2 mmol CdSe and CdSe/CdS) containing 1.0 mL methanol and stirred for 30 min. Then 10.0 mL water was added into the mixture and kept the stirring for another 20 minutes. The solution was separated into two phases finally and the QDs and CSQDs were transferred into the water phase. The underlying organic phase was discarded and the aqueous phase containing the QDs was collected. The free MPA ligand in the QDs aqueous solution was isolated by precipitating the QDs with the addition of methanol. The supernatant was discarded and the precipitate was then re-dissolved in water for the next step use.

#### 4.2.4. Synthesis of Carboxylic acid functionalized CQDs.

Synthesis of CQDs was carried out using a previously reported procedure<sup>290</sup>. In brief, 6 g of citric acid in a glass beaker was taken and covered with a lid. It was heated at 205°C until the solid completely melt. The solution was maintained at this temperature for another 15 min. After cooling to room temperature, 50 mL of 0.25 M sodium hydroxide (NaOH) was added to the reaction mixture. The resulting solution was then adjusted to pH 6.0 with 0.05 M NaOH, followed by dialysis using a 1 kDa cut off membrane for 3 days before subsequent use. The colloidal solution of CQD was evaporated by vacuum evaporator at 40°C. The size of as-synthesized dots was determined using TEM analysis.

### 4.3. Results and Discussions

#### 4.3.1. CdSe/CdS CSQDs for uranium detection

XRD patterns of OA capped CdSe QDs and CdSe/CdS CSQDs are shown in Figure 4-1A. XRD pattern shows that synthesized QDs and CSQDs have zinc blende structure. The hump at 20° is because of glass. FTIR studies have been carried out to understand the mode of binding of OA with QDs and are shown in Figure 4-1B. FTIR spectrum of the pure oleic acid (Figure 4-1B, e) shows two sharp bands at 2924 and 2854  $\text{cm}^{-1}$  and were attributed to the asymmetric and symmetric stretch of CH band respectively<sup>298</sup>. An intense peak at 1710  $\text{cm}^{-1}$  was observed due to the existence of the C=O stretch of –COOH group and the band at 1285  $\text{cm}^{-1}$  confirms the presence of the C–O stretch. FTIR spectra of OA coated QDs (Figure 4-1B, a) and CSQDs (Figure 4-1B, b, c, d) show that there is no peak at 1710  $\text{cm}^{-1}$  and 1285  $\text{cm}^{-1}$  which were present in the FTIR spectrum of OA. Also, a new peak appears at 1532  $\text{cm}^{-1}$ . This observation clearly indicates that OA binds to the  $\text{Cd}^{2+}$  ions on the surface of QDs through chelation<sup>295</sup>. XRD and FTIR studies were also carried out after ligand exchange with MPA and are shown in Figure 4-1C and 1D respectively. XRD patterns of MPA capped QDs and

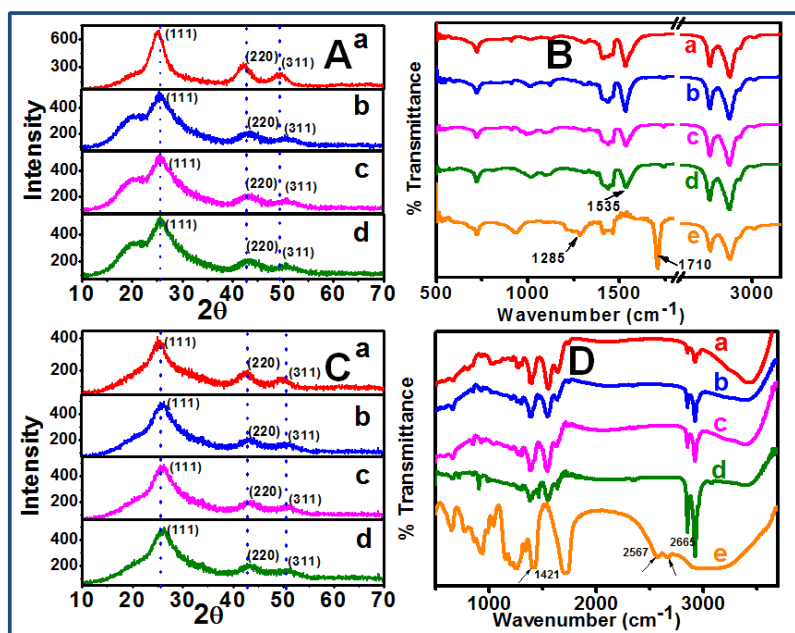


**Figure 4-1A.** XRD spectra of OA capped (a) CdSe QDs (b) CdSe@CdS 2.5 (c) CdSe@CdS 3.5 (d) CdSe@CdS 4.5 CSQDs. **B:** FTIR spectra of OA capped (a) CdSe QDs (b) CdSe@CdS 2.5 (c) CdSe@CdS 3.5 (d) CdSe@CdS 4.5 CSQDs (e) pure OA. **C:** XRD spectra of MPA capped (a) CdSe QDs (b) CdSe@CdS 2.5 (c) CdSe@CdS 3.5 (d) CdSe@CdS 4.5 CSQDs. **D:** FTIR spectra of MPA capped (a) CdSe QDs (b) CdSe@CdS 2.5 (c) CdSe@CdS 3.5 (d) CdSe@CdS 4.5 CSQDs (e) pure MPA.

CSQDs suggest that the synthesized QDs have a cubic structure. FTIR spectrum of pure MPA (Figure 4-1D, e) shows a vibration peak at  $1421\text{ cm}^{-1}$  corresponding to  $-\text{CH}_2$  wagging vibration and two peaks at  $2665\text{ cm}^{-1}$  and  $2567\text{ cm}^{-1}$  which correspond to S-H stretching bond<sup>47</sup>. FTIR spectra of MPA capped QDs and CSQDs did not show any peak corresponding to  $-\text{SH}$  group which suggests the binding of MPA molecule to QDs through sulphur. ICP-OES analysis in CdSe/CdS 1, CdSe/CdS 2 and CdSe/CdS 3 CSQDs were carried out to find the thickness of CdS shell over CdSe core. ICP-OES result indicates that the thickness of CdS shell in CdSe/CdS 1, CdSe/CdS 2 and CdSe/CdS 3 are 2.5, 3.5 and 4.5 ML respectively (1 ML = 0.35 nm). Hereafter these particles will be abbreviated as CdSe@CdS 2.5, CdSe@CdS 3.5 and CdSe@CdS 4.5 corresponding to 2.5, 3.5 and 4.5 ML of CdS on CdSe core.

Steady state absorption and luminescence studies have been carried out in OA capped CdSe QDs and are shown as Figure 4-2. These measurements suggest that QDs have a sharp excitonic peak and high luminescence QY as given in Table 4-1. As mentioned that the main aim of the present investigation is to detect uranium at ultra trace level and to understand the mechanism of detection. For this, it is important to make these QDs water dispersible. To do this, ligand exchange experiment with MPA was carried out and steady state absorption studies of MPA capped QDs with uranium were performed and are shown in Figure 4-3A, inset. The first excitonic peak for CdSe QDs appears at 551 nm (Figure 4-3A, a) by which the size is calculated to be ~3.3 nm using sizing curve<sup>153</sup>. Optical absorption spectrum of QDs with uranium at 50  $\mu$ M concentrations (Figure 4-3A, g) and pure uranium at 50  $\mu$ M concentrations (Figure 4-3A, g) was also recorded. Steady state optical absorption studies clearly confirm that there is no complex formation between QDs and uranium in the ground state. To determine the applicability of these QDs for uranium detection, steady state optical luminescence studies were carried out by adding different concentrations of uranium in QDs sample and exciting the samples at 500 nm and are shown in Figure 4-3A. Interestingly on an addition of low concentrations of uranium (1 nM -100 nM) an increment in luminescence intensity (Figure 4-3A) was observed. This increment in luminescence intensity of QDs on an addition of adsorbates has been observed earlier also<sup>299, 300</sup> and assigned to the surface modification of QDs. At higher concentrations of uranium (>1  $\mu$ M), quenching in QDs luminescence intensity was observed and luminescence was found to be completely quenched at 50  $\mu$ M concentrations (Figure 4-3A).

**Table 4-1:** QY of OA and MPA capped CdSe QDs and CdSe/CdS CSQDs by taking rhodamine 6G as standard.

Quantum Yield	CdSe	CdSe@CdS 2.5	CdSe@CdS 3.5	CdSe@CdS 4.5
OA Capped	32.4%	90.7%	72.67%	65%
MPA Capped	2%	15.5%	29.5%	10.85%

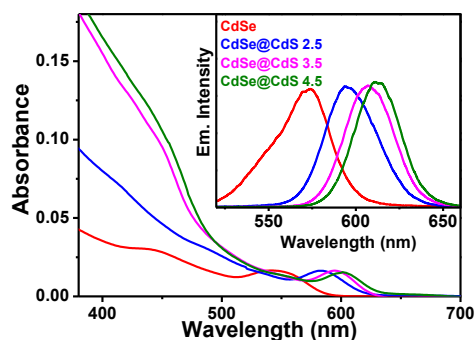


**Figure 4-2.** Steady state absorption and emission (inset) spectra of OA capped CdSe QDs and CdSe/CdS CSQDs. Both the spectra are normalized.

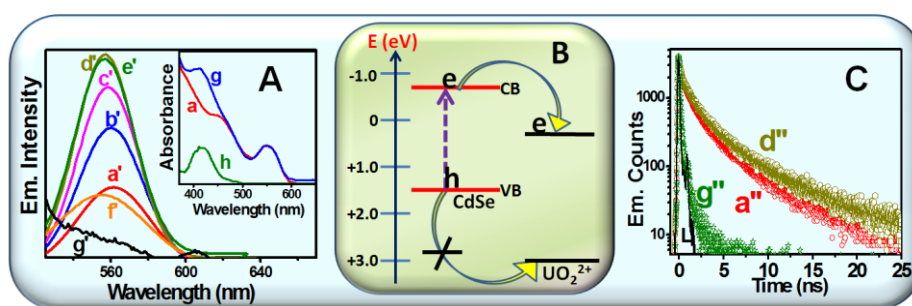


**Figure 4-3 (A).** Steady state emission spectra of CdSe QDs with and without uranium (VI) (a') Pure QDs (b') QDs/1 nM uranium (c') QDs/10 nM uranium (d') QDs/100 nM uranium (e') QDs/1  $\mu$ M uranium (f) QDs/10  $\mu$ M uranium (g') QDs/50  $\mu$ M uranium. **Inset:** Steady state absorption spectra of CdSe QDs with and without uranium (a) Pure QDs (g) QDs/50  $\mu$ M uranium (h) 50  $\mu$ M uranium. **(B)** Schematic diagram of energy level of CdSe QDs and uranyl depicting electron transfer process from QDs to uranyl. **(C)** Time resolved emission spectra of (a'') CdSe QDs (d'') QDs/100 nM uranium (g'') QDs/50  $\mu$ M uranium. (L) Lamp profile.  $\lambda_{\text{ex}}$  – 445 nm,  $\lambda_{\text{em}}$  – 570 nm.

Earlier many authors have carried out similar studies where they have used luminescence quenching as a probe to detect metal ion. Dutta et. al.<sup>51</sup> have used CdS QDs as a probe to detect uranyl ions via photoluminescence quenching of CdS QDs. However, they have not proposed any mechanism which is extremely important to understand the process fundamentally and to design the system more efficiently. In Scheme 4-1 it was mentioned

that there are three mechanisms by which metal ion can interact with QDs surface. In the present investigation, the possibility of mechanism 4-1A can be ruled out as thiols have a much higher binding affinity for  $\text{Cd}^{2+}$  ions as compared to uranium<sup>222, 223</sup>. The third mechanism of interaction, i.e. cation exchange at QDs surface is also not favourable because  $\text{UO}_2^{2+}$  and  $\text{Cd}^{2+}$  have different sizes. Therefore, the second mechanism i.e. interaction of metal ions with ligands on QDs surface seems to be the most probable mechanism. To support it, zeta potential of pure QDs and QDs with uranium was measured and is given in Table 4-2. Zeta potential of pure QDs is found to be -14.55 mV. This negative zeta potential is due to the presence of carboxylic acid present on the QDs surface which exists as carboxylate in solution. On addition of 50  $\mu\text{M}$  uranium, zeta potential values decrease and are found to be -7.05 mV (Table 4-2). This decrement in zeta potential value indicates the interaction of uranium with surface carboxylic groups, which suggests that the interaction takes place through mechanism 4-1B. As mentioned in Scheme 4-1B that ligand interaction with metal ions can lead to luminescence quenching by two mechanisms, energy transfer or CT. Luminescence quenching by energy transfer is not possible in this system, as there is no overlap between the emission spectra of CdSe QDs and absorption spectra of uranium (Figure 4-3A). The other process i.e. luminescence quenching by CT can occur if one of the charge carriers, either electron or hole can be transferred from photo-excited QDs to uranium. Now to understand the feasibility of CT, it is important to know the energy levels of QDs and uranium. The reduction potential of  $\text{UO}_2^{2+}$  is found to be  $\sim 0.07 \text{ eV}$ <sup>301</sup>. Oxidation potential was determined by adding the absorption offset energy to the reduction potential and is found to be +2.7 eV. VB and CB level of QDs are found to be +1.65 and -0.64 eV respectively<sup>196</sup>.

**Table 4-2.** Zeta potential of QDs and CSQDs before and after uranium interaction.

Zeta Potential (mV)	CdSe	CdSe@CdS 2.5	CdSe@CdS 3.5	CdSe@CdS 4.5
Without uranium	-14.55	-15.37	-13.06	-39.44
With uranium	-7.05	-5.59	-9.75	-10.33

Redox level of  $\text{UO}_2^{2+}$  and QDs shows that the ET from photo-excited QDs to uranium is a thermodynamically favourable process as shown in Figure 4-3B. Therefore the luminescence quenching of QDs has been assigned to the ET from QDs to uranium. To corroborate the above process and to monitor ET rate, time resolved emission studies were carried out by exciting the samples at 445 nm laser light and monitoring the emission at 570 nm and is shown in Figure 4-3C. Figure 4-3C, a" shows the luminescence decay trace of pure CdSe QDs which can be fitted multi-exponentially with time constants of 0.2 ns (60%), 0.8 ns (30%) and  $> 4$  ns (10%) with an average time constant of 0.76 ns (Table 4-3). The faster time constant of 0.2 ns can be assigned to the trapping time of hole into the MPA shell which leads to a large reduction in QY of MPA coated QDs<sup>258</sup> (32.4% of OA capped CdSe QDs vs 2% of MPA capped CdSe QDs, Table 4-1). Now it is interesting to observe that on addition of 100 nM uranium the decay trace is almost same (Figure 4-3C, d") as that of pure QDs (Figure 4-3C, a"). This suggests that at low concentration of uranium surface modification is the major process as compared to ET thereby we have not observed any faster decay in QDs luminescence trace. The similar observation has also been observed in steady state luminescence studies (Figure 4-3A). However, at higher concentration of uranium, 50  $\mu\text{M}$ , the decay trace of QDs become very fast and found to decay with pulse width limited time (Figure 4-3C, g"). Time-resolved emission studies suggest that ET reaction from photo-

**Table 4-3:** Time resolved fitting parameters of MPA capped CdSe and CdSe/CdS CSQDs with and without uranium ( $\lambda_{\text{ex}} = 445$  nm).

Sample	$\tau_1$ (ns)	$\tau_2$ (ns)	$\tau_3$ (ns)	$\tau_{\text{avg}}$ (ns)	$k_{\text{ET}}$ ( $\text{S}^{-1}$ )
CdSe	0.2 (60%)	0.8 (30%)	$>4$ (10%)	0.76	
CdSe/U	$<0.1$ (100%)				
CdSe/CdS@2.5	0.8 (37.5)	10 (56.5)	$>30$ (6%)	7.75	
CdSe/CdS@2.5/U	0.5 (62.5)	1.5 (31.5)	$>6$ (6)	0.93	$9.4 \times 10^8$
CdSe/CdS@3.5	0.8 (25%)	10 (65%)	$>30$ (10%)	9.7	
CdSe/CdS@3.5/U	0.5 (50.5)	2 (35.5%)	$>6$ (14%)	1.8	$4.5 \times 10^8$
CdSe/CdS@4.5	0.8 (62.5)	10 (35.7)	$>30$ (1.8)	1.67	
CdSe/CdS@4.5/U	0.5 (57.5)	1.5 (31.8)	$>6$ (10.7)	1.2	$2.35 \times 10^8$

excited CdSe QDs to uranium takes place in sub-nanosecond time scale.

To understand this process further, CdSe/CdS CSQDs with three different shell thicknesses were synthesized and steady state optical absorption and luminescence studies were carried out in the absence and in presence of uranium. The as-synthesized CSQDs have quasi type II band alignment where an electron can be delocalized into the shell while hole will be localized in the CdSe core<sup>302-305</sup>. Steady state optical absorption studies suggest no complex formation between CSQDs and uranium. Steady state luminescence studies have been carried out by exciting the samples at 500 nm. Figure 4-4A shows steady state luminescence studies of CdSe@CdS 2.5 CSQDs in the absence and in presence of uranium. It is interesting to observe from Figure 4-4A that on an addition of uranium at low concentrations (100 nM) luminescence intensity increases (Figure 4-4A, b) however, at higher concentrations quenching in luminescence was observed (Figure 4-4A, d). Similar behaviour was also observed for bare QDs where at low concentrations, an increment in QDs luminescence intensity was observed while at high concentrations, quenching in luminescence was observed. Similar studies were also carried out with the other two CSQDs, CdSe@CdS 3.5 and CdSe@CdS 4.5 and are shown in Figure 4-4B and 4-4C respectively.

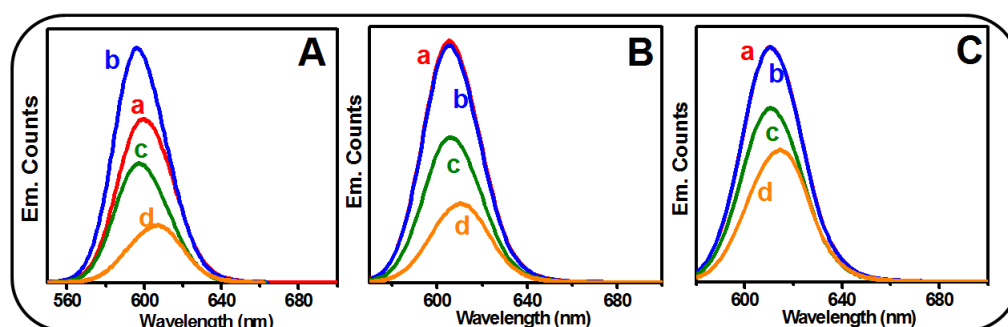


**Figure 4-4.** Steady state emission spectra of **A:** CdSe@CdS 2.5, **B:** CdSe@CdS 3.5 and, **C:** CdSe@CdS 4.5 CSQDs in absence and presence of uranium (a) Pure CSQDs (b) CSQDs/100 nM uranium (c) QDs/10  $\mu$ M uranium (d) QDs/100  $\mu$ M uranium.

Interestingly in both the cases, no increment in luminescence intensity was observed at a low concentration of uranium, however, a quenching in luminescence was observed at higher concentration ( $>10 \mu\text{M}$ ). It indicates that a low concentration of uranium modifies the surface of both CdSe QDs and CdSe@CdS 2.5 CSQDs which leads to an increment in luminescence intensity. However, no such increment of luminescence intensity was observed with thicker CdS shell. These peculiar behaviours are depicted in Figure 4-5. On photo-excitation of QDs e-h pairs are generated. Redox level of CdSe QDs and oxidation potential of Cd-MPA<sup>306</sup> suggests that HT from QDs to MPA is a thermodynamically favourable process. This results in trapping of the hole into MPA which results in a large reduction of luminescence yield of MPA capped QDs and is shown as process a, in Figure 4-5A. Now on the addition of uranium, it interacts with the carboxylate group of MPA ligand as shown by zeta potential studies, leading to the formation of Cd-MPA-Uranium complex at QDs surface. The oxidation potential of newly formed Cd-MPA-uranium complex will be more as compared to Cd-MPA complex. This creates a thermodynamic barrier for HT process and hole will be localized in CdSe core as shown by process b in Figure 4-5A. This will result in an increment in luminescence intensity and has also been observed in steady state luminescence measurements (Figure 4-3A). However, as mentioned that ET process from QDs to uranium is thermodynamically favourable, at higher concentrations of uranium, ET from QDs to uranium is dominating process which leads to a complete quenching in QDs luminescence, as depicted by process c in Figure 4-5A. Similar studies were also carried out in CdSe/CdS CSQDs with different shell thickness. Here in CdS shell will create a thermodynamic barrier for HT process. Earlier many researchers have demonstrated that HT in such systems is still possible where the holes can be leaked through the thin shell of CdS<sup>307-309</sup>. Although, the probability of HT process decreases with increases in shell thickness. To demonstrate this, experiments were carried out with three different CdS shell thicknesses, 2.5, 3.5 and 4.5 ML.

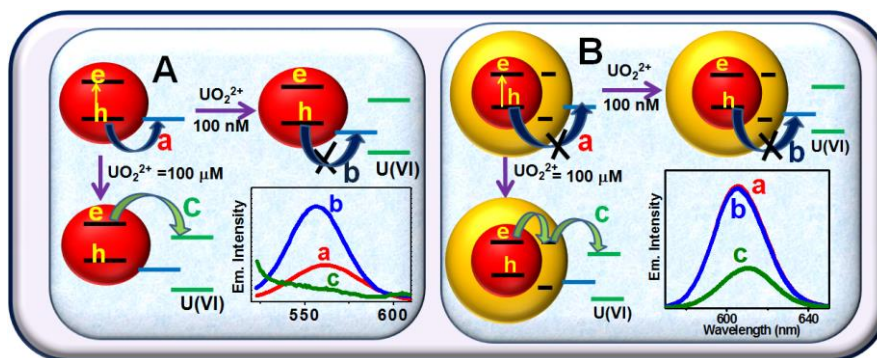


**Figure 4-5.** Different processes involved on the interaction of uranium in (A) CdSe QDs and in (B) CdSe@CdS 3.5 CSQDs. Process a refers to the photo-excitation of QDs and CSQDs to generate e-h pair followed by hole delocalization into MPA shell. Process b refers to the hole delocalization process on an addition of uranium at 100 nm concentrations. Process c refers to the ET process from photo-excited QDs and CSQDs to uranium leading to luminescence quenching.

An increment in luminescence intensity was observed on addition of uranium at low concentrations in CdSe@CdS 2.5 CSQDs however, no such behaviours were observed for higher shell thickness. This suggests that hole leaking is possible at 2.5 ML of CdS shell however, no leaking was observed for higher shell thickness. This is shown schematically in Figure 4-5B. For CdSe@CdS 3.5, photo-excitation of QDs generates e-h pair. HT in presence of CdS shell is thermodynamically not feasible, therefore, uranium addition will not affect HT processes as depicted by process a and b in Figure 4-5B respectively. This has been shown in steady state luminescence measurements also where no enhancement in luminescence intensity was observed on addition of low concentration of uranium (Figure 4-4B). At higher concentrations of uranium, ET from QDs to uranium is a dominating process (process c, Figure 4-5B) thereby, quenching in QDs luminescence was observed (Figure 4-4B). To confirm the above processes, a separate experiment of QDs and CSQDs with EDTA was carried out. EDTA acts as a hole transporting molecule for QDs (oxidation potential of

EDTA with respect to NHE is -0.2 eV, Figure 4-6). Steady state luminescence measurements with EDTA suggests luminescence quenching only in CdSe QDs and CdSe@CdS 2.5 CSQDs but not in CdSe@CdS 3.5 and CdSe@CdS 4.5 CSQDs (Figure 4-7). This further confirms that the HT is possible only in CdSe QDs and CdSe@CdS 2.5 CSQDs but not in CdSe@CdS 3.5 and CdSe@CdS 4.5 CSQDs.

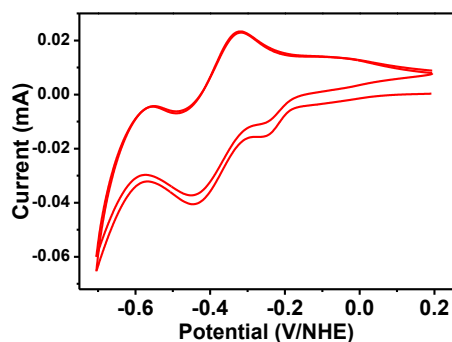


**Figure 4-6.** Redox potential of EDTA with respect to NHE in water.

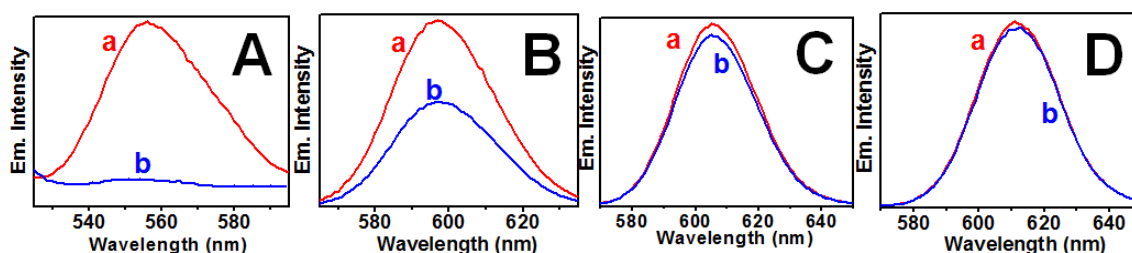


**Figure 4-7.** Steady state luminescence spectra of CdSe QDs and CdSe/CdS CSQDs with (b) and without EDTA (a). (A) CdSe QDs (B) CdSe@CdS 2.5 (C) CdSe@CdS 3.5 (D) CdSe@CdS 4.5 CSQDs.

As observed in steady state measurements that ET from QDs and CSQDs to uranium is thermodynamically favourable, to confirm this process and to understand the effect of shell thickness on ET rate, time resolved studies were carried out by exciting the samples at 445 nm laser light and monitoring the emission at emission maxima positions (600, 610 and 620 nm for CdSe@CdS 2.5, CdSe@CdS 3.5 and CdSe@CdS 4.5 respectively) and are shown in Figure 4-8. It is clearly seen from Figure 4-8 that luminescence decay trace becomes faster on

the addition of uranium at high concentrations, suggesting ET process from QDs to uranium (Figure 4-8A, c, d) however, at low concentrations the decay trace is almost similar to that of pure CSQDs. A similar observation has also been observed for pure CdSe QDs as shown in Figure 4-3C. ET rate from QDs to uranium and CSQDs to uranium was determined using equation 4-1.

$$k_{ET} = 1/\tau_{QD/uranium} - 1/\tau_{QD} = 1/\tau_{ET} \quad (4-1)$$

where  $k_{ET}$  is ET rate,  $\tau_{QD/uranium}$  is the lifetime of QDs/uranium composite and  $\tau_{QD}$  is the lifetime of pure QDs. Since  $\tau_{QD/uranium}$  is pulse width limited, therefore  $k_{ET}$  could not be determined correctly for QDs/uranium composite system.  $k_{ET}$  in CSQDs/uranium composite systems have been determined and is given in Table 4-3. Logarithm of ET rate as a function

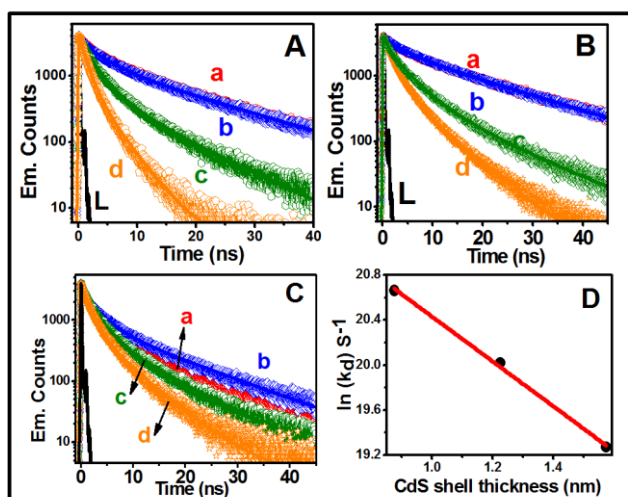


**Figure 4-8.** Time resolved emission spectra of (A) CdSe@CdS 2.5 ( $\lambda_{em} = 600$  nm), (B) CdSe@CdS 3.5 ( $\lambda_{em} = 610$  nm) and, (C) CdSe@CdS 4.5 (a) Pure CSQDs (b) QDs/100 nM uranium (c) QDs/10  $\mu$ M uranium (d) QDs/100  $\mu$ M uranium (L) Lamp profile.  $\lambda_{ex} = 445$  nm. (D) Plot of ET rate as a function of CdS shell thickness.

of CdS shell thickness was plotted and shown in Figure 4-8D. It was observed that ET rate decreases exponentially with the thickness of CdS shell and can be fitted using equation 4-2.

$$k(d) = k_0 e^{-\beta d} \quad (4-2)$$

where  $k_0$  is the ET rate for bare QDs,  $k(d)$  is the ET rate as a function of shell thickness,  $\beta$  is the decay constant and  $d$  is CdS shell thickness.  $\beta$  and  $k_0$  value for the present study is calculated to be  $1.98 \text{ nm}^{-1}$  and  $5 \times 10^9 \text{ S}^{-1}$ . Thickness dependence ET dynamics in CdSe/CdS CSQDs with methyl viologen was earlier demonstrated by Jia et. al.<sup>307</sup>. They have also observed that ET rate decreases exponentially with increase in CdS shell thickness.

As the main aim of the present investigation is to detect uranium by fluorescence quenching of QDs and CSQDs and to study the mechanism of detection. It is already demonstrated that the ET process from QDs and CSQDs to uranium is responsible for detection. Now to determine the sensitivity of these QDs and CSQDs for uranium, steady state emission studies were performed with the different concentration of uranium. Here it is important to mention that the sensitivity was determined only for CdSe@CdS 3.5 and CdSe@CdS 4.5 CSQDs but not for CdSe QDs and CdSe@CdS 2.5 CSQDs because in former only luminescence quenching was observed, however in later both quenching and surface modification was observed which makes the analysis complicated and detection unreliable. Figure 4-9A and 4-9B shows the emission spectra of CdSe@CdS 3.5 and CdSe@CdS 4.5 CSQDs with different concentrations of uranium. It is clear from Figure 4-9A and 4-9B that with increase uranium concentration, emission intensity decreases. This decrement has been quantified using Stern-Volmer equation as given below

$$I_0/I = 1 + K_{SV} [\text{UO}_2^{2+}] \quad (4-3)$$

where  $I_0$  and  $I$  are the photoluminescence intensities of CSQDs in absence and presence of  $\text{UO}_2^{2+}$  ions,  $K_{SV}$  is the Stern-Volmer luminescence quenching constant and  $[\text{UO}_2^{2+}]$  is the concentration of uranyl ions. Stern-Volmer plot for CdSe@CdS 3.5 and CdSe@CdS 4.5 CSQDs with uranium is shown in Figure 4-9A and 4-9B inset. A linear relationship between  $\text{UO}_2^{2+}$  concentrations and  $I_0/I$  was observed, with sensitivity 0.169, 0.106 l/mg for CdSe@CdS 3.5 and CdSe@CdS 4.5 CSQDs respectively. From this, limit of detection (LoD)

was calculated as shown below and is found to be 74.5 and 140 ppb for CdSe@CdS 3.5 and CdSe@CdS 4.5 CSQDs respectively.

$$\text{LoD} = 3\sigma/\text{the slope of the calibration curve}$$

where  $\sigma$  corresponds to the standard deviation of the photoluminescence peak.

$$\text{LoD (for CdSe@CdS 3.5)} = 3 \times 4.2 \times 10^{-3} / 0.169$$

$$= 74.5 \mu\text{g/l}$$

$$\text{Similarly, LoD (for CdSe@CdS 4.5)} = 3 \times 4.9 \times 10^{-3} / 0.105$$

$$= 140 \mu\text{g/l}$$

$$\text{Limit of Quantification (LoQ)} = 3.3 \times \text{LoD},$$

$$\text{LoQ (for CdSe@CdS 3.5)} = 3.3 \times 74.5 = 245.85 \mu\text{g/L},$$

$$\text{and LoQ (for CdSe@CdS 4.5)} = 3.3 \times 140 \mu\text{g/L} = 462 \mu\text{g/L}$$

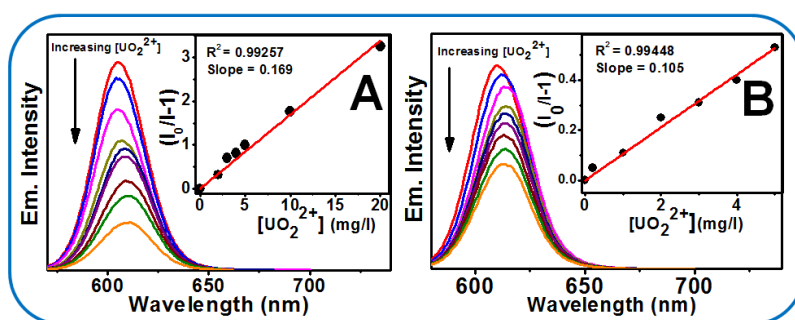


**Figure 4-9.** Emission spectra of CSQDs with different concentrations of  $\text{UO}_2^{2+}$  in DI water (A) CdSe@CdS 3.5 (B) CdSe@CdS 4.5 CSQDs. Uranium concentration increases from  $1 \mu\text{M}$  to  $100 \mu\text{M}$ . **Inset:** Stern-Volmer plot of (A) CdSe@CdS 3.5 and (B) CdSe@CdS 4.5 CSQDs with uranium.

**Table 4-4:** Photoluminescence intensities of 5 batches (A1 to A5) of CSQDs

Sample	A1	A2	A3	A4	A5	$\sigma$
CdSe@CdS 3.5	2888531.266	2888531.270	2888531.260	2888531.265	2888531.269	$4.2 \times 10^{-3}$
CdSe@CdS 4.5	2994348.311	2994348.305	2994348.315	2994348.317	2994348.308	$4.9 \times 10^{-3}$

### 4.3.2. CQDs as a probe for fluoride ion detection

The size and morphology of the CQDs were first characterized by HRTEM. HRTEM image indicates that the formed CQDs are spherical in shape with an average diameter of  $4 \pm 0.3$  nm and are well dispersed from each other as shown in Figure 4-10A. HRTEM measurement also reveals the crystalline nature of synthesized dots with a lattice spacing of 0.33 nm and is consistent with (006) diffraction plane of graphitic carbons (JCPDS 26-1076). This observation suggests that the CQDs obtained herein are of graphitic structure<sup>310</sup>. XRD pattern of synthesized dots was recorded and are shown in Figure 4-10B. XRD shows a broad diffraction peak at  $\sim 23.7^\circ$  suggesting nanoparticle formation<sup>285</sup>. FTIR spectrum was recorded to determine the surface functional groups and is shown in Figure 4-10C. FTIR spectrum

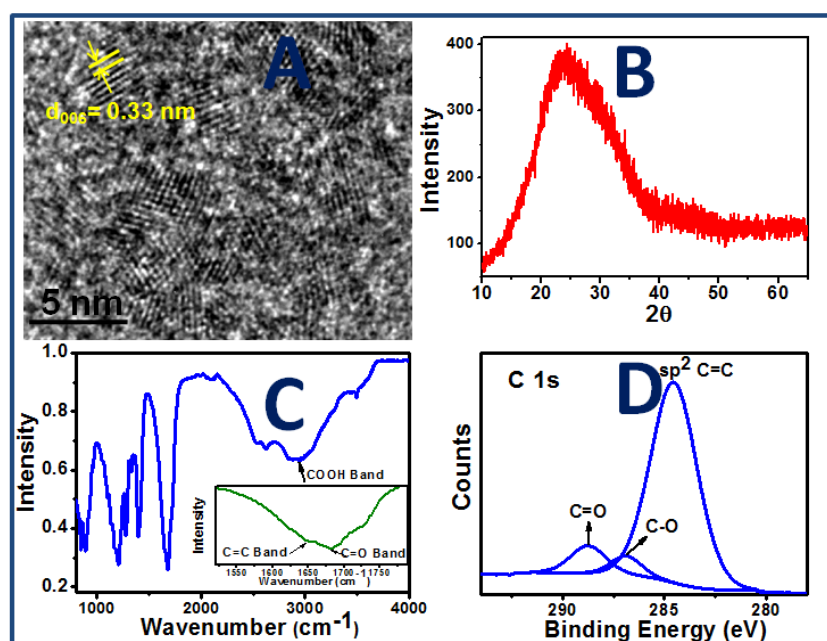


**Figure 4-10** (A). HRTEM image of CQDs, (B) XRD pattern of CQDs, (C) FTIR spectrum of CQDs, (D) Deconvoluted spectrum of C 1s XPS.

shows a very broad trough in the range of 2500-3300  $\text{cm}^{-1}$  that clearly signifies the presence of acid -OH group on the surface of CQDs. FTIR peak at 1680  $\text{cm}^{-1}$  corresponds to the carboxylic acid C=O group<sup>310</sup>, and peak at 1550  $\text{cm}^{-1}$  signifies the presence of C=C graphitic

carbon in CQDs<sup>285</sup>. FTIR data confirms that the formed CQDs are decorated with surface COOH functional groups. C 1s XPS spectrum of the synthesized dots was recorded and is shown as Figure 7-1D. Deconvoluted XPS spectrum shows three peaks at 284.5 eV, 286.9 eV and 288.8 eV corresponding to the  $sp^2$  C=C, C-O and C=O respectively<sup>311</sup>. This again confirms that the formed CQDs have a graphitic structure with surface carboxylic acid functional groups.

To determine the optical properties of these dots steady state optical absorption spectrum was recorded and is shown in Figure 4-11A, inset. Steady state optical absorption spectrum suggests that CQDs have strong absorption in UV region with a hump at 350 nm. The band at 350 nm has been assigned to the  $n-\pi^*$  transition corresponding to the carboxyl functional groups on the surface and the strong absorption below 300 nm suggests the  $\pi-\pi^*$  transition of the conjugated C=C units in the carbon core as reported earlier also<sup>285</sup>. Steady state emission spectrum was recorded by exciting the sample at different wavelengths and is

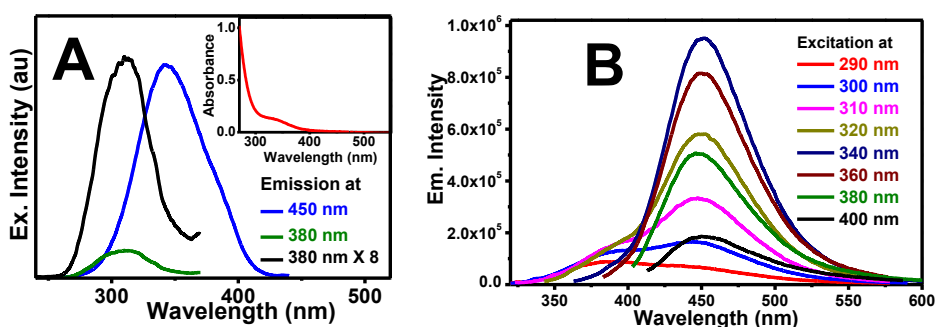


**Figure 4-11 (A).** Steady state excitation spectra of CQDs at two different emission wavelengths,  $\lambda_{em}$ - 450 nm and 380 nm. **Inset:** Steady state absorption spectrum of CQDs. **(B)**

Steady state emission spectra of CQDs at different excitation wavelengths. CQDs concentration was 50 ppm.

shown in Figure 4-11B. Steady state emission spectra clearly reveal that on photo-excitation at 290-320 nm CQDs exhibit two emission bands peaking at 385 nm and 450 nm. However,

the emission band at 385 nm vanishes as the sample was excited at wavelengths greater than 340 nm. The excitation spectrum of these dots was also recorded to find the states responsible for emission and are shown in Figure 4-11A. Excitation spectra indicate the presence of two bands peaking at 310 nm and 343 nm that corresponds to the  $\lambda_{em}$  385 and 450 nm respectively. This suggests that the emission band at 385 nm corresponds to  $\pi$ - $\pi^*$  transition of the conjugated C=C units in the carbon core whereas the emission band at 450 nm corresponds to the  $n$ - $\pi^*$  transition of carboxyl functional groups on the surface of CQDs. It is interesting to observe from Figure 4-11B that the emission intensity at 385 nm is much less as compared to at 450 nm. It shows that the surface state emission dominates over core emission in the synthesized dots. Another feature to be noted from Figure 4-11B is that there is no change in the emission peak position as the excitation wavelength is changed. Earlier many authors have carried out similar studies where they have shown that the emission spectra of CQDs are a function of excitation wavelength and both position as well as intensity changes with a change in excitation wavelength<sup>285, 286, 292, 293, 312</sup>. They have suggested that such a change in position is due to the different size of CQDs present in the sample<sup>286, 312</sup>. However, in the present investigation, only emission intensity changes with a change in excitation wavelengths while no change in emission position was observed. This observation further suggests that the synthesized dots are nearly monodisperse in nature and have a similar type of emissive surface defects.

As mentioned above that the main aim was to use these CQDs for fluoride ion detection. For this, the first interaction of CQDs with  $\text{Eu}^{3+}$  was monitored. Since  $\text{Eu}^{3+}$  is a hard acid, it can interact with a hard base, fluoride ion and a fluoride ion sensitive probe can be realized. Earlier few reports were available for fluoride ion detection<sup>63, 313</sup> based on this interaction. Butler<sup>63</sup> have used two different complexes of europium for the detection of fluoride ion. However, the synthesis of these complexes was a challenging task. Singh et

al.<sup>313</sup> have proposed CdTe QDs coupled  $\text{Eu}^{3+}$  system for selective detection of fluoride ions. However, the toxicity of cadmium based QDs are well known and their application in a real environment is a question of debate. To overcome these difficulties and realizing a more economical and environmental friendly probe, a coupled system of CQDs with  $\text{Eu}^{3+}$  was chosen and steady state absorption and emission studies were carried out. Steady state absorption studies suggest no complex formation between CQDs and  $\text{Eu}^{3+}$  as shown in Figure 4-12. Steady state emission studies were carried out by exciting the samples at two different wavelengths and monitoring the emission. Figure 4-13A shows the steady state luminescence spectra of CQDs with different concentrations of  $\text{Eu}^{3+}$  by exciting the samples at 280 nm corresponding to the carbon core excitation and monitoring the emission. It is interesting to observe from Figure 4-13A that on an addition of  $\text{Eu}^{3+}$  emission intensity decreases. Similar

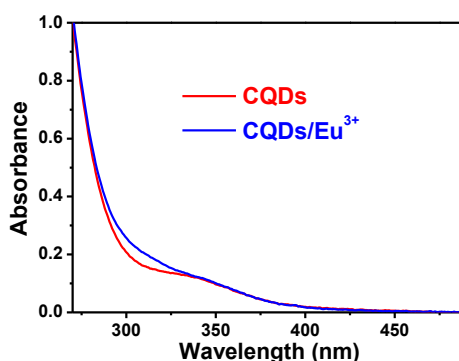


**Figure 4-12.** Steady state absorption spectra of CQDs and CQDs/ $\text{Eu}^{3+}$  complex.

studies were also carried out by exciting the samples at 340 nm corresponding to the surface state excitation and monitoring the emission and is shown in Figure 4-13B. There also decrement in emission intensity on an addition of  $\text{Eu}^{3+}$  was observed. However, the decrement was more in surface state emission as compared to core emission. These results were compared and shown in Figure 4-13C. From Figure 4-13C it is clear that the effect of  $\text{Eu}^{3+}$  addition is more pronounced in surface state emission as compared to core emission. Earlier Singh et al.<sup>313</sup> have also carried out similar studies where they have monitored a

quenching in CdTe QDs emission after interaction with  $\text{Eu}^{3+}$  and assigned to the aggregation of QDs. In the present study also similar features were observed. Earlier many authors demonstrated that CQDs are excellent electron donors and used them in a variety of applications<sup>292, 314, 315</sup>. Das et al.<sup>292</sup> have used these dots for degradation of organic pollutants where they have shown that ET from CQDs to pollutants is responsible for degradation. Zhou et al.<sup>296</sup> have used CQDs for detection of  $\text{Hg}^{2+}$  ions. They have shown that ET process from CQDs to  $\text{Hg}^{2+}$  ions leads to luminescence quenching of CQDs. Wang et al.<sup>314</sup> have demonstrated the application of these dots for detection of different derivatives of toluene and for photo-conversion of  $\text{Ag}^+$  to Ag through ET process from CQDs. In the present study also decrement in luminescence intensity of both core and surface state on an addition of  $\text{Eu}^{3+}$  was observed and might be due to ET process from CQDs to  $\text{Eu}^{3+}$ .

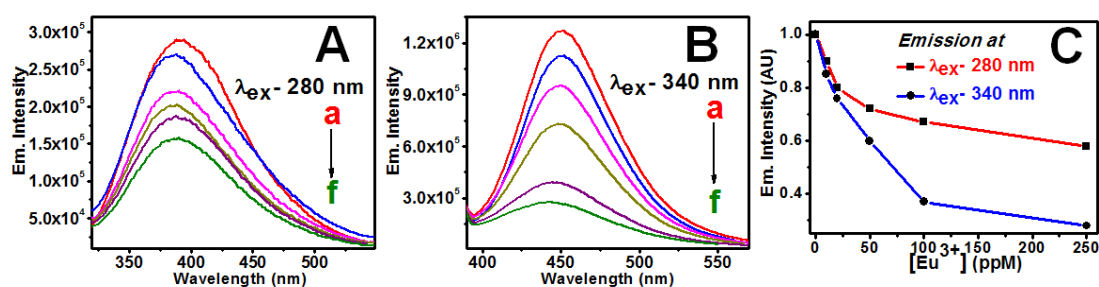


**Figure 4-13 (A) and (B).** Steady state emission spectrum of CQDs in absence and presence of different concentration of  $\text{Eu}^{3+}$  (A)  $\lambda_{\text{ex}}$ - 280 nm, (B)  $\lambda_{\text{ex}}$ - 340 nm, (a)  $[\text{Eu}^{3+}] = 0$  ppm (b)  $[\text{Eu}^{3+}] = 10$  ppm, (c)  $[\text{Eu}^{3+}] = 20$  ppm, (d)  $[\text{Eu}^{3+}] = 50$  ppm, (e)  $[\text{Eu}^{3+}] = 100$  ppm, (f)  $[\text{Eu}^{3+}] = 250$  ppm. (C) Comparison of emission intensity of CQDs on addition of  $\text{Eu}^{3+}$  at two different excitation wavelengths,  $\lambda_{\text{ex}}$ - 280 nm and  $\lambda_{\text{ex}}$ - 340 nm. CQDs concentration for all above experiments was 50 ppm.

To demonstrate this, time resolved emission studies were carried out and are shown as Figure 4-14A and 4-14B. Figure 4-14A shows the time resolved emission decay traces of CQDs in the absence and in presence of  $\text{Eu}^{3+}$  by exciting the samples at 292 nm and monitoring the

emission at 340 nm that corresponds to core state excitation and emission respectively. It is interesting to observe from Figure 4-14A that on an addition of  $\text{Eu}^{3+}$ , emission decay traces are faster (Figure 4-14A, b, and 4-14A, c) as compared to pure CQDs (Figure 4-14A, a). This observation suggests that ET process from CQDs to  $\text{Eu}^{3+}$  is favourable thereby, a faster emission decay trace on an addition of  $\text{Eu}^{3+}$  was observed. Similar studies were also carried out by exciting the samples at 374 nm and monitoring the emission at 450 nm that corresponds to surface state excitation and emission respectively and are shown in Figure 4-14B. Here also faster emission decay trace on an addition of  $\text{Eu}^{3+}$  (Figure 4-14B, b and 4-14B, c) as compared to without  $\text{Eu}^{3+}$  addition (Figure 4-14B, a) was observed. This again suggests ET process from CQDs to  $\text{Eu}^{3+}$ . Now it is interesting to observe from Figure 4-14A and 4-14B that the luminescence decay trace at the surface state (Figure 4-14B) is much faster as compared to at the core state (Figure 4-14A). Similar behaviours were also observed in steady state luminescence study where more decrement in surface state luminescence as compared to core state luminescence was observed after  $\text{Eu}^{3+}$  addition (Figure 4-14C). As understood that ET is a distance dependent phenomenon and the rate of ET decreases as distance increases<sup>307</sup>. The faster decay in surface state emission as compared to core state might be due to less distance of ET in former as compared to later. Now to check the feasibility of another mechanism that is the aggregation of CQDs on an addition of  $\text{Eu}^{3+}$ , zeta potential measurements of CQDs in absence and in the presence of  $\text{Eu}^{3+}$  were carried out and are given in Table 4-5. Zeta potential value for pure CQDs suggests that the surface charge is negative. The negative surface charge is due to the presence of COOH groups present on CQDs surface. This negative charge allows CQDs to be well separated from each other and chances of aggregation will be minimum as suggested by HRTEM measurements also (Figure 4-10A). Now on the addition of  $\text{Eu}^{3+}$  surface charge decreases and becomes very less as given in Table 4-5. This suggests the interaction of  $\text{Eu}^{3+}$  ions with the surface COOH

groups. After  $\text{Eu}^{3+}$  addition CQDs interact with each other via  $\text{Eu}^{3+}$  thereby leading to an aggregation of CQDs. This is confirmed by taking HRTEM image of CQDs after  $\text{Eu}^{3+}$  addition and is shown as Figure 4-14C. HRTEM measurement clearly shows aggregation of CQDs after  $\text{Eu}^{3+}$  addition. The similar observation was also supported by steady state absorption studies where on an addition of  $\text{Eu}^{3+}$ , the surface absorption peak shape changes and becomes less confined suggesting an interaction of  $\text{Eu}^{3+}$  with COOH functional groups on CQDs surface (Figure 4-12). This observation suggests that the faster luminescence quenching of surface state as compared to core state is also due to aggregation of CQDs on an addition of  $\text{Eu}^{3+}$ . Therefore in present investigation, both ET and aggregation are responsible for surface state luminescence quenching of CQDs on an addition of  $\text{Eu}^{3+}$ . These processes are shown diagrammatically in Scheme 4-2. On photoexcitation of CQDs both core, as well

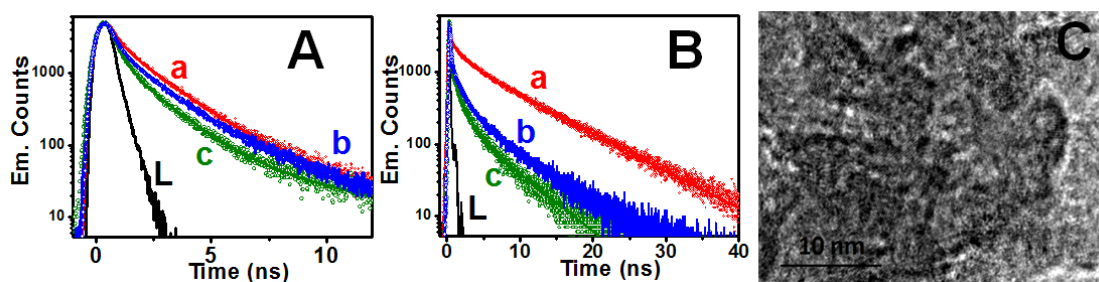
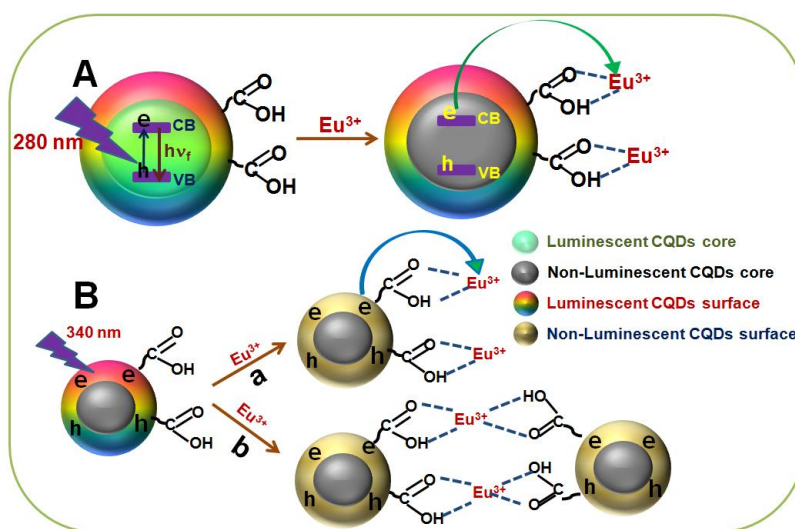


**Figure 4-14 (A) and (B).** Time resolved emission decay trace of CQDs in presence of  $\text{Eu}^{3+}$ , (A)  $\lambda_{\text{ex}} = 292 \text{ nm}$ ,  $\lambda_{\text{em}} = 340 \text{ nm}$ , (B)  $\lambda_{\text{ex}} = 374 \text{ nm}$ ,  $\lambda_{\text{em}} = 450 \text{ nm}$ , (a) pure CQDs, (b) CQDs + 50 ppm  $\text{Eu}^{3+}$ , (c) CQDs + 250 ppm  $\text{Eu}^{3+}$ . CQDs concentration for all the above experiments was 50 ppm. **C:** HRTEM image of CQDs on an addition of 2500 ppm of  $\text{Eu}^{3+}$ . CQDs concentration for HRTEM measurements was 500 ppm.

**Table 4-5:** Zeta potential values of CQDs in presence and absence of  $\text{Eu}^{3+}$  and fluoride ions.

Concentration ratio [CQDs: $\text{Eu}^{3+}$ ]	Zeta Potential (mV)	Concentration ratio [CQDs: $\text{Eu}^{3+}$ : $\text{F}^-$ ]	Zeta Potential (mV)
No $\text{Eu}^{3+}$ addition	$-145 \pm 15$	No $\text{Eu}^{3+}$ and $\text{F}^-$ addition	$-145 \pm 15$
2.5:1	$-10 \pm 1$	2.5:1:1	$-70 \pm 5$
1:1	$9 \pm 1$	1:1:1	$-10 \pm 1$
1:2	$20 \pm 3$	1:2	$2 \pm 3$

as surface state, will be excited as shown in Scheme 4-2A and 4-2B respectively. Now on  $\text{Eu}^{3+}$  addition luminescence quenching occurs however only ET from CQDs to  $\text{Eu}^{3+}$  is responsible for core state luminescence quenching as shown in Scheme 4-2A while both ET as well as aggregation are responsible for surface state luminescence quenching as shown in Scheme 4-2B. The aggregation induced luminescence quenching effects will be pronounced at surface state position but not in the core as  $\text{Eu}^{3+}$  binds to the surface COOH groups of CQDs as shown in Scheme 4-2B and confirmed by zeta potential and HRTEM studies (Figure 4-14C). Earlier many authors have shown the quenching of QDs luminescence in presence of foreign ions<sup>51, 285, 294, 313</sup> and assigned either to the CT process or aggregation but in present investigation it was observed that both the mechanisms are responsible for luminescence quenching.



**Scheme 4-2.** CQDs and its interaction with  $\text{Eu}^{3+}$ . (A) Photoexcitation of core state of CQDs and subsequent electron transfer to  $\text{Eu}^{3+}$  (B) Photoexcitation of surface state of CQDs and subsequent electron transfer to  $\text{Eu}^{3+}$  (a) and aggregation of CQDs on  $\text{Eu}^{3+}$  addition (b).

As demonstrated above that on an addition of  $\text{Eu}^{3+}$  ions photoluminescence of CQDs quenches (*off*). This system was used as a photoluminescent *on-off-on* probe for detection of fluoride ions. As already shown that the surface state is more luminescent as compared to

core state (Figure 4-11). Also, the effect of  $\text{Eu}^{3+}$  addition is much more pronounced in the surface state as compared to core state. Taking into account both of these factors steady state photoluminescence experiment of CQDs/ $\text{Eu}^{3+}$  system with fluoride ions was carried out by exciting the surface state. Here it is important to mention that for fluoride ion detection, 1:1 concentration ratio of CQDs: $\text{Eu}^{3+}$  was chosen. Although, experiments were carried out with a higher concentration of  $\text{Eu}^{3+}$  also, satisfactory results were not obtained and change in luminescence intensity was marginal on an addition of low concentration of fluoride ion. Therefore, a concentration ratio of 1:1 of CQDs and  $\text{Eu}^{3+}$  was chosen. Figure 4-15A shows the change in photoluminescence intensity of CQDs/ $\text{Eu}^{3+}$  system on an addition of fluoride ions. It is interesting to observe from Figure 4-15A that the luminescence intensity increases with increase in concentrations of fluoride ion. This observation suggests that on an addition of fluoride ions CQDs restores its photoluminescence properties (*on*) and this change in luminescence intensity can be used to quantify fluoride ion concentrations. The corresponding calibration curve was also plotted and is shown in Figure 4-15B. It is worthy to note from Figure 4-15B that the calibration curve shows linearity in the concentration range 1-25 ppm of fluoride ion with  $R^2$  value of 0.991. Photoluminescence intensity of pure CQDs on an addition of fluoride ion was also monitored and is shown in Figure 4-16. From Figure 4-16 it is clear that there is no effect of only fluoride ion addition in CQDs emission intensity. This observation suggests that the interaction between fluoride ions and  $\text{Eu}^{3+}$  is involved in using CQDs as a probe for fluoride ion detection. To validate it further, experiments were carried out with a higher concentration of fluoride ions (>50 ppm). Interestingly a precipitate formation was observed in CQDs/ $\text{Eu}^{3+}$  sample after adding higher concentrations of fluoride ion. The precipitate was separated and its XRD pattern was recorded and are shown as Figure 4-17A. XRD pattern shows the formation of  $\text{EuF}_3$  in the sample. This observation further suggests that fluoride ion interacts with  $\text{Eu}^{3+}$  leading to the

formation of  $\text{EuF}_3$  as shown in Figure 4-15 bottom panel. TEM image of CQDs/ $\text{Eu}^{3+}$  with 100 ppm fluoride ion was also taken and are shown as Figure 4-17B, inset. TEM image shows the formation of needle shaped crystal of  $\text{EuF}_3$ . HRTEM image of these crystals is shown in Figure 4-17B that again confirms the formation of  $\text{EuF}_3$ . These observations clearly suggest that fluoride ion interact with the  $\text{Eu}^{3+}$  ions bonded with CQDs surface and form

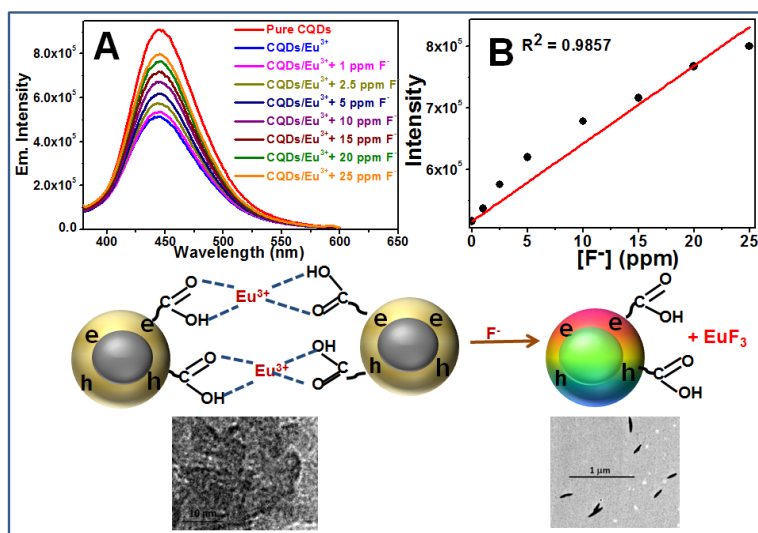


**Figure 4-15 (A).** Photoluminescence spectra of CQDs- $\text{Eu}^{3+}$  with an increase in the concentration of fluoride ion in water. **(B)** Respective graphical relationship of the Photoluminescence intensity against the concentration of fluoride ion. CQDs and  $\text{Eu}^{3+}$  concentration are 50 ppm each. The bottom panel shows the mechanism of interaction involved.

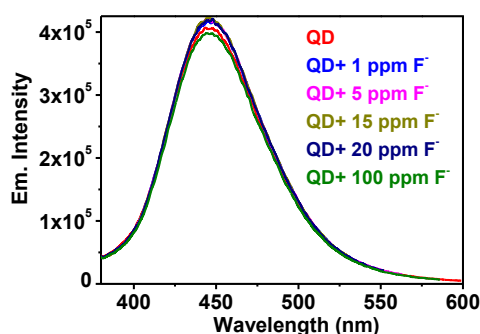


**Figure 4-16.** Photoluminescence spectra of CQDs with increase in the concentration of fluoride ion in water. CQDs concentration is 50 ppm.

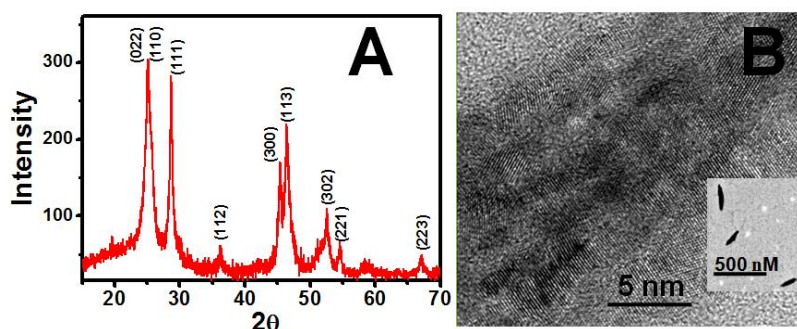


**Figure 4-17 (A).** XRD pattern of  $\text{EuF}_3$ , **(B)** HRTEM image of  $\text{EuF}_3$ . **(B) Inset:** TEM image of  $\text{EuF}_3$ .

$\text{EuF}_3$ . This leads to the removal of  $\text{Eu}^{3+}$  from the surface of CQDs thereby, an increment in luminescence intensity of CQDs/ $\text{Eu}^{3+}$  after addition of fluoride ion was observed. Elemental analysis of the precipitate was also carried out that shows the presence of europium and fluoride in the sample. To support it further zeta potential value after fluoride ion addition was measured and are given in Table 4-5. Zeta potential value of CQDs/ $\text{Eu}^{3+}$  becomes negative after fluoride addition that clearly suggests that fluoride ion take away  $\text{Eu}^{3+}$  from CQDs surface thereby surface charge again becomes negative. Earlier Singh et al.<sup>313</sup> have also used the similar strategy for fluoride ion detection. However, they have used cadmium based QDs and the toxicity of cadmium is well known. Therefore, their application in a real environment is a question of debate. Here carbon based QDs were used that are completely green and cost effective. Therefore, using CQDs as a probe is both environmentally and economically more appreciable as compared to cadmium based QDs.

As mentioned that CQDs coupled  $\text{Eu}^{3+}$  system can be used for the detection of fluoride ions, but in any environmental sample lot of other competing ions are also present. Therefore, to find the selectivity of the suggested probe for fluoride ion detection, steady state luminescence measurements of CQDs/ $\text{Eu}^{3+}$  in presence of other major competing ions such as  $\text{Cl}^-$ ,  $\text{Br}^-$ ,  $\text{I}^-$ ,  $\text{NO}_3^-$ ,  $\text{CH}_3\text{COO}^-$  and  $\text{NO}_3^-$  were carried out and are shown as Figure 4-18. It is

interesting to observe from Figure 4-18 that only in presence of fluoride ion, luminescence intensity recovers to its original position while in presence of other ions such changes were not observed. This observation suggests that the suggested probe is selective for fluoride ion and can be used to detect fluoride ion in environmental samples. This high specificity could be attributed to the specific and strong interaction of  $\text{Eu}^{3+}$  towards fluoride ion as compared to other ions. The probe was also tested for the detection of fluoride ion in toothpaste sample.

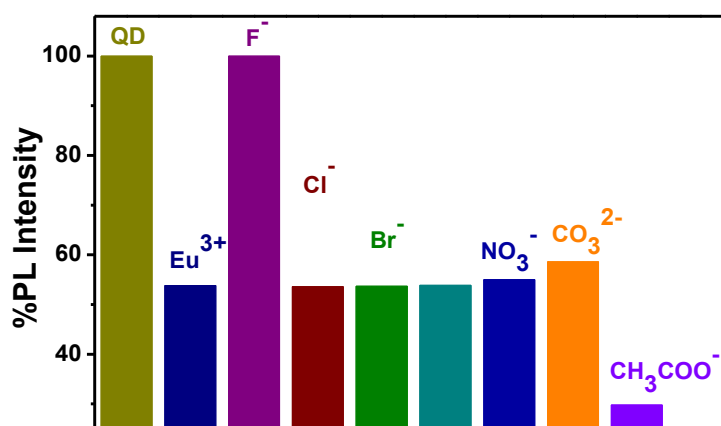


**Figure 4-18.** Bar diagram for the selectivity test results obtained with the addition of different anions into the CQDs/ $\text{Eu}^{3+}$  system. CQDs and  $\text{Eu}^{3+}$  concentration are 50 ppm each. Concentrations of anions are 100 ppm each.

For this 1 g toothpaste was accurately weighed and dissolved in 30.0 ml water and stirred at  $70^\circ\text{C}$  for 3 h in a polypropylene vessel. The resulting solution was cooled to room temperature and then filtered with a membrane filter (pore size 0.45  $\mu\text{m}$ ) to eliminate solids in suspension. The insoluble part was washed several times with water, and the resulting solution was diluted to 200 ml with water for further use. The concentration of fluoride ion in the sample was observed to be  $\sim 350 \pm 20 \mu\text{M}$  that matches well with the result obtained from IC  $\sim 380 \pm 10 \mu\text{M}$ .

#### 4.4. Conclusions

To conclude, in the first part of this chapter, oleic acid capped CdSe and CdSe/CdS CSQDs with three different thicknesses of CdS shell were synthesized and characterized. Ligand exchange experiments with MPA were performed to make these QDs and CSQDs water dispersible. The as synthesized QDs and CSQDs were tested for uranium detection at trace level by fluorescence quenching of QDs and CSQDs. Interestingly on an addition of uranium at low concentrations ( $<1 \mu\text{M}$ ), an increment in luminescence intensity was observed in both CdSe QDs and CdSe@CdS 2.5 CSQDs however, no such behaviours were observed in CdSe@CdS 3.5 and CdSe@CdS 4.5 CSQDs. At high concentration of uranium, luminescence quenching was observed in all four QDs and CSQDs. Zeta potential measurements were have carried out which confirm the binding of uranium with QDs and CSQDs. Time resolved studies confirm that the mechanism of luminescence quenching is ET process from QDs and CSQDs to uranium. Stern-Volmer plot suggests that the LoD of this method is 74.5 ppb. To the best of our knowledge, this is the first report where an ultra trace level detection of uranium using quasi type II CSQDs has been demonstrated and a clear mechanism for interaction has been given. This in turn, will help to design more efficient systems for detection.

The second part of this chapter demonstrates a green, economic, rapid, sensitive, and specific photoluminescent *on-off-on* probe for the detection of fluoride ions. The probe is based on CQDs and  $\text{Eu}^{3+}$  where a clear explanation on the working principle of the probe was mentioned. On an addition of  $\text{Eu}^{3+}$  ions photoluminescence of CQDs quenched (*switch-off*). This has been assigned to the both ET from CQDs to  $\text{Eu}^{3+}$  ions and aggregation of CQDs on addition of  $\text{Eu}^{3+}$  and is confirmed by the time resolved measurements and HRTEM studies respectively. Interestingly on an addition of fluoride ions luminescence intensity again increases (*switch-on*). This has been assigned to the formation of  $\text{EuF}_3$  that has subsequently

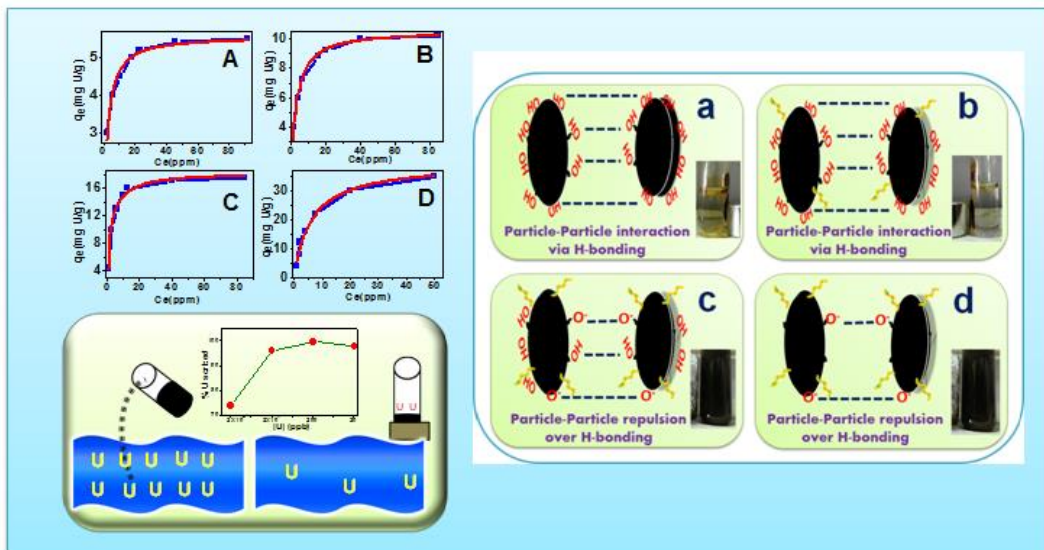
been confirmed by XRD and HRTEM measurements. Furthermore, the probe is found to be selective for fluoride ions and was also tested for the real sample. To the best of our knowledge, this is the first report where CQDs coupled  $\text{Eu}^{3+}$  system is used as a photoluminescent probe for speedy and specific sensing of fluoride ions. The suggested probe is environmental friendly and cost effective and allows the detection of fluoride ions in real environmental samples.





# CHAPTER-5

## Metal Ion Extraction Using Magnetic and Functionalized Magnetic Nanoparticles



➤ *Journal of Hazardous Materials* 335, 2017, 152-161



### 5.1. Introduction

Energy crises is one of the major issue now days, as the major source of energy coal is depleting very fast. At the same time use of coal involves the emission of toxic gases which leads to the climate change. Therefore, to meet the future energy demand and transform the world's energy systems to combat climate change, it is utmost important to explore the other alternative sources of energy which are clean and do not have any detrimental effect on the environment<sup>2</sup>. It includes solar energy, wind energy, tidal energy, nuclear energy, hydrothermal energy, etc. and a lot of research is going on to develop these alternative and clean sources of energy. Out of these nuclear power plants are one of the economical and carbon-free energy sources<sup>316</sup>. Countries like France and Ukraine produce 76.3 and 56.5% respectively<sup>317</sup>, of their total energy requirement from nuclear energy only. However, the sustainability of any nuclear energy programme depends upon the availability of nuclear fuel and uranium is one of the key elements for that purpose. Most of the nuclear reactors worldwide use uranium as fuel. For this purpose it is extremely important to extract uranium from different matrices. Sea water is considered as one of the largest source of uranium. Around 4.5 billion metric tons of uranium is present in sea water which is approximately 1000 times larger than the amount of uranium in terrestrial ores<sup>30, 318, 319</sup>. Hence the extraction of uranium from seawater can be an attractive solution to supply future nuclear fuel feeds. However the major problem with this is the presence of other competing ions and low concentration of uranium ( $\sim 3.3$  ppb)<sup>319, 320</sup>. Both these factors lead to the extraction of uranium from sea water matrix highly difficult and challenging and different strategies are being employed to accomplish this. Except the use of uranium in nuclear fuel it is also one of the most toxic heavy metal<sup>261, 321</sup> and its removal from environmental matrix is necessary if the concentration is above certain limits<sup>30</sup>.

Now days a number of materials have been developed to extract uranium and from different environmental matrices<sup>30, 322-332</sup>. It includes ion exchangers<sup>30</sup>, polymers<sup>322-324, 326, 330, 331</sup>, composite materials<sup>325, 327, 329, 332</sup> etc. However, in most of the cases either the experiments were carried out with simulated sea water<sup>322, 323, 325-327, 329</sup> or in presence of higher (~ppm) concentration of uranium<sup>322, 325-327, 332</sup>. Both these factors alter the real sea water conditions and therefore the potential of such materials to be used directly in sea water is uncertain and has to be investigated. Recently a number of ligands containing amidoxime binding moiety has been investigated for extraction of uranium from sea water<sup>324, 333</sup>. It has been observed that sorption upto 3.3 g U/kg sorbent is achievable in marine test using these ligands but the method is costly as well as high sorption of other seawater cations (e.g., vanadium) is a problem<sup>333</sup>. Manos and Kanatzidis<sup>30</sup> have shown the use of layered metal sulphides for uranium extraction from sea water but studies are limited and a lot of work is still needed in this direction. Ling and Zhang<sup>334</sup> have shown the use of Fe nanoparticles (NPs) for the extraction of uranium from sea water simulator at a concentration of ~2.3 ppb. All these studies suggests that a lot of work is still needed to find an eco-friendly and cost effective sorbent with high sorption capacity for uranium from sea water matrix.

Recently magnetic NPs got a lot of attention because of their low toxicity and superparamagnetic properties<sup>82, 83</sup>. They are used in number of application including catalysis<sup>83, 86</sup>, biotechnology/biomedicine<sup>84, 85</sup>, magnetic resonance imaging<sup>87</sup>, data storage<sup>88</sup> and environmental remediation<sup>89-93</sup>, etc. These NPs are also being used for the extraction of uranium<sup>335-344</sup>, however limited studies have been done and to the best of our knowledge till now no report is available on the extraction of uranium from sea water using magnetic NPs. One of the most important properties of magnetic NPs which make them suitable for use as compared to other materials is their magnetic behaviour. Bare superparamagnetic NPs such as Fe<sub>3</sub>O<sub>4</sub> can be dispersible in water because of the repulsion between particles that possess

like charges on surface, small size and non-magnetic at zero magnetic field. Under external magnetic field, these supermagnetic NPs tend to agglomerate because of magnetic dipole interaction. Also, NPs have high surface area as well as pores. Many metal ions and dyes can be sorbed over the NPs surface as well as they can occupy pores or lattice sites of NPs. Such incorporated/ adsorbed NPs can be attracted towards the magnetic field and this concept can be used for removal of toxic materials from the environment.

In this chapter,  $\text{Fe}_3\text{O}_4$  and humic acid (HA) coated  $\text{Fe}_3\text{O}_4$  NPs were synthesized and their applicability for uranium extraction from water and sea water matrix was demonstrated. Strong complexation ability of HA can change the binding capacity and sorption characteristics<sup>93, 345, 346</sup> of NPs for uranium. Effect of uranium concentration and HA coating on sorption characteristics has been evaluated. Experiments were also conducted with different amount of NPs to determine the minimum amount required for maximum sorption. Effect of HA coating on particle settlement was also studied.

## **5.2. Experimental**

### **5.2.1. Materials**

Ferric chloride hexahydrate ( $\text{FeCl}_3 \cdot 6\text{H}_2\text{O}$ ), HA were procured from Aldrich. Ferrous sulphate heptahydrate ( $\text{FeSO}_4 \cdot 7\text{H}_2\text{O}$ ) was procured from SISCO research laboratories. AR grade sodium hydroxide (NaOH), ammonium hydroxide ( $\text{NH}_4\text{OH}$ ) and sodium chloride (NaCl) was used. All chemicals were used without further purification. Nanopure water was used to make samples of different concentrations and pH.

### **5.2.2. Synthesis of $\text{Fe}_3\text{O}_4$ NPs.**

$\text{Fe}_3\text{O}_4$  NPs were synthesised by co-precipitation route as reported earlier<sup>93</sup> with slight modification. In brief 15.2 g of  $\text{FeCl}_3 \cdot 6\text{H}_2\text{O}$  and 7.7 g of  $\text{FeSO}_4 \cdot 7\text{H}_2\text{O}$  were added in 300 ml of water. The solution was stirred continuously followed by the addition of 25 ml of  $\text{NH}_3$ . An

immediate colour change from red to black was observed indicating the formation of Fe<sub>3</sub>O<sub>4</sub> NPs. The solution was heated to 90 °C for 30 min and then cool down to room temperature. The black precipitate of Fe<sub>3</sub>O<sub>4</sub> NPs was collected using a magnet. Supernatant was decanted and particle was washed 3 times with Milli-Q water to remove excess ammonia and finally with acetone to remove the excess water present.

### 5.2.3. Synthesis of HA coated Fe<sub>3</sub>O<sub>4</sub> NPs.

HA coated Fe<sub>3</sub>O<sub>4</sub> NPs were synthesized using reported procedure with slight modification<sup>93</sup>. Different amount of HA were added to the reaction mixture to synthesize Fe<sub>3</sub>O<sub>4</sub> NPs with variable coating of HA. 15.2 g of FeCl<sub>3</sub>.6H<sub>2</sub>O and 7.7 g of FeSO<sub>4</sub>.7H<sub>2</sub>O were added in 300 ml of water. The solution was stirred continuously followed by the addition of 25 ml of NH<sub>3</sub>. A solution of HA (0.5, 1 and 1.5 g HA in 125 ml, 1M NaOH) was added to the reaction mixture and was heated to 90 °C for 30 min and then cool down to room temperature. A black precipitate of HA coated Fe<sub>3</sub>O<sub>4</sub> NPs was obtained which was collected using a magnet. Supernatant was decanted and particles were washed 3 times with Milli-Q water to remove excess ammonia and finally with acetone to remove excess water present. The above particles were abbreviated as Fe<sub>3</sub>O<sub>4</sub>/HA 1, Fe<sub>3</sub>O<sub>4</sub>/HA 2 and Fe<sub>3</sub>O<sub>4</sub>/HA 3 corresponding to HA amount of 0.5, 1 and 1.5 g respectively.

## 5.3. Results and Discussions

### 5.3.1. Structural and morphology studies

XRD pattern of Fe<sub>3</sub>O<sub>4</sub> NPs (Figure 5-1A, a) and HA coated Fe<sub>3</sub>O<sub>4</sub> NPs (Figure 5-1A, b, c, d) are shown in Figure 5-1A. The synthesized NPs have cubic structure with lattice parameter  $a = 8.37 \text{ \AA}$ . Average crystallite size of Fe<sub>3</sub>O<sub>4</sub> NPs and HA coated Fe<sub>3</sub>O<sub>4</sub> NPs was found to be ~15 nm and ~12 nm respectively after correcting with silicon as a standard. To confirm the coating of HA on NPs, FTIR studies have been carried out. FTIR spectra of

$\text{Fe}_3\text{O}_4$ ,  $\text{Fe}_3\text{O}_4/\text{HA}$  3 and HA are shown in Figure 5-1B. The FTIR spectrum of HA (Figure 5-1B,c) shows an intense signal centered at  $3395\text{ cm}^{-1}$  which has been assigned to the N–H/O–H stretching vibrations, confirming the presence of alcohols/phenols, amines/amides and possibly carboxylic acid<sup>347</sup>. An intense band at  $1590\text{ cm}^{-1}$  can be assigned to the C=O stretching vibration in the carboxylate function and also to the C=C stretching vibration in the aromatic ring and alkene groups. The bending vibrations of methyl and methylene groups appear at  $1370\text{ cm}^{-1}$  and the stretching vibration of the C–O bond in alcohols, phenols and ethers appears as an overlapped bands between  $1000$  and  $1200\text{ cm}^{-1}$ . Pure  $\text{Fe}_3\text{O}_4$  NPs does not show any peak at  $1030$  and  $1010\text{ cm}^{-1}$  (Figure 5-1B, a) however on HA coating on NPs, these characteristic peak appears in FTIR spectrum of  $\text{Fe}_3\text{O}_4/\text{HA}$  3 NPs as shown in Figure 5-1B, b and Figure 5-1B, inset. This confirms the coating of HA on  $\text{Fe}_3\text{O}_4$  NPs. TG analysis has been carried out in synthesized NPs and is shown in Figure 5-1C. TG analysis reveals that in

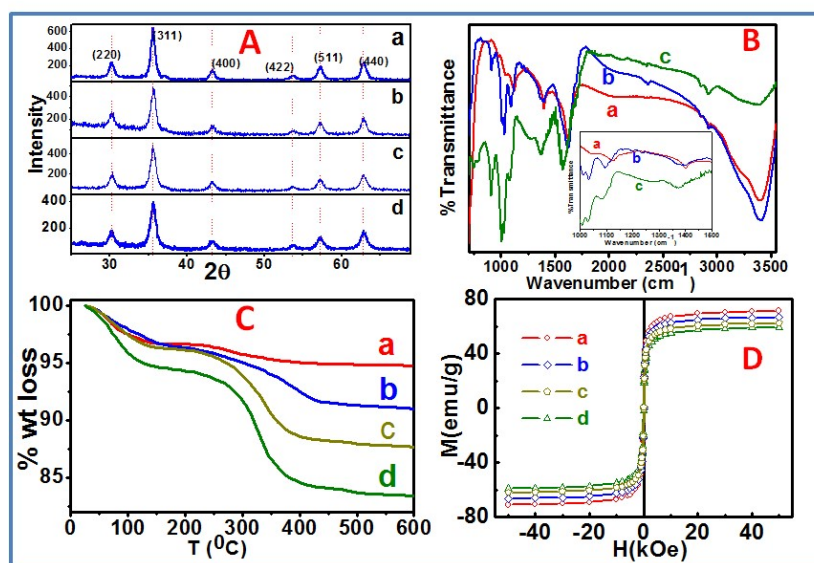


**Figure 5-1 (A).** XRD pattern of (a)  $\text{Fe}_3\text{O}_4$  (b)  $\text{Fe}_3\text{O}_4/\text{HA}$  1 (c)  $\text{Fe}_3\text{O}_4/\text{HA}$  2 (d)  $\text{Fe}_3\text{O}_4/\text{HA}$  3 NPs after correcting with silicon as a standard. **(B)** FTIR spectra of (a)  $\text{Fe}_3\text{O}_4$  (b)  $\text{Fe}_3\text{O}_4/\text{HA}$  3 NPs (c) HA. **Inset** shows the FTIR spectra of all three compounds in expanded view. **(C)** TG analysis of (a)  $\text{Fe}_3\text{O}_4$  (b)  $\text{Fe}_3\text{O}_4/\text{HA}$  1 (c)  $\text{Fe}_3\text{O}_4/\text{HA}$  2 (d)  $\text{Fe}_3\text{O}_4/\text{HA}$  3 NPs. **(D)** Magnetic measurements of (a)  $\text{Fe}_3\text{O}_4$  (b)  $\text{Fe}_3\text{O}_4/\text{HA}$  1 (c)  $\text{Fe}_3\text{O}_4/\text{HA}$  2 (d)  $\text{Fe}_3\text{O}_4/\text{HA}$  3 NPs.

$\text{Fe}_3\text{O}_4/\text{HA}$  1,  $\text{Fe}_3\text{O}_4/\text{HA}$  2 and  $\text{Fe}_3\text{O}_4/\text{HA}$  3 an appreciable weight loss occur at  $\sim 300 - 350$  °C (Figure 5-1C, b, c, d respectively) as compared in bare  $\text{Fe}_3\text{O}_4$  NPs (Figure 5-1C, a). Since HA is an organic ligand, it is expected to decompose  $\sim 300-400$  °C. This indicates a successful coating of NPs with HA. At the same time, % weight loss is more in  $\text{Fe}_3\text{O}_4/\text{HA}$  3 as compared to  $\text{Fe}_3\text{O}_4/\text{HA}$  2 and  $\text{Fe}_3\text{O}_4/\text{HA}$  1 which suggests that an increase in HA amount during synthesis results in higher surface coverage of NPs with HA. Magnetic measurements were also performed in bare  $\text{Fe}_3\text{O}_4$  and HA coated  $\text{Fe}_3\text{O}_4$  NPs. Saturation magnetization value for bare  $\text{Fe}_3\text{O}_4$  NPs was observed to be  $\sim 70$  emu/g (Figure 5-1D, a) while for  $\text{Fe}_3\text{O}_4/\text{HA}$  1,  $\text{Fe}_3\text{O}_4/\text{HA}$  2 and  $\text{Fe}_3\text{O}_4/\text{HA}$  3 the value was  $\sim 66$ ,  $\sim 63$  and  $\sim 60$  emu/g respectively (Figure 5-1D, b, c, d). This suggests that in presence of HA there is a little decrement in saturation magnetization value of  $\text{Fe}_3\text{O}_4$  NPs which again confirms the HA coating on  $\text{Fe}_3\text{O}_4$  NPs. The content of HA in  $\text{Fe}_3\text{O}_4/\text{HA}$  1,  $\text{Fe}_3\text{O}_4/\text{HA}$  2 and  $\text{Fe}_3\text{O}_4/\text{HA}$  3 was calculated to be  $\sim 5.7$ , 10 and 14.3% (w/w) respectively.

CHNS analysis has been done in synthesised samples and in pure HA. CHNS analysis reveals that the % C in  $\text{Fe}_3\text{O}_4$ ,  $\text{Fe}_3\text{O}_4/\text{HA}$  1,  $\text{Fe}_3\text{O}_4/\text{HA}$  2 and  $\text{Fe}_3\text{O}_4/\text{HA}$  3 NPs was 0.1, 2.6, 5.3 and 6.7% respectively while in pure HA it is 48%. The % HA content (w/w) in  $\text{Fe}_3\text{O}_4/\text{HA}$  1,  $\text{Fe}_3\text{O}_4/\text{HA}$  2 and  $\text{Fe}_3\text{O}_4/\text{HA}$  3 NPs was calculated to be 5.5, 11 and 13.9% respectively. From magnetic measurements the % HA content (w/w) in  $\text{Fe}_3\text{O}_4/\text{HA}$  1,  $\text{Fe}_3\text{O}_4/\text{HA}$  2 and  $\text{Fe}_3\text{O}_4/\text{HA}$  3 NPs was calculated to be  $\sim 5.7$ , 10 and 14.3% (w/w) respectively and is in close agreement with the value obtained from CHNS analysis. BET analysis has been carried out in all the samples to determine surface area. BET analysis shows that the surface area of  $\text{Fe}_3\text{O}_4$ ,  $\text{Fe}_3\text{O}_4/\text{HA}$  1,  $\text{Fe}_3\text{O}_4/\text{HA}$  2, and  $\text{Fe}_3\text{O}_4/\text{HA}$  3 NPs was 89.5, 102.8, 121.4 and 121.4  $\text{m}^2/\text{g}$  respectively. This indicates that upon HA coating surface area increases which might be due to a slight decrease in primary size of NPs. It shows that the coating of HA results in particle

size decrement. This might be due to its large structure which hinders particle - particle interaction due to steric repulsion among HA molecules coat on NPs surface.

TEM and HRTEM images of  $\text{Fe}_3\text{O}_4$  and  $\text{Fe}_3\text{O}_4/\text{HA}$  3 NPs were taken and are shown in Figure 5-2. TEM images suggest formation of spherical NPs with cubic structure. Particle size was observed to be  $\sim 15$  nm.

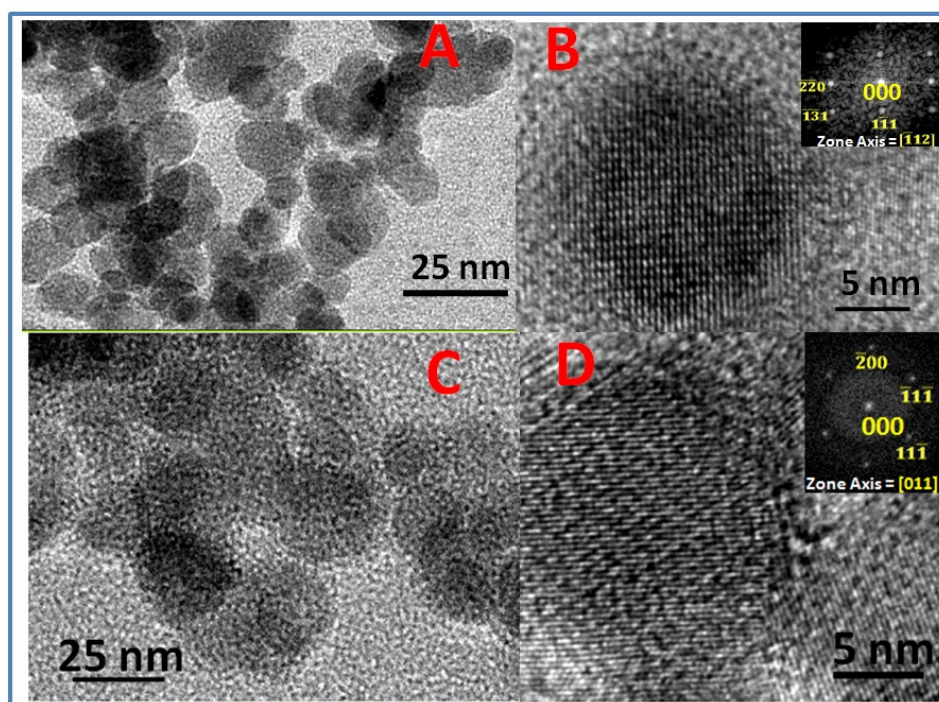


**Figure 5-2 (A).** TEM image of  $\text{Fe}_3\text{O}_4$  NPs. **(B)** HRTEM image of a single  $\text{Fe}_3\text{O}_4$  NPs. **(C)** TEM image of  $\text{Fe}_3\text{O}_4/\text{HA}$  3 NPs **(B)** HRTEM images of  $\text{Fe}_3\text{O}_4/\text{HA}$  3 NPs

### 5.3.2. Sorption Studies of uranium on $\text{Fe}_3\text{O}_4$ and HA coated $\text{Fe}_3\text{O}_4$ NPs

Sorption studies of uranium on  $\text{Fe}_3\text{O}_4$  and HA coated  $\text{Fe}_3\text{O}_4$  NPs has been carried out. Since sorption is governed by both sorbent and sorbate, it is important to understand the properties of both. In present study,  $\text{Fe}_3\text{O}_4$  and HA coated  $\text{Fe}_3\text{O}_4$  NPs as used as sorbent. As surface of  $\text{Fe}_3\text{O}_4$  NPs contains hydroxyl groups, these hydroxyl groups can interact with uranium thereby leading to its sorption. Experiments were also carried out with HA coated  $\text{Fe}_3\text{O}_4$  NPs where some of the hydroxyl groups in  $\text{Fe}_3\text{O}_4$  NPs were replaced by HA. Since HA

has different functional groups associated, coating of HA on bare Fe<sub>3</sub>O<sub>4</sub> NPs can change its binding capacity towards uranium. In order to determine this, sorption studies of uranium with all four NPs were carried out at different concentration of uranium. Figure 5-3 shows

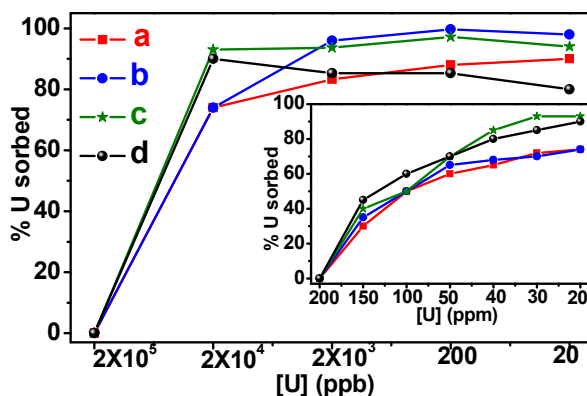


**Figure 5-3.** % Uranium sorbed on NPs surface at different concentration of uranium. (a)

Fe<sub>3</sub>O<sub>4</sub> (b) Fe<sub>3</sub>O<sub>4</sub>/HA 1 (c) Fe<sub>3</sub>O<sub>4</sub>/HA 2 (d) Fe<sub>3</sub>O<sub>4</sub>/HA 3. V/m ratio was kept at 200 mL/g.

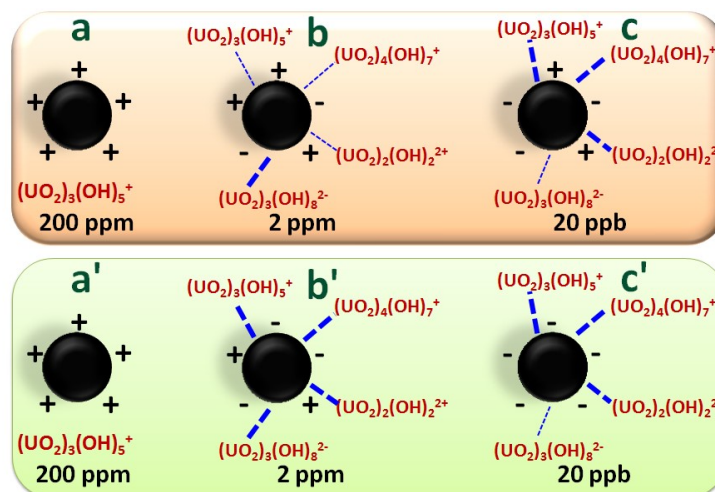
the sorption of uranium on all four NPs at 20 ppb-200 ppm concentrations of uranium. V/m ratio was kept at 200 mL/g, where V is the volume (mL) of testing solution, and m is the amount of NPs (g) used in the experiment. Interestingly 70-99% uranium sorption was observed on all four NPs at 20 ppb-20 ppm uranium concentrations. This high sorption of uranium might be due to strong interaction of uranium with NPs surface. Recently Singer et al.<sup>333</sup> have also studied the sorption of uranium on magnetite surface where they have shown that the high sorption of uranium over magnetite might be due to the reduction of U(VI) to U(IV). Experiments were also carried out with 200 ppm of uranium concentration where no sorption was observed. As is well known from the literature<sup>348-350</sup> that uranium sorption on any surface is highly governed by its species to be sorbed. Therefore, to understand these behaviours it was important to understand the speciation of uranium at different concentration and on different NPs surface. For this the pH of all solutions was measured after NPs addition and are given in Table 5-1. Earlier many authors have studied the speciation of uranium under different conditions<sup>348-350</sup>. It was observed that the major species of uranium at 200

ppm concentration under the prevailing pH (Table 5-1) is  $(\text{UO}_2)_3(\text{OH})_5^{+}$ <sup>350</sup>. As mentioned above that no sorption of uranium at 200 ppm concentration was observed, it shows that this species of uranium was not able to interact with the NPs surface. Since sorption of any species on a surface is mainly governed by electrostatic interactions, it was important to understand the surface charge on NPs surface. To determine this zeta potential studies of all four NPs under different conditions were carried out and are given in Table 5-1. It is clear from Table 5-1 that the zeta potential value of bare  $\text{Fe}_3\text{O}_4$  NPs without any addition of uranium is very less and is close to its point of zero charge however, with increase in HA coating zeta potential value becomes more and more negative as reported earlier also<sup>346</sup>. As observed that on addition of 200 ppm uranium the pH of the solution decreases appreciably (Table 5-1), zeta potential studies were carried out at this pH without addition of uranium. Zeta potential study suggests that the surface charge of all four NPs is positive. This suggests that there will be no columbic interaction between NPs surface and  $(\text{UO}_2)_3(\text{OH})_5^{+}$  and therefore no sorption was observed at 200 ppm concentration. This is also shown schematically in Scheme 5-1 where both  $\text{Fe}_3\text{O}_4$  and  $\text{Fe}_3\text{O}_4/\text{HA}$  3 NPs has positive charge on the surface (Scheme 5-1a, upper panel and bottom panel) and no interaction of uranium species with NPs surface was observed due to columbic repulsion. Now it is interesting to observe that at 20 ppb-20 ppm uranium concentrations, a strong sorption of uranium was observed on NPs surface. At 20 ppm and lower concentrations, the major species of uranium in pH 6-7.8, pH of studied solution (Table 5-1) are  $(\text{UO}_2)_3(\text{OH})_5^{+}$ ,  $(\text{UO}_2)_4(\text{OH})_7^{+}$ ,  $\text{UO}_2)_2(\text{OH})_2^{2+}$ ,  $(\text{UO}_2)_3(\text{OH})_8^{2-}$ . It shows that these species of uranium interact strongly with NPs surface thereby leading to high sorption. Sorption experiments were also performed at 20-200 ppm uranium concentrations and more than 60% sorption was observed at uranium (concentration less than 50 ppm. This might again due to the interaction of different uranium species with NPs surface. Now it is interesting to observe that with decrease in concentration

of uranium from 20 ppm to 20 ppb, the sorption onto  $\text{Fe}_3\text{O}_4$  and  $\text{Fe}_3\text{O}_4/\text{HA}$  1 surface increases while reverse was observed for  $\text{Fe}_3\text{O}_4/\text{HA}$  3. This might be due to the formation of  $(\text{UO}_2)_3(\text{OH})_8^{2-}$  which dominates in higher pH range<sup>350</sup>. As is evident from Table 5-1 that with decrease in uranium concentration the pH of solution increases. At the same time the pH of the solution is more for  $\text{Fe}_3\text{O}_4/\text{HA}$  3 and  $\text{Fe}_3\text{O}_4/\text{HA}$  2 as compared to  $\text{Fe}_3\text{O}_4/\text{HA}$  1 and  $\text{Fe}_3\text{O}_4$  NPs (Table 5-1). These two observations suggests that the formation of  $(\text{UO}_2)_3(\text{OH})_8^{2-}$  species will be more at lower uranium concentration and in case of  $\text{Fe}_3\text{O}_4/\text{HA}$  3 as compared to  $\text{Fe}_3\text{O}_4/\text{HA}$  1 and  $\text{Fe}_3\text{O}_4$  NPs. Since the surface charge of  $\text{Fe}_3\text{O}_4/\text{HA}$  3 is negative at prevailing pH, this suggests that there will be columbic repulsion between the negatively charged surface and  $(\text{UO}_2)_3(\text{OH})_8^{2-}$  species and therefore, sorption decreases with decrease in concentration of uranium in case of  $\text{Fe}_3\text{O}_4/\text{HA}$  3. In case of  $\text{Fe}_3\text{O}_4$  and  $\text{Fe}_3\text{O}_4/\text{HA}$  1 the surface charge is very less. As the pH of the solution increases the surface becomes more and more negative. It leads to more interaction of positively charged species  $(\text{UO}_2)_3(\text{OH})_5^+$ ,  $(\text{UO}_2)_4(\text{OH})_7^+$ ,  $(\text{UO}_2)_2(\text{OH})_2^{2+}$  with negatively charged surface therefore the sorption increases with decrease in concentration (Scheme 5-1c, upper panel) . Experiments were also carried out with 2 ppb uranium concentration where it was observed that the concentration of

**Table 5-1:** pH, Zeta potential of NPs in presence and absence of different concentrations of uranium. The variation in results is within  $\pm 5\%$ .

Sample	pH	[U] added	Zeta Potential (mV)
$\text{Fe}_3\text{O}_4$	6.36	0	+5.5
$\text{Fe}_3\text{O}_4/\text{HA}$ 1	6.4	0	-6
$\text{Fe}_3\text{O}_4/\text{HA}$ 2	7.3	0	-31.7
$\text{Fe}_3\text{O}_4/\text{HA}$ 3	7.9	0	-34
$\text{Fe}_3\text{O}_4$	4.8	0	+0.15
$\text{Fe}_3\text{O}_4/\text{HA}$ 1	4.6	0	+0.25
$\text{Fe}_3\text{O}_4/\text{HA}$ 2	5	0	-0.05
$\text{Fe}_3\text{O}_4/\text{HA}$ 3	5.3	0	-1
$\text{Fe}_3\text{O}_4$	4.7	200 ppm	+0.0426
$\text{Fe}_3\text{O}_4/\text{HA}$ 1	4.8	200 ppm	+0.02
$\text{Fe}_3\text{O}_4/\text{HA}$ 2	5.1	200 ppm	+3.85
$\text{Fe}_3\text{O}_4/\text{HA}$ 3	5.4	200 ppm	-4



**Scheme 5-1.** Interaction of Fe<sub>3</sub>O<sub>4</sub> (upper panel) and Fe<sub>3</sub>O<sub>4</sub>/HA 3 NPs (lower panel) with different species of uranium at different uranium concentrations (a, a') 200 ppm (b, b') 2 ppm (c, c') 20 ppb uranium.

uranium after NPs sorption was <0.4 ppb. The extraction well below 2 ppb suggests that these NPs can be effectively using in water treatment if the concentration reaches above the limits<sup>28</sup>.

As mentioned above that 70-99% uranium sorption was observed at 20 ppb – 20 ppm uranium concentrations, maximum sorption capacity of these NPs for uranium was determined. For this, sorption studies of uranium with all four NPs at different initial concentration of uranium were carried out. Figure 5-4 shows the sorption experiment of uranium with all four NPs. The results were fitted with Langmuir isotherm and maximum sorption capacity was observed to be 5.5, 10.5, 18 and 39.4 mg of U/g of NPs on Fe<sub>3</sub>O<sub>4</sub>, Fe<sub>3</sub>O<sub>4</sub>/HA 1, Fe<sub>3</sub>O<sub>4</sub>/HA 2 and Fe<sub>3</sub>O<sub>4</sub>/HA 3 NPs respectively. These results clearly indicate that with increase in HA coating on NPs the sorption capacity of the material increases and the sorption capacity was minimum in case of bare Fe<sub>3</sub>O<sub>4</sub> NPs while it is maximum for Fe<sub>3</sub>O<sub>4</sub>/HA 3 NPs having the maximum amount of HA coating. It clearly shows that presence of HA coating increases the amount of uranium sorbed on NPs surface. Earlier Yang and co-

workers<sup>346</sup> have studied the sorption of Eu(III) using HA coated Fe<sub>3</sub>O<sub>4</sub> NPs where they have also observed ~99% Eu(III) sorption. High sorption of Eu(III) by HA coated Fe<sub>3</sub>O<sub>4</sub> NPs was assigned due to the plentiful surface sites provided by the surface-coated HA. Similarly Liu et. al.<sup>93</sup> have studied the sorption of heavy metals using HA coated Fe<sub>3</sub>O<sub>4</sub> NPs where they have observed that 99% of Hg(II) and Pb(II) and over 95% of Cu(II) and Cd(II) can be sorbed using these NPs.

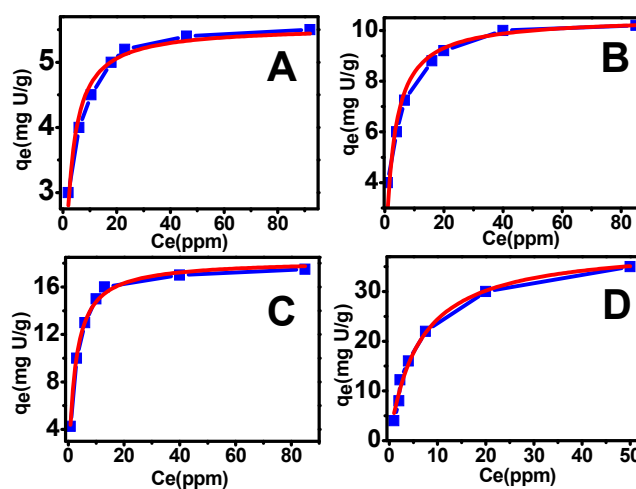


**Figure 5-4.** Equilibrium data for uranium sorption ( $V/m=1000$  mL/g, contact time  $\sim 1$ h, initial uranium concentration 5-100 ppm) (A) Fe<sub>3</sub>O<sub>4</sub>, (B) Fe<sub>3</sub>O<sub>4</sub>/HA 1, (C) Fe<sub>3</sub>O<sub>4</sub>/HA 2, (D) Fe<sub>3</sub>O<sub>4</sub>/HA 3. Red line represents the fitting of data with Langmuir model.

One of the main advantages of using magnetic NPs for detoxification is its easy separation from matrix using magnetic field. As in present study also magnetic NPs were used, it was important to study the effect of magnetic field on particle settlement. For this, settlement of NPs in presence of magnetic field with and without uranium addition was monitored. Interestingly, in presence of magnetic field Fe<sub>3</sub>O<sub>4</sub> and Fe<sub>3</sub>O<sub>4</sub>/HA 1 NPs were immediately settled (Figure 5-5a, b) however no settlement was observed for Fe<sub>3</sub>O<sub>4</sub>/HA 2 and Fe<sub>3</sub>O<sub>4</sub>/HA 3 NPs (Figure 5-5c, d) and sample needs to be centrifuged at high speed for its separation from the matrix. Similar behaviours were also observed on addition of uranium and even in absence of magnetic field where for Fe<sub>3</sub>O<sub>4</sub> and Fe<sub>3</sub>O<sub>4</sub>/HA 1 NPs particle

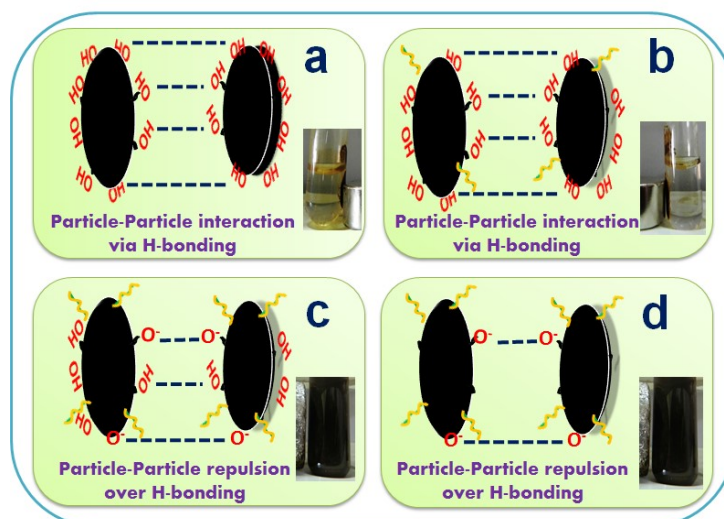


**Figure 5-5.** Settlement of NPs in presence and absence of 20 ppb-20 ppm uranium concentrations (a)  $\text{Fe}_3\text{O}_4$  (b)  $\text{Fe}_3\text{O}_4/\text{HA}$  1 (c)  $\text{Fe}_3\text{O}_4/\text{HA}$  2 (d)  $\text{Fe}_3\text{O}_4/\text{HA}$  3 NPs. **Inset:** Picture of real samples in presence of magnet.

settlement was observed after  $\sim 4$  h while no settlement was observed for  $\text{Fe}_3\text{O}_4/\text{HA}$  2 and  $\text{Fe}_3\text{O}_4/\text{HA}$  3 NPs even if we keep it overnight. Since the settlement of any particle depends upon the particle-particle interaction that in turn is governed by their surface charge, it was important to understand the surface charge on NPs with and without uranium addition. As we have mentioned above that surface charge of NPs is an important parameter as it decides their sorption characteristics, it is also an important parameter as it governs particle-particle interaction which finally decides the settlement characteristics of NPs. For this, zeta potential values of all four NPs under different conditions were measured and are given in Table 5-1. It is clear from Table 5-1 that the zeta potential value of pure  $\text{Fe}_3\text{O}_4$  NPs is very less and is close to its point of zero charge as mentioned earlier also, while with increase in HA coating zeta potential value becomes more and more negative. It is interesting to note that in case of both  $\text{Fe}_3\text{O}_4$  and  $\text{Fe}_3\text{O}_4/\text{HA}$  1, zeta potential value is very less. This suggests that the coulombic repulsion between the particles is very less and particles can interact via each other through hydrogen bonding thereby gets agglomerated and settle very fast. This is shown pictorially in

Figure 5-5a where surface of  $\text{Fe}_3\text{O}_4$  NPs contain hydroxyl groups which can interact via each other through hydrogen bonding and ultimately gets settled. Similar is the case with  $\text{Fe}_3\text{O}_4/\text{HA}$  1 as shown in Figure 5-5b where some of the hydroxyl groups are replaced by HA however hydrogen bonding still dominates over columbic repulsion and particle gets settled. However, in case of  $\text{Fe}_3\text{O}_4/\text{HA}$  2 and  $\text{Fe}_3\text{O}_4/\text{HA}$  3 an opposite behaviour was observed because the negative charge on the surface is very high. Here the columbic repulsion among the particles dominates and no settlement of the particles was observed (Figure 5-5c, d). Now on addition of uranium, the pH of solution remains almost same as that of parent solution without addition of uranium and the similar reasoning can be applied for particle settlement. This is also supported by experimental observation where on addition 20 ppb – 20 ppm uranium particle settlement was observed to be very fast for  $\text{Fe}_3\text{O}_4$  and  $\text{Fe}_3\text{O}_4/\text{HA}$  1 while it was very slow for  $\text{Fe}_3\text{O}_4/\text{HA}$  2 and  $\text{Fe}_3\text{O}_4/\text{HA}$  3 and samples needs to be centrifuged at high speed for a longer time. This observation is important in terms of application of these NPs in real environmental matrix where  $\text{Fe}_3\text{O}_4/\text{HA}$  1 is better choice among all four NPs as it provides higher sorption as well as faster settlement in presence of magnetic field. HA coating also helps to increase the stability of bare  $\text{Fe}_3\text{O}_4$  NPs as reported earlier<sup>91, 342, 343</sup>. All these properties are very important for simple and efficient use of any sorbent material for environmental remediation.

Since uranium is the key material for nuclear reactors and sea water is known to contain a large amount of uranium, experiments were performed with sea water to exploit the use of these NPs for the extraction of uranium. Earlier Kim et. al.<sup>333</sup> have shown the extraction of uranium from sea water matrix using amidoxime based polymeric adsorbent. They have shown that 3.3 mg uranium can be extracted /g of sorbent from sea water. However, preparation of adsorbent is difficult and requires radiation source and other conditioning processes. Similarly Manos and Kanatzidis<sup>28</sup> have shown the use of layered metal sulfides

for the extraction of uranium from sea water matrix. However, the equilibration time was kept ~12 h and particles need to be centrifuged to separate from sea water matrix. To maintain these conditions in any practical application is a difficult task. To overcome above difficulties, these NPs were used for extraction of uranium from sea water matrix. For this, sorption experiments were carried out in sea water samples. 10 mL of sea water was taken and 10 ppb uranium and 20 mg NPs were added to it. The samples were sonicated for 1 h followed by separation using a permanent magnet and wherever necessary by centrifuge. The concentration of uranium in samples was determined by plotting calibration curve using laser fluorimeter. For calibration curve, 2, 4, 6, 8 and 10 ppb of uranium was added in 10 mL of sea water and processed as described in experimental section. Sea water blank was also prepared in which no uranium was added and this value was subtracted to plot the calibration curve as shown in Figure 5-6. Now it was interesting to observe from Figure 5-6 that on addition of 20 mg NPs the concentration of uranium in sea water decreases and is less than 10 ppb. At the same time this decrease is different for different NPs and is more in case of HA

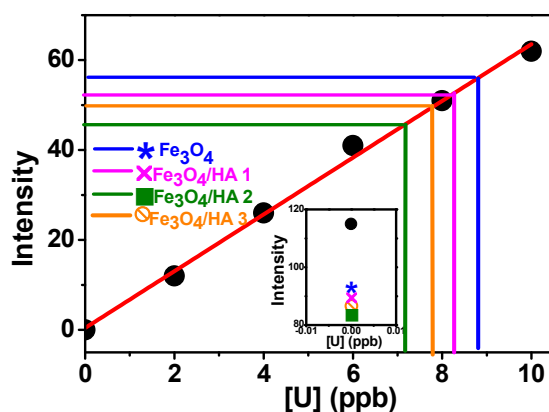


**Figure 5-6.** Calibration curve and concentration of uranium after sorption with all four NPs in different sea water samples. The initial concentration of added uranium was 10 ppb. **Inset** shows that extraction of uranium from sea water matrix without any addition of uranium externally. Black dot (•) shows the intensity corresponding to the natural concentration of uranium in each sea water prior to sorption with NPs.

coated  $\text{Fe}_3\text{O}_4$  NPs as compared to bare ones. This suggests that HA coating helps in the extraction of uranium from sea water.

As mentioned above that these NPs can be used to extract uranium from sea water at 10 ppb added concentrations, experiments were performed to check whether it is possible to extract uranium directly from sea water without any external addition or not. For this, samples were processed in a similar way but without addition of uranium. Here a reagent blank was also prepared by taking 5 ml sea water simulator<sup>326</sup> and its value was subtracted from the sea water blank value. Figure 5-6 inset shows the blank value in each sea water which is marked as black dot. The intensity corresponding to this is due to naturally occurring concentration of uranium present in sea water. Now it is interesting to observe from Figure 5-6 inset that in most of the sea water samples on addition of NPs this intensity decreases and this decrement is more in case of HA coated  $\text{Fe}_3\text{O}_4$  NPs as compared to bare one. This suggests that on NPs addition some of uranium was captured by NPs thereby leading to decrement in intensity. This observation clearly indicates that  $\text{Fe}_3\text{O}_4$  NPs and HA coated  $\text{Fe}_3\text{O}_4$  NPs can extract uranium directly from sea water matrix and with HA coating the extraction is much more effective as compared to bare particles. Although, exact amount of uranium that can be extracted cannot be measured but result indicates that these NPs can be effectively used to extract uranium from sea water matrix. The result shows the potential of these NPs in comparison to other methods developed which has limitations such as difficult synthesis, tedious separation from matrix, larger contact time, costly. Herein, an alternative method which can overcome most of these limitations and can be effectively used for uranium extraction from water and sea water matrix was demonstrated.

#### **5.4. Conclusions**

To conclude, this chapter demonstrates the application of  $\text{Fe}_3\text{O}_4$  and HA coated  $\text{Fe}_3\text{O}_4$  NPs for sorption of uranium.  $\text{Fe}_3\text{O}_4$  and HA coated  $\text{Fe}_3\text{O}_4$  NPs with different amount of HA

coating were synthesized and used for sorption studies of uranium. Experiments were conducted at different concentrations of uranium, where no sorption was observed at 200 ppm while 70-99% sorption was observed at lower concentrations, 20 ppm-20 ppb. These results were explained on the basis of interaction of NPs with uranium species that exist in solution under prevailing conditions. Maximum sorption capacity of these materials for uranium was also evaluated and it was found that with increase in HA content, sorption capacity increases. As observed that these NPs can extract uranium even in ppb concentration level, their use for uranium extraction from sea water matrix was explored. Interestingly, these NPs can be effectively used for uranium extraction from sea water and in presence of HA coating the extraction was more. Settlement of these NPs in presence of uranium was also monitored where it was observed that only  $\text{Fe}_3\text{O}_4$  and  $\text{Fe}_3\text{O}_4/\text{HA}$  1 NPs gets settled while no settlement was observed for  $\text{Fe}_3\text{O}_4/\text{HA}$  2 and  $\text{Fe}_3\text{O}_4/\text{HA}$  3 NPs. This observation indicates that  $\text{Fe}_3\text{O}_4$  and  $\text{Fe}_3\text{O}_4/\text{HA}$  1 are better materials as compared to other two in terms of their ease of separation from the matrix, though sorption studies suggests HA coated  $\text{Fe}_3\text{O}_4$  NPs are better as compared to bare NPs for extraction. Considering both of these factors,  $\text{Fe}_3\text{O}_4/\text{HA}$  1 are the best choice among all four NPs having high extraction capacity and easy separation from the matrix. This material has an advantage over other studied materials of being low cost, easy preparation, nontoxic, easily separable and faster extraction where none of the other studied material fulfils all these properties. The development of such low cost and effective methods for uranium extraction from sea water matrix can leads to the sustainment of nuclear energy to a reality.



# CHAPTER-6

## Summary and Outlook



### **6.1. Summary**

In the present thesis work, application of nanomaterials for solar energy conversion and environmental remediation has been demonstrated. Accordingly, the work carried out in the present thesis was divided. Chapter 3 demonstrate the application of semiconductor nanocrystals, II-VI CdX QDs for QDSC application. Chapter 4 demonstrate the application of QDs as a sensor for uranium and fluoride ions. Chapter 5 demonstrate the application of magnetic NPs for sorption of uranium. Different characterization techniques such as XRD, HRTEM, FTIR, zeta potential, TCSPC, femtosecond fluorescence upconversion and transient absorption spectroscopy were used to characterize the sample and to understand their properties. The work carried out in different chapters and information obtained is summarized below.

In chapter 3, coupled system of QDs with different molecular adsorbates has been demonstrated. It is well known that one of the major limitations in QDSC is the slow hole transfer rate. The main emphasis of this chapter was to investigate a series of different molecules which can extract hole at a comparable rate to that of an electron from QDs and monitor their ultrafast charge transfer dynamics. This chapter was divided into three sections. In the first section of this chapter, a coupled system of CdSe QDs with PGR dye was demonstrated, where both QDs and dye absorb solar radiation. At the same time the energetic of the process suggests that on photo-excitation of QDs, hole transfer from QDs to PGR and on photo-excitation of dye, electron transfer from dye to QDs is thermodynamically favourable processes. Therefore, a grand charge separation can be realized in this system. Transient absorption spectroscopy confirms this mechanism and formation of PGR cation radical was detected in the transient absorption spectrum of CdSe/PGR composite system. The formation of PGR cation radical was a bi-exponential process with ~150 fs and ~500 fs timescale where 150 fs timescale has been assigned to the electron injection time from dye to

QDs while 500 fs time has been assigned to the hole transfer time from QDs to PGR. Charge recombination between PGR cation radical and electron in CdSe QDs was observed to be slow >200 ps suggesting grand charge separation in this system. Higher solar radiation absorption, faster charge carrier extraction and slow charge recombination are the main requirements to achieve high efficiency QDSC and the system studied have all these properties. Therefore using this system a higher efficient QDSC can be realized.

In the second part of this chapter, hot hole extraction processes from QDs to catechol and thiols were demonstrated. It is established that the efficiency of QDSC can reach up to 66% if hot charge carriers can be extracted prior to their cooling. Earlier few reports were available on hot electron extraction from QDs while no report was available on hot hole extraction. In this section, a composite system of CdSe QDs with catechols and thiols were chosen where hot hole extraction from QDs has been demonstrated. Femtosecond fluorescence upconversion technique was used to determine hot hole extraction process and hot hole extraction time was observed to be ~250 fs and ~300 fs for catechols and thiols respectively. Such fast hot hole extraction from QDs materials can lead to high efficiency in QDSC. It is also reported that the stability of bare QDs is an issue and covering QDs with a shell improve its stability as well as optical properties. The work carried out in this section also demonstrate the hot hole extraction from CdSe QDs to thiol in presence of type 1, ZnS shell and hot hole extraction time was determined to be ~500 fs. Higher stability of CdSe/ZnS CSQDs as compared to pure CdSe QDs and hot hole extraction promotes its application in QDSC.

In the third part of this chapter, charge carrier dynamics of CdX QDs with nitro catechol (NCAT), a hole transporting molecule for QDs was studied. Here also the main aim was hole extraction but interestingly an interfacial complex formation between CdX QDs and nitro catechol (NCAT) was observed. This complexation results from the interaction between

$\text{Cd}^{2+}$  ions on QDs surface and NCAT. Time-resolved emission and femtosecond transient measurements were carried out to monitor the effect of this complexation on charge carrier dynamics and it was observed that complex formation favours better charge separation. Experiment with CdTe/NCAT composite system suggests that on complex formation charge separation occurs even if the process is not thermodynamically favourable. This study helps in understanding the effect of an interface in charge carrier dynamics of QDs and suggests that because of interfacial complex formation charge separation is favoured which can lead to a high efficiency in QDSC.

To summarize, this chapter deals with the hole extraction process from QDs, in search of which different molecules were selected and different processes such as super-sensitization, hot hole extraction, and interfacial complex formation were revealed.

In chapter 4 of the thesis, QDs as a probe to detect uranium and fluoride ions has been demonstrated. Uranium a well known nephrotoxic element has a maximum permissible contamination level in drinking water ~35 ppb as suggested by WHO. Therefore it is very important to detect uranium at such trace concentrations. A number of techniques were available for this purpose but those techniques have limitations such as complex instrumentation and costly. In the first section of this chapter, application of CdSe/CdS CSQDs for detection of uranium at trace concentrations was demonstrated and a detection limit of ~75 ppb was achieved. Along with detection, mechanism of detection was also demonstrated which allow selecting the best detection system among the synthesized ones for uranium detection. The study suggests the application of QDs for uranium detection and demonstrates that understanding detection mechanism at a fundamental level helps to design more efficient detection probes.

In the second part of this chapter, a green, selective, sensitive and economic probe for fluoride ion has been demonstrated. The chosen probe was based on carbon QDs (CQDs) and  $\text{Eu}^{3+}$ , where photoluminescence property of CQDs was used to detect fluoride ions. On an addition of  $\text{Eu}^{3+}$ , the photoluminescence of CQDs quenched (*switch-off*) and on the addition of fluoride ions luminescence regenerated (*switch-on*). This was assigned to the binding of  $\text{Eu}^{3+}$  with surface  $-\text{COOH}$  groups on CQDs surface and subsequent removal on addition of fluoride ions. Formation of  $\text{EuF}_3$  was confirmed by XRD and HRTEM measurements. The experiments were also carried out in presence of other competing ions which suggests that the probe was selective for fluoride ions. The probe was also tested for analysis of fluoride ions in toothpaste sample where result matches well with that obtained from ion chromatography. The suggested probe was green, economical, and selective and can be used for detection of fluoride in real samples. Also, a mechanism of detection was demonstrated which helps to understand the detection probe in a better way.

Along with detection, it is also important to find the suitable host matrix to trap toxic ions from different environmental matrices. Chapter 5 of the present thesis work focus on this issue, where  $\text{Fe}_3\text{O}_4$  and humic acid (HA) coated  $\text{Fe}_3\text{O}_4$  NPs, with different amount of HA coating were synthesized and their application for uranium extraction was demonstrated. It was observed that ~90% uranium sorb on NPs surface and sorption increases with increases in HA concentrations. Application of these NPs for uranium extraction from sea water matrix was also demonstrated which suggests that these NPs can be effectively used for uranium extraction from sea water matrix. With an increase in HA coating both sorption as well as the stability of NPs increases suggesting that HA coated  $\text{Fe}_3\text{O}_4$  NPs are better as compared to bare NPs for sorption of uranium.

## 6.2. Outlook

Present thesis work involves a composite system of QDs and CSQDs with different molecules that can extract hole from QDs at a comparable rate to that of electron and a higher efficient QDSC can be realized. Work with CdSe QDs and PGR dye as a composite system suggests grand charge separation and higher solar radiation absorption in this system. Both of these processes are necessary to achieve higher efficiency QDSC. Work with composite systems of CdSe QDs with catechols and thiols suggest hot hole extraction from QDs where it has been reported that efficiency of QDSC can reach to ~66% if hot charge carriers can be extracted. Experiment in presence of ZnS shell suggests that hot hole extraction is still possible in presence of type 1 shell over CdSe core. ZnS shell not only passivates trap states in CdSe QDs but also provide chemical stability to CdSe QDs. Hot hole extraction time was observed to be ~300 fs in case of CdSe/thiol and ~500 fs in CdSe/ZnS/thiol composite system. Such hot hole extraction process using catechols and thiols was not reported earlier and can provide a further step to enhance QDSC efficiency. Work with CdX/NCAT composite system suggests an interfacial complex formation at QDs surface which results because of interaction between excess  $\text{Cd}^{2+}$  ions on QDs surface and NCAT. Time-resolved emission and transient absorption measurement suggests that this complex formation favours better charge separation and can change the charge carrier dynamics of pure CdX/NCAT composite system where under solar excitation, both QDs and complex will be excited. Therefore a proper knowledge of interface in any two coupled system is necessary to understand the property of their composite.

Work with CdSe/CdS CSQDs as a uranium detection probe suggests that electron transfer process from QDs to uranium is responsible for its detection. It was also demonstrated that electron transfer rate decreases with an increase in shell thickness. Therefore, bare CdSe QDs will be better for uranium detection as compared to CSQDs.

However, study suggests that the detection of uranium using CdSe QDs was not reliable and therefore, CSQDs with different thickness of CdS shell were synthesized and best system among synthesized one was selected for uranium detection. Here understanding detection mechanism at a fundamental level helped to tune the system and to obtain a better detection probe. This study will help in future to suggest better detection probe for uranium, where further tuning within CSQDs structure as well as on surface can be carried out to obtain better detection limit. For fluoride ion detection, a composite system of CQDs and  $\text{Eu}^{3+}$  was demonstrated where  $\text{Eu}^{3+}$  binds selectively with fluoride ion and a fluoride detection probe has been realized. Here photoluminescence property of CQDs was used for fluoride ion detection and applicability of this probe in real toothpaste sample was also demonstrated. This method has advantages such as green, sensitive, selective and low cost as compared to other reported methods for fluoride ion detection. The suggested method can be used in the future to detect fluoride ion in real environmental samples.

Work with magnetic NPs as a sorbent suggests that these NPs can be effectively used to extract uranium from water samples. These NPs has an advantage as compared to other reported material of being non-toxic. Also, these NPs can be separated from the matrix by application of magnetic field and therefore, their separation is much easier as compared to other materials and tedious processes of separation such as high speed centrifugation can be avoided.

---

**References**

1. Liu, C.-j.; Burghaus, U.; Besenbacher, F.; Wang, Z. L. *ACS Nano* **2010**, 4, (10), 5517-5526.
2. Orr, F. M. *ACS Energy Letters* **2016**, 113-114.
3. Dresselhaus, M. S.; Thomas, I. L. *Nature* **2001**, 414, (6861), 332-337.
4. Chapin, D. M.; Fuller, C. S.; Pearson, G. L. *Journal of Applied Physics* **1954**, 25, (5), 676-677.
5. Goetzberger, A.; Luther, J.; Willeke, G. *Solar Energy Materials and Solar Cells* **2002**, 74, (1-4), 1-11.
6. Green, M. A. *Progress in Photovoltaics: Research and Applications* **2005**, 13, (5), 447-455.
7. Green, M. A.; Emery, K.; Hishikawa, Y.; Warta, W.; Dunlop, E. D. *Progress in Photovoltaics: Research and Applications* **2015**, 23, (1), 1-9.
8. Mathew, S.; Yella, A.; Gao, P.; Humphry-Baker, R.; CurchodBasile, F. E.; Ashari-Astani, N.; Tavernelli, I.; Rothlisberger, U.; NazeeruddinMd, K.; Grätzel, M. *Nat Chem* **2014**, 6, (3), 242-247.
9. Kamat, P. V. *The Journal of Physical Chemistry C* **2007**, 111, (7), 2834-2860.
10. Carey, G. H.; Abdelhady, A. L.; Ning, Z.; Thon, S. M.; Bakr, O. M.; Sargent, E. H. *Chemical Reviews* **2015**.
11. Alivisatos, A. P. *Science* **1996**, 271, (5251), 933-937.
12. Peng, Z. A.; Peng, X. *Journal of the American Chemical Society* **2000**, 123, (1), 183-184.
13. Shockley, W.; Queisser, H. J. *Journal of Applied Physics* **1961**, 32, (3), 510-519.
14. Ross, R. T.; Nozik, A. J. *Journal of Applied Physics* **1982**, 53, (5), 3813-3818.
15. Bercx, M.; Sarmadian, N.; Saniz, R.; Partoens, B.; Lamoen, D. *Phys. Chem. Chem. Phys.* **2016**, 18, 20542 -20549.

16. Pyatia, R.; Richter, M. M. *Annu. Rep. Prog. Chem., Sect. C*, **2007**, 103, 12–78.
17. Orvig, C.; Abrams, M. J. *Chemical Reviews* **1999**, 99, (9), 2201-2204.
18. Que, E. L.; Domaille, D. W.; Chang, C. J. *Chemical Reviews* **2008**, 108, (5), 1517-1549.
19. McRae, R.; Bagchi, P.; Sumalekshmy, S.; Fahrni, C. J. *Chemical Reviews* **2009**, 109, (10), 4780-4827.
20. Benounis, M.; Jaffrezic-Renault, N.; Halouani, H.; Lamartine, R.; Dumazet-Bonnamour, I. *Materials Science and Engineering: C* **2006**, 26, (2–3), 364-368.
21. Quang, D. T.; Kim, J. S. *Chemical Reviews* **2010**, 110, (10), 6280-6301.
22. Lou, Y.; Zhao, Y.; Zhu, J.-J. *Nanoscale Horizons* **2016**, 1, (2), 125-134.
23. Rhee, H.-W.; Choi, H.-Y.; Han, K.; Hong, J.-I. *Journal of the American Chemical Society* **2007**, 129, (15), 4524-4525.
24. Lee, J. W.; Jung, H. S.; Kwon, P. S.; Kim, J. W.; Bartsch, R. A.; Kim, Y.; Kim, S.-J.; Kim, J. S. *Organic Letters* **2008**, 10, (17), 3801-3804.
25. Chang, C. J.; Nolan, E. M.; Jaworski, J.; Okamoto, K.-I.; Hayashi, Y.; Sheng, M.; Lippard, S. J. *Inorganic Chemistry* **2004**, 43, (21), 6774-6779.
26. Kim, H. J.; Lee, S. J.; Park, S. Y.; Jung, J. H.; Kim, J. S. *Advanced Materials* **2008**, 20, (17), 3229-3234.
27. Jung, H. S.; Kwon, P. S.; Lee, J. W.; Kim, J. I.; Hong, C. S.; Kim, J. W.; Yan, S.; Lee, J. Y.; Lee, J. H.; Joo, T.; Kim, J. S. *Journal of the American Chemical Society* **2009**, 131, (5), 2008-2012.
28. Sapunar-Postruznik, J.; Bazulic, D.; Kubala, H.; Balint, L. *Science of The Total Environment* **1996**, 177, (1), 31-35.
29. Tchounwou, P. B.; Ayensu, W. K.; Ninashvili, N.; Sutton, D. *Environmental Toxicology* **2003**, 18, (3), 149-175.

30. Manos, M. J.; Kanatzidis, M. G. *Journal of the American Chemical Society* **2012**, 134, (39), 16441-16446.
31. Du, J.; Hu, M.; Fan, J.; Peng, X. *Chemical Society Reviews* **2012**, 41, (12), 4511-4535.
32. Ma, J.; Dasgupta, P. K. *Analytica Chimica Acta* **2010**, 673, (2), 117-125.
33. Wade, C. R.; Broomsgrove, A. E. J.; Aldridge, S.; Gabbai, F. P. *Chemical Reviews* **2010**, 110, (7), 3958-3984.
34. Gore, A. H.; Vatre, S. B.; Anbhule, P. V.; Han, S.-H.; Patil, S. R.; Kolekar, G. B. *Analyst* **2013**, 138, (5), 1329-1333.
35. Frigerio, C.; Ribeiro, D. S. M.; Rodrigues, S. S. M.; Abreu, V. L. R. G.; Barbosa, J. A. C.; Prior, J. A. V.; Marques, K. L.; Santos, J. L. M. *Analytica Chimica Acta* **2012**, 735, 9-22.
36. Butler, O. T.; Cook, J. M.; Harrington, C. F.; Hill, S. J.; Rieuwert, J.; Miles, D. L. *Journal of Analytical Atomic Spectrometry* **2006**, 21, (2), 217-243.
37. Li, Y.; Chen, C.; Li, B.; Sun, J.; Wang, J.; Gao, Y.; Zhao, Y.; Chai, Z. *Journal of Analytical Atomic Spectrometry* **2006**, 21, (1), 94-96.
38. Martínez-Mañez, R.; Sancenón, F. *Chemical Reviews* **2003**, 103, (11), 4419-4476.
39. Kang, S. O.; Llinares, J. M.; Powell, D.; VanderVelde, D.; Bowman-James, K. *Journal of the American Chemical Society* **2003**, 125, (34), 10152-10153.
40. Schmidtchen, F. P.; Berger, M. *Chemical Reviews* **1997**, 97, (5), 1609-1646.
41. Sui, B.; Kim, B.; Zhang, Y.; Frazer, A.; Belfield, K. D. *ACS Applied Materials & Interfaces* **2013**, 5, (8), 2920-2923.
42. Liu, X. Y.; Bai, D. R.; Wang, S. *Angewandte Chemie* **2006**, 118, (33), 5601-5604.
43. Hudnall, T. W.; Kim, Y.-M.; Bebbington, M. W. P.; Bourissou, D.; Gabbai, F. P. *Journal of the American Chemical Society* **2008**, 130, (33), 10890-10891.
44. Chan, Y.-H.; Chen, J.; Liu, Q.; Wark, S. E.; Son, D. H.; Batteas, J. D. *Analytical Chemistry* **2010**, 82, (9), 3671-3678.

- 
45. Chen, Y.; Rosenzweig, Z. *Analytical Chemistry* **2002**, 74, (19), 5132-5138.
46. Huang, D.; Niu, C.; Ruan, M.; Wang, X.; Zeng, G.; Deng, C. *Environmental Science & Technology* **2013**, 47, (9), 4392-4398.
47. Ke, J.; Li, X.; Zhao, Q.; Hou, Y.; Chen, J. *Scientific Reports* **2014**, 4, 5624.
48. Li, L.; Chen, Y.; Tian, G.; Akpe, V.; Xu, H.; Gan, L.-M.; Skrtic, S.; Luo, Y.; Brismar, H.; Fu, Y. *The Journal of Physical Chemistry C* **2014**, 118, (19), 10424-10433.
49. Jin, L.-H.; Han, C.-S. *Analytical Chemistry* **2014**, 86, (15), 7209-7213.
50. Dong, Y.; Wang, R.; Li, G.; Chen, C.; Chi, Y.; Chen, G. *Analytical Chemistry* **2012**, 84, (14), 6220-6224.
51. Dutta, R. K.; Kumar, A. *Analytical Chemistry* **2016**, 88, (18), 9071-9078.
52. Dutta Chowdhury, A.; Doong, R.-a. *ACS Applied Materials & Interfaces* **2016**, 8, (32), 21002-21010.
53. Mohamed Ali, E.; Zheng, Y.; Yu, H.-h.; Ying, J. Y. *Analytical Chemistry* **2007**, 79, (24), 9452-9458.
54. Wu, P.; Zhao, T.; Wang, S.; Hou, X. *Nanoscale* **2014**, 6, (1), 43-64.
55. Aragay, G.; Pons, J.; Merkoçi, A. *Chemical Reviews* **2011**, 111, (5), 3433-3458.
56. Hudnall, T. W.; Chiu, C.-W.; Gabbai, F. P. *Accounts of Chemical Research* **2009**, 42, (2), 388-397.
57. Gale, P. A. *Coordination Chemistry Reviews* **2003**, 240, (1-2), 191-221.
58. Yamaguchi, S.; Akiyama, S.; Tamao, K. *Journal of the American Chemical Society* **2001**, 123, (46), 11372-11375.
59. Kim, S. Y.; Park, J.; Koh, M.; Park, S. B.; Hong, J.-I. *Chemical Communications* **2009**, (31), 4735-4737.
60. Vázquez, M.; Fabbrizzi, L.; Taglietti, A.; Pedrido, R. M.; González-Noya, A. M.; Bermejo, M. R. *Angewandte Chemie* **2004**, 116, (15), 1996-1999.

- 
61. Kim, T.-H.; Swager, T. M. *Angewandte Chemie International Edition* **2003**, 42, (39), 4803-4806.
62. Zheng, F.; Zeng, F.; Yu, C.; Hou, X.; Wu, S. *Chemistry – A European Journal* **2013**, 19, (3), 936-942.
63. Butler, S. J. *Chemical Communications* **2015**, 51, (54), 10879-10882.
64. Liu, J.-M.; Lin, L.-p.; Wang, X.-X.; Jiao, L.; Cui, M.-L.; Jiang, S.-L.; Cai, W.-L.; Zhang, L.-H.; Zheng, Z.-Y. *Analyst* **2013**, 138, (1), 278-283.
65. Mohapatra, S.; Sahu, S.; Nayak, S.; Ghosh, S. K. *Langmuir* **2015**, 31, (29), 8111-8120.
66. Basu, A.; Suryawanshi, A.; Kumawat, B.; Dandia, A.; Guin, D.; Ogale, S. B. *Analyst* **2015**, 140, (6), 1837-1841.
67. Baruah, U.; Gogoi, N.; Majumdar, G.; Chowdhury, D. *Carbohydrate Polymers* **2015**, 117, 377-383.
68. White, D. A.; Labayru, R. *Industrial & Engineering Chemistry Research* **1991**, 30, (1), 207-210.
69. Duff, M. C.; Hunter, D. B.; Hobbs, D. T.; Fink, S. D.; Dai, Z.; Bradley, J. P. *Environmental Science & Technology* **2004**, 38, (19), 5201-5207.
70. Sarina, S.; Bo, A.; Liu, D.; Liu, H.; Yang, D.; Zhou, C.; Maes, N.; Komarneni, S.; Zhu, H. *Chemistry of Materials* **2014**, 26, (16), 4788-4795.
71. Chen, R.; Tanaka, H.; Kawamoto, T.; Asai, M.; Fukushima, C.; Kurihara, M.; Ishizaki, M.; Watanabe, M.; Arisaka, M.; Nankawa, T. *ACS Applied Materials & Interfaces* **2013**, 5, (24), 12984-12990.
72. Chen, K.; Kang, Y.-S.; Zhao, Y.; Yang, J.-M.; Lu, Y.; Sun, W.-Y. *Journal of the American Chemical Society* **2014**, 136, (48), 16744-16747.

73. Yuan, L.-Y.; Bai, Z.-Q.; Zhao, R.; Liu, Y.-L.; Li, Z.-J.; Chu, S.-Q.; Zheng, L.-R.; Zhang, J.; Zhao, Y.-L.; Chai, Z.-F.; Shi, W.-Q. *ACS Applied Materials & Interfaces* **2014**, 6, (7), 4786-4796.
74. Mertz, J. L.; Fard, Z. H.; Malliakas, C. D.; Manos, M. J.; Kanatzidis, M. G. *Chemistry of Materials* **2013**, 25, (10), 2116-2127.
75. Luca, V.; Tejada, J. J.; Vega, D.; Arrachart, G.; Rey, C. *Inorganic Chemistry* **2016**.
76. Bo, A.; Sarina, S.; Liu, H.; Zheng, Z.; Xiao, Q.; Gu, Y.; Ayoko, G. A.; Zhu, H. *ACS Applied Materials & Interfaces* **2016**, 8, (25), 16503-16510.
77. Demir, S.; Brune, N. K.; Van Humbeck, J. F.; Mason, J. A.; Plakhova, T. V.; Wang, S.; Tian, G.; Minasian, S. G.; Tylliszczak, T.; Yaita, T.; Kobayashi, T.; Kalmykov, S. N.; Shiwaku, H.; Shuh, D. K.; Long, J. R. *ACS Central Science* **2016**, 2, (4), 253-265.
78. Shkrob, I. A.; Tisch, A. R.; Marin, T. W.; Muntean, J. V.; Kaminski, M. D.; Kropf, A. J. *Industrial & Engineering Chemistry Research* **2011**, 50, (8), 4686-4696.
79. Yang, D.; Sarina, S.; Zhu, H.; Liu, H.; Zheng, Z.; Xie, M.; Smith, S. V.; Komarneni, S. *Angewandte Chemie International Edition* **2011**, 50, (45), 10594-10598.
80. Sasaki, Y.; Tachimori, S. *Solvent Extraction and Ion Exchange* **2002**, 20, (1), 21-34.
81. Li, Q.; Easter, N. J.; Shang, J. K. *Environmental Science & Technology* **2009**, 43, (5), 1534-1539.
82. Thorat, N. D.; Shinde, K. P.; Pawar, S. H.; Barick, K. C.; Betty, C. A.; Ningthoujam, R. S. *Dalton Transactions* **2012**, 41, (10), 3060-3071.
83. Lu, A.-H.; Salabas, E. L.; Schüth, F. *Angewandte Chemie International Edition* **2007**, 46, (8), 1222-1244.
84. Mornet, S.; Vasseur, S.; Grasset, F.; Duguet, E. *Journal of Materials Chemistry* **2004**, 14, (14), 2161-2175.
85. Gupta, A. K.; Gupta, M. *Biomaterials* **2005**, 26, (18), 3995-4021.

- 
86. Tsang, S. C.; Caps, V.; Paraskevas, I.; Chadwick, D.; Thompsett, D. *Angewandte Chemie International Edition* **2004**, 43, (42), 5645-5649.
87. Li, Z.; Wei, L.; Gao, M. Y.; Lei, H. *Advanced Materials* **2005**, 17, (8), 1001-1005.
88. Hyeon, T. *Chemical Communications* **2003**, (8), 927-934.
89. Takafuji, M.; Ide, S.; Ihara, H.; Xu, Z. *Chemistry of Materials* **2004**, 16, (10), 1977-1983.
90. Kaur, M.; Zhang, H.; Martin, L.; Todd, T.; Qiang, Y. *Environmental Science & Technology* **2013**, 47, (21), 11942-11959.
91. Chandra, V.; Park, J.; Chun, Y.; Lee, J. W.; Hwang, I.-C.; Kim, K. S. *ACS Nano* **2010**, 4, (7), 3979-3986.
92. Liu, M.; Chen, C.; Hu, J.; Wu, X.; Wang, X. *The Journal of Physical Chemistry C* **2011**, 115, (51), 25234-25240.
93. Liu, J.-f.; Zhao, Z.-s.; Jiang, G.-b. *Environmental Science & Technology* **2008**, 42, (18), 6949-6954.
94. Klimov, V. I. *Los Alamos science* **2003**, 28(28), 214-220.
95. Kudera, S.; Zanella, M.; Giannini, C.; Rizzo, A.; Li, Y.; Gigli, G.; Cingolani, R.; Ciccarella, G.; Spahl, W.; Parak, W. J.; Manna, L. *Adv. Mater.* **2007**, 19, (4), 548-552.
96. Widmann, F.; Simon, J.; Daudin, B.; Feuillet, G.; Rouvière, J. L.; Pelekanos, N. T.; Fishman, G. *Phys. Rev. B* **1998**, 58, (24), R15989-R15992.
97. Ashcroft, N. W.; Mermin, N. D., *Solid State Physics*. Saunders, W.B., Orlando, FL: 1976.
98. Norris, D. J., *Measurement and Assignment of the Size-Dependent Optical Spectrum in Cadmium Selenide (CdSe) Quantum Dots*. 1995.
99. Guzelian, A. A.; Banin, U.; Kadavanich, A. V.; Peng, X.; Alivisatos, A. P. *Appl. Phys. Lett.* **1996**, 69, (10), 1432-1434.
100. Berry, C. R. *Physical Review* **1967**, 153, (3), 989-992.
101. Meehan, E. J.; Miller, J. K. *J. Phys. Chem.* **1968**, 72, (5), 1523-1529.

- 
102. Brus, L. E. *J. Chem. Phys.* **1984**, 80, (9), 4403-4409.
103. Efros, A. L. *Sov. Phys. Semicond.-USSR* **1982**, 16, 772.
104. Efros, A. L.; Rosen, M.; Kuno, M.; Nirmal, M.; Norris, D. J.; Bawendi, M. *Phys. Rev. B* **1996**, 54, (7), 4843-4856.
105. Efros, A. L. *Phys. Rev. B* **1992**, 46, (12), 7448-7458.
106. Xia, J.-B. *Phys. Rev. B* **1989**, 40, (12), 8500-8507.
107. Hellwege, K. H., in *Landolt-Bornstein Numerical Data and Functional Relationships in Science and Technology, New Series*. Springer-Verlag, Berlin: 1982; Vol. Vol. 17b, Group III.
108. Gfroerer, T. H.; Sturge, M. D.; Kash, K.; Yater, J. A.; Plaut, A. S.; Lin, P. S. D.; Florez, L. T.; Harbison, J. P.; Das, S. R.; Lebrun, L. *Phys. Rev. B* **1996**, 53, (24), 16474-16480.
109. Klimov, V. I., *Nanocrystal Quantum Dots*. Second ed.; CRC Press: Boca Raton, 2010.
110. Klimov, V. I. *Annual Review of Physical Chemistry* **2007**, 58, (1), 635-673.
111. Kambhampati, P. *Accounts of Chemical Research* **2010**, 44, (1), 1-13.
112. Cooney, R. R.; Sewall, S. L.; Dias, E. A.; Sagar, D. M.; Anderson, K. E. H.; Kambhampati, P. *Physical Review B* **2007**, 75, (24), 245311.
113. Sewall, S.; Cooney, R.; Anderson, K.; Dias, E.; Kambhampati, P. *Physical Review B* **2006**, 74, (23), 235328.
114. Sewall, S. L.; Cooney, R. R.; Anderson, K. E. H.; Dias, E. A.; Sagar, D. M.; Kambhampati, P. *J. Chem. Phys.* **2008**, 129, (8), 084701-8.
115. Jones, M.; Lo, S. S.; Scholes, G. D. *The Journal of Physical Chemistry C* **2009**, 113, (43), 18632-18642.
116. Henry, C. H.; Nassau, K. *Phys. Rev. B* **1970**, 1, (4), 1628-1634.
117. Klimov, V.; Haring Bolivar, P.; Kurz, H. *Physical Review B* **1995**, 52, (7), 4728-4731.
118. Inoshita, T.; Sakaki, H. *Physical Review B* **1992**, 46, (11), 7260-7263.

119. Klimov, V. I.; Schwarz, C. J.; McBranch, D. W.; Leatherdale, C. A.; Bawendi, M. G. *Physical Review B* **1999**, 60, (4), R2177-R2180.
120. Beard, M. C.; Luther, J. M.; Semonin, O. E.; Nozik, A. J. *Accounts of Chemical Research* **2013**, 46, (6), 1252-1260.
121. Klimov, V. I. *The Journal of Physical Chemistry B* **2000**, 104, (26), 6112-6123.
122. Balet, L. P.; Ivanov, S. A.; Piryatinski, A.; Achermann, M.; Klimov, V. I. *Nano Letters* **2004**, 4, (8), 1485-1488.
123. Pan, Z.; Zhang, H.; Cheng, K.; Hou, Y.; Hua, J.; Zhong, X. *ACS Nano* **2012**, 6, (5), 3982-3991.
124. Kim, S.; Fisher, B.; Eisler, H.-J.; Bawendi, M. *J. Am. Chem. Soc.* **2003**, 125, (38), 11466-11467.
125. Lo, S. S.; Mirkovic, T.; Chuang, C.-H.; Burda, C.; Scholes, G. D. *Advanced Materials* **2011**, 23, (2), 180-197.
126. Hewa-Kasakarage, N. N.; El-Khoury, P. Z.; Tarnovsky, A. N.; Kirsanova, M.; Nemitz, I.; Nemchinov, A.; Zamkov, M. *ACS Nano* **2010**, 4, (4), 1837-1844.
127. Wu, K.; Hill, L. J.; Chen, J.; McBride, J. R.; Pavlopolous, N. G.; Richey, N. E.; Pyun, J.; Lian, T. *ACS Nano* **2015**, 9, (4), 4591-4599.
128. Chuang, C.-H.; Lo, S. S.; Scholes, G. D.; Burda, C. *J. Phys. Chem. Lett.* **2010**, 1, (17), 2530-2535.
129. Allione, M.; Ballester, A.; Li, H.; Comin, A.; Movilla, J. L.; Climente, J. I.; Manna, L.; Moreels, I. *ACS Nano* **2013**, 7, (3), 2443-2452.
130. Kobayashi, Y.; Chuang, C.-H.; Burda, C.; Scholes, G. D. *The Journal of Physical Chemistry C* **2014**, 118, (29), 16255-16263.
131. Lam, C.; Zhang, Y. F.; Tang, Y. H.; Lee, C. S.; Bello, I.; Lee, S. T. *Journal of Crystal Growth* **2000**, 220, (4), 466-470.

132. Ancona, M. G.; Kooi, S. E.; Kruppa, W.; Snow, A. W.; Foos, E. E.; Whitman, L. J.; Park, D.; Shirey, L. *Nano Letters* **2003**, 3, (2), 135-138.
133. Burda, C.; Chen, X.; Narayanan, R.; El-Sayed, M. A. *Chemical Reviews* **2005**, 105, (4), 1025-1102.
134. El-Sayed, M. A. *Accounts of Chemical Research* **2004**, 37, (5), 326-333.
135. Murray, C. B.; Sun, S.; Gaschler, W.; Doyle, H.; Betley, T. A.; Kagan, C. R. *IBM J. Res. Dev.* **2001**, 45, (1), 47-56.
136. Liu, H.; Owen, J. S.; Alivisatos, A. P. *J. Am. Chem. Soc.* **2007**, 129, (2), 305-312.
137. Steckel, J. S.; Yen, B. K. H.; Oertel, D. C.; Bawendi, M. G. *J. Am. Chem. Soc.* **2006**, 128, (40), 13032-13033.
138. Marcus, R. A. *J. Chem. Phys.* **1956**, 24, (5), 966-978.
139. Marcus, R. A. *Annu. Rev. Phys. Chem.* **1964**, 15, (1), 155-196.
140. Watson, D. F.; Meyer, G. J. *Annu. Rev. Phys. Chem.* **2005**, 56, (1), 119-156.
141. Warren, B. E., *X-Ray Diffraction*. Dover Publications: 1990.
142. Authier, A., *Dynamical Theory of X-Ray Diffraction*. IUCr & Oxford Science Publication: 2001.
143. Joint Committee on Powder Diffraction Standards (JCPDS), International Centre for Diffraction Data (ICDD), Swarthmore, PA. .
144. Cowley, J. M.; Smith, D. J. *Acta Crystallographica Section A* **1987**, 43, (6), 737-751.
145. Williams, D. B.; Carter, C. B., *Transmission Electron Microscopy: A Textbook for Materials Science*. 2009; Vol. 2<sup>nd</sup> ed.
146. Reimer, L., *Transmission electron microscopy: physics of image formation and microanalysis*. Springer: 1997.
147. Erni, R., *Aberration-Corrected Imaging in Transmission Electron Microscopy: An Introduction*. Imperial College Press, London: 2010.

- 
148. Reimer, L.; Kohl, H., *Transmission electron microscopy: Physics of Image Formation*. Springer Science + Business Media: 2008; Vol. 4<sup>th</sup> edition.
149. Otten, M. T.; Coene, W. M. J., *Ultramicroscopy*. 1993; Vol. 48, p 77.
150. Michalowsky, L.; ; Magnettechnik; ; Leipzig, F., 1993.
151. Bu, K. H. J.; Boer., s. a. F. R. d., *Physics of Magnetism and Magnetic Materials*. Kluwer Academic/Plenum Publishers: 2003.
152. K.E.Jarvis, A. L.; Gray, R. S. H., *andbook of Inductively couples Mass Spectrometry*. Blabkie, Chapman and Hall: Glasgow: New York, 1992.
153. Yu, W. W.; Qu, L.; Guo, W.; Peng, X. *Chemistry of Materials* **2003**, 15, (14), 2854-2860.
154. Hollas, J. M., *Modern Spectroscopy*. 3rd Ed. ed.; John Wiley and Sons: 1996.
155. Bernath, P. F., *Spectra of atoms and molecules*. Oxford University Press: 1995.
156. Smith, B. C., *Quantitative Spectroscopy: Theory and Practice*. Academic Press: 2002.
157. Lakowicz, J. R., *Principles of Fluorescence Spectroscopy*. 3rd ed.; Springer: New York, 2006.
158. Albani, J. R., *Principles and applications of Fluorescence Spectroscopy*. Blackwell Publishing: 2007.
159. Lackowicz, J. R., *Principles of fluorescence spectroscopy, 3rd ed*. Springer: New York, 2006.
160. Gilbert, A. B., J.; Wagner, P. J., *Essential of Molecular Photochemistry* Blackwell science Inc.: Cambridge, USA, 1991.
161. Birks, J. B., *Photo Physics of Aromatic Molecules* Wiley-Interscience: New York, 1970.
162. Crosby, G. A.; Demas, J. N. *J. Phys. Chem.* **1971**, 75, (8), 991-1024.

- 
163. O'Connor, D. V.; Phillips, D., *Time-Correlated Single-Photon Counting*. Academic Press: London: 1984.
164. Becker, W., *Advanced Time-Correlated Single Photon Counting Techniques*. Springer: 2005.
165. Demas, J. N., *Excited state lifetime measurement*. Academic press: : New York,, 1983.
166. Ware, W. R., *Creation and detection of the Excited State*. Lamola, A. A., Ed.; Marcel Dekker: New York, 1971; Vol. Vol. 1, Part A.
167. Kahlow, M. A.; Jarzęba, W. o.; DuBruil, T. P.; Barbara, P. F. *Rev. Sci. Instrum.* **1988**, 59, (7), 1098-1109.
168. Shah, J. *IEEE Journal of Quantum Electronics* **1988**, 24, (2), 276-288.
169. Foggi, P.; Bussotti, L.; Neuwahl, F. V. R. *International Journal of Photoenergy* **2001**, 3, (2).
170. Shah, J., *Ultrafast spectroscopy of semiconductors and semiconductor nanostructures*. 2<sup>nd</sup> Ed., Springer: 1999.
171. Moulton, P. F. *Journal of the Optical Society of America B* **1986**, 3, (1), 125-133.
172. Harrison, J.; Finch, A.; Rines, D. M.; Rines, G. A.; Moulton, P. F. *Opt. Lett.* **1991**, 16, (8), 581-583.
173. Demtröder, W., *Laser Spectroscopy: Basic concept and instrumentation*. 3<sup>rd</sup> edition, Springer (India) Private Limited: 2004.
174. Sanchez, A.; Fahey, R. E.; Strauss, A. J.; Aggarwal, R. L. *Opt. Lett.* **1986**, 11, (6), 363-364.
175. Abramczyk, H., *Introduction to Laser Spectroscopy*. Elsevier: 2005.
176. Steinmeyer, G.; Sutter, D. H.; Gallmann, L.; Matuschek, N.; Keller, U. *Science* **1999**, 286, (5444), 1507-1512.

- 
177. Brabec, T.; Spielmann, C.; Curley, P. F.; Krausz, F. *Opt. Lett.* **1992**, 17, (18), 1292-1294.
178. Asaki, M. T.; Huang, C.-P.; Garvey, D.; Zhou, J.; Kapteyn, H. C.; Murnane, M. M. *Opt. Lett.* **1993**, 18, (12), 977-979.
179. Sarukura, N.; Ishida, Y.; Nakano, H. *Opt. Lett.* **1991**, 16, (3), 153-155.
180. Zhu, X.; Piché, M.; Goodnob, G. D.; Miller, R. J. D. *Optics Communications* **1998**, 145, (1-6), 123-127.
181. Martin, M. M.; Hynes, J. T., *Femtochemistry and Femtobiology: Ultrafast Events in Molecular Science*. Elsevier, 1<sup>st</sup> edition: 2004.
182. Strickland, D.; Mourou, G. *Optics Communications* **1985**, 56, (3), 219-221.
183. Rullière, C., *Femtosecond Laser Pulses: Principles and Experiments*. Springer Science + Business Media: 2005.
184. Georges, P.; Estable, F.; Salin, F.; Poizat, J. P.; Grangier, P.; Brun, A. *Opt. Lett.* **1991**, 16, (3), 144-146.
185. Treacy, E. *IEEE Journal of Quantum Electronics* **1969**, 5, (9), 454-458.
186. Norris, D. J.; Efros, A. L.; Rosen, M.; Bawendi, M. G. *Physical Review B* **1996**, 53, (24), 16347-16354.
187. Steigerwald, M. L.; Brus, L. E. *Accounts of Chemical Research* **1990**, 23, (6), 183-188.
188. Norris, D. J.; Bawendi, M. G. *Physical Review B* **1996**, 53, (24), 16338-16346.
189. Schaller, R. D.; Pietryga, J. M.; Klimov, V. I. *Nano Letters* **2007**, 7, (11), 3469-3476.
190. Schaller, R. D.; Sykora, M.; Pietryga, J. M.; Klimov, V. I. *Nano Letters* **2006**, 6, (3), 424-429.
191. Yang, Y.; Rodríguez-Córdoba, W.; Lian, T. *Nano Letters* **2012**, 12, (8), 4235-4241.
192. Ellingson, R. J.; Beard, M. C.; Johnson, J. C.; Yu, P.; Micic, O. I.; Nozik, A. J.; Shabaev, A.; Efros, A. L. *Nano Letters* **2005**, 5, (5), 865-871.

193. Pandey, A.; Guyot-Sionnest, P. *Science* **2008**, 322, 929-932.
194. Sanehira, E. M.; Marshall, A. R.; Christians, J. A.; Harvey, S. P.; Ciesielski, P. N.; Wheeler, L. M.; Schulz, P.; Lin, L. Y.; Beard, M. C.; Luther, J. M. *Science Advances* **2017**, 3.
195. Yella, A.; Lee, H.-W.; Tsao, H. N.; Yi, C.; Chandiran, A. K.; Nazeeruddin, M. K.; Diau, E. W.-G.; Yeh, C.-Y.; Zakeeruddin, S. M.; Grätzel, M. *Science* **2011**, 334, (6056), 629-634.
196. Tvrđy, K.; Frantsuzov, P. A.; Kamat, P. V. *Proceedings of the National Academy of Sciences* **2011**, 108, (1), 29-34.
197. Morris-Cohen, A. J.; Peterson, M. D.; Frederick, M. T.; Kamm, J. M.; Weiss, E. A. *The Journal of Physical Chemistry Letters* **2012**, 3, (19), 2840-2844.
198. Spanhel, L.; Weller, H.; Henglein, A. *Journal of the American Chemical Society* **1987**, 109, (22), 6632-6635.
199. Ramsden, J. J.; Grätzel, M. *Chemical Physics Letters* **1986**, 132, (3), 269-272.
200. Tisdale, W. A.; Williams, K. J.; Timp, B. A.; Norris, D. J.; Aydil, E. S.; Zhu, X.-Y. *Science* **2010**, 328, (5985), 1543-1547.
201. Rossetti, R.; Beck, S. M.; Brus, L. E. *Journal of the American Chemical Society* **1984**, 106, (4), 980-984.
202. Burda, C.; Green, T. C.; Link, S.; El-Sayed, M. A. *The Journal of Physical Chemistry B* **1999**, 103, (11), 1783-1788.
203. Robel, I.; Kuno, M.; Kamat, P. V. *Journal of the American Chemical Society* **2007**, 129, (14), 4136-4137.
204. Boulesbaa, A.; Issac, A.; Stockwell, D.; Huang, Z.; Huang, J.; Guo, J.; Lian, T. *Journal of the American Chemical Society* **2007**, 129, (49), 15132-15133.
205. Morris-Cohen, A. J.; Frederick, M. T.; Cass, L. C.; Weiss, E. A. *Journal of the American Chemical Society* **2011**, 133, (26), 10146-10154.
206. Song, N.; Zhu, H.; Jin, S.; Lian, T. *ACS Nano* **2011**, 5, (11), 8750-8759.

- 
207. Boulesbaa, A.; Huang, Z.; Wu, D.; Lian, T. *The Journal of Physical Chemistry C* **2009**, 114, (2), 962-969.
208. Huang, J.; Huang, Z.; Yang, Y.; Zhu, H.; Lian, T. *Journal of the American Chemical Society* **2010**, 132, (13), 4858-4864.
209. Huang, J.; Huang, Z.; Jin, S.; Lian, T. *The Journal of Physical Chemistry C* **2008**, 112, (49), 19734-19738.
210. Sharma, S. N.; Pillai, Z. S.; Kamat, P. V. *The Journal of Physical Chemistry B* **2003**, 107, (37), 10088-10093.
211. Klimov, V.; Mikhailovsky, A.; McBranch, D.; Leatherdale, C.; Bawendi, M. *Physical Review B* **2000**, 61, (20), R13349-R13352.
212. Burda, C.; Link, S.; Mohamed, M.; El-Sayed, M. *The Journal of Physical Chemistry B* **2001**, 105, (49), 12286-12292.
213. Kamat, P. V.; Christians, J. A.; Radich, J. G. *Langmuir* **2014**, 30, (20), 5716-5725.
214. Chakrapani, V.; Baker, D.; Kamat, P. V. *Journal of the American Chemical Society* **2011**, 133, (24), 9607-9615.
215. Choi, H.; Nicolaescu, R.; Paek, S.; Ko, J.; Kamat, P. V. *ACS Nano* **2011**, 5, (11), 9238-9245.
216. Shalom, M.; Albero, J.; Tachan, Z.; Martínez-Ferrero, E.; Zaban, A.; Palomares, E. *The Journal of Physical Chemistry Letters* **2010**, 1, (7), 1134-1138.
217. Mora-Seró, I.; Bisquert, J. *The Journal of Physical Chemistry Letters* **2010**, 1, (20), 3046-3052.
218. Williams, K. J.; Nelson, C. A.; Yan, X.; Li, L.-S.; Zhu, X. *ACS Nano* **2013**, 7, (2), 1388-1394.
219. Pandey, A.; Guyot-Sionnest, P. *The Journal of Physical Chemistry Letters* **2010**, 1, (1), 45-47.

220. Dong, Y.; Choi, J.; Jeong, H.-K.; Son, D. H. *Journal of the American Chemical Society* **2015**, 137, (16), 5549-5554.
221. Jing, P.; Ji, W.; Yuan, X.; Qu, S.; Xie, R.; Ikezawa, M.; Zhao, J.; Li, H.; Masumoto, Y. *ACS Applied Materials & Interfaces* **2015**, 7, (15), 7938-7944.
222. Frederick, M. T.; Amin, V. A.; Swenson, N. K.; Ho, A. Y.; Weiss, E. A. *Nano Letters* **2013**, 13, (1), 287-292.
223. Koole, R.; Schapotschnikow, P.; de Mello Donegá, C.; Vlugt, T. J. H.; Meijerink, A. *ACS Nano* **2008**, 2, (8), 1703-1714.
224. Jin, S.; Harris, R. D.; Lau, B.; Aruda, K. O.; Amin, V. A.; Weiss, E. A. *Nano Letters* **2014**, 14, (9), 5323-5328.
225. Pan, Z.; Mora-Seró, I.; Shen, Q.; Zhang, H.; Li, Y.; Zhao, K.; Wang, J.; Zhong, X.; Bisquert, J. *Journal of the American Chemical Society* **2014**, 136, (25), 9203-9210.
226. Kim, S.; Kang, M.; Kim, S.; Heo, J.-H.; Noh, J. H.; Im, S. H.; Seok, S. I.; Kim, S.-W. *ACS Nano* **2013**, 7, (6), 4756-4763.
227. Sablon, K. A.; Little, J. W.; Mitin, V.; Sergeev, A.; Vagidov, N.; Reinhardt, K. *Nano Letters* **2011**, 11, (6), 2311-2317.
228. Tyrakowski, C. M.; Shamirian, A.; Rowland, C. E.; Shen, H.; Das, A.; Schaller, R. D.; Snee, P. T. *Chemistry of Materials* **2015**, 27, (21), 7276-7281.
229. Beane, G.; Boldt, K.; Kirkwood, N.; Mulvaney, P. *The Journal of Physical Chemistry C* **2014**, 118, (31), 18079-18086.
230. Kilina, S.; Cui, P.; Fischer, S. A.; Tretiak, S. *The Journal of Physical Chemistry Letters* **2014**, 5, (20), 3565-3576.
231. Sykora, M.; Petruska, M. A.; Alstrum-Acevedo, J.; Bezel, I.; Meyer, T. J.; Klimov, V. I. *Journal of the American Chemical Society* **2006**, 128, (31), 9984-9985.

232. Jin, S.; Tagliazucchi, M.; Son, H.-J.; Harris, R. D.; Aruda, K. O.; Weinberg, D. J.; Nepomnyashchii, A. B.; Farha, O. K.; Hupp, J. T.; Weiss, E. A. *The Journal of Physical Chemistry C* **2015**, 119, (9), 5195-5202.
233. Maity, P.; Debnath, T.; Chopra, U.; Ghosh, H. N. *Nanoscale* **2015**, 7, (6), 2698-2707.
234. Debnath, T.; Maity, P.; Maiti, S.; Ghosh, H. N. *The Journal of Physical Chemistry Letters* **2014**, 5, (16), 2836-2842.
235. Dworak, L.; Roth, S.; Wachtveitl, J. *The Journal of Physical Chemistry C* **2017**, 121, (5), 2613-2619.
236. Maity, P.; Debnath, T.; Ghosh, H. N. *The Journal of Physical Chemistry Letters* **2013**, 4, (23), 4020-4025.
237. Peterson, M. D.; Jensen, S. C.; Weinberg, D. J.; Weiss, E. A. *ACS Nano* **2014**, 8, (3), 2826-2837.
238. Duxbury, D. F. *Chemical Reviews* **1993**, 93, (1), 381-433.
239. Maity, P.; Debnath, T.; Akbar, A.; Verma, S.; Ghosh, H. N. *The Journal of Physical Chemistry C* **2013**, 117, (34), 17531-17539.
240. Baker, D. R.; Kamat, P. V. *Langmuir* **2010**, 26, (13), 11272-11276.
241. Hines, D. A.; Kamat, P. V. *ACS Applied Materials & Interfaces* **2014**, 6, (5), 3041-3057.
242. Frederick, M. T.; Amin, V. A.; Weiss, E. A. *The Journal of Physical Chemistry Letters*, 634-640.
243. Knowles, K. E.; Frederick, M. T.; Tice, D. B.; Morris-Cohen, A. J.; Weiss, E. A. *The Journal of Physical Chemistry Letters* **2012**, 3, (1), 18-26.
244. Rawalekar, S.; Kaniyankandy, S.; Verma, S.; Ghosh, H. N. *The Journal of Physical Chemistry C* **2010**, 114, (3), 1460-1466.
245. Kaniyankandy, S.; Rawalekar, S.; Verma, S.; Ghosh, H. N. *The Journal of Physical Chemistry C* **2011**, 115, (5), 1428-1435.

246. Ramakrishna, G.; Ghosh, H. N.; Singh, A. K.; Palit, D. K.; Mittal, J. P. *The Journal of Physical Chemistry B* **2001**, 105, (51), 12786-12796.
247. Klimov, V. I.; McBranch, D. W.; Leatherdale, C. A.; Bawendi, M. G. *Physical Review B* **1999**, 60, (19), 13740-13749.
248. Knowles, K. E.; Peterson, M. D.; McPhail, M. R.; Weiss, E. A. *The Journal of Physical Chemistry C* **2013**, 117, (20), 10229-10243.
249. Permogorov, S. *physica status solidi (b)* **1975**, 68, (1), 9-42.
250. Cho, C.-H.; Aspetti, C. O.; Turk, M. E.; Kikkawa, J. M.; Nam, S.-W.; Agarwal, R. *Nat Mater* **2011**, 10, (9), 669-675.
251. Mondal, R.; Bansal, B.; Mandal, A.; Chakrabarti, S.; Pal, B. *Physical Review B* **2013**, 87, (11), 115317.
252. Mora-Seró, I.; Giménez, S.; Fabregat-Santiago, F.; Gómez, R.; Shen, Q.; Toyoda, T.; Bisquert, J. *Accounts of Chemical Research* **2009**, 42, (11), 1848-1857.
253. Barea, E. M.; Shalom, M.; Giménez, S.; Hod, I.; Mora-Seró, I.; Zaban, A.; Bisquert, J. *Journal of the American Chemical Society* **2010**, 132, (19), 6834-6839.
254. Smith, A. M.; Mohs, A. M.; Nie, S. *Nat Nano* **2009**, 4, (1), 56-63.
255. Debnath, T.; Maity, P.; Ghosh, H. N. *Chemistry – A European Journal* **2014**, 20, (41), 13305-13313.
256. Kamat, P. V. *Accounts of Chemical Research* **2012**, 45, 1906.
257. Debnath, T.; Maity, P.; Banerjee, T.; Das, A.; Ghosh, H. N. *The Journal of Physical Chemistry C* **2015**, 119, (7), 3522-3529.
258. Harris, R. D.; Bettis Homan, S.; Kodaimati, M.; He, C.; Nepomnyashchii, A. B.; Swenson, N. K.; Lian, S.; Calzada, R.; Weiss, E. A. *Chemical Reviews* **2016**.
259. Zhu, H.; Lian, T. *Energy & Environmental Science* **2012**, 5, (11), 9406-9418.

260. Huang, J.; Stockwell, D.; Huang, Z.; Mohler, D. L.; Lian, T. *Journal of the American Chemical Society* **2008**, 130, (17), 5632-5633.
261. VanEngelen, M. R.; Szilagyi, R. K.; Gerlach, R.; Lee, B. D.; Apel, W. A.; Peyton, B. M. *Environmental Science & Technology* **2011**, 45, (3), 937-942.
262. Trenfield, M. A.; McDonald, S.; Kovacs, K.; Leshner, E. K.; Pringle, J. M.; Markich, S. J.; Ng, J. C.; Noller, B.; Brown, P. L.; van Dam, R. A. *Environmental Science & Technology* **2011**, 45, (7), 3075-3081.
263. Schnug, E.; Lottermoser, B. G. *Environmental Science & Technology* **2013**, 47, (6), 2433-2434.
264. Yang, C.-T.; Han, J.; Gu, M.; Liu, J.; Li, Y.; Huang, Z.; Yu, H.-Z.; Hu, S.; Wang, X. *Chemical Communications* **2015**, 51, (59), 11769-11772.
265. Rathore, D. P. S. *Talanta* **2008**, 77, (1), 9-20.
266. Altmaier, M.; Gaona, X.; Fanghänel, T. *Chemical Reviews* **2013**, 113, (2), 901-943.
267. Abbasi, S. A. *International Journal of Environmental Analytical Chemistry* **1989**, 36, (3), 163-172.
268. Tang, Q.; Yuan, Y.; Xiao, X.; Guo, P.; Hu, J.; Ma, D.; Gao, Y. *Microchimica Acta* **2013**, 180, (11), 1059-1064.
269. Peled, Y.; Krent, E.; Tal, N.; Tobias, H.; Mandler, D. *Analytical Chemistry* **2015**, 87, (1), 768-776.
270. Dhara, S.; Misra, N. L.; Aggarwal, S. K. *Spectrochimica Acta Part B: Atomic Spectroscopy* **2008**, 63, (12), 1395-1398.
271. Angeli, V.; Biagi, S.; Ghimenti, S.; Onor, M.; D'Ulivo, A.; Bramanti, E. *Spectrochimica Acta Part B: Atomic Spectroscopy* **2011**, 66, (11-12), 799-804.
272. Resch-Genger, U.; Grabolle, M.; Cavaliere-Jaricot, S.; Nitschke, R.; Nann, T. *Nat Meth* **2008**, 5, (9), 763-775.

273. Li, G.-S.; Zhang, D.-Q.; Yu, J. C. *Environmental Science & Technology* **2009**, 43, (18), 7079-7085.
274. Li, H.; He, X.; Kang, Z.; Huang, H.; Liu, Y.; Liu, J.; Lian, S.; Tsang, C. H. A.; Yang, X.; Lee, S.-T. *Angewandte Chemie International Edition* **2010**, 49, (26), 4430-4434.
275. Kamat, P. V. *The Journal of Physical Chemistry C* **2008**, 112, (48), 18737-18753.
276. Wang, Y.; Hu, R.; Lin, G.; Roy, I.; Yong, K.-T. *ACS Applied Materials & Interfaces* **2013**, 5, (8), 2786-2799.
277. Bruchez, M.; Moronne, M.; Gin, P.; Weiss, S.; Alivisatos, A. P. *Science* **1998**, 281, (5385), 2013-2016.
278. Chavali, R.; Gunda, N. S. K.; Naicker, S.; Mitra, S. K. *Analytical Chemistry Research* **2015**, 6, 26-31.
279. Cametti, M.; Rissanen, K. *Chemical Society Reviews* **2013**, 42, (5), 2016-2038.
280. Roy, A.; Datar, A.; Kand, D.; Saha, T.; Talukdar, P. *Organic & Biomolecular Chemistry* **2014**, 12, (13), 2143-2149.
281. Zheng, X.; Zhu, W.; Liu, D.; Ai, H.; Huang, Y.; Lu, Z. *ACS Applied Materials & Interfaces* **2014**, 6, (11), 7996-8000.
282. Zhou, Y.; Zhang, J. F.; Yoon, J. *Chemical Reviews* **2014**, 114, (10), 5511-5571.
283. Hinterholzinger, F. M.; Rühle, B.; Wuttke, S.; Karaghiosoff, K.; Bein, T. *Scientific Reports* **2013**, 3, 2562.
284. Kim, S. Y.; Hong, J.-I. *Organic Letters* **2007**, 9, (16), 3109-3112.
285. Dhenadhayalan, N.; Lin, K.-C.; Suresh, R.; Ramamurthy, P. *The Journal of Physical Chemistry C* **2016**, 120, (2), 1252-1261.
286. Wang, Y.; Hu, A. *Journal of Materials Chemistry C* **2014**, 2, (34), 6921-6939.

287. Sun, Y.-P.; Zhou, B.; Lin, Y.; Wang, W.; Fernando, K. A. S.; Pathak, P.; Meziani, M. J.; Harruff, B. A.; Wang, X.; Wang, H.; Luo, P. G.; Yang, H.; Kose, M. E.; Chen, B.; Veca, L. M.; Xie, S.-Y. *Journal of the American Chemical Society* **2006**, 128, (24), 7756-7757.
288. Qian, Z.; Shan, X.; Chai, L.; Ma, J.; Chen, J.; Feng, H. *ACS Applied Materials & Interfaces* **2014**, 6, (9), 6797-6805.
289. Bhunia, S. K.; Saha, A.; Maity, A. R.; Ray, S. C.; Jana, N. R. *Scientific Reports* **2013**, 3, 1473.
290. Loo, A. H.; Sofer, Z.; Bouša, D.; Ulbrich, P.; Bonanni, A.; Pumera, M. *ACS Applied Materials & Interfaces* **2016**, 8, (3), 1951-1957.
291. Liu, Z.; Chen, X.; Zhang, X.; Gooding, J. J.; Zhou, Y. *Advanced Healthcare Materials* **2016**, 5, (12), 1380-1380.
292. Das, R. K.; Kar, J. P.; Mohapatra, S. *Industrial & Engineering Chemistry Research* **2016**, 55, (20), 5902-5910.
293. Xu, H.; Yang, X.; Li, G.; Zhao, C.; Liao, X. *Journal of Agricultural and Food Chemistry* **2015**, 63, (30), 6707-6714.
294. Gogoi, N.; Barooah, M.; Majumdar, G.; Chowdhury, D. *ACS Applied Materials & Interfaces* **2015**, 7, (5), 3058-3067.
295. Li, H.; Zhai, J.; Sun, X. *Langmuir* **2011**, 27, (8), 4305-4308.
296. Zhou, L.; Lin, Y.; Huang, Z.; Ren, J.; Qu, X. *Chemical Communications* **2012**, 48, (8), 1147-1149.
297. Xie, R.; Kolb, U.; Li, J.; Basché, T.; Mews, A. *Journal of the American Chemical Society* **2005**, 127, (20), 7480-7488.
298. Zhang, L.; He, R.; Gu, H.-C. *Applied Surface Science* **2006**, 253, (5), 2611-2617.
299. Jang, E.; Jun, S.; Chung, Y.; Pu, L. *The Journal of Physical Chemistry B* **2004**, 108, (15), 4597-4600.

300. Aldana, J.; Wang, Y. A.; Peng, X. *Journal of the American Chemical Society* **2001**, 123, (36), 8844-8850.
301. J.J Katz, G. T. S., L.R. Morss *Chapman and Hall LTD, London* **1986**, 1, (2), 169-442.
302. Gong, K.; Kelley, D. F. *The Journal of Physical Chemistry Letters* **2015**, 6, (9), 1559-1562.
303. Qin, H.; Niu, Y.; Meng, R.; Lin, X.; Lai, R.; Fang, W.; Peng, X. *Journal of the American Chemical Society* **2014**, 136, (1), 179-187.
304. van Embden, J.; Jasieniak, J.; Mulvaney, P. *Journal of the American Chemical Society* **2009**, 131, (40), 14299-14309.
305. Gong, K.; Martin, J. E.; Shea-Rohwer, L. E.; Lu, P.; Kelley, D. F. *The Journal of Physical Chemistry C* **2015**, 119, (4), 2231-2238.
306. Calzada, R.; Thompson, C. M.; Westmoreland, D. E.; Edme, K.; Weiss, E. A. *Chemistry of Materials* **2016**.
307. Jia, Y.; Chen, J.; Wu, K.; Kaledin, A.; Musaev, D. G.; Xie, Z.; Lian, T. *Chemical Science* **2016**, 7, (7), 4125-4133.
308. Ding, T. X.; Olshansky, J. H.; Leone, S. R.; Alivisatos, A. P. *Journal of the American Chemical Society* **2015**, 137, (5), 2021-2029.
309. Maity, P.; Debnath, T.; Ghosh, H. N. *The Journal of Physical Chemistry C* **2015**, 119, (46), 26202-26211.
310. Tian, L.; Ghosh, D.; Chen, W.; Pradhan, S.; Chang, X.; Chen, S. *Chemistry of Materials* **2009**, 21, (13), 2803-2809.
311. Jia, X.; Li, J.; Wang, E. *Nanoscale* **2012**, 4, (18), 5572-5575.
312. Dekaliuk, M. O.; Viagin, O.; Malyukin, Y. V.; Demchenko, A. P. *Physical Chemistry Chemical Physics* **2014**, 16, (30), 16075-16084.

313. Singh, P.; Prabhune, A. A.; Tripathi, C. S. P.; Guin, D. *ACS Sustainable Chemistry & Engineering* **2017**, 5, (1), 982-987.
314. Wang, X.; Cao, L.; Lu, F.; Mezziani, M. J.; Li, H.; Qi, G.; Zhou, B.; Harruff, B. A.; Kermarrec, F.; Sun, Y.-P. *Chemical Communications* **2009**, (25), 3774-3776.
315. Fernando, K. A. S.; Sahu, S.; Liu, Y.; Lewis, W. K.; Gulians, E. A.; Jafariyan, A.; Wang, P.; Bunker, C. E.; Sun, Y.-P. *ACS Applied Materials & Interfaces* **2015**, 7, (16), 8363-8376.
316. Busquim e Silva, R.; Kazimi, M. S.; Hejzlar, P. *Energy & Environmental Science* **2010**, 3, (8), 996-1010.
317. Nuclear Share of Electricity Generation. In IAEA: 2015.
318. Sather, A. C.; Berryman, O. B.; Rebek, J. *Journal of the American Chemical Society* **2010**, 132, (39), 13572-13574.
- 319 Davies, R. V.; Kennedy, J.; McIlroy, R. W.; Spence, R.; Hill, K. M. *Nature* **1964**, 203, (4950), 1110-1115.
320. Tabushi, I.; Kobuke, Y.; Nishiya, T. *Nature* **1979**, 280, (5724), 665-666.
321. Trenfield, M. A.; Ng, J. C.; Noller, B. N.; Markich, S. J.; Dam, R. A. v. *Environmental Science & Technology* **2011**, 45, (7), 3082-3089.
322. Chatterjee, S.; Bryantsev, V. S.; Brown, S.; Johnson, J. C.; Grant, C. D.; Mayes, R. T.; Hay, B. P.; Dai, S.; Saito, T. *Industrial & Engineering Chemistry Research* **2016**, 55, (15), 4161-4169.
323. Zeng, Z.; Wei, Y.; Shen, L.; Hua, D. *Industrial & Engineering Chemistry Research* **2015**, 54, (35), 8699-8705.
324. Das, S.; Oyola, Y.; Mayes, R. T.; Janke, C. J.; Kuo, L. J.; Gill, G.; Wood, J. R.; Dai, S. *Industrial & Engineering Chemistry Research* **2016**, 55, (15), 4103-4109.

325. Piechowicz, M.; Abney, C. W.; Zhou, X.; Thacker, N. C.; Li, Z.; Lin, W. *Industrial & Engineering Chemistry Research* **2016**, *55*, (15), 4170-4178.
326. Sellin, R.; Alexandratos, S. D. *Industrial & Engineering Chemistry Research* **2013**, *52*, (33), 11792-11797.
327. Carboni, M.; Abney, C. W.; Taylor-Pashow, K. M. L.; Vivero-Escoto, J. L.; Lin, W. *Industrial & Engineering Chemistry Research* **2013**, *52*, (43), 15187-15197.
328. Park, J.; Jeters, R. T.; Kuo, L.-J.; Strivens, J. E.; Gill, G. A.; Schlafer, N. J.; Bonheyo, G. T. *Industrial & Engineering Chemistry Research* **2016**, *55*, (15), 4278-4284.
329. Vivero-Escoto, J. L.; Carboni, M.; Abney, C. W.; deKrafft, K. E.; Lin, W. *Microporous and Mesoporous Materials* **2013**, *180*, 22-31.
330. Parker, B. F.; Knight, A. S.; Vukovic, S.; Arnold, J.; Francis, M. B. *Industrial & Engineering Chemistry Research* **2016**, *55*, (15), 4187-4194.
331. Oyola, Y.; Janke, C. J.; Dai, S. *Industrial & Engineering Chemistry Research* **2016**, *55*, (15), 4149-4160.
332. Chouyyok, W.; Warner, C. L.; Mackie, K. E.; Warner, M. G.; Gill, G. A.; Addleman, R. S. *Industrial & Engineering Chemistry Research* **2016**, *55*, (15), 4195-4207.
333. Kim, J.; Tsouris, C.; Oyola, Y.; Janke, C. J.; Mayes, R. T.; Dai, S.; Gill, G.; Kuo, L.-J.; Wood, J.; Choe, K.-Y.; Schneider, E.; Lindner, H. *Industrial & Engineering Chemistry Research* **2014**, *53*, (14), 6076-6083.
334. Ling, L.; Zhang, W.-x. *Journal of the American Chemical Society* **2015**, *137*, (8), 2788-2791.
335. Galhoum, A. A.; Mahfouz, M. G.; Atia, A. A.; Abdel-Rehem, S. T.; Gomaa, N. A.; Vincent, T.; Guibal, E. *Industrial & Engineering Chemistry Research* **2015**, *54*, (49), 12374-12385.

336. Singer, D. M.; Chatman, S. M.; Ilton, E. S.; Rosso, K. M.; Banfield, J. F.; Waychunas, G. A. *Environmental Science & Technology* **2012**, 46, (7), 3821-3830.
337. Zhang, X.; Wang, J.; Li, R.; Dai, Q.; Gao, R.; Liu, Q.; Zhang, M. *Industrial & Engineering Chemistry Research* **2013**, 52, (30), 10152-10159.
338. Wang, L.; Yang, Z.; Gao, J.; Xu, K.; Gu, H.; Zhang, B.; Zhang, X.; Xu, B. *Journal of the American Chemical Society* **2006**, 128, (41), 13358-13359.
339. Sadeghi, S.; Azhdari, H.; Arabi, H.; Moghaddam, A. Z. *Journal of Hazardous Materials* **2012**, 215–216, 208-216.
340. Zhao, Y.; Li, J.; Zhao, L.; Zhang, S.; Huang, Y.; Wu, X.; Wang, X. *Chemical Engineering Journal* **2014**, 235, (Complete), 275-283.
341. Sayin, S.; Yilmaz, M. *Journal of Chemical & Engineering Data* **2011**, 56, (5), 2020-2029.
342. Rezaei, A.; Khani, H.; Masteri-Farahani, M.; Rofouei, M. K. *Analytical Methods* **2012**, 4, (12), 4107-4114.
343. Tan, L.; Wang, J.; Liu, Q.; Sun, Y.; Zhang, H.; Wang, Y.; Jing, X.; Liu, J.; Song, D. *Colloids and Surfaces A: Physicochemical and Engineering Aspects* **2015**, 466, 85-91.
344. Fan, F.-L.; Qin, Z.; Bai, J.; Rong, W.-D.; Fan, F.-Y.; Tian, W.; Wu, X.-L.; Wang, Y.; Zhao, L. *Journal of Environmental Radioactivity* **2012**, 106, 40-46.
345. Illés, E.; Tombácz, E. *Colloids and Surfaces A: Physicochemical and Engineering Aspects* **2003**, 230, (1–3), 99-109.
346. Yang, S.; Zong, P.; Ren, X.; Wang, Q.; Wang, X. *ACS Applied Materials & Interfaces* **2012**, 4, (12), 6891-6900.
347. Rodrigues, A.; Brito, A.; Janknecht, P.; Proenca, M. F.; Nogueira, R. *Journal of Environmental Monitoring* **2009**, 11, (2), 377-382.

348. Leggett, C. J.; Endrizzi, F.; Rao, L. *Industrial & Engineering Chemistry Research* **2016**, 55, (15), 4257-4263.
349. Ilton, E. S.; Wang, Z.; Boily, J.-F.; Qafoku, O.; Rosso, K. M.; Smith, S. C. *Environmental Science & Technology* **2012**, 46, (12), 6604-6611.
350. Krestou A, P. D. *The European Journal of Mineral Processing and Environmental Protection* **2004**, 4, (2), 113-129.